2014-07-28

Extending the Novel A-FEM to Model Arbitrary Cracking in Thermo-elastic Solids

Bao-Chan Do
University of Miami, dobaochan@gmail.com

UNIVERSITY OF MIAMI

EXTENDING THE NOVEL A-FEM TO MODEL ARBITRARY CRACKING IN THERMO-ELASTIC SOLIDS

By

Bao-Chan Do

A DISSERTATION

Submitted to the Faculty
of the University of Miami
in partial fulfillment of the requirements for
the degree of Doctor of Philosophy

Coral Gables, Florida

August 2014

UNIVERSITY OF MIAMI

A dissertation submitted in partial fulfillment of
the requirements for the degree of
Doctor of Philosophy

EXTENDING THE NOVEL A-FEM TO MODEL ARBITRARY CRACKING IN THERMO-ELASTIC SOLIDS

Bao-Chan Do

Approved:

_____ Qingda Yang, Ph.D. Associate Professor of Mechanical and Aerospace Engineering	_____ Weiyong Gu, Ph.D. Professor of Mechanical and Aerospace Engineering
_____ Ryan Karkkainen, Ph.D. Assistant Professor of Mechanical and Aerospace Engineering	_____ Ali Ghahremaninezhad, Ph.D. Assistant Professor of Civil, Architectural and Environmental Engineering
_____ James W. Giancaspro, Ph.D. Associate Professor of Civil, Architectural and Environmental Engineering	_____ M. Brian Blake, Ph.D. Dean of the Graduate School

DO, BAO-CHAN (Ph.D., Mechanical Engineering)
Extending the Novel A-FEM to Model Arbitrary Cracking in Thermo-elastic Solids (August 2014)

Abstract of a dissertation at the University of Miami.

Dissertation supervised by Associate Professor Qingda Yang.
No. of pages in text. (169)

A novel finite element capable of arbitrary cracking in solids under coupled thermo-mechanical loading has been formulated and implemented into the commercial software package ABAQUS as a user-defined element. The thermal-mechanical augmented finite element method (TM-AFEM) is an extension of the Augmented Finite Element Method (A-FEM) which includes temperature degrees of freedom (DoFs) so steady-state or transient temperature evolution and their direct effects on fracture processes in solids can be explicitly considered. The formulation incorporates a thermo-mechanical cohesive zone model (TM-CZM) to account for load and heat transfer across the intra-element weak and strong discontinuities (i.e. material interfaces and cracks). A novel condensing method is used to express the internal DoFs, both mechanical and thermal, as explicit functions of the external DoFs. It has been demonstrated through several numerical examples that, the TM-AFEM can provide a general framework for realistic simulation of thermal fracture problems both at single elemental level and at structural level. The advantages of the TM-AFEM include: (1) arbitrary crack initiation and propagation without *a priori* knowledge of the crack path; (2) greatly improved numerical efficiency as compared to similar advanced methods such as X-FEM or PNM because the TM-AFEM does not need extra external DoFs for crack evolution; and (3) the capability of accounting for multiple, complex crack evolution and interactions.

Dedicated to:

My parents, Đỗ Ngộc Khôi and Nguyễn Thị Bé.

Sắt đã mài thành kim.

Acknowledgement

I want to first express my deep gratitude towards my advisor for the past four years, Dr. Qingda Yang. This study would not have been possible without his guidance, support and patience. Both academically and personally, I have learned and benefitted greatly from him, and for that I cannot thank him enough.

Second, I wish also to show my appreciation for the members of my Ph.D. proposal and dissertation committee, Dr. Weiyong Gu, Dr. Jizhou Song, Dr. Ryan Lee Karkkainen, Dr. James W. Giancaspro and Dr. Ali Ghahremaninezhad, for their insight, feedback and suggestions towards the benefit of my study.

Third, a tremendous thanks to my colleagues. I must give special mention and thanks to Dr. Wei Liu and Dr. Seyedreza Mohammadizadeh whose work is the very foundation of this study. This dissertation would not have been possible without either of them. I wish to also thank Mr. Derek Schesser for his technical expertise and friendship as well as Dr. Medhi Naderi from whom I have learned greatly and had many fruitful discussions .

Fourth, I need to acknowledge my dear family and friends. I want to thank them all for being a part of my life and enriching it with their presence.

Finally, I want to acknowledge the joint financial support of NASA through the Florida Space Grant Consortium, the Department of Mechanical and Aerospace Engineering at the University of Miami and the National Hypersonic Science Center (NHSC, jointly funded by AFOSR and NASA, AFOSR Contract No. FA9550-09-1-0477).

TABLE OF CONTENTS

Page

LIST OF FIGURES viii
LIST OF TABLES xi
Chapter 1 Introduction 1
1.1 Overview 1
1.2 Why is Simulation of Thermal Fracture Needed? 1
1.3 Thermo-elasticity 3
1.4 Fracture Mechanics 6
1.4.1 Linear Elastic Fracture Mechanics 7
1.5 Cohesive Zone Models 10
1.6 Thermo-Mechanical Cohesive Zone Models 12
1.7 Numerical Methods for Arbitrary Cracking in Solids 13
1.8 Research Goal 16
Chapter 2 Two-Dimensional Thermo-Mechanical Cohesive Element 18
2.1 Overview 18
2.2 Problem Statement 18
2.3 Finite Element Formulation for Cohesive Elements 20
2.4 Piece-Wise Linear Thermo-Mechanical Cohesive Law 22
2.4.1 Mechanical Cohesive Law 22
2.4.2 Heat Transfer Cohesive Law 26
2.5 Thermo-Mechanical Cohesive Element 28
2.5.1 Cohesive Integration 33
2.5.2 Standard Cohesive Stress Integration Schemes 35
2.5.3 Improved Cohesive Stress Integration Schemes 36
2.5.4 Cohesive Heat Flux Integration 41
2.6 Element Validation 43
2.6.1 Single Element Mode I Wedge Opening Response 43
2.6.2 Cohesive Heat Transfer Response 47
2.6.3 Multiple Element Example, Mode I Opening of a DCB 55
2.7 Summary 61
Chapter 3 Single Crack Formulation for 1D ACTM-FE 64
3.1 Overview 64

3.2 Strength of Materials Approach to a Thermo-elastic Bar 64
3.3 FEM Approach to a Thermo-elastic Bar 71
3.3.1 Mechanical Process 72
3.3.2 Heat Transfer Process 77
3.4 Thermo-Mechanical FE Equations 81
3.5 Summary 84
Chapter 4 Single Crack Formulation for 2-D TM-AFEM 85
4.1 Overview 85
4.2 Problem Statement 85
4.2.1 Thermo-elastic Domain With No Discontinuity 85
4.2.2 Thermo-elastic Domain With a Discontinuity 87
4.3 Formulation of TM-AFEM with a Single Crack 88
4.3.1 TM-AFEM With no Discontinuity 89
4.3.2 Single Embedded Discontinuity for 4 Node Rectangular Elements 90
4.3.3 Heat Transfer FE Equations for 4 Node TM-AFEM With Two Subdomains 94
4.3.4 Mechanical FE Equations for 4 Node TM-AFEM With Two Subdomains 98
4.3.5 Subdomain Configurations for TM-AFEM with a Single Crack 103
4.4 Numerical Implementation 105
4.5 Single Element Validation 106
4.5.1 Comparison of TM-AFEM and Analytical Solutions to 1D Thermo-elastic Bar 106
4.5.2 Cohesive Heat Transfer Response 111
4.6 Summary 116
Chapter 5 Application of TM-AFEM Elements and Future Study 117
5.1 Overview 117
5.2 Crack Propagation in Single Edge Notch Test Configuration 118
5.3 Double Cantilever Beam 124
5.4 Two-Layered Composite Beam 128
5.5 Transverse Ply Cracking in Cross-ply Laminates 133
5.6 Crack Patterns in Thermal Barrier Coating (TBCs) Systems 137
5.6.1 Geometry and Thermo-elastic Properties of TBC Numerical Model 138
5.6.2 Determination of Cohesive Properties and Crack Initiation Criterion 140
5.6.3 Boundary Conditions for Simulation of a TBC System 141
5.6.4 Effect of Applied Temperature Gradient and Coating Thickness on Surface Cracks 142

5.6.5 Crack patterns in TBC Systems 143
5.7 Discussion on the Utility of TM-AFEM Elements for Thermal Fracture 147
5.8 Future Study 149
References 150
Appendix A Vectors and Matrices for TMCZ Element 160
A.1 Linear operators and interpolation matrices 160
A.2 Stresses at the integration points 160
A.3 Heat fluxes at the integration points 162
Appendix B Vectors and Matrices for TM-AFEM Element 164
B.1 Matrices for TM-AFEM With No Discontinuity 164
Appendix C Shape Functions and Quadrature Rules for Pentagonal Subdomains 166

LIST OF FIGURES

Page

Figure 1.1: The three fracture modes: (a) opening (b) in-plane shear and (c) out-of-plane shear. 6
Figure 1.2: Polar coordinates at the crack tip for a plate with a crack under applied tensile stress. 9
Figure 1.3: General definition of the traction-separation law for CZMs. 12
Figure 2.1: Body cut by a cohesive crack under thermo-mechanical loading. 19
Figure 2.2: (a) Mode-I Traction Separation Law; (b) Mode-II traction Separation Law. Numbers in red denote the respective segment numbers. 23
Figure 2.3: Bilinear cohesive heat transfer law. Numbers in blue denote the respective segment number. 27
Figure 2.4: Relationship between physical crack, cohesive law and cohesive element. .. 28
Figure 2.5: Illustration of a 4-node plane cohesive element from un-deformed configuration to deformed configuration. The cohesive crack separations are the relative displacements between node pair 4-1 and 3-2 and a reference line connects the midpoints between node pairs 1-4 and 2-3. 29
Figure 2.6: Cohesive forces and heat flows at the nodes of a deformed element. 31
Figure 2.7: Deformed cohesive element with displacement jumps in global and local, crack oriented coordinate systems. 32
Figure 2.8: (a) A DCM in mode I opening; (b) CZM of physical crack with two cohesive elements. 37
Figure 2.9: Approximation of stress distribution with (a) NCI scheme and (b) GI scheme. 38
Figure 2.10: Improved integration schemes with moving integration points for (a) NCI and (b) GI schemes. 39
Figure 2.11: Single cohesive element in Mode I wedge opening. 44
Figure 2.12: Numerical performance of different integration methods on single element under wedge opening mode for (a) two integration point and (b) three integration points schemes. 45
Figure 2.13: Model setup for comparison of cohesive heat transfer. 47
Figure 2.14: Influence of cohesive heat transfer coefficient on the temperature jump across the interface. 49
Figure 2.15: Temperature profile vs. displacement under steady state condition heat transfer for (a) mode I opening (b) mode II sliding (c) mixed mode (d) mode I wedge opening. 53
Figure 2.16: Temperature profile vs. displacement under transient heat transfer for 5 seconds for (a) mode I opening (b) mode II sliding (c) mixed mode (d) mode I wedge opening. 54
Figure 2.17: (a) The opening stress distribution in a DCB with E =10^5 N/mm^2, Γ_I = 1.0 N/mm, and $\hat{\sigma}$ = 50 N/mm^2; (b) Numerically determined l_c/t as a function of $E\Gamma_I / \hat{\sigma}^2 t$ (the curve labeled as FEM+CZM) as compared to that obtained with the approximate expression of Equation (2.61) (left vertical axis). The

discrepancy associated with the approximate expression is also plotted in this figure (right vertical axis). 57
Figure 2.18: Comparison of DCB results for all integration methods with 2 integration points with characteristic mesh size of (a) l_e/l_{ch} = 0.28; (b) l_e/l_{ch} = 0.56; (c) l_e/l_{ch} = 1.12; (d) l_e/l_{ch} = 1.66. 58
Figure 2.19: Averaged numerical error for (a) 2 integration points and (b) 3 integration points as a function of mesh size for the mode-I fracture of the DCBs..... 60
Figure 2.20: Comparison of DCB results for all integration methods with 3 integration points with characteristic mesh size of (a) l_e/l_{ch} = 1.12; (b) l_e/l_{ch} = 1.66.... 61
Figure 3.1: A bar in longitudinal tension due to some thermo-mechanical loading progresses from (a) a thermo-elastic stage (b) to a point of cohesive crack initiation (c) where afterwards a bridged cohesive crack is determined by (d) a rectangular mechanical cohesive law..... 64
Figure 3.2: Load-temperature curve of a fixed thermo-elastic bar contracting. 68
Figure 3.3: (a) Trapezoidal cohesive law. (b) Temperature-separation curve. (c) Load-temperature curve. 70
Figure 3.4: Heat transfer cohesive laws (a) rectangular (b) trapezoidal. 78
Figure 4.1:Thermo-elastic body under thermo-mechanical loading. 85
Figure 4.2: Thermo-elastic body with an internal discontinuity. 87
Figure 4.3: Rectangular-rectangular subdomains cut configuration for a 4 node rectangular element associated DoFs, loads and heat flows. 91
Figure 4.4: Triangular-pentagonal subdomains cut configuration for a 4 node rectangular element with associated DoFs, loads and heat flows. 92
Figure 4.5: (a) Thermo-elastic element (b) Traction-separation law (c) Heat Transfer Law. 107
Figure 4.6: (a) Load-displacement and (b) Load-temperature curves for thermo-mechanical cohesive law. 110
Figure 4.7: (a) Displacement only (b) temperature only (c) displacement and temperature boundary conditions for 1D comparison. 111
Figure 4.8: (a) Load-displacement and (b) load-temperature curves from TM-AFEM element. 111
Figure 4.9 : Node numbering for comparison between two bulk CPS4T elements bridged by a TM-CZM element and a single TM-AFEM element. 112
Figure 4.10 : Temperature at nodes for (a) steady state heat and (b) transient transfer for 5 s across a cohesive crack using TM-CZM and bulk CPS4T elements for Mode I opening. 113
Figure 4.11 : Temperature at nodes for (a) steady state heat and (b) transient transfer for 5 s across a cohesive crack using TM-CZM and bulk CPS4T elements for wedge opening. 115
Figure 5.1 : Configuration for single edge notch test for (b) mechanical loading and (b) an equivalent thermal loading. 118
Figure 5.2: (a) Normalized crack length versus normalized critical stress and (b)) nominal strain length versus nominal strain for a SENT fracture configuration. 121
Figure 5.3: Maximum in-plane strain contours for SENT configuration for mesh size of 1240 elements in different stages of edge crack propagation. 122

Figure 5.4: Nominal strain versus normalized critical stress curves for LEFM solution and equivalent mechanical and thermal loadings. 123
Figure 5.5 : Configuration for a DCB under (a) displacement control loading (b) displacement control wedge opening and (c) equivalent thermal condition for wedge opening. 124
Figure 5.6 : Load-displacement plot for DCB comparing analytical and numerical results with the influence of temperature. 127
Figure 5.7 : Load-displacement curves for a top surface node at the left end. 127
Figure 5.8: A beam consisting of two layers bonded together. 128
Figure 5.9 : Temperatures and thermal stresses in a two-layered beam for (a) uniform temperature distribution; (b) thermal stress due to uniform temperature; (c) linear temperature distribution; and (d) thermal stress due to linear temperature. 131
Figure 5.10: A cross-ply laminate, $[0/90_n/0]_T$, under uniaxial stress exhibiting transverse cracking in the 90-plies. 133
Figure 5.11 : Geometry and material properties for TM-AFEM models of T300/934 $[0/90_n/0]_T$ laminates. 133
Figure 5.12: Applied stress σ_a vs. crack density in T300/934 $[0/90_n/0]_T$ laminates using Equation (5.28) to estimate cohesive strengths. 134
Figure 5.13: Applied stress σ_a vs. crack density in $[0/90_n/0]_T$ laminates using cohesive strengths that best fit experimental data. 135
Figure 5.14: Example of a TBC with surface, interface and edge cracks. 137
Figure 5.15 : Idealized cross section of TBC test specimen used for numerical model with TM-AFEM elements. 138
Figure 5.16: Boundary conditions for uniform temperature change across the ceramic coating surface favorable for (a) surface and interface cracks and (b) edge cracks. 141
Figure 5.17 : The (a) number of surface cracks initiated and (b) average crack depth as functions of θ_0 for the boundary conditions in Figure 5.16(a). 142
Figure 5.18: Cracking patterns as a result of applied temperature gradient of $\Delta\theta$ = -1000 K for the boundary condition in Figure 5.16(a) for (a) l_c = 0.25 mm and (b) l_c = 0.75 mm. 144
Figure 5.19: Cracking patterns as a result of applied temperature gradient of $\Delta\theta$ = -1000 K for the free edge boundary condition in Figure 5.16(b) for (a) l_c = 0.25 mm and (b) l_c = 0.75 mm. 146
Figure C.1: One to one isoparametric mapping of (a) arbitrary physical pentagon element to (b) reference pentagon element. 167
Figure C.2: Barycentric coordinates for Wachpress functions. 168

LIST OF TABLES

Page

Table 2.1: Summary of integration points and weights for various integration methods. 41
Table 5.1: Geometric and material properties for SENT specimen models. 124
Table 5.2: Geometry and material properties for DCB model..... 125
Table 5.3: Geometric and material properties for two layer bi-material composite beam. 132
Table 5.4: Cohesive properties for TM-AFEM model of two layer composite beam. ... 132
Table 5.5: Mechanical properties of T300/934. 136
Table 5.6: Cohesive parameters for different number of 90 plies. 136
Table 5.7: Temperature independent thermo-elastic properties of material regions in the TBC..... 139
Table 5.8 : Cohesive properties for the material regions of TBC for surface-interface cracks. 141
Table C.1: Gaussian Integration Points and Weights for Reference Pentagon..... 166

Chapter 1 Introduction

1.1 Overview

This chapter is part literature review and part discussion of the relevant topics concerning a novel augmented finite element method (A-FEM) for fracture in the context of coupled temperature-mechanical problems. The importance of a numerical model capable of predicting thermal fracture is put in context by first discussing the engineering applications and problems of interest. Thermal fracture involves integrating the theories of classical (linear) thermo-elasticity and fracture mechanics. Emphasis is placed on the derivation of equations relevant to numerical simulation of thermal fracture in a finite element method (FEM) context.

1.2 Why is Simulation of Thermal Fracture Needed?

Space planes, nuclear fusion reactors, gas turbines and aircraft engines are all applications where the high heat flux environment is hostile and damaging for typical metallic engineering materials. A solution has been to protect these metal substrates with ceramic thermal barrier coatings (TBCs). This results in a layered material system where the coating is a thin film subjected to residual stress. Hutchinson et. al. [1]-[2] studied such a material system and in particular cracking of pre-tensioned films. For an elastic, homogeneous film-substrate system where the substrate is infinitely thick, they proposed a dimensionless number Z that quantifies the driving force for the different cracking patterns that can occur. A related class of materials, ceramic matrix composites (CMCs), have similarly been applied to high heat flux applications. Integral textile CMCs for example have been fabricated into components such as rocket nozzles, turbine engine combustor liners, thermal protection systems, and hypersonic flow path components [3].

Failure of the material in any of these applications can be catastrophic and highly undesirable from an engineering point of view. Thermal stress induced fracture in high temperature materials is an ongoing area of research. Knowledge of the failure mechanisms of these materials is invaluable for their design and application.

Thermal loads have been observed to cause the ceramic coatings to crack, delaminate and spall [4], [5]. For purposes of the design of high temperature systems, much work has been done to study the mechanisms of crack initiation and propagation in TBCs under high heat flux conditions for various parameters such as coating thickness, coating composition, maximum heat flux and duration of heating cycles [2], [6]–[16]. Studies investigating the influence of heat flux conditions on the behavior of cracked structures have provided evidence that the energy release rate due to thermal effects could be significant [17]–[21]. This has also been shown to be the case for interface cracks in high temperature coatings under steady state heat transfer where the energy release rate has appreciable dependence on the assumed conductance across the crack surfaces [2], [22]–[24].

Simulation based engineering offers an enticing incentive in research and development for these high temperature materials, and by extension the systems they form the components of, because calibrated simulations can potentially greatly decrease the number of actual, physical tests necessary to ensure design requirements are met, thereby expediting the development process and lowering the costs associated with performing a full matrix of validation tests [25]. In the greater context, the purpose of simulating fracture in a thermo-mechanical environment is to expand the range of

applicable engineering materials and to provide rich information relevant for design that may be difficult if not impossible to obtain experimentally.

Modeling the thermal fracture prevalent in these high temperature material systems is a great challenge. Differences in properties of the materials that constitute the composites lead to complex local distributions of temperature and stress. The situation is exacerbated by the wide range of possible loading conditions, both thermal and mechanical, that in reality interact with each other in coupled thermo-mechanical process. Furthermore, numerical simulations must take into account the temperature dependence of material properties that can result in drastic changes in structural behavior. For example, it has been observed that a brittle material can behave in a ductile manner in a high temperature environment [26]. Successful simulation requires the integration of thermo-elasticity, fracture mechanics and advanced numerical methods for arbitrary cracking. As a first step towards this endeavor, the focus of this dissertation is to develop and implement a method for the analysis of thermo-elastic solids capable of arbitrary cracking.

1.3 Thermo-elasticity

Here the basic relations of a classical (linear) thermo-elastic body as detailed in [27] are presented. The linear thermo-elastic process involving u_i, ε_{ij}, σ_{ij}, θ, q_i (i.e. displacement, strain, stress, temperature change and heat flux, in that order) corresponding to body forces b_i and an external heat source r acting on body Ω is described by the following set of equations in index notation

$$\varepsilon_{ij} = \frac{1}{2}\left(u_{i,j} + u_{j,i}\right), \tag{1.1}$$

$$\sigma_{ij,j} + b_i = \rho \ddot{u}_i, \tag{1.2}$$

$$-q_{i,i} + r = C_E \dot{\theta} - \vartheta_0 M_{ij} \dot{\varepsilon}_{ij}, \tag{1.3}$$

$$\sigma_{ij} = C_{ijkl} \varepsilon_{kl} + M_{ij} \theta, \tag{1.4}$$

$$q_i = -k_{ij} \theta_{,j}. \tag{1.5}$$

Here, ρ and C_E are the density and specific heat at zero strain respectively. Likewise, C_{ijkl}, M_{ij} and k_{ij} are the elasticity, stress-temperature and thermal conductivity tensors. Absolute temperature is denoted by ϑ, and $\vartheta_0 > 0$ is a constant reference temperature such that the body is stress free at this temperature, i.e.

$$\sigma_{ij}\left(t = 0, \vartheta_0\right) = 0. \tag{1.6}$$

A linear thermo-elastic body assumes small strain conditions

$$\left|\varepsilon_{ij}\right|, \left|\dot{\varepsilon}_{ij}\right| \le \epsilon, \tag{1.7}$$

where ϵ is a small number. If the elasticity and thermal conductivity tensors are invertible, the elastic compliance tensor K_{ijkl}, the thermal expansion tensor A_{ij}, the thermal resistivity tensor λ_{ij} and the specific heat at zero stress C_S are given by

$$K_{ijkl} = \left(C_{ijkl}\right)^{-1}, \tag{1.8}$$

$$\lambda_{ij} = \left(k_{ij}\right)^{-1}, \tag{1.9}$$

$$A_{ij} = -K_{ijkl} M_{kl}, \tag{1.10}$$

$$C_S = C_E - \vartheta_0 M_{ij} A_{ij}. \tag{1.11}$$

These quantities must satisfy the conditions

$$K_{ijkl} = K_{jikl} = K_{ijlk} = K_{klij}, \tag{1.12}$$

$$A_{ij} = A_{ji},\ C_S > 0, \tag{1.13}$$

$$K_{ijkl} \sigma_{ij} \sigma_{kl} > 0, \tag{1.14}$$

$$\lambda_{ij} = \lambda_{ji},\ \lambda_{ij} q_i q_j > 0 . \tag{1.15}$$

The preceding equations apply to a homogeneous anisotropic material. When the body is inhomogeneous, the quantities $\rho, C_E, k_{ij}, M_{ij}$ and C_{ijkl} are material functions, dependent on their location within the body.

For a homogeneous isotropic body and assuming small strain deformation (i.e. $M_{ij} = -(3\lambda + 2\mu)\alpha\delta_{ij}$), Equations (1.1)-(1.5) simplify to

$$\varepsilon_{ij} = \frac{1}{2}\left(u_{i,j} + u_{j,i}\right), \tag{1.16}$$

$$\sigma_{ij,j} + b_i = \rho \ddot{u}_i , \tag{1.17}$$

$$-q_{i,i} + r = C_E \dot{\theta} + (3\lambda + 2\mu)\alpha \vartheta_0 \dot{\varepsilon}_{kk} , \tag{1.18}$$

$$\sigma_{ij} = 2\mu\varepsilon_{ij} + \lambda\varepsilon_{kk}\delta_{ij} - (3\lambda + 2\mu)\alpha\theta\delta_{ij} , \tag{1.19}$$

$$q_i = -k\theta_{,i,i} , \tag{1.20}$$

where λ and μ are the Lamé constants, α is the coefficient of thermal expansion, k is the thermal conductivity coefficient and δ_{ij} is the Kronecker delta. The material properties must satisfy the conditions

$$\begin{array}{llll} \rho > 0, & \mu > 0, & 3\lambda + 2\mu > 0, \\ k > 0, & C_E > 0, & \end{array} . \tag{1.21}$$

Eliminating strain, stress and heat flux from Equations (1.1)-(1.5) gives the so called displacement-temperature description

$$\rho \ddot{u}_i = \left(C_{ijkl} u_{k,l}\right)_{,j} + \left(M_{ij}\theta\right)_{,j} + b_i , \tag{1.22}$$

$$C_E \dot{\theta} = \left(k_{ij}\theta_{,j}\right)_{,i} + \vartheta_0 M_{ij} \dot{u}_{i,j} + r . \tag{1.23}$$

These equations are the displacement-temperature description of the linear thermo-elastic process in a body Ω.

1.4 Fracture Mechanics

Fracture mechanics is concerned with the study of cracks and attempts to characterize a material's resistance or "toughness" to fracture [28]. Illustrated in Figure 1.1 are the three fracture modes in solids. The opening mode (mode I) occurs when a tensile stress acts normally to the plane of the crack. The sliding mode (mode II) concerns the shear stress that is perpendicular to the crack front and parallel to the crack plane. Finally, the tearing mode (mode III) is when the shear stress is parallel to both the crack plane and the crack front. The most common mode in brittle fracture is mode I.

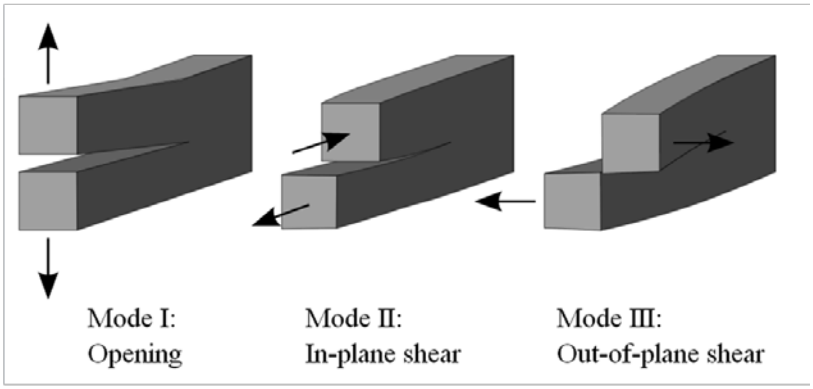

Figure 1.1: The three fracture modes: (a) opening (b) in-plane shear and (c) out-of-plane shear.

The work of Inglis [29] in 1913 demonstrated that in the presence of sharp corners, notches or cracks, nearby local stress is magnified many times from the far field applied stress. In other words, a stress concentration factor κ based on geometry determines the magnitude of the stress field near a crack tip or flaw.

Griffith's paper in 1920 [30] set forth the notion of an energy balance criterion based on the viewpoint of minimum potential energy for fracture. According to Griffith, two conditions must be met for crack growth. First, the stress at the crack tip reaches the critical value needed to break the material bonds. Second, the magnitude of the strain energy released equals to or exceeds the magnitude of surface energy needed to create new crack surfaces. This condition can be expressed as

$$\frac{\mathrm{d}U_s}{\mathrm{d}a} \geq \frac{\mathrm{d}U_\gamma}{\mathrm{d}a}, \tag{1.24}$$

where U_s is the strain energy, U_γ is the surface energy and da is the crack length increment. While this theory is in excellent agreement for brittle materials such as the glass that Griffith studied, inconsistencies result when applied towards other engineering materials that exhibit some degree of ductility.

1.4.1 Linear Elastic Fracture Mechanics

The basis of linear elastic fracture mechanics (LEFM) is Irwin's modification [31] to Griffith's energy criterion. The energy dissipation due to plastic deformation U_p is accounted for via an extra term in the energy balance equation proposed by Griffith as

$$\frac{\mathrm{d}U_s}{\mathrm{d}a} \geq \frac{\mathrm{d}U_\gamma}{\mathrm{d}a} + \frac{\mathrm{d}U_p}{\mathrm{d}a}. \tag{1.25}$$

For brittle materials, the surface energy term dominates. In ductile materials, the plastic dissipation term dominates. Irwin's modification also introduces a stress intensity factor K defined for all three cracking modes. K in general is a function of the applied stress σ_a, the crack length a and the specimen geometry factor Y

$$K = \sigma_a Y \sqrt{\pi a} \tag{1.26}$$

and has the property of being additive for the same type of loading, which allows for a single K to be derived as the sum of individual loads for a complex loading system by the principle of superposition.

Stresses and displacements are proportional to K, and their respective fields can be expressed as

$$\sigma_{ij} = \frac{K}{\sqrt{2\pi r}} f_{ij}\left(\vartheta\right) + \text{higher order terms}, \tag{1.27}$$

$$u_i = K\sqrt{r} g_i\left(\vartheta\right) + \text{higher order terms}, \tag{1.28}$$

where $\left(r, \vartheta\right)$ is a polar coordinate system at the crack tip as shown in Figure 1.2, r is the distance from the crack tip and ϑ is the angle with respect to the plane of the crack. The functions $f_{ij}\left(\vartheta\right)$ and $g_i\left(\vartheta\right)$ are dimensionless functions that depend on the geometry.

K is related to the strain energy release rate G, which is the energy dissipated during fracture per unit of newly created crack surface area, given by

$$G = -\frac{d\left(U - V\right)}{dA}, \tag{1.29}$$

where U is the potential energy available for crack growth, V is the work done by external loads and A is the crack area. It has been shown in [32] that for a crack in mode I loading

$$G = \begin{cases} \dfrac{K_I^2}{E}, & \text{plane stress} \\ K_I^2 \dfrac{1-\nu^2}{E}, & \text{plane stain} \end{cases}, \tag{1.30}$$

where E is Young's modulus and ν is Poisson's ratio.

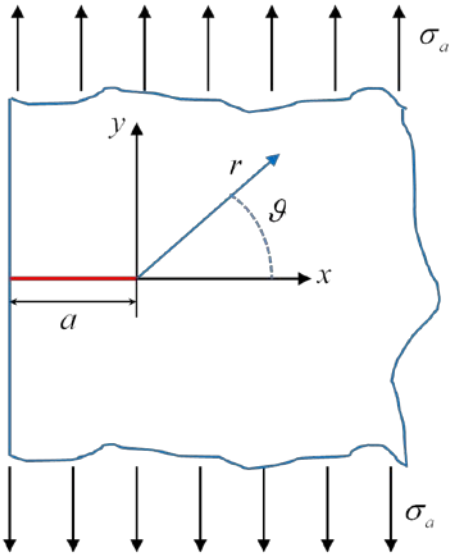

Figure 1.2: Polar coordinates at the crack tip for a plate with a crack under applied tensile stress.

Equation (1.27) implies that at the crack tip, i.e. $r = 0$, σ_{ij} approaches infinity but in reality, once the stress reaches the yield strength of the material, plastic deformation occurs in a localized region surrounding the crack tip. The approximate size of this so-called plastic zone can be shown to be

$$r_p = \frac{K^2}{2\pi\sigma_{ys}^2}, \tag{1.31}$$

where r_p is the radius of plastic zone and σ_{ys} is the yield strength of the material. The equations of LEFM are not valid in this plastic zone.

However, if small scale yielding (SSY) conditions apply, i.e. the geometry of the crack is much larger than the plastic zone, in the region $r_p < r << a$, the equations of LEFM hold and the criterion for crack growth is

$$K \geq K_c. \tag{1.32}$$

The quantity K_c is the fracture toughness, a material property that characterizes a material's resistance to fracture and defines the onset of crack extension. Alternatively, another criterion for crack growth is

$$G \geq G_c, \tag{1.33}$$

where G_c is a material property independent of applied loads and specimen geometry known as the critical fracture energy or toughness.

1.5 Cohesive Zone Models

For fracture of "brittle" materials such as glass and many ceramics where the crack tip plastic deformation is small and fracture energy is low, LEFM is an excellent analysis method. But for "ductile" materials where fracture energy is high, LEFM is inapplicable because the size of the nonlinear zone ahead of the crack tip is significant when compared to the dimensions of the cracked geometry [33]. Furthermore, LEFM can only be used to analyze bodies with preexisting cracks. These two restrictions severely limit the utility of LEFM for a large variety of materials such as metals, cement and many composites. A different approach that overcomes these shortcomings is the so called cohesive zone model (CZM) first proposed by Dugdale [34] and Barenblatt [34]-[35]. It has been widely used to model crack growth in a variety of different materials including concrete [37], ceramics [38], polymers [39], metals [40] and interfaces between different material regions [41].

The CZM is understood as a constitutive assumption that in general is composed of three main parts [42]

1) The stress-strain behavior of the material in the absence of cohesive cracks.
2) The initiation criterion to determine the condition of crack formation and orientation.
3) The evolution law for the cohesive crack that in its most basic form relates the stress between cohesive surfaces to the separation between them.

As an example, for quasi-brittle materials, the standard formulation for CZMs assumes a linear elastic isotropic stress-strain behavior where the initiation criterion for cracks is when the maximum principal stress σ_1 reaches a predefined cohesive strength $\hat{\sigma}$, and the formed crack is oriented perpendicular to the principal stress direction associated with σ_1. This is the so-called maximum principal stress criterion. The evolution law for mode I is taken to be a traction-separation curve as seen in Figure 1.3 where σ is the cohesive stress and δ is the separation between the cohesive surfaces. This formulation assumes that the fracture energy G_c (the area under the traction-separation curve) is constant and no energy dissipates outside of the cohesive zone. As Hillerborg introduced in [43], if the traction-separation law in Figure 1.3 is approximated as a linear curve, a characteristic length or cohesive zone length, l_{coh}, can be defined as

$$l_{coh} = \frac{EG_c}{\hat{\sigma}^2}, \tag{1.34}$$

where E is the elastic modulus. This length scale relates to the size of the cohesive zone ahead of the crack tip for a very large specimen.

In the literature, popular CZMs differ mainly in shape and model parameters. Any two of the three independent parameters (cohesive strength $\hat{\sigma}$, fracture energy G_c and critical separation δ_c) are sufficient to define a CZM [44]–[46]. The attractiveness of

CZM lies in its simplicity and adaptability in defining multiple mechanisms for a wide range of materials. A cohesive law can be defined to represent several mechanisms in a fracture process zone. Examples include the modeling of the fracture process across delamination and splitting cracks [47], [48], human cortical bone [49], [50] and failure in composites [51], [52].

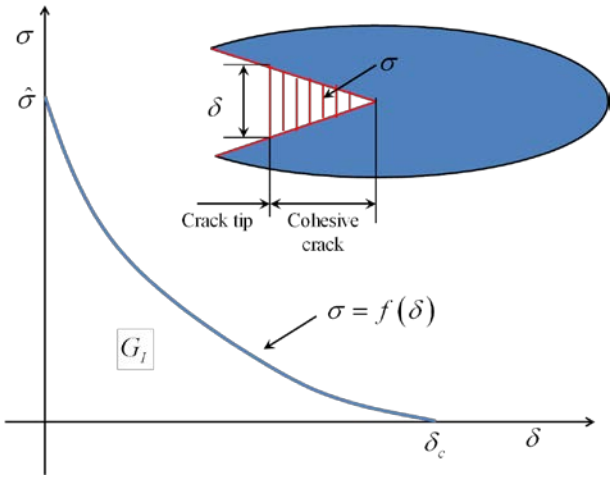

Figure 1.3: General definition of the traction-separation law for CZMs.

1.6 Thermo-Mechanical Cohesive Zone Models

CZMs have primarily been used in analyzing problems of mechanical loading only. A small though substantial body of research has been done on the topic of fracture in a coupled thermo-mechanical context. The effects of a temperature dependent cohesive zone was investigated by Costanzo and Walton [53] for steady-state dynamic crack propagation in a heat conducting elastic body. Their results indicated that temperature dependent solutions significantly differed from those derived purely from mechanical dependence. Bjerke and Lambros [54], under the assumption that excess fracture energy supplied in the crack tip region is converted into heat within the cohesive zone, demonstrated that a thermally dissipative cohesive zone model gives results in excellent

agreement with experiment for temperature predictions around the crack for the case of a single craze during dynamic fracture of polymethyl methacrylate (PMMA). Both of these works reveal a set of fracture problems where temperature effects cannot be ignored and the capability of CZMs in incorporating these temperature effects. Three related works by Hattiangadi and Siegmund [55]–[57] may be the earliest adoption of extending CZM to include the heat transfer process for implementation within FEM. These works focused on developing cohesive conductance laws to model the heat transfer in front of the crack tip, within the fracture process zone and across the separated crack. Their basic approach was to regard the heat transfer process in an interface context, and their formulation gave full consideration to the observation that material deterioration influences the conductance and stress carrying capability of the cohesive zone with the resulting model possessing a coupling between stress and heat analysis. Later work built upon this thermo-mechanical cohesive zone model (TM-CZM) framework to establish laws suitable for analysis of heterogeneous solids and structural systems with contacting/interacting components [58] and thermo-mechanical fatigue of solders in electronic chip packages under active power cycling [59]. Implemented as a cohesive element within FEM, the drawback of CZMs and TM-CZMs is that only problems where crack locations are known *a priori* are applicable since cohesive elements need to be pre-defined in a structural mesh.

1.7 Numerical Methods for Arbitrary Cracking in Solids

The use of cohesive elements in the preceding section where *a priori* knowledge of crack locations is required is the first of two main approaches to modeling of cohesive fracture within the FEM framework: (1) discrete inter-element cracks and (2) discrete

intra-element cracks. When the crack path is known in advance, the discrete inter-element cracks approach allows for crack growth to evolve from the initial boundary value problem. But for arbitrary cracking problems, remeshing, which is computationally expensive, is necessary. Discrete intra-element cracking obviates the need to remesh by accounting for the discontinuity at the element level. Some recent advanced numerical methods developed to model arbitrary cracking problems in solids take the discrete intra-element approach. They include the extended finite element method (X-FEM) [60]–[65] and the phantom node method (PNM) [66]–[72]. Extra nodal DoFs (as in X-FEM) or phantom nodes (as in PNM) are added within the finite element framework to account for discrete discontinuities. For simulation of non-interacting cracks, these methods have been shown to be relatively mesh independent and computationally efficient. In modeling complex crack configurations where cracks can merge and branch, however, the extra DoFs associated with each crack creates an extra numerical burden for tracing their interaction. Another disadvantage of these methods is the difficulty of integration into standard FE programs because dimensions of local and global stiffness matrices must be dynamically modified in accordance with crack interaction [63], [73]. Thus a method that reduces or eliminates the need for additional DoFs or nodes is highly desired.

Two methods have been devised to reduce or eliminate the need for additional DoFs or nodes. The first is the phase-field method [74]–[76] which reduces the need of varying DoFs by approximating a fracture surface with a highly concentrated yet continuous phase-field to smooth the boundary of the crack over a small region. Fracture surfaces then need not to be tracked algorithmically. This method has the major advantage of allowing the fracture surfaces to evolve from the solution of a coupled system of partial

differential equations but at the price of mesh dependence. Sharp discontinuities associated with an interface or a crack surface require an extremely refined mesh to resolve and thus the computational cost is extremely high. Furthermore, there are serious ambiguities regarding the nonzero stresses at crack wake surfaces.

The second method, the embedded discontinuity approach, undertaken by several research groups [77]–[82] is an extension of earlier research in smeared localization models [83]–[85]. In this method, displacement jumps with certain deformation modes (constant and/or linear mode) are used in addition to the normal continuous displacement field to enrich the elemental strain field. Coefficients of the deformation modes are considered as additional DoFs that are either assigned to additional nodes as a global DoF such as in [82], [86] or fully condensed at the elemental level as in [80], [81]. Condensing the internal DoFs is preferred because it eliminates the extra DoFs. However, in many cases the assumed deformation modes are not permissible with the subdomain elemental deformation modes. Thus stress locking is possible with this method. Another difficulty is that the process of embedding multiple discontinuities in an element to allow for arbitrary crack merging and branching is tedious and difficult.

The novel Augmented Finite Element Method (A-FEM) solves the aforementioned disadvantages of the various methods by constructing augmented elements that can treat arbitrary intra-element cracking without additional nodes or DoFs. It has been demonstrated in [87]–[89] that this novel formulation has the following advantages: (1) it does not need to assume deformation modes *a priori* for discontinuities as in the standard embedded discontinuity approach; (2) it permits smooth transition from a weak discontinuity to a strong one; (3) it allows for repeated elemental augmentation to enable

multiple, interactive intra-element discontinuities; and (4) it can be implemented easily into any standard FE packages, including commercial software packages as an add-in to the element library.

1.8 Research Goal

The ultimate goal of this study is to extend the work of Liu, Mohammed and Yang [87]–[89] on arbitrary fracture in solids from a purely mechanical process to a thermo-mechanical one so that it can be applicable to a wider range of engineering problems of interest. The novel A-FEM procedure for arbitrary cracking in solids augments standard finite elements (FEs) with internal nodes that are condensed out of the global FE equations using stress continuity relations and utilizes a CZM to eliminate the singularity at the crack tip. By introducing a temperature degree of freedom (DoF) to the formulation, the mechanical process must be coupled with the thermal one via a coefficient of thermal expansion and a TM-CZM becomes necessary to describe the crack behavior which now needs to account for both load and heat transfer across the crack surface.

To do so, the basic principles of a TM-CZ element are first introduced in Chapter 2. Details of the thermo-mechanical cohesive law are discussed and improvements to cohesive stress integration schemes are given in this chapter. The chapter concludes with numerical examples that demonstrate the results of the improvements as well as the capabilities of the element in modeling heat transfer across a cohesive surface.

Chapter 3 uses the condensation procedure of the novel A-FEM and its key concepts and assumptions to derive the formulation for the thermo-mechanical augmented finite element method (TM-AFEM) a simple case, the 1D quasi-static, steady state heat transfer

problem. An argument is made for simplifying the thermo-mechanical cohesive law that describes cohesive stress and heat flux upon crack separation by assuming that upon separation, the heat transfer can be modeled as an interface problem with a constant coefficient of heat transfer. This removes the dependence of temperature on the crack separation and reduces the degree of nonlinearity and the complexity of the resulting FE equations for the general problem of arbitrary cracking during a thermo-mechanical process.

The integration of the TM-CZ law into the A-FEM framework given in Chapter 4 produces a 2D TM-AFEM capable of modeling arbitrary fracture under both mechanical and thermal influences. Furthermore, the mechanical and heat transfer processes are related via the coefficient of thermal expansion which relates the temperature change of the material as a thermal strain. The TM-AFEM element is evaluated with comparison to known analytical and numerical solutions.

This dissertation concludes with Chapter 5 where the TM-AFEM element is used in a variety of numerical examples. A general discussion of the strengths and future improvements to the TM-AFEM element implemented from the current derivation follows. The chapter ends with possible avenues for future work.

Chapter 2 Two-Dimensional Thermo-Mechanical Cohesive Element

2.1 Overview

This chapter begins from the problem statement of a body with a cohesive crack under thermo-mechanical loading. First, from the conservation laws and boundary conditions, the strong form of the problem is presented. The weak form of the problem is then defined following a general finite element procedure. Then the problems associated with traditional integration schemes for cohesive stress integration are addressed and several improvements are given. The chapter concludes with the results of validation tests for a TMCZ element and examples demonstrating the improvements of new integration schemes. Significant portions of this chapter are reprinted from [90].

2.2 Problem Statement

Consider the body defined as a domain Ω bounded by Γ that is partially divided by a crack denoted as the internal boundary Γ_c shown in Figure 2.1. Cracks are defined as internal cohesive surfaces that can transfer heat and load before they completely fail. The domain is subjected to a prescribed displacement ($\bar{\mathbf{u}}$) and a traction ($\bar{\mathbf{t}}$) boundary condition on the boundaries Γ_u and Γ_t, respectively. Likewise, the temperature $\bar{\theta}$ and heat flux $\bar{q}$ are prescribed on boundaries Γ_θ and Γ_q.

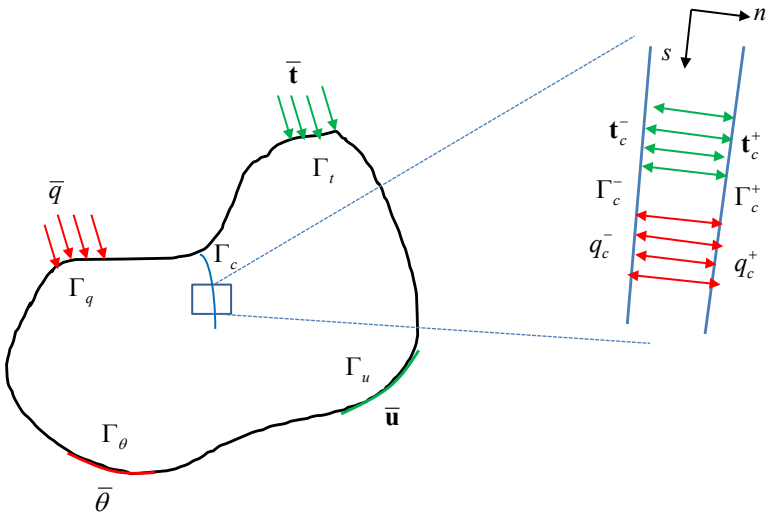

Figure 2.1: Body cut by a cohesive crack under thermo-mechanical loading.

Two surfaces Γ_c^+ and Γ_c^- are created by the cohesive crack, and the traction and heat flux vectors $\mathbf{t}$ and q must satisfy the following continuity conditions at the interface

$$\mathbf{t}_c^+ = -\mathbf{t}_c^- = \mathbf{t}_c, \tag{2.1}$$

$$q_c^+ = -q_c^- = q_c. \tag{2.2}$$

Here, the subscript c denotes that the tractions and heat fluxes are on the surfaces created by the cohesive crack while the superscripts + and − denote the respective surface association. A local coordinate system normal and tangential to the cohesive surfaces is denoted by n and s as seen in Figure 2.1. Assuming that the body is under static equilibrium and undergoing transient heat transfer, load and heat balance gives

$$\nabla \bullet \boldsymbol{\sigma} + \mathbf{b} = \mathbf{0}, \tag{2.3}$$

$$\rho c \frac{\partial \theta}{\partial t} + \nabla \bullet \mathbf{q} - Q = 0, \tag{2.4}$$

where $\boldsymbol{\sigma}$ is the Cauchy stress tensor, $\mathbf{b}$ the body force vector, ρ the density, c the specific heat, $\mathbf{q}$ the heat flux surface density vector, Q the internal heat volumetric source and $\nabla\bullet(\ )$ denotes the divergence.

It can be shown that the weak form of the balance equations are

$$\int_\Omega \boldsymbol{\sigma} : \nabla \delta \mathbf{u} \, \mathrm{d}\Omega = \int_\Omega \mathbf{b} \bullet \delta \mathbf{u} \, \mathrm{d}\Omega + \int_{\Gamma_t} \overline{\mathbf{t}} \bullet \delta \mathbf{u} \, \mathrm{d}\Gamma + \int_{\Gamma_c^+} \mathbf{t}_c^+ \bullet \delta \mathbf{u}_c^+ \, \mathrm{d}\Gamma + \int_{\Gamma_c^-} \mathbf{t}_c^- \bullet \delta \mathbf{u}_c^- \, \mathrm{d}\Gamma \,, \quad (2.5)$$

$$\int_\Omega \rho c \frac{\partial \theta}{\partial t} \delta\theta \, \mathrm{d}\Omega + \int_\Omega \mathbf{q} \bullet \nabla \delta\theta \, \mathrm{d}\Omega = \int_\Omega Q \delta\theta \, \mathrm{d}\Omega + \int_{\Gamma_q} \overline{q} \delta\theta \, \mathrm{d}\Gamma + \int_{\Gamma_c^+} q_c^+ \delta\theta_c^+ \, \mathrm{d}\Gamma + \int_{\Gamma_c^-} q_c^- \delta\theta_c^- \, \mathrm{d}\Gamma, \quad (2.6)$$

where $\mathbf{u}_c^+, \mathbf{u}_c^-, \theta_c^+, \theta_c^-$ are the displacements and temperatures on the cohesive surfaces and the condition that $\delta\mathbf{u} = \mathbf{0}$ on Γ_u and $\delta\theta = 0$ on Γ_θ has been used in deriving Equations (2.5) and (2.6). The displacement and temperature jumps across the cohesive surface can be expressed as $\Delta\mathbf{u}_c = \mathbf{u}_c^+ - \mathbf{u}_c^-$ and $\Delta\theta_c = \theta_c^+ - \theta_c^-$, and using the continuity conditions of Equations (2.1) and (2.2), the weak forms can be expressed as

$$\int_\Omega \boldsymbol{\sigma} : \nabla \delta \mathbf{u} \, \mathrm{d}\Omega = \int_\Omega \mathbf{b} \bullet \delta \mathbf{u} \, \mathrm{d}\Omega + \int_{\Gamma_t} \overline{\mathbf{t}} \bullet \delta \mathbf{u} \, \mathrm{d}\Gamma + \int_{\Gamma_c} \mathbf{t}_c \bullet \delta \Delta \mathbf{u}_c \, \mathrm{d}\Gamma \,, \quad (2.7)$$

$$\int_\Omega \rho c \frac{\partial \theta}{\partial t} \delta\theta \, \mathrm{d}\Omega + \int_\Omega \mathbf{q} \bullet \nabla \delta\theta \, \mathrm{d}\Omega = \int_\Omega Q \delta\theta \, \mathrm{d}\Omega + \int_{\Gamma_t} \overline{q} \delta\theta \, \mathrm{d}\Gamma + \int_{\Gamma_c} q_c \delta \Delta\theta_c \, \mathrm{d}\Gamma \,. \quad (2.8)$$

The presence of the cohesive crack results in additional terms that reflect the discontinuity in the displacement and temperature fields.

2.3 Finite Element Formulation for Cohesive Elements

For a finite element with n nodes, the primary variables (or nodal DOFs), displacement $\mathbf{u}$ and temperature θ, are approximated by interpolation functions N_i from nodal values u_i and θ_i

$$\mathbf{u} = \sum_{i=1}^{n} N_i u_i \,, \quad (2.9)$$

$$\theta = \sum_{i=1}^{n} N_i \theta_i \,. \quad (2.10)$$

Substituting Equations (2.9) and (2.10) into Equations (2.7) and (2.8) gives

$$\int_\Omega \boldsymbol{\sigma} : \nabla \mathbf{N} \, d\Omega = \int_\Omega \mathbf{b} \bullet \mathbf{N} \, d\Omega + \int_{\Gamma_t} \overline{\mathbf{t}} \bullet \mathbf{N} \, d\Gamma + \int_{\Gamma_c} \mathbf{t}_c \bullet \mathbf{N} \, d\Gamma , \tag{2.11}$$

$$\int_\Omega \rho c \frac{\partial \theta}{\partial t} \mathbf{N} \, d\Omega + \int_\Omega \mathbf{q} \bullet \nabla \mathbf{N} \, d\Omega = \int_\Omega Q \mathbf{N} \, d\Omega + \int_{\Gamma_t} \overline{q} \mathbf{N} \, d\Gamma + \int_{\Gamma_c} q_c \mathbf{N} \, d\Gamma . \tag{2.12}$$

Note that the boundary integrals over Γ_c are terms associated with the cohesive zone and are equal to the cohesive forces and heat flows.

A cohesive element approximates the load and heat transfer between the surfaces of the cohesive crack. Cohesive tractions and heat fluxes at the interface are considered to be functions of the displacement and/or temperature jumps across the cohesive surfaces depending on the cohesive laws used. A thermo-mechanical cohesive element has no volume and mass and therefore Equations (2.11) and (2.12) reduce to

$$-\int_{\Gamma_t} \overline{\mathbf{t}} \bullet \mathbf{N} \, d\Gamma = \int_{\Gamma_c} \mathbf{t}_c \bullet \mathbf{N} \, d\Gamma = \mathbf{f} , \tag{2.13}$$

$$-\int_{\Gamma_t} \overline{q} \mathbf{N} \, d\Gamma = \int_{\Gamma_c} q_c \mathbf{N} \, d\Gamma = \mathbf{p} . \tag{2.14}$$

Since the capacitance term disappears, the steady state and transient forms of the finite element equation are identical. To get the finite element equation for a cohesive element, note that the general form of Equations (2.13) and (2.14) when combined must be

$$\begin{bmatrix} \mathbf{K}_{uu} & \mathbf{K}_{u\theta} \\ \mathbf{K}_{\theta u} & \mathbf{K}_{\theta\theta} \end{bmatrix} \begin{Bmatrix} \mathbf{u} \\ \boldsymbol{\theta} \end{Bmatrix} = \begin{Bmatrix} \mathbf{f} \\ \mathbf{p} \end{Bmatrix}, \tag{2.15}$$

where $\mathbf{K}_{ij}$ is a submatrix in which the subscripts u and θ denote association with the respective displacements and temperature DOFs at each node, $\mathbf{u}$ and $\boldsymbol{\theta}$ are nodal displacement and temperature vectors, and $\mathbf{f}_c$ and $\mathbf{p}_c$ are the external load and heat flow vectors. Since in the most general case, $\mathbf{t}_c = \mathbf{t}_c \left(\Delta \mathbf{u}_c , \Delta \theta_c \right)$ and $q_c = q_c \left(\Delta \mathbf{u}_c , \Delta \theta_c \right)$, the

submatrices are simply the partial derivatives of the external load and heat flux vectors with respect to the nodal values of the displacement and temperature

$$\mathbf{K}_{uu} = \frac{\partial \mathbf{f}_c}{\partial \mathbf{u}}, \quad \mathbf{K}_{u\theta} = \frac{\partial \mathbf{f}_c}{\partial \theta}, \\ \mathbf{K}_{\theta u} = \frac{\partial \mathbf{p}_c}{\partial \mathbf{u}}, \quad \mathbf{K}_{\theta\theta} = \frac{\partial \mathbf{p}_c}{\partial \theta} \tag{2.16}$$

2.4 Piece-Wise Linear Thermo-Mechanical Cohesive Law

In this section, a simple cohesive law is presented to describe the load and heat flux across the cohesive surfaces. A key point of the cohesive laws used in this dissertation is that they are linear piece-wise functions. In this form, the cohesive law can be indexed by segments which allows the nonlinear equations associated with the embedded cohesive discontinuity to be formulated using the linear equation of an assumed cohesive segment. This greatly reduces the computational expenses required to solve the nonlinear fracture problem because a consistency check algorithm described in [89] can be used to expedite the solution process. The basic premise of the consistency check algorithm is that once a cohesive segment is assumed, the local equilibrium equation with the embedded cohesive discontinuity is linear and the solution can be obtained analytically. Whether the solution of this linear problem is correct or not is validated by a consistency check to see if the solution falls within the assumed segments.

2.4.1 Mechanical Cohesive Law

The mixed-mode cohesive law used in this dissertation is shown in Figure 2.2 where δ_{nc} and δ_{sc} are the critical normal and shear crack separations under pure mode conditions beyond which complete fracture occurs and cohesive stresses are zero. Characteristic normal ($\hat{\sigma}_1$ and $\hat{\sigma}_2$) and shear ($\hat{\tau}_1$ and $\hat{\tau}_2$) cohesive stresses mark where

changes in cohesive stiffness occur. The overall shape of the trapezoidal curves are determined from these stresses and the characteristic normal (δ_{n1} and δ_{n2}) and shear (δ_{s1} and δ_{s2}) crack separations. Cohesive stress and separations are defined in the local coordinate system (s,n) where s is tangential and n is perpendicular to the crack plane, (Figure 2.1).

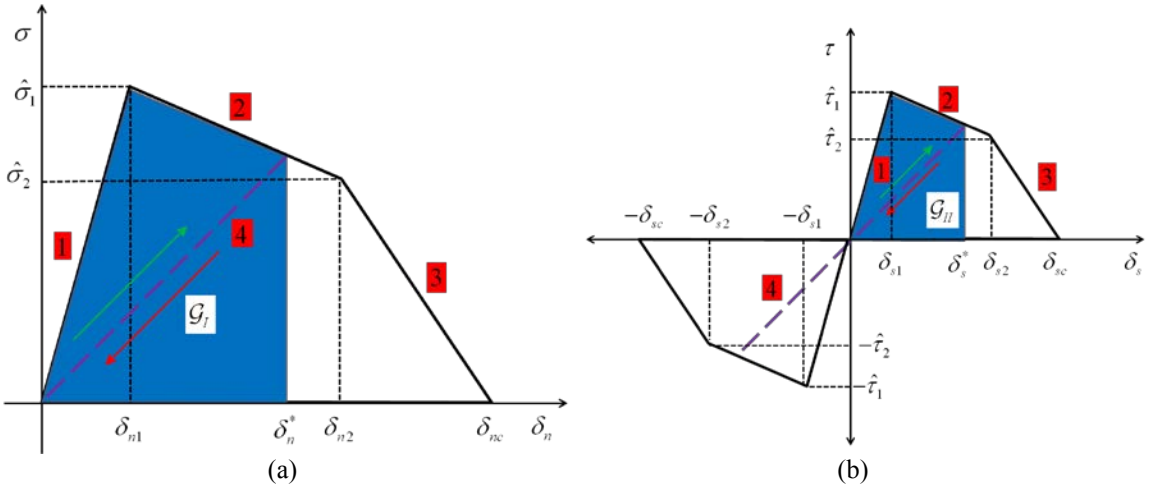

Figure 2.2: (a) Mode-I Traction Separation Law; (b) Mode-II traction Separation Law. Numbers in red denote the respective segment numbers.

Each linear segment of the traction separation law is indexed with free indices $i, j \in [1,4]$. Each segment is defined in terms of a characteristic stress ($\hat{\tau}^{(i)}$ or $\hat{\sigma}^{(j)}$), characteristic crack separation ($\delta_s^{(i)}$ or $\delta_n^{(j)}$) and a constant stiffness ($\alpha_s^{(i)}$ or $\alpha_n^{(j)}$) such that for the cohesive model

$$\hat{\sigma}^{(1)} = \hat{\sigma}_1, \quad \hat{\sigma}^{(2)} = \hat{\sigma}_2, \quad \hat{\sigma}^{(3)} = 0, \quad \hat{\tau}^{(1)} = \hat{\tau}_1, \quad \hat{\tau}^{(2)} = \hat{\tau}_2, \quad \hat{\tau}^{(3)} = 0, \tag{2.17}$$

$$\delta_n^{(1)} = \delta_{n1}, \quad \delta_n^{(2)} = \delta_{n2}, \quad \delta_n^{(3)} = \delta_{nc}, \quad \delta_s^{(1)} = \delta_{s1}, \quad \delta_s^{(2)} = \delta_{s2}, \quad \delta_s^{(3)} = \delta_{sc}, \tag{2.18}$$

$$\alpha_s^{(i)} = \frac{\hat{\tau}^{(i)} - \hat{\tau}^{(i-1)}}{\delta_s^{(i)} - \delta_s^{(i-1)}}, \quad \alpha_n^{(j)} = \frac{\hat{\sigma}^{(j)} - \hat{\sigma}^{(j-1)}}{\delta_n^{(j)} - \delta_n^{(j-1)}}, \tag{2.19}$$

where $\hat{\sigma}^{(0)} = \hat{\tau}^{(0)} = 0$ and $\delta_n^{(0)} = \delta_s^{(0)} = 0$. Crack separation ranges consistent with the indexed segments are defined as

$$\vec{\delta}_s^{(i)} = \left(\delta_s^{(i-1)}, \delta_s^{(i)}\right] \quad \vec{\delta}_n^{(j)} = \left(\delta_n^{(j-1)}, \delta_n^{(j)}\right]. \tag{2.20}$$

From these relations, the piece-wise linear cohesive law may be expressed as

$$\begin{aligned} \tau\left(\delta_s\right) &= \operatorname{sgn}\left(\delta_s\right)\left[\hat{\tau}^{(i-1)} + \alpha_s^{(i)}\left(\left|\delta_s\right| - \delta_s^{(i-1)}\right)\right], \quad \left|\delta_s\right| \in \vec{\delta}_s^{(i)} \;\&\&\; \left|\delta_s\right| > \delta_s^*, \\ \sigma\left(\delta_n\right) &= \hat{\sigma}^{(j-1)} + \alpha_n^{(j)}\left(\delta_n - \delta_n^{(j-1)}\right), \qquad\qquad \delta_n \in \vec{\delta}_n^{(j)} \;\&\&\; \delta_n > \delta_n^*, \end{aligned} \tag{2.21}$$

where signum function $\operatorname{sgn}\left(\cdot\right)$ used is defined as

$$\operatorname{sgn}\left(x\right) = \begin{cases} 1, & x > 0 \\ 0, & x = 0 \\ -1, & x < 0 \end{cases}. \tag{2.22}$$

The variables δ_n^* and δ_s^* are the maximum crack separation reached for mode I and mode II respectively. These maximum crack separations are solution-dependent variables used to account for the irreversibility of the cohesive model associated with the unloading/reloading segment indicated by index 4. They have corresponding normal and shear cohesive stresses $\hat{\sigma}^*$ and $\hat{\tau}^*$ that can be calculated from Equation (2.21). In segment 4 then, the traction separation law is given by

$$\begin{aligned} \tau\left(\delta_s\right) &= \operatorname{sgn}\left(\delta_s\right)\alpha_s^{(4)}\left|\delta_s\right|, \quad \left|\delta_s\right| \in \vec{\delta}_s^{(4)}, \\ \sigma\left(\delta_n\right) &= \alpha_n^{(4)}\delta_n, \qquad\qquad \delta_n \in \vec{\delta}_n^{(4)} \end{aligned} \tag{2.23}$$

where the cohesive slopes and separation ranges for segment 4 are

$$\begin{aligned} \alpha_s^{(4)} &= \frac{\hat{\tau}^*}{\delta_s^*}, \qquad \alpha_n^{(4)} = \frac{\hat{\sigma}^*}{\delta_n^*}, \\ \vec{\delta}_s^{(4)} &= \left[0, \delta_s^*\right], \quad \vec{\delta}_n^{(4)} = \left[-\infty, \delta_n^*\right] \end{aligned}. \tag{2.24}$$

This indexing procedure applies to any piece-wise linear function and thus other cohesive laws that can be linearized and expressed in a similar form.

Under mixed mode conditions, it is assumed that the total fracture energy $\mathcal{G}$ is taken to be the sum of its mode I (opening) and mode II (shear) components

$$\mathcal{G} = \mathcal{G}_I + \mathcal{G}_{II}, \tag{2.25}$$

where the components are calculated from the traction separation law as

$$\mathcal{G}_I = \int_0^{\delta_n} \sigma\left(\delta_n\right) \mathrm{d}\delta; \quad \mathcal{G}_{II} = \int_0^{\delta_s} \tau\left(\delta_s\right) \mathrm{d}\delta. \tag{2.26}$$

Normal and shear crack separations then are interdependent and complete fracture is to occur when the following critical condition is reached via [91]

$$\frac{\mathcal{G}_I^*}{\Gamma_I} + \frac{\mathcal{G}_{II}^*}{\Gamma_{II}} = 1, \tag{2.27}$$

where Γ_I and Γ_{II} are the mode I and mode II fracture toughness in the linear elastic fracture mechanics (LEFM) context, which are equal to the total areas under the respective traction separation curves. This mixed-mode cohesive law is further explained in [92]–[94]. It guarantees correct mode mixity when LEFM conditions are satisfied with the benefit of not requiring the mode mixity to be specified because it evolves as a result of the local equilibrium of stresses.

Cohesive traction is the vector sum of normal and shear components along the crack plane. Therefore,

$$\mathbf{t}_c\left(\boldsymbol{\delta}\right) = \sigma\left(\delta_n\right)\hat{\mathbf{n}} + \tau\left(\delta_s\right)\hat{\mathbf{s}}, \tag{2.28}$$

where $\hat{\mathbf{n}}$ and $\hat{\mathbf{s}}$ are the unit vectors normal and tangential to the crack plane.

2.4.2 Heat Transfer Cohesive Law

In the literature of thermo-mechanical cohesive zone models, the cohesive zone heat flux q_c is taken to be the product of a cohesive conductance coefficient h_c and the temperature jump across the cohesive crack $\Delta\theta_c$, i.e.

$$q_c = h_c \Delta\theta_c . \tag{2.29}$$

Cohesive heat transfer laws have been formulated using an assumption of both one dimensional [55]–[57], [59] and two dimensional [58] heat transfer across the crack. In all of these formulations, determination of h_c involved consideration of fracture damage and depending on the physical process at hand, a simple conductance law or a very complex one derived from a micromechanics point of view that includes heat fluxes due to bridging fibers, gas trapped in the crack and radiation.

For the purpose of this investigation, a piece-wise linear cohesive heat transfer law that captures key aspects of heat transfer through an interface based on physical considerations is adopted. The assumptions made in formulating the thermal part of the thermo-mechanical cohesive law are as follows:

1) **Cohesive heat flux is independent of tangential crack opening and depends only on normal crack opening**. For small deformations, it can be argued that heat flux normal to the crack surface dominates over the tangential heat flux because the thermal gradient is largest normal to the crack surface and the influence of the tangential crack opening is negligible.
2) **The crack conductance law as a function of normal crack opening is a curve that can be approximated as a piece-wise linear function**. As discussed earlier

in the mechanical part of the cohesive law, the piece-wise linear form is necessary in formulating the FE equations because a linear segment can be assumed.

3) **Characteristic thermal cohesive properties are independent of temperature**. This assumption is valid if in a given temperature range thermal material properties remain more or less constant.

4) **Heat dissipation as a result of fracture is negligible**. Excess fracture energy over the amount required for crack formation does not result in heat generation on the crack surfaces.

5) **Cohesive heat transfer is reversible**. Cohesive heat conductance can be recovered if crack separations decrease.

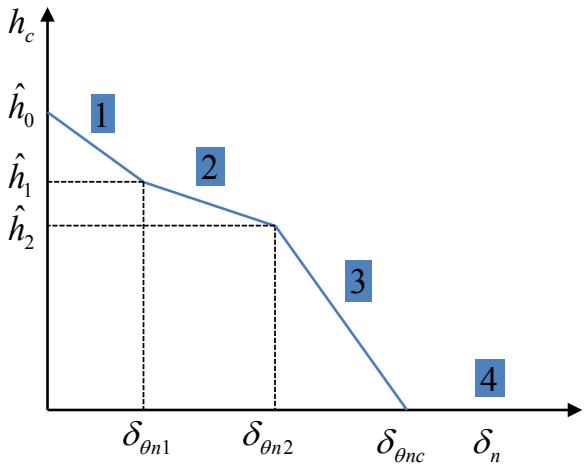

Figure 2.3: Bilinear cohesive heat transfer law. Numbers in blue denote the respective segment number.

The cohesive heat transfer law shown in Figure 2.3 can be indexed and expressed similarly to its mechanical equivalent. Define the characteristic heat transfer coefficient $\hat{h}^{(k)}$, the characteristic crack separation $\delta_n^{(k)}$ and the constant slope $\beta_n^{(k)}$ as

$$\hat{h}^{(0)} = \hat{h}_0, \quad \hat{h}^{(1)} = \hat{h}_1, \quad \hat{h}^{(2)} = \hat{h}_2, \quad \hat{h}^{(3)} = 0, \quad \hat{h}^{(4)} = 0 \tag{2.30}$$

$$\delta_{\theta n}^{(0)} = 0, \quad \delta_{\theta n}^{(1)} = \delta_{\theta n1}, \quad \delta_{\theta n}^{(2)} = \delta_{\theta n2}, \quad \delta_{\theta n}^{(3)} = \delta_{\theta nc}, \quad \delta_{\theta n}^{(4)} = \infty, \tag{2.31}$$

$$\beta_n^{(k)} = \frac{\hat{h}^{(k)} - \hat{h}^{(k-1)}}{\delta_n^{(k)} - \delta_n^{(k-1)}}, \tag{2.31}$$

where $k \in [1,4]$ is the cohesive segment index. Then the cohesive heat transfer coefficient as a function of normal crack separation is

$$h_c(\delta_n) = \hat{h}^{(k-1)} + \beta_n^{(k)}\left(\delta_n - \delta_{\theta n}^{(k-1)}\right), \quad \delta_n \in \ddot{\delta}_{\theta n}^{(k)}. \tag{2.32}$$

Therefore from Equation (2.29), cohesive heat flux as a function of normal crack separation and the cohesive temperature jump is given by

$$q_c(\delta_n, \Delta\theta_c) = \left[\hat{h}^{(k-1)} + \beta_n^{(k)}\left(\delta_n - \delta_{\theta n}^{(k-1)}\right)\right]\Delta\theta_c, \quad \delta_n \in \Delta\delta_{\theta n}^{(k)}. \tag{2.33}$$

Note that this particular form of the cohesive law can easily be changed to make the cohesive heat transfer coefficient constant until it drops to zero at some critical separation by imposing the conditions that $\delta_{\theta n1} = \delta_{\theta n2} = \delta_{\theta nc}$ and $\hat{h}_0 = \hat{h}_1 = \hat{h}_2$.

2.5 Thermo-Mechanical Cohesive Element

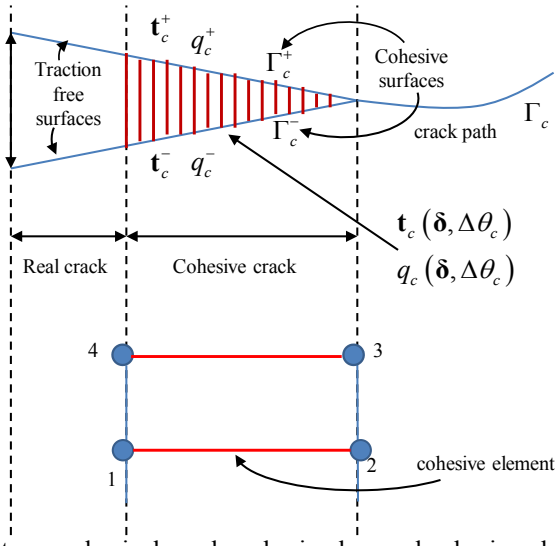

Figure 2.4: Relationship between physical crack, cohesive law and cohesive element.

In the CZM, a cohesive law is typically formulated into a special element, the so called cohesive element with its nodes shared with the abutting solid elements. Linear displacement distribution along the bonding edge is preferred for a cohesive element because it guarantees a monotonic change of crack separations within the element as it evolves toward failure. High-order elements with mid-nodes run the risk of contact at the mid-node pairs even if the crack separations at the corner nodes undergo monotonic changes [95], [96]. It has been clearly demonstrated in [97] that contact at node pairs is a major source for numerical instability. Therefore, the cohesive elements in this study are exclusively linear with 4 nodes. The relationship between a physical crack, the cohesive law and the cohesive element is shown in Figure 2.4. Both cohesive traction and heat flux are present on the cohesive surfaces created by the crack and are generally functions of the displacement and temperature jumps between the interface surfaces.

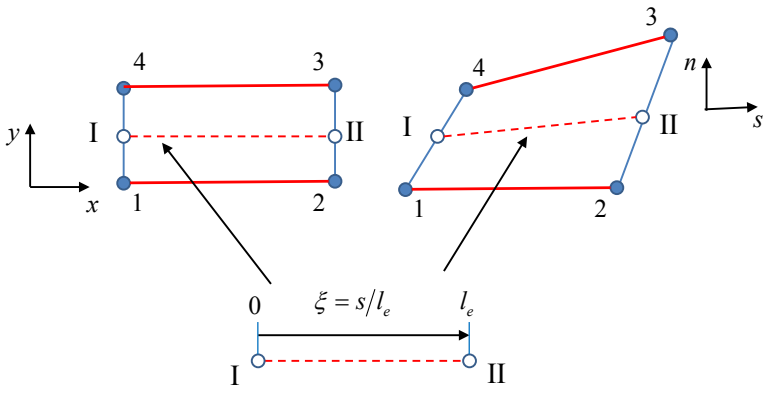

Figure 2.5: Illustration of a 4-node plane cohesive element from un-deformed configuration to deformed configuration. The cohesive crack separations are the relative displacements between node pair 4-1 and 3-2 and a reference line connects the midpoints between node pairs 1-4 and 2-3.

A reference line is defined as one connecting the midpoints between the node pairs 4-1 and 3-2, marked as I and II respectively, as seen in Figure 2.5. This 4 node, linear cohesive interface element is shown in both a reference undeformed state aligned with

global coordinate system (x, y) and a deformed state aligned with local coordinate system (s, n). Each of its four nodes has displacement and temperature DOFs $\mathbf{u} = \{u_1, v_1, u_2, v_2, u_3, v_3, u_4, v_4\}^T$ and $\boldsymbol{\theta} = \{\theta_1, \theta_2, \theta_3, \theta_4\}^T$. The length of the element reference line is given by

$$l_e = \sqrt{\left(\frac{1}{2}(x_3 + x_2) - \frac{1}{2}(x_1 + x_4)\right)^2 + \left(\frac{1}{2}(y_3 + y_2) - \frac{1}{2}(y_1 + y_4)\right)^2}, \quad (2.34)$$

where x_1, x_2, x_3, x_4 and y_1, y_2, y_3, y_4 are the nodal coordinates in the global Cartesian coordinate system. In two dimensions, Equations (2.13) and (2.14) are integrated over this reference line to give the equivalent nodal force and heat flow vectors $\{\mathbf{f}\} = \{F_{s1}, F_{n1}, F_{s2}, F_{n2}, F_{s3}, F_{n3}, F_{s4}, F_{n4}\}^T$ and $\{\mathbf{p}\} = \{P_1, P_2, P_3, P_4\}^T$ in the local coordinate system illustrated in Figure 2.6. By the continuity conditions of Equations (2.1) and (2.2), the cohesive nodal forces and heat flows in the same node pair must be equal in magnitude and opposite in direction, thus

$$\begin{Bmatrix} F_{s4} \\ F_{n4} \\ F_{s3} \\ F_{n3} \end{Bmatrix} = \begin{Bmatrix} -F_{s1} \\ -F_{n1} \\ -F_{s2} \\ -F_{n2} \end{Bmatrix} = \begin{Bmatrix} l_e \int_0^1 \tau(\xi)(1-\xi)\,\mathrm{d}\xi \\ l_e \int_0^1 \sigma(\xi)(1-\xi)\,\mathrm{d}\xi \\ l_e \int_0^1 \tau(\xi)(\xi)\,\mathrm{d}\xi \\ l_e \int_0^1 \sigma(\xi)(\xi)\,\mathrm{d}\xi \end{Bmatrix}, \quad (2.35)$$

$$\begin{Bmatrix} P_4 \\ P_3 \end{Bmatrix} = \begin{Bmatrix} -P_1 \\ -P_2 \end{Bmatrix} = \begin{Bmatrix} l_e \int_0^1 q_c(\xi)(1-\xi)\,\mathrm{d}\xi \\ l_e \int_0^1 q_c(\xi)(\xi)\,\mathrm{d}\xi \end{Bmatrix}. \quad (2.36)$$

The integrals are expressed in terms of a natural coordinate $\xi = s/l_e$, defined along the length of the reference line in the local coordinate system.

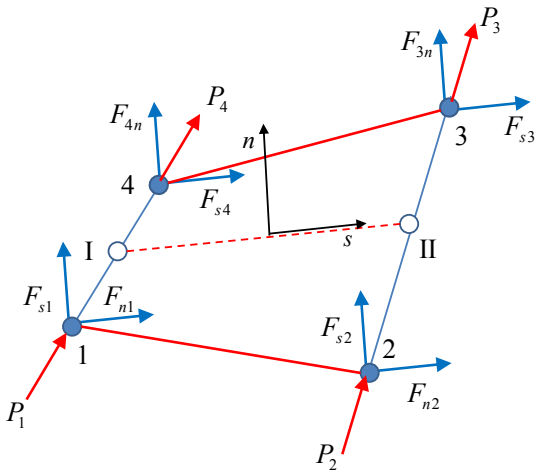

Figure 2.6: Cohesive forces and heat flows at the nodes of a deformed element.

If the cohesive law is the one described in Section 2.4, the cohesive stress and heat flux are functions crack separation and temperature jump along the reference line. The node pair displacement jump vector $\Delta\mathbf{u} = \{u_4 - u_1, v_4 - v_1, u_3 - u_2, v_3 - v_2\}^T$ is obtained from the nodal displacements vector $\mathbf{u}$ by a linear operator matrix $\mathbf{L}_{\Delta u}$ as

$$\Delta\mathbf{u} = [\mathbf{L}_{\Delta u}]\{\mathbf{u}\}. \tag{2.37}$$

Likewise, $\mathbf{L}_{\Delta\theta}$ is a linear operator matrix relating the nodal temperatures $\boldsymbol{\theta}$ to the temperature jump at the node pairs $\Delta\boldsymbol{\theta} = \{\theta_4 - \theta_1, \theta_3 - \theta_2\}^T$ so that

$$\Delta\boldsymbol{\theta} = [\mathbf{L}_{\Delta\theta}]\{\boldsymbol{\theta}\}. \tag{2.38}$$

In the deformed state shown in Figure 2.7, the reference line can rotate and may no longer coincide with the global coordinate system. Thus the node pair displacement jumps need to be transformed into the local coordinate system to obtain the normal and shear interface separation equivalents (δ_n and δ_s) used in the cohesive laws.

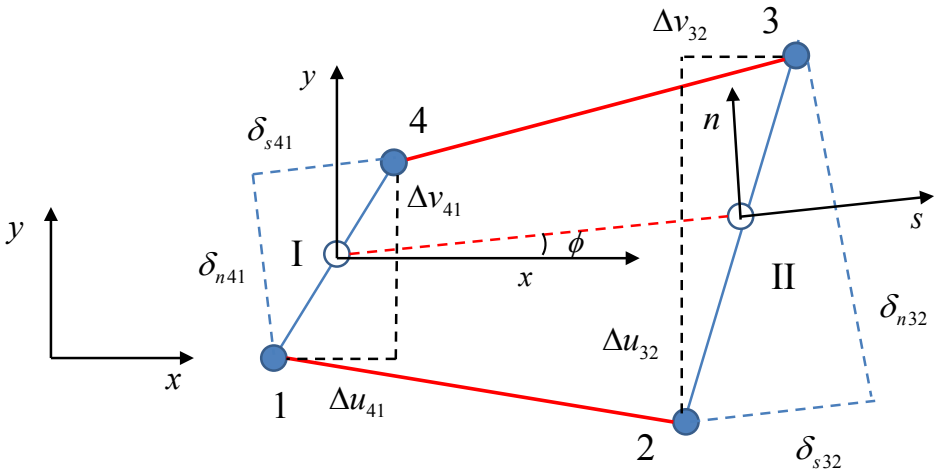

Figure 2.7: Deformed cohesive element with displacement jumps in global and local, crack oriented coordinate systems.

Define the rotation angle ϕ as

$$\phi = \tan^{-1}\left(\frac{y_3 + y_2 - y_1 - y_4}{x_3 + x_2 - x_1 - x_4}\right), \tag{2.39}$$

so that a rotation matrix can be expressed as

$$\mathbf{R} = \begin{bmatrix} \cos\phi & \sin\phi \\ -\sin\phi & \cos\phi \end{bmatrix}. \tag{2.40}$$

Global node pair displacement jumps $\Delta\mathbf{u} = \{\Delta u_{41}, \Delta v_{41}, \Delta u_{32}, \Delta v_{32}\}^T$ at midpoints I and II can be transformed to their local normal and tangential equivalents $\boldsymbol{\delta} = \{\delta_{s41}, \delta_{n41}, \delta_{s32}, \delta_{n32}\}^T$ by the relation

$$\boldsymbol{\delta} = \begin{bmatrix} \mathbf{R} & \mathbf{0} \\ \mathbf{0} & \mathbf{R} \end{bmatrix}\{\Delta\mathbf{u}\} = \text{Diag}[\mathbf{R};\mathbf{R}][\mathbf{L}_{\Delta u}]\{\mathbf{u}\}. \tag{2.41}$$

Here the operator Diag[•] denotes forming a diagonal matrix where the diagonal elements are composed of the quantity • being operated on.

The linearly distributed crack separations and temperature jump at any point on the reference line can be interpolated from their respective node pair values at midpoints I and II by shape functions in terms of ξ. Thus at a given ξ on the reference line

$$\left\{\delta_s(\xi), \delta_n(\xi)\right\}^T = \left[\mathbf{N}_{\Delta u}(\xi)\right] \mathrm{Diag}\left[\mathbf{R}; \mathbf{R}\right]\left[\mathbf{L}_{\Delta u}\right]\{\mathbf{u}\}, \tag{2.42}$$

$$\Delta\theta_c(\xi) = \left[\mathbf{N}_{\Delta\theta}(\xi)\right]\left[\mathbf{L}_{\Delta\theta}\right]\{\boldsymbol{\theta}\}, \tag{2.43}$$

where $\mathbf{N}_{\Delta u}$ and $\mathbf{N}_{\Delta\theta}$ are the displacement and temperature jump interpolation matrices respectively. Specific forms of the linear operators and the interpolation matrices are given in Appendix A.1.

2.5.1 Cohesive Integration

The general form of the numerical integration for Equations (2.35) and (2.36) using N integration points can be written as

$$\begin{Bmatrix} F_{s4} \\ F_{n4} \\ F_{s3} \\ F_{n3} \end{Bmatrix} = \begin{Bmatrix} -F_{s1} \\ -F_{n1} \\ -F_{s2} \\ -F_{n2} \end{Bmatrix} \approx \frac{l_e}{2} \begin{Bmatrix} \sum_{i=A,B,\ldots}^{N} w_i \tau(\xi_i)(1-\xi_i) \\ \sum_{i=A,B,\ldots}^{N} w_i \sigma(\xi_i)(1-\xi_i) \\ \sum_{i=A,B,\ldots}^{N} w_i \tau(\xi_i)(\xi_i) \\ \sum_{i=A,B,\ldots}^{N} w_i \sigma(\xi_i)(\xi_i) \end{Bmatrix}, \tag{2.44}$$

$$\begin{Bmatrix} P_4 \\ P_3 \end{Bmatrix} = \begin{Bmatrix} -P_1 \\ -P_2 \end{Bmatrix} \approx \frac{l_e}{2} \begin{Bmatrix} \sum_{i=A,B,\ldots}^{N} w_i q_c(\xi_i)(1-\xi_i) \\ \sum_{i=A,B,\ldots}^{N} w_i q_c(\xi_i)(\xi_i) \end{Bmatrix}. \tag{2.45}$$

where $\xi_i = (1+\eta_i)/2$ is the natural coordinate corresponding to the integration point η_i and w_i is the associated weight.

Numerical integration of the cohesive stress, Equation (2.44), in particular significantly effects the numerical stability, efficiency and accuracy of the cohesive element in fracture analysis. A limitation in CZM analyses is that the characteristic mesh size has to be less than 1/3 ~ 1/5 of the cohesive zone size to achieve reasonable numerical accuracy and stability because of the softening part of traction-separation law that governs the damaging processes at the crack tip regions [92], [98]. Therefore fracture analysis at the structural level is computationally expensive since the cohesive zone size is typically much smaller than the structural dimensions. Some researchers proposed using reduced cohesive strength to artificially increase the cohesive zone length and achieve numerical stability to lessen the strict requirement for mesh size [98], [99]. But such numerical treatments should be used only when the existing crack length is much larger than the cohesive zone length because they result in incorrect crack-tip stress fields.

In the literature, either the standard two integration point Gaussian integration (GI) or Newton-Cotes Integration (NCI) scheme (trapezoidal rule) was used for cohesive stress integration. However, which integration scheme or if any other scheme is more effective in cohesive fracture analysis remains an open research topic. For fracture problems in 2D or 3D solids, the NCI scheme appears to be a better solution because it provides a more accurate nodal stress evaluation and is numerically more stable, while standard GI scheme can cause undesired spurious oscillations of the traction field and hence is less numerically stable [95], [99]. In more recent studies [51], [100], [101], which used shell elements in conjunction with cohesive elements, a comparison reveals that the NCI scheme resulted in an odd wrinkling mode in thin laminates undergoing delamination process that is absent from the GI scheme, making it the more accurate of the two. In a

subsequent section, via a simple single element comparison, it will be demonstrated that such standard integration schemes are insufficient to resolve the nonlinear cohesive stress distribution, inevitable in a crack-tip cohesive element, especially when the element size is not much smaller than the cohesive zone size.

Another shortcoming of the existing cohesive elements is that, even if a much refined cohesive element mesh is used, the resulting crack front always zigzags because the front has to be in conformation with the bonded structural FEM mesh. In order to accurately capture the smooth crack front, a partially bonded cohesive element has to be introduced. To characterize an arbitrary crack front that cuts through a cohesive element, an accurate geometric description of the crack front is needed and the cohesive stress integration over the (intra-element) debonded zone and fully bonded zone has to be separately treated.

2.5.2 Standard Cohesive Stress Integration Schemes

To make the integration methods more easily amendable to derivation and numerical implementation, note that Equation (2.44) can be written in matrix form as

$$\begin{Bmatrix} F_{s4} \\ F_{n4} \\ F_{s3} \\ F_{n3} \end{Bmatrix} = \begin{Bmatrix} -F_{s1} \\ -F_{n1} \\ -F_{s2} \\ -F_{n2} \end{Bmatrix} = \frac{l_e}{2} \begin{bmatrix} w_A(1-\xi_A) & 0 & \cdots & w_N(1-\xi_N) & 0 \\ 0 & w_A(1-\xi_A) & \cdots & 0 & w_N(1-\xi_N) \\ w_A\xi_A & 0 & \cdots & w_N\xi_N & 0 \\ 0 & w_A\xi_A & \cdots & 0 & w_N\xi_N \end{bmatrix} \begin{Bmatrix} \tau_A \\ \sigma_A \\ \vdots \\ \tau_N \\ \sigma_N \end{Bmatrix}. \quad (2.46)$$

From Equation (2.46), it can be seen that the general form of the cohesive stress integration matrix for standard integration schemes of N integration points is a matrix of dimension $4 \times 2N$ given by

$$\mathbf{T}_{\mathbf{std}\Delta u} = \frac{l_e}{2} \begin{bmatrix} w_A(1-\xi_A) & 0 & \cdots & w_N(1-\xi_N) & 0 \\ 0 & w_A(1-\xi_A) & \cdots & 0 & w_N(1-\xi_N) \\ w_A\xi_A & 0 & \cdots & w_N\xi_N & 0 \\ 0 & w_A\xi_A & \cdots & 0 & w_N\xi_N \end{bmatrix}. \quad (2.47)$$

Since the cohesive law described in Section 2.4 is used, it can be shown that (see Appendix A.2) the cohesive stresses at N integration points can be expressed as

$$\begin{Bmatrix} \tau_A \\ \sigma_A \\ \vdots \\ \tau_N \\ \sigma_N \end{Bmatrix} = \{\boldsymbol{\sigma}_0\} + [\boldsymbol{\alpha}_0][\mathbf{N}_{\mathbf{std}\Delta u}]\,\mathrm{Diag}[\mathbf{R};\mathbf{R}][\mathbf{L}_{\Delta u}]\{\mathbf{u}\}. \tag{2.48}$$

Of importance is the $2N \times 4$ interpolation matrix $\mathbf{N}_{\mathbf{std}\Delta u}$ that interpolates the node-pair crack separations at the N natural coordinates ξ_i that correspond to the integration points η_i. For standard integration schemes, the interpolation matrix has the general form

$$\mathbf{N}_{\mathbf{std}\Delta u} = \begin{bmatrix} 1-\xi_A & 0 & \xi_A & 0 \\ 0 & 1-\xi_A & 0 & \xi_A \\ \cdots & \cdots & \cdots & \cdots \\ 1-\xi_N & 0 & \xi_N & 0 \\ 0 & 1-\xi_N & 0 & \xi_N \end{bmatrix}. \tag{2.49}$$

Both the integration and interpolation matrix are presented here because the improved integration schemes introduced later require only simple modifications to these matrices.

2.5.3 Improved Cohesive Stress Integration Schemes

Standard integration methods like NCI and GI have fixed integration points, an inflexibility that is a major source of numerical instability and inaccuracy. This problem is illustrated in Figure 2.8(a) where the CZM is applied to a double cantilever beam in mode I opening. The focus is on the region near the crack tip. In Figure 2.8(b), the stress distribution along the reference plane of two cohesive elements (1 and 2) connected by a shared node pair (midpoint II) is shown. The domain of these two connected reference planes consists of three regions corresponding to the fracture zone of the physical crack,

the cohesive zone and the elastic zone . Physically, the crack tip ends somewhere within the first element, and at this location that marks the end of the physical crack region, there is zero stress. In the subsequent cohesive zone, the stress is a function of crack opening and the stress gradually increases to the peak cohesive stress at the location where the crack opening is zero. This is now the elastic zone region where the stress in this case drops and becomes negative to reflect the compressive stress state to the right of the cohesive zone in the elastic region that occurs due to bending. Numerically, when the cohesive element size approaches or is larger than the cohesive zone size as in Figure 2.8(b), the deformations or cohesive damage states at a node-pair, computed from the two neighboring cohesive elements that share the node-pair, are significantly inconsistent from each other because the integration points do not move to reflect the moving crack tip and the size of the cohesive element is too large to accurately resolve the actual stress distribution.

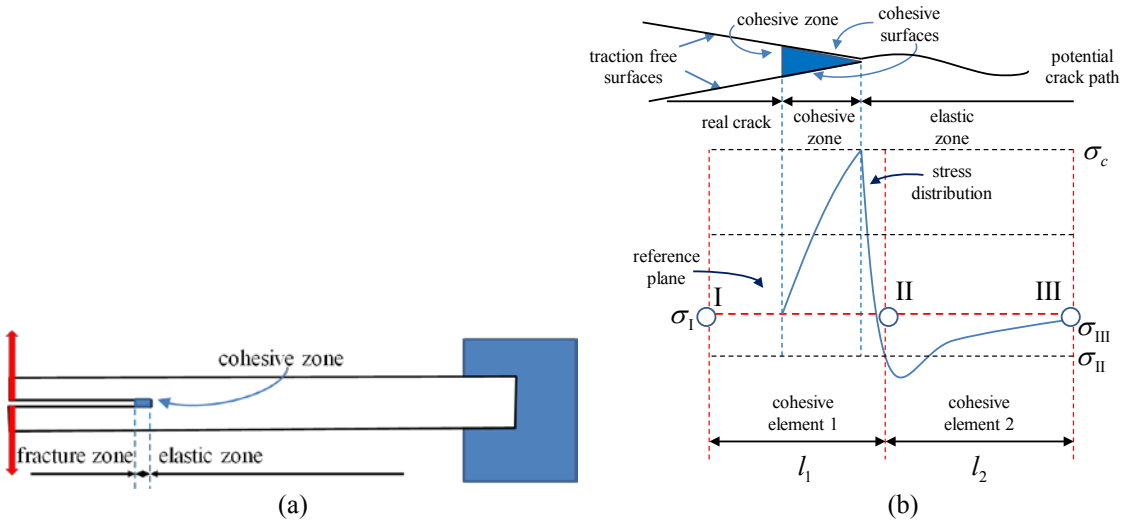

Figure 2.8: (a) A DCM in mode I opening; (b) CZM of physical crack with two cohesive elements.

Suppose that the cohesive stress distribution is integrated using the two integration point NCI scheme (trapezoidal rule) that approximates the stress as a linear distribution between the stress values at the midpoints I and II for cohesive element 1 and midpoints II and III for cohesive element 2 as in Figure 2.9(a). Note that the integration of the cohesive stress at midpoints I and II in cohesive element 1 fails to capture the peak in the stress distribution. In fact, the tensile stress distribution is approximated incorrectly as a compressive stress distribution. This results in inconsistent cohesive damage states at the node pair midpoints and leads to significant numerical oscillation as well as convergence difficulty. When a two point GI scheme is used as in Figure 2.9(b), the stress approximation is much better because the integration points have shifted and are more aligned with the actual stress distribution. But this scheme still underestimates the peak stress because of the inflexibility of having fixed integration points.

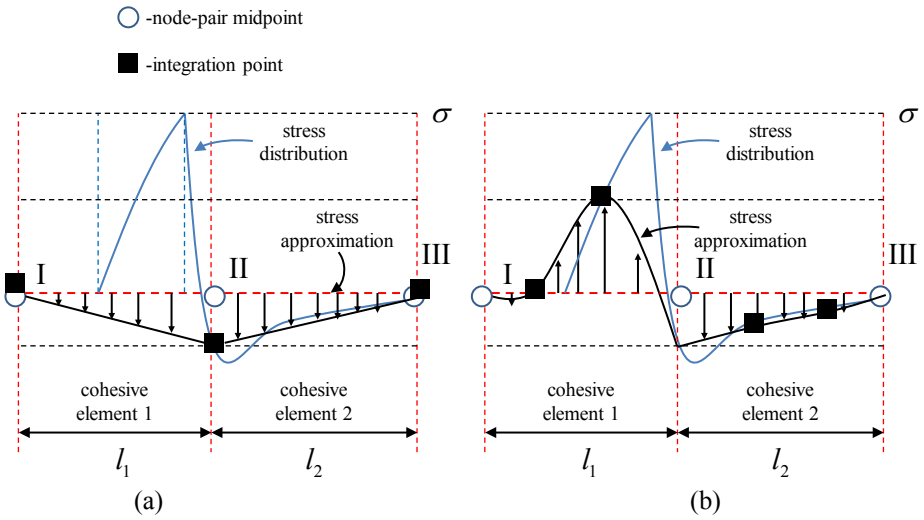

Figure 2.9: Approximation of stress distribution with (a) NCI scheme and (b) GI scheme.

Several improved integration methods can significantly improve the numerical accuracy, stability and robustness of the cohesive element. Here the focus is on two

possibilities that require only minimal modifications to the existing programs/subroutines for cohesive stress integration. These two possible improvement techniques are (1) increasing the number of integration points and (2) permitting the integration points to move in accordance with the actual physical crack-tip. More integration points theoretically better approximates the nonlinear cohesive stress distribution, and allowing the integration points to move as needed to conform to the actual crack-tip ensures better consistency in stress states, especially in the cases that one of the node-pairs has failed but the other one remains bonded (thus the crack-tip is within the element).

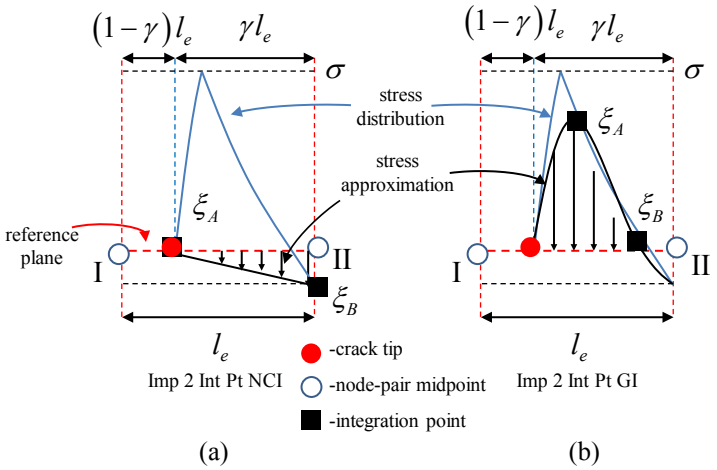

Figure 2.10: Improved integration schemes with moving integration points for (a) NCI and (b) GI schemes.

This method of moving integration points is illustrated in Figure 2.10 for both NCI and GI with two integration points. In both cases, the improvement to the stress approximation is significant. The error of the compressive stress distribution approximated by the NCI scheme with respect to the actual stress is dampened, and the GI approximation now more accurately captures the rise in stress. To modify the formulation, it is noted that the crack-tip is located somewhere along the reference line at

$(1-\gamma)l_e$ and the remaining bonded area is γl_e in length as seen in Figure 2.10. Thus the cohesive stress integration of Equation (2.35) has new limits and becomes

$$\begin{Bmatrix} F_{s4} \\ F_{n4} \\ F_{s3} \\ F_{n3} \end{Bmatrix} = \begin{Bmatrix} -F_{s1} \\ -F_{n1} \\ -F_{s2} \\ -F_{n2} \end{Bmatrix} = \begin{Bmatrix} l_e \int_{1-\gamma}^{1} \tau(\xi)(1-\xi)\,\mathrm{d}\xi \\ l_e \int_{1-\gamma}^{1} \sigma(\xi)(1-\xi)\,\mathrm{d}\xi \\ l_e \int_{1-\gamma}^{1} \tau(\xi)(\xi)\,\mathrm{d}\xi \\ l_e \int_{1-\gamma}^{1} \sigma(\xi)(\xi)\,\mathrm{d}\xi \end{Bmatrix}. \tag{2.50}$$

From this relation, the improved general integration matrix for N integration points can be derived to be

$$\mathbf{T}_{\mathbf{imp}\Delta u} = \frac{\gamma l_e}{2} \begin{bmatrix} w_A\gamma(1-\xi_A) & 0 & \cdots & w_N\gamma(1-\xi_N) & 0 \\ 0 & w_A\gamma(1-\xi_A) & \cdots & 0 & w_N\gamma(1-\xi_N) \\ w_A(1-\gamma+\gamma\xi_A) & 0 & \cdots & w_N(1-\gamma+\gamma\xi_N) & 0 \\ 0 & w_A(1-\gamma+\gamma\xi_A) & \cdots & 0 & w_N(1-\gamma+\gamma\xi_N) \end{bmatrix}. \tag{2.51}$$

The improved interpolation matrix is derived by noting that the natural coordinate in this case is given by $\xi_i' = 1-\gamma+\gamma\xi_i$. By substituting ξ_i' into Equation (2.49), the improved interpolation matrix is found to be

$$\mathbf{N}_{\mathbf{imp}\Delta u} = \begin{bmatrix} \gamma(1-\xi_A) & 0 & 1-\gamma+\gamma\xi_A & 0 \\ 0 & \gamma(1-\xi_A) & 0 & 1-\gamma+\gamma\xi_A \\ \cdots & \cdots & \cdots & \cdots \\ \gamma(1-\xi_N) & 0 & 1-\gamma+\gamma\xi_N & 0 \\ 0 & \gamma(1-\xi_N) & 0 & 1-\gamma+\gamma\xi_N \end{bmatrix}. \tag{2.51}$$

The derived interpolation and integration matrices for standard methods, Equations (2.47) and (2.49), and for improved integration methods, Equation (2.51) and (2.51), enable simple implementation of the different integration methods. Table 1.1 summarizes a variety of integration methods with respective integration points η_i and weights w_i

$(i = A, B, \cdots N)$ explicitly given. A note on the mixed methods such as GI&SDI2. These methods use the integration points of the first scheme for integration until one of the node-pair states 'fails' and then the remaining bonded area is integrated with the points given in the table.

Table 2.1: Summary of integration points and weights for various integration methods

Method	**No. of Integration Points**	**Label**	**Integration Points** $\eta_i \in [-1,1]$	**Integration Weights** w_i
Standard Eqns (2.47) & (2.49)	2 (I,II)	GI2	$-1/\sqrt{3}, 1/\sqrt{3}$	$1,1$
	2(I,II)	NCI2	$-1,1$	$1,1$
	3 (I,II,II)	GI3	$-\sqrt{3/5}, 0, \sqrt{3/5}$	$5/9, 8/9, 5/9$
	3 (I,II,II)	NCI3	$-1,0,1$	$1/3, 4/3, 1/3$
Improved Eqns (2.51) & (2.49)	2 (I,II)	IMP_GI2	$-1/\sqrt{3}, 1/\sqrt{3}$	$1,1$
	2(I,II)	GI&SDI2	$-1/2, 1/2$	$1,1$
	2(I,II)	NCI&SDI2	$-1/2, 1/2$	$1,1$
	3 (I,II,II)	IMP_GI3	$-\sqrt{3/5}, 0, \sqrt{3/5}$	$5/9, 8/9, 5/9$
	3 (I,II,II)	IMP_NCI3	$-1,0,1$	$1/3, 4/3, 1/3$
	3 (I,II,II)	GI&SDI3	$-2/3, 0, 2/3$	$2/3, 2/3, 2/3$
	3 (I,II,II)	NCI&SDI3	$-2/3, 0, 2/3$	$2/3, 2/3, 2/3$

GI2 – standard Gaussian Integration method with 2 integration points
IMP_GI2 – improved Gaussian Integration method with 2 integration points
GI&SDI2 – mixed Gaussian and subdomain method with 2 integration points
GI3 – standard Gaussian Integration method with 3 integration points
IMP_GI3 – improved Gaussian Integration method with 3 integration points
GI&SDI3 – mixed Gaussian and subdomain method with 3 integration points
NCI2 -- standard Newton-Cotes Integration method with 2 integration points (trapezoidal rule)
NCI&SDI2 -- mixed Newton-Cotes and subdomain method with 2 integration points
NCI3 -- standard Newton-Cotes Integration method with 3 integration points (Simpson's rule)
IMP_NCI3 -- improved Newton-Cotes Integration method with 3 integration points
NCI&SDI3 -- mixed Newton-Cotes and subdomain method with 3 integration points

2.5.4 Cohesive Heat Flux Integration

Provided that the cohesive heat transfer law is of the form detailed in Section 2.4.2, cohesive heat flux integration is very much an extension of the cohesive stress integration detailed prior. Equation (2.45) can be rewritten as

$$\begin{Bmatrix} P_4 \\ P_3 \end{Bmatrix} = \begin{Bmatrix} -P_1 \\ -P_2 \end{Bmatrix} = \frac{l_e}{2}\begin{bmatrix} w_A(1-\xi_A) & \cdots & w_N(1-\xi_N) \\ w_A\xi_A & \cdots & w_N\xi_N \end{bmatrix}\begin{Bmatrix} q_A \\ \vdots \\ q_N \end{Bmatrix}. \tag{2.52}$$

As shown in Appendix A.3, the cohesive heat fluxes at N integration points can be expressed as

$$\begin{Bmatrix} q_A \\ \vdots \\ q_N \end{Bmatrix} = \mathrm{Diag}\left[\{\mathbf{h}_0\} + [\boldsymbol{\beta}_0][\mathbf{N}_{\mathbf{std}\theta u}]\,\mathrm{Diag}[\mathbf{R};\mathbf{R}][\mathbf{L}_{\Delta u}]\{\mathbf{u}\}\right][\mathbf{N}_{\mathbf{std}\Delta\theta}][\mathbf{L}_{\Delta\theta}]\{\boldsymbol{\theta}\}. \tag{2.53}$$

It follows that the standard integration and interpolation matrices and their improved counterparts for cohesive heat flux integration are

$$\mathbf{T}_{\mathbf{std}\Delta\theta} = \frac{l_e}{2}\begin{bmatrix} w_A(1-\xi_A) & \cdots & w_N(1-\xi_N) \\ w_A\xi_A & \cdots & w_N\xi_N \end{bmatrix}, \tag{2.54}$$

$$\mathbf{N}_{\mathbf{std}\theta u} = \begin{bmatrix} 0 & 1-\xi_A & 0 & \xi_A \\ \vdots & \vdots & \vdots & \vdots \\ 0 & 1-\xi_N & 0 & \xi_N \end{bmatrix}, \tag{2.55}$$

$$\mathbf{N}_{\mathbf{std}\Delta\theta} = \begin{bmatrix} 1-\xi_A & \xi_A \\ \vdots & \vdots \\ 1-\xi_N & \xi_N \end{bmatrix}, \tag{2.56}$$

$$\mathbf{T}_{\mathbf{imp}\theta} = \frac{\gamma l_e}{2}\begin{bmatrix} w_A(1-\xi_A) & \cdots & w_N(1-\xi_N) \\ w_A\left(1-\gamma+\gamma\xi_A\right) & \cdots & w_N\left(1-\gamma+\gamma\xi_N\right) \end{bmatrix}, \tag{2.57}$$

$$\mathbf{N}_{\mathbf{imp}\theta u} = \begin{bmatrix} 0 & \gamma\left(1-\xi_A\right) & 0 & 1-\gamma+\gamma\xi_A \\ \vdots & \vdots & \vdots & \vdots \\ 0 & \gamma\left(1-\xi_N\right) & 0 & 1-\gamma+\gamma\xi_N \end{bmatrix}, \tag{2.58}$$

$$\mathbf{N}_{\mathbf{imp}\Delta\theta} = \begin{bmatrix} \gamma\left(1-\xi_A\right) & 1-\gamma+\gamma\xi_A \\ \vdots & \vdots \\ \gamma\left(1-\xi_N\right) & 1-\gamma+\gamma\xi_N \end{bmatrix}. \tag{2.59}$$

Schemes summarized in Table 2.1 are readily applied to these relations.

2.6 Element Validation

This section focuses on the mechanical and heat transfer capabilities of the described cohesive element. A cohesive element with all eleven integration schemes listed in Table 2.1 has been implemented in ABAQUS (6.10) as a user-defined element (UEL). The shortcomings of standard schemes for cohesive stress integration and the improvements in accuracy and numerical stability from proposed schemes are demonstrated through a single element and double cantilever beam (DBC) examples. Further, the basic response of the element for heat transfer problems is also demonstrated and evaluated for both steady state and transient cases.

2.6.1 Single Element Mode I Wedge Opening Response

All the integration schemes listed in Table 2.1 perform well and yield almost identical results given uniform loading and with fixed fracture mode ratio. Performance among the integration schemes significantly differ however, if there is significant stress variation within a single cohesive element. The single element shown in Figure 2.11 demonstrates such a case. A mode I wedge opening is modeled by the single element by having both top and bottom edges of the cohesive element rigid while the left nodes 1 and 4 are loaded symmetrically with an increasing vertical displacement $\left(v_4 = -v_1 = u^*\right)$ and the right nodes 2 and 3 are hinged $\left(u_2 = u_3 = v_2 = v_3 = 0\right)$ so that the cohesive stress at this node-pair is always zero.

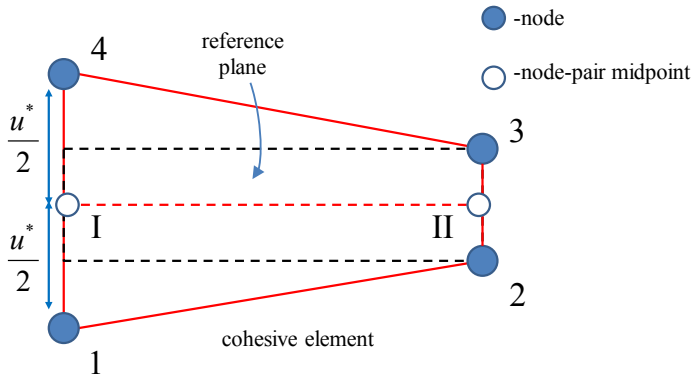

Figure 2.11: Single cohesive element in Mode I wedge opening.

The cohesive zone length l_e is 2 mm. A simple triangular shaped mode-I cohesive law is used here where the toughness is $\Gamma_I = 0.05$ N/mm, cohesive strength is $\hat{\sigma} = 1.0$ N/mm^2, and the initial elastic stiffness is $\alpha_{n0} = \hat{\sigma} / \delta_1 = 10^7$ N/mm^3. The critical separation is $\delta_{nc} = 0.1$ mm, and the separation corresponding to the peak stress is δ_{n1}.

It can be shown that an analytical expression for the load (per unit width) and load-point displacement can be derived as below [90]:

$$\frac{F}{\hat{\sigma} l_e} = \begin{cases} \dfrac{1}{3}\dfrac{u^*}{\delta_{n1}}, & (u^*/\delta_{n1} \le 1), \\ \dfrac{1}{2} + \dfrac{1}{3}\left(\dfrac{u^*}{\delta_{n1}}\right)^2 - \dfrac{1}{2}\left(\dfrac{u^*}{\delta_{n1}}\right)^{-2} - \left(\dfrac{1}{\delta_{nc}/\delta_{n1} - 1}\right)\left[\dfrac{1}{3}\left(\dfrac{u^*}{\delta_{n1}}\right) + \dfrac{1}{6}\left(\dfrac{u^*}{\delta_{n1}}\right)^{-2} - \dfrac{1}{2}\right], & (1 < u^*/\delta_{n1} \le \delta_{nc}/\delta_{n1}), \\ \dfrac{1}{3}\left(\dfrac{u^*}{\delta_{n1}}\right)^{-2} + \dfrac{1}{2}\left(\dfrac{\delta_{nc}/\delta_{n1}}{\delta_{nc}/\delta_{n1} - 1}\right) - \left(\dfrac{1}{\delta_{nc}/\delta_{n1} - 1}\right)\left(\dfrac{u^*}{\delta_{n1}}\right)^{-2}\left[\dfrac{1}{2}\dfrac{\delta_{nc}}{\delta_{n1}} + \dfrac{1}{3}\left(\dfrac{\delta_{nc}}{\delta_{n1}}\right)^{-1} - \dfrac{1}{3}\right], & (u^*/\delta_{n1} > \delta_{nc}/\delta_{n1}), \end{cases}$$

(2.60)

where u^* is the applied displacement at the left edge.

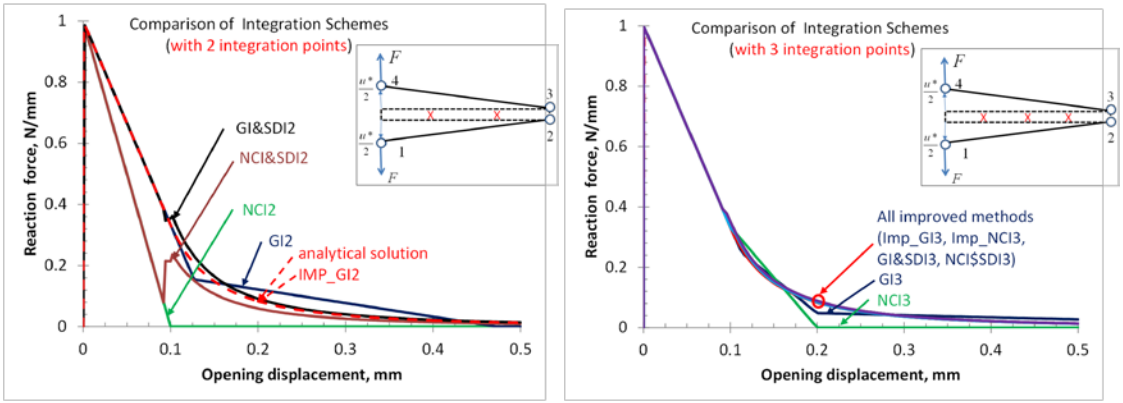

(a) (b)

Figure 2.12: Numerical performance of different integration methods on single element under wedge opening mode for (a) two integration point and (b) three integration points schemes.

The reaction forces at load-point as functions of opening displacements for various integration schemes are summarized in Figure 2.12 along with the analytical solution, the dashed line, in the same figure as a means for comparison. The energy dissipation associated with the entire elemental fracture process, i.e., the area enclosed by the load-displacement curve and the two axes, should be exactly 0.1 N/mm given the specified parameters. Figure 2.12(a) shows the numerical results obtained with 2 integration points where a few key conclusions can be drawn.

First, both standard NCI (NCI2) and standard GI (GI2) capture the peak load rather accurately, but the NCI2 significantly under-predicts the energy dissipation by 50%. In this case, GI2 clearly captures the energy dissipation much better (within ~ 5%) than NCI2. The sudden kink in the GI2 load-displacement curve is due to failure of the left integration point. As detailed earlier, the significantly under-predicted energy dissipation by the NCI2 is due to the premature failure prediction inherent to this method by non-moving integration points. The non-moving integration point effect for GI2 is less significant because the integration points of GI2 are within the range between the node-pairs. For NCI2, the integration points are taken at the location of the node-pairs, and thus

element failure (i.e., zero stress everywhere in the element) occurs when the left node-pair displacement reaches the critical opening displacement (δ_c), because at this point the stresses at both node-pairs become zero. Since the crack-tip is within the element, the cohesive stress is actually non-zero everywhere except at the two node-pairs (the left node-pair stress is zero because $\delta_n = u^* > \delta_c$, and the right node-pair stress is zero because $\delta_n = 0$).

Another notable result is that solution accuracy increased notably for improved methods (IMP_GI2, GI&SDI2, and NCI&SDI2) as compared to their respective standard integration schemes. Of all the improved methods, IMP_GI2's resulting load-displacement curve is almost an exact replica of the analytical curve. GI&SDI2 is also very accurate except that there is a small oscillation associated with switching of integration from Gaussian integration to subdomain integration. For NCI&SDI2, the solution enhancement mainly comes from the switching into SDI after one of the node-pair fails, indicated by the significantly jump of reaction force in the load-displacement curve.

Figure 2.12(b) shows the numerical results obtained with 3 integration points. Compared to results obtained with the two integration points in Figure 2.12(a), the solution accuracy for both standard methods (GI3 and NCI3) has been much improved because of the better approximation of the cohesive stress distribution with an extra integration point. However, the effect of non-moving integration points remains significant. The energy dissipation result of NCI3 is still under-evaluated by ~ 15% because it still suffers from the pre-mature failure (but it is much delayed as compared to the NCI2). Adding an extra integration point however resulted in a major improvement

from NCI2, which underestimates the energy dissipation by 50%. Figure 2.12(b) also shows major solution enhancement for the improved methods based on Newton-Cotes integration, IMP_NCI3 and NCI&SDI3. The load-displacement curves of these methods are now almost indistinguishable from the analytical result. Solution enhancement of the Gaussian-based improved methods, IMP_GI3 and GI&SDI3, is limited because for these methods, the results obtained with 2 integration points (IMP_GI2 and GI&SDI2) are already sufficiently close to the analytical solution.

2.6.2 Cohesive Heat Transfer Response

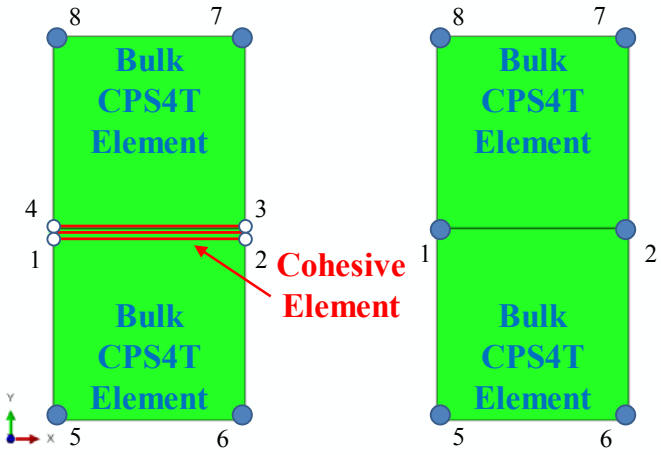

Figure 2.13: Model setup for comparison of cohesive heat transfer.

Comparison is made between the temperature distributions of bulk elements bridged and unbridged by a cohesive element. The desired temperature gradient is created by prescribing temperatures on the top and bottom surfaces through nodes 5-8 as seen in Figure 2.13. To the left, the model setup consists of two standard, coupled thermal-displacement plane stress elements in ABAQUS, CPS4T, defined by nodes 5, 6, 2, 1 and 4, 3, 7, 8 respectively, connected and sharing nodes with a TMCZ element of zero

thickness defined by nodes 1, 2, 3, 4. Bulk elements are thermoelastic, isotropic and square with an area of $1\ \mathrm{m}^2$. The modulus is $E = 100$ GPa, Poisson's ratio $\nu = 0.25$, thermal conductivity $k = 1.0\ \mathrm{W \cdot m^{-1} \cdot K^{-1}}$, density $\rho = 1.0\ \mathrm{kg \cdot m^{-3}}$ and specific heat $c = 1.0\ \mathrm{J \cdot kg^{-1} \cdot K^{-1}}$. To examine only the heat transfer process, the coefficient of thermal expansion is set to be $\alpha = 0\ \mathrm{K^{-1}}$ to negate the thermal influence on the mechanical loading.

A piecewise linear cohesive thermo-mechanical law described in Section 2.4 is assumed where damage effects are neglected so that the cohesive heat transfer coefficient is strictly a function of normal crack opening. The cohesive zone length l_e is 1 m. Normal and shear fracture parameters are assumed equal where the toughness is $\Gamma = 10$ N/m, cohesive strength is $\hat{\sigma} = 10^6\ \mathrm{N/m^2}$, and the initial elastic stiffness is $\alpha_0 = 10^9\ \mathrm{N/m^3}$. The critical separation is $\delta_c = 0.1$ m, and the separation corresponding to the peak stress is $\delta_1 = 0.001$ m. Characteristic separations for the heat transfer law are assumed identical to the mechanical law, i.e. $\delta_{\theta n1} = \delta_{n\theta 2} = 0$ and $\delta_{\theta nc} = \delta_c$. The cohesive heat transfer coefficient is taken to be linearly decreasing from some initial value ($\hat{h}_0 = \hat{h}_1 = \hat{h}_2 = h_c$) until normal crack separation reaches δ_c and $h_c = 0$ for $\delta_n > \delta_c$.

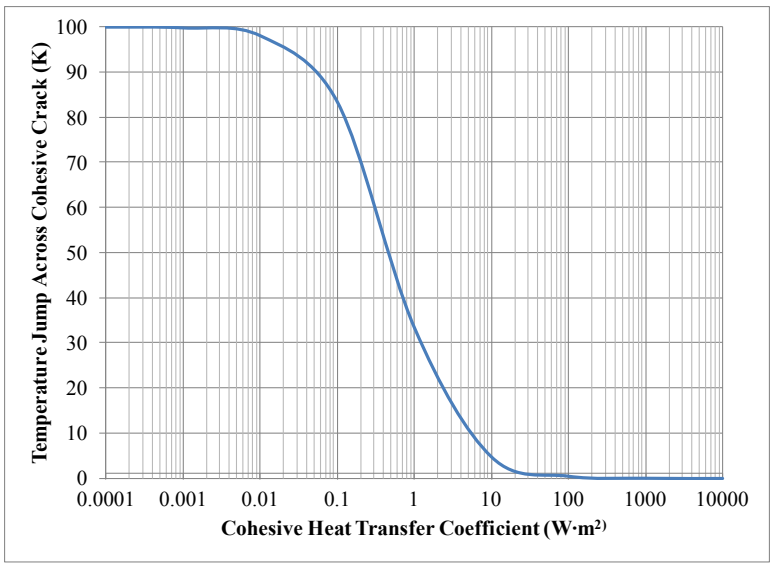

Figure 2.14: Influence of cohesive heat transfer coefficient on the temperature jump across the interface.

First, the significance of the overall cohesive heat transfer coefficient h_c is examined. Its influence on the temperature jump across the cohesive crack is shown in Figure 2.14. From the single interface element model setup described, a temperature gradient of $\Delta T = 100$ K is imposed by the boundary conditions $\theta_7 = \theta_8 = 100$ K and $\theta_5 = \theta_6 = 0$ K under a steady state condition. Mechanically, the elements are constrained to remain static. The temperature change or jump is between node-pairs 4-1 and 3-2, which are equal, of the thermo-mechanical cohesive element. Choice of h_c has a significant effect on the nodal temperatures of the cohesive element. Figure 2.14 shows that the thermo-mechanical cohesive element exhibits the expected behavior in the limiting values of h_c. As $h_c \to 0$, the temperature change $\Delta\theta \to 100$ K because the interface surfaces become adiabatic and the temperatures on the respective surfaces settle to the prescribed values of the now separated domains. As $h_c \to \infty$, the temperature change $\Delta\theta \to 0$ K because the surfaces conduct heat perfectly and behave as if no interface exists.

Four cases are considered to demonstrate how the thermal-mechanical cohesive element behaves: (1) mode I or normal opening $-v_1 = -v_2 = v_3 = v_4 = 0.15$ m; (2) mode II or tangential sliding $u_3 = u_4 = 0.15$ m; (3) mixed mode or normal and tangential opening $u_3 = u_4 = v_3 = v_4 = 0.15$ m; and (4) mode I wedge or hinged opening $-v_1 = v_4 = 0.15$ m. Note that prescribed displacements are chosen to be larger than the critical separation value for the cohesive law in order to see the transition from conducting cohesive surfaces to adiabatic cohesive surfaces and allow for the evaluation of the resulting temperature distribution and comparison with the interface free model setup. Mechanically, elements are constrained so that the prescribed displacement is uniform and bulk elements remain rigid. Again a temperature gradient of $\Delta T = 100$ K is imposed by the boundary conditions $\theta_7 = \theta_8 = 100$ K and $\theta_5 = \theta_6 = 0$ K. The boundary conditions are applied as step functions so that prescribed values are applied by the second increment. Both steady state and transient cases are considered where $h_c = 1.0\ \mathrm{W \cdot m^{-2} \cdot K^{-1}}$.

It is expected that cases (1) and (3) should have identical temperature profiles because the cohesive transfer coefficient is only a function of normal crack separation and the boundary conditions applied in both cases result in the same normal crack separation. For case (2), the coefficient of cohesive heat transfer remains constant and so the temperatures at the interface nodes should settle to values that give a temperature jump of $\Delta\theta \approx 33$ K because $h_c = 1.0\ \mathrm{W \cdot m^{-2} \cdot K^{-1}}$ according to Figure 2.14. Case (4) should have a temperature distribution that has features of both case (1) and (2) due to the wedge

opening which causes node-pair 3-2 to be completely failed (therefore adiabatic) and the node-pair 4-1 to be completely bonded (where $h_c = 1.0\ \mathrm{W \cdot m^{-2} \cdot K^{-1}}$).

Figure 2.15 shows the temperature-displacement curves of the cohesive element for all four loading cases along with the no interface temperature at nodes 1 and 2 in the two bulk element setup under steady state conditions. The no interface temperature represents the temperature at the center of the distance between the applied boundary conditions and thus is always half the value of the applied temperature gradient, 50 K. In all loading cases the responses are as expected. For the mode I opening of case (1), Figure 2.15(a) shows that the temperature jump between the top cohesive surface (nodes 3 and 4) and bottom cohesive surface (nodes 1 and 2) is initially $\Delta\theta \approx 33\ \mathrm{K}$ as expected for the given h_c. As the displacement increases and h_c decreases, the temperature jump grows larger until the temperature jump is equal to the temperature gradient when the critical separation is reached at 0.1 m displacement. At further displacement after 0.1 m the cohesive surfaces are adiabatic and thus cohesive surfaces temperatures remain constant. There is a clear transition in the temperature-displacement curves from reducing heat transfer to adiabatic surfaces. No such change occurs in case (2) because the displacement results in a completely shear crack separation which has no effect on the coefficient of cohesive heat transfer. From Figure 2.15(b), it can be seen that the temperatures at the cohesive surfaces settle at temperatures such that the temperature jump between cohesive surfaces is a constant $\Delta\theta \approx 33\ \mathrm{K}$ because h_c remains constant. Temperature curves in Figure 2.15(c) are identical to curves in Figure 2.15(a) indicating that h_c is a function of normal crack separation only and the equivalency of loading cases (1) and (3) that give the same normal separation. In case (4), the node pair temperature

jumps reflect the cohesive damage state. Node pair 4-1 remains bonded while node pair 3-2 is completely debonded, i.e. $h_c = 1.0\ \mathrm{W \cdot m^{-2} \cdot K^{-1}}$ at 4-1 and $h_c = 0\ \mathrm{W \cdot m^{-2} \cdot K^{-1}}$ at 3-2. This means, one node pair transfers heat at a reduced conductance while the other does not at all. As seen in Figure 2.15(d), temperature jumps occur at both node pairs, $\Delta\theta_{14} \approx 50\ \mathrm{K}$ for node pair 4-1 and $\Delta\theta_{32} \approx 73\ \mathrm{K}$ for node pair 3-2 when wedge opening displacement reaches 0.15 m. Note that a higher temperature jump is associated with the adiabatic, debonded pair as expected.

Transient cases are examined in a time duration of 5 seconds from an initial uniform temperature of $0\ \mathrm{K}$. As before, boundary conditions are applied as step functions so that prescribed values are reached instantaneously. Again, it can be seen that temperature-displacement curves in Figure 2.16(a) and Figure 2.16(c) are identical. The nonlinear temperature-displacement curves converging to a temperature jump of $\Delta\theta \approx 100\ \mathrm{K}$ again indicate a reduction in heat transfer capability with increasing displacement. Figure 2.16(b) shows that the temperatures at both the top and bottom cohesive surfaces converge to their steady state temperatures so that the temperature jump is $\Delta\theta \approx 33\ \mathrm{K}$. Similarly, the nodal temperatures-displacement curves in Figure 2.16(d) converge to steady state values that result in temperature jumps $\Delta\theta_{14} \approx 50\ \mathrm{K}$ for node pair 4-1 and $\Delta\theta_{32} \approx 73\ \mathrm{K}$ for node pair 3-2. Under transient conditions, the temperature profiles for each loading case have the same expected behavior as under steady state conditions. As seen in Figure 2.16(a)-(d), the main difference from the steady state responses is that transient temperature curves are nonlinear due a time dependence but converge to steady state values as time duration becomes large.

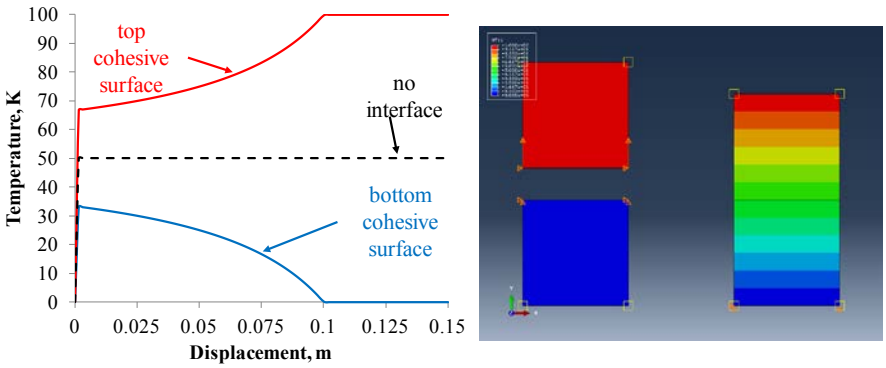

(a)

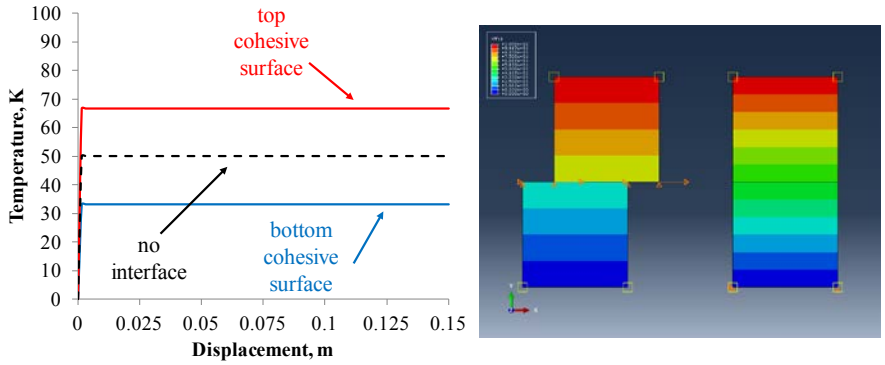

(b)

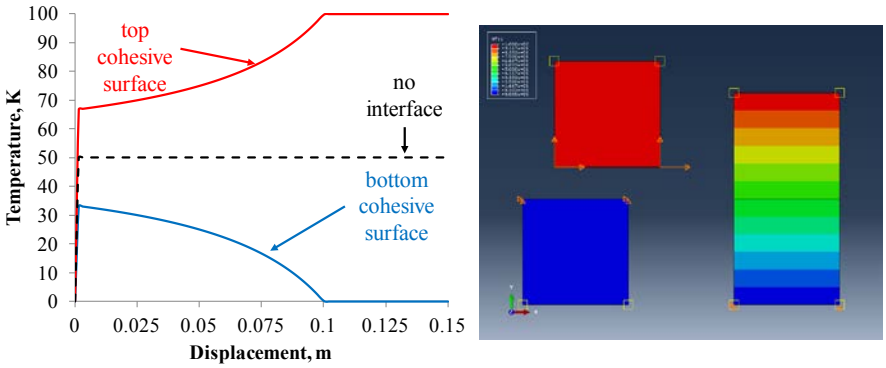

(c)

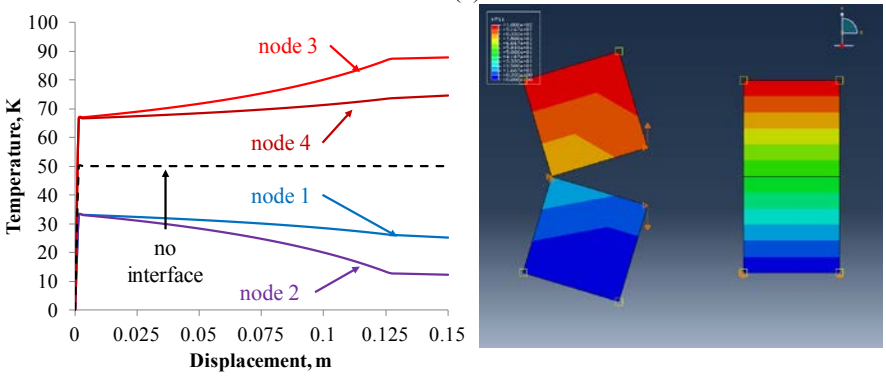

(d)

Figure 2.15: Temperature profile vs. displacement under steady state condition heat transfer for (a) mode I opening (b) mode II sliding (c) mixed mode (d) mode I wedge opening.

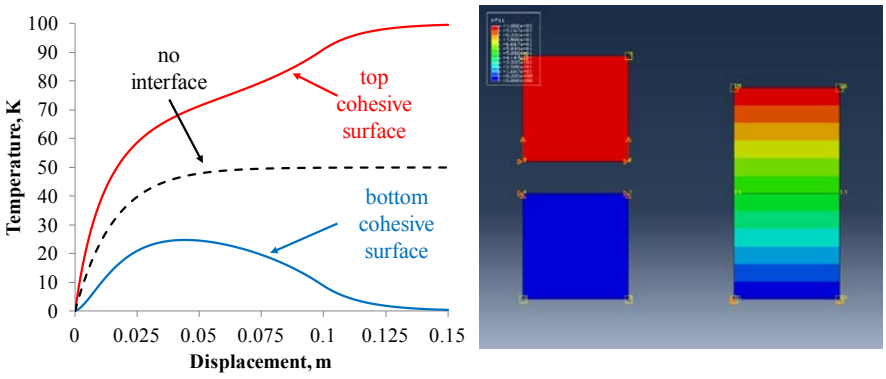

(a)

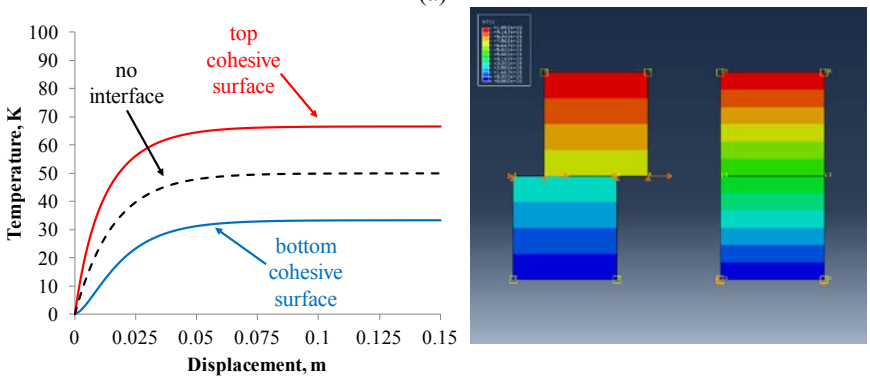

(b)

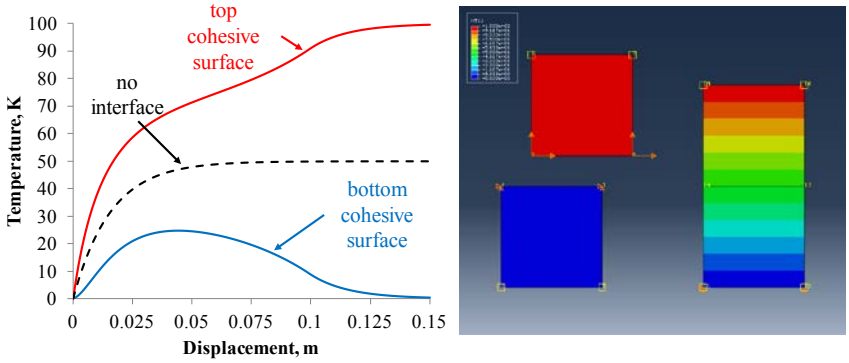

(c)

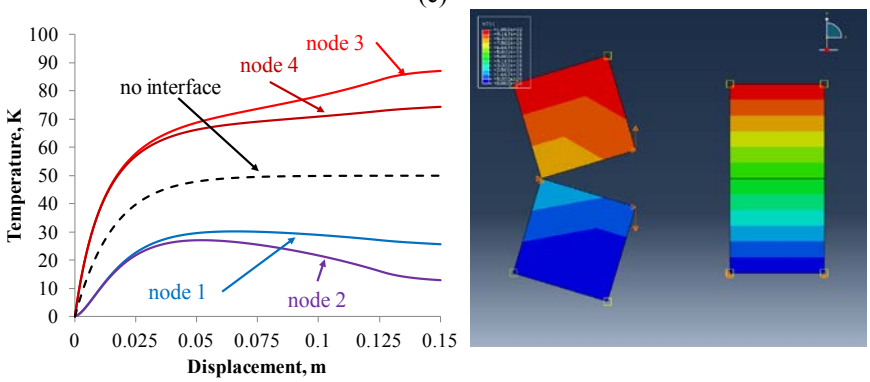

(d)

Figure 2.16: Temperature profile vs. displacement under transient heat transfer for 5 seconds for (a) mode I opening (b) mode II sliding (c) mixed mode (d) mode I wedge opening.

2.6.3 Multiple Element Example, Mode I Opening of a DCB

To test the subroutine's numerical capability, a model of a bonded double cantilever beam (DCB) under mode-I transverse loading was chosen because (1) an analytical solution is available; and (2) for a typical engineering material, the mode-I cohesive zone is usually the smallest and poses the most numerical difficulties.

The DCBs are discretized into a mesh of 100 x 8 = 800 plane-stress solid elements (CPS4 in ABAQUS). The thicknesses of the DCBs are fixed at $2t$ = 5.0 mm (i.e., the mesh size along the beam thickness, l_t, direction is fixed at 0.625 mm). The beam lengths are adjusted according to the mesh sizes used as discussed below. The two halves of each DCB are connected by a layer of cohesive elements with zero bond thickness, as shown by the inset of Figure 2.17(a). All the DCBs are fully bonded before loading (i.e., no initial crack with finite length) and their left edges are subjected to displacement-controlled loading as indicated in Figure 2.17(a).

The mesh size along the cohesive crack plane (l_e) is critical in assessing the numerical performance of the cohesive zone model results. In the literature for cohesive model analyses where standard integration methods were used, there is typically a size constraint that l_e be 3 to 5 times smaller than the cohesive zone size (l_{ch}), i.e., $l_e / l_{ch} < 1/3 \sim 1/5$. In this study, both l_e and l_{ch} are altered systematically to assess the numerical performance of the improved integration methods with a wider range of l_e to l_{ch} ratios. Further, there are additional numerical uncertainties associated with the use of 2D plane elements in simulating the beam bending problems, especially when the elemental aspect ratio (l_e/l_t) is large. To minimize this uncertainty, the mesh sizes along the crack plane are restricted to $l_e / l_t < 3$ for all cases.

The mesh size (l_e) is to be normalized by the cohesive zone length of the crack, l_{ch}. The cohesive zone size for fracture problems in beam-like structures is not only a material constant, but also a function of structural dimension. There is no universal solution to l_{ch} but an approximate expression that can estimate the cohesive zone size for isotropic DCBs has been given by [102]

$$\frac{l_{ch}}{t} = 1.01\left(\frac{E\Gamma_{\mathrm{I}}}{\hat{\sigma}^2 t}\right)^{\frac{1}{4}}. \tag{2.61}$$

This expression provides a rough estimate of the cohesive zone size and acts as a guide of how to adjust the elastic and cohesive parameters in order to achieve different relative mesh sizes of l_e/l_{ch}, with minimal change of the mesh size l_e. The beam modulus (E) is varied from 0.5 x 10^5 to 1.0 x 10^7 N/mm^2, and the mode I cohesive strength ($\hat{\sigma}$) is varied from 50 to 100 N/mm^2, to achieve various cohesive zone lengths. The Poisson's ratio of the DCB is $\nu = 0.3$. The mode-I cohesive law used is a triangular type and has a fixed fracture toughness and initial stiffness of $\Gamma_{\mathrm{I}} = 1.0$ N/mm and $\alpha_{n1} = 1.0\times10^5$ N/mm^3 for all the cases.

The cohesive zone length as a function of $E\Gamma_{\mathrm{I}}/\hat{\sigma}^2 t$ is computed using a much refined mesh of l_e = 0.25 mm and the determination of the cohesive zone size is illustrated by the example in Figure 2.17(a). This figure shows the opening stress distribution in a DCB with $\Gamma_{\mathrm{I}} = 1.0$ N/mm and $\hat{\sigma} = 50$ N/mm^2. The cohesive zone length corresponds to the interval in which the cohesive stress decreases from the peak cohesive strength to zero, which in the figure is effectively 3.5 mm.

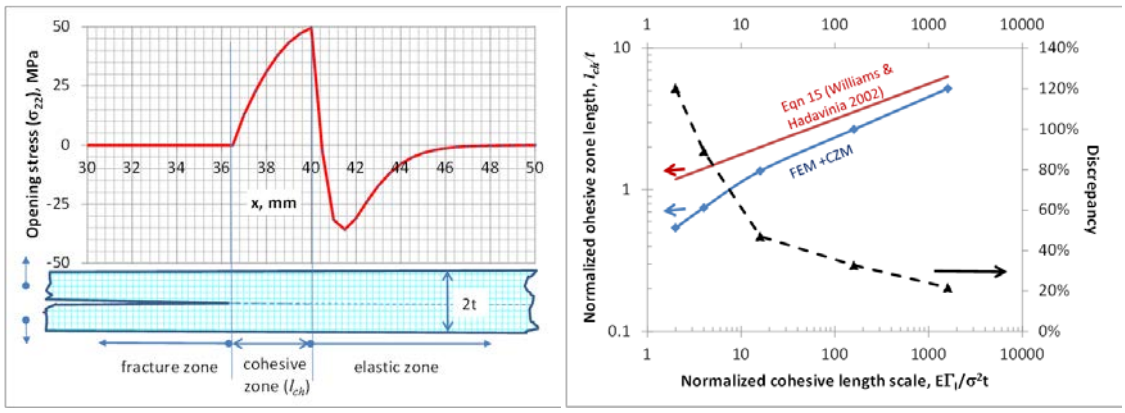

(a) (b)

Figure 2.17: (a) The opening stress distribution in a DCB with E =10^5 N/mm^2, Γ_I = 1.0 N/mm, and $\hat{\sigma}$ = 50 N/mm^2; (b) Numerically determined l_c/t as a function of $E\Gamma_I / \hat{\sigma}^2 t$ (the curve labeled as FEM+CZM) as compared to that obtained with the approximate expression of Equation (2.61) (left vertical axis). The discrepancy associated with the approximate expression is also plotted in this figure (right vertical axis).

The numerically obtained normalized cohesive zone length (l_{ch}/t) as a function of $E\Gamma_I / \hat{\sigma}^2 t$ is shown in Figure 2.17(b). Also plotted in this figure is the approximate solution of Equation (2.61) (left vertical axis) and the numerical discrepancies associated with it (right vertical axis). It is seen that Equation (2.61) works only when $E\Gamma_I / \hat{\sigma}^2 t$ is very large, i.e. when the cohesive zone length (l_{ch}/t) is much larger than 1. This is expected because Equation (2.61) is derived from beam bending consideration, and in general Equation (2.61) overestimates the cohesive zone size by 20% ~ 100%.

To investigate the mesh sensitivity of the present cohesive element, the normalized cohesive element mesh sizes are varied from l_e/l_{ch} = 0.14 to l_e/l_{ch} = 1.66. The simulated load-displacement curves are compared to the analytical solution based on beam bending analysis [72]

$$F = \left(\frac{\Gamma_I^{\,3} E h^3}{108 u^2} \right)^{\frac{1}{4}} \tag{2.62}$$

where u is the applied displacement at the load points.

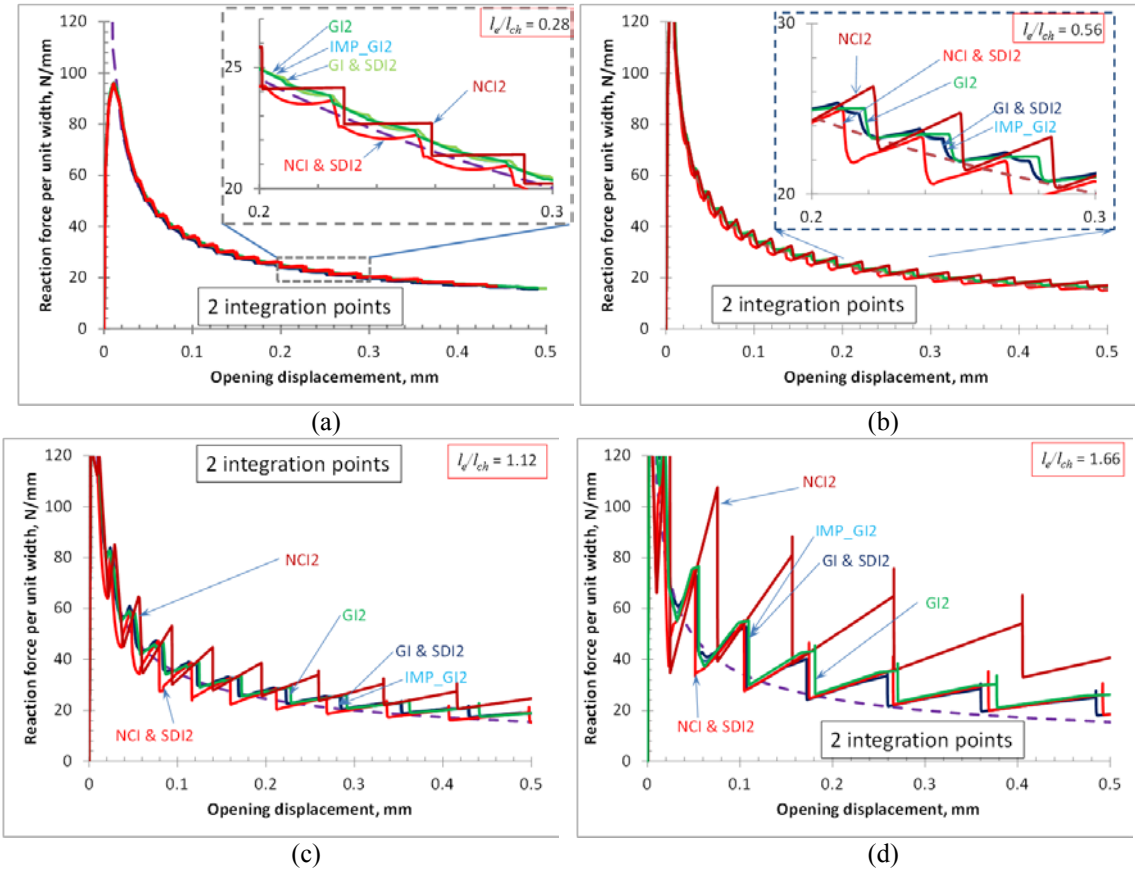

Figure 2.18: Comparison of DCB results for all integration methods with 2 integration points with characteristic mesh size of (a) l_e/l_{ch} = 0.28; (b) l_e/l_{ch} = 0.56; (c) l_e/l_{ch} = 1.12; (d) l_e/l_{ch} = 1.66.

The analytical and numerical results obtained with 2 integration points are summarized in the plots of Figure 2.18. Figure 2.18(a) compares the numerical performance of all integration methods for mesh l_e / l_{ch} = 0.28. With such a small mesh size, all numerical results agree very well with the analytical result. As the mesh size increases to more than half of the cohesive zone size (l_e / l_{ch} = 0.56, Figure 2.18(b)), the results obtained with Newton-Cotes integration based methods, NCI2 and NCI & SDI2, become oscillatory around the analytical curve; the curves obtained from GI based methods (i.e. GI2, IMP_GI2, and GI & SDI2), however, remain very smooth and close to the analytical curve. When the mesh size further increases to be slightly larger than the

cohesive zone length (l_e / l_{ch} = 1.12, Figure 2.18(c)), both NDCI & SDI2 and NCI2 results become strongly oscillatory and they significantly deviate away from the analytical solution. Gaussian integration based methods also show some moderate oscillations but the solution remain stable and with reasonable numerical accuracy. Even as the mesh size becomes much larger than the cohesive zone size (l_e / l_{ch} = 1.66, Figure 2.18(d)), the improved methods still capture the load-displacement curves reasonably well although the oscillation becomes significant. The curve obtained with the NCI2 is a clear outlier with significant numerical error.

Figure 2.19(a) gives the averaged numerical error as a function of normalized mesh sizes. Several conclusions can be immediately drawn from this figure. First, the numerical accuracy of the Gaussian integration based methods, GI2, IMP_GI2, and GI & SDI2, is more than 2 times better than the standard NCI result of NCI2, if the same mesh sizes are used. The NCI2 can achieve the similar solution accuracy only when the mesh size is very small ($l_e/l_{ch} < 0.2$). Second, among all the improved integration methods, the NCI & SDI2 has much better solution accuracy for small and moderate meshes, i.e., $l_e/l_{ch} < 0.5$. However, for larger mesh size, $l_e/l_{ch} > 0.6$, the advantage diminishes and the method is much less stable than the Gaussian based methods. Third, it appears that all the improved methods have a convergence rate of slightly less 2, as indicated by the average slopes of the curves in this log-log plot. This is very encouraging given the fact that the negative slope in a cohesive law usually leads to a much lesser convergence rate compared to the optimal rate of 2.

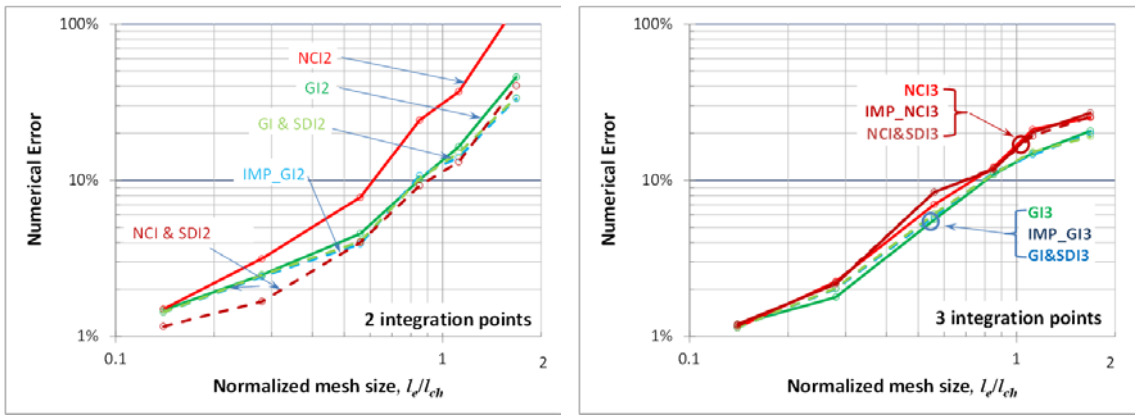

(a) (b)

Figure 2.19: Averaged numerical error for (a) 2 integration points and (b) 3 integration points as a function of mesh size for the mode-I fracture of the DCBs.

In general the numerical accuracy can be further improved by using more integration points, especially for larger meshes and for the Newton-Cotes based method. The numerical results obtained with 3 integration points for mesh sizes l_e/l_{ch} = 1.12 and 1.66 are plotted in Figure 2.20 (for smaller mesh sizes, the results are not much different from those obtained with 2 integration points shown in Figure 2.18(a) and (b)). The associated numerical error is plotted in Figure 2.19(b).

Using 3 integration points greatly improves the numerical accuracy for the Newton-Cotes based methods. For example, from NCI2 to NCI 3 the numerical error is reduced from ~40% to ~20% for l_e/l_{ch} = 1.12, and from ~130% to ~25% for l_e/l_{ch} = 1.66. For Gaussian based methods, the improvement for mesh size l_e/l_{ch} = 1.12 is not very much (from 16% to 14%) but for l_e/l_{ch} = 1.66 the improvement is appreciable from ~40% to 20%. With the use of 3 integration points, the overall numerical accuracy of Newton-Cotes based methods (NCI3, IMP_NCI3, and NCI & SDI3) is close to that of the Gaussian integration based methods (GI3, IMP_GI3, and GI & SDI3). However, the Newton-Cotes based methods are numerically less stable than the Gaussian based methods as demonstrated in [90]. The numerical cost associated with using 3 integration

points as compared to the 2 integration points is on average 20% with the results showing that the numerical gain by using more than 3 integration points is minimal.

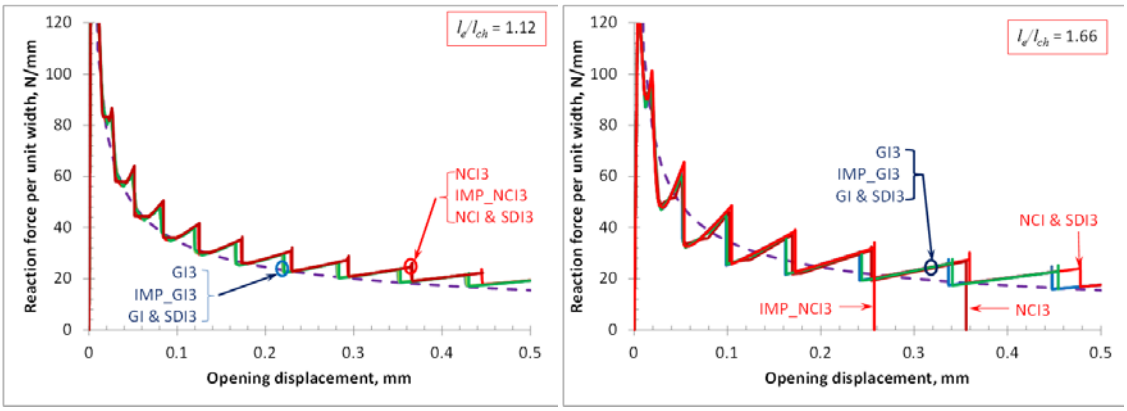

(a) (b)

Figure 2.20: Comparison of DCB results for all integration methods with 3 integration points with characteristic mesh size of (a) l_e/l_{ch} = 1.12; (b) l_e/l_{ch} = 1.66.

The improvement in solution accuracy by the improved methods proposed in this paper enables the use of much larger mesh size as allowed by the standard NCI2. For example, with an error tolerance of 10%, the proposed cohesive element allows for the use of maximum mesh size (for 4-node plane elements) of about l_e/l_{ch} ~1, which is significantly larger than the mesh size of l_e/l_{ch} < 1/3-1/5 as required by the standard methods of NCI2 and GI2.

2.7 Summary

This chapter presented and evaluated several integration schemes to investigate the improvement if any in accuracy of the cohesive stress integration for linear cohesive elements and ease the restriction on cohesive element size of the widely used standard Gaussian integration (GI) and Newton-Cotes integration (NCI) method (the element size be smaller than 1/3~1/5 of the cohesive zone size). The new cohesive stress integration

schemes involved increasing the number of integration points (from 2 to 3) and explicitly considering the moving crack-tip within an element. To that end, the key elements in constructing a cohesive element, the stress integration matrices for both standard and improved integration schemes with any number of integration points, have been explicitly derived. The performance of eleven integration schemes, the standard GI with 2 and 3 integration points (GI2 and GI3), the improved GI with 2 and 3 integration points (IMP_GI2 and IMP_GI3), the mixed GI and subdomain integration (SDI) with 2 and 3 integration points (GI&SDI2, GI&SDI3), the standard NCI with 2 and 3 integration points (NCI2 and NCI3), the improved NCI with 3 integration points (IMP_NCI3), and the mixed NCI and SDI with 2 and 3 integration points (NCI&SDI2 and NCI&SDI3), have been evaluated through analyzing the crack propagation problem in DCBs and comparing the numerical solutions with the analytical solutions. The key conclusions are summarized below:

1) For the NCI-based methods, integration schemes with 3 integration points (NCI3, IMP_NCI3, and NCI&SDI3) greatly outperform those schemes with only 2 integration points (NCI2 and NCI&SDI2) in numerical accuracy, stability, and robustness. NCI2 and NCI&SDI2 can lead to premature failure of the entire cohesive element and the predicted energy dissipation can be in significant error (up to 50%). Among the NCI-based schemes, the improved schemes with 3 integration points (NCI3, IMP_NCI3, or NCI&SDI3) are recommended.

2) For the GI-based integration methods, using 2 integration points appears to be sufficient because additional gains on numerical accuracy by using 3 or more integration points are limited. The improved schemes (IMP_GI2, IMP_GI3, GI&SDI2, GI&SDI3) in general outperform the respective standard methods (GI2 and GI3) in both numerical accuracy and stability. Among the GI-based schemes, the standard scheme with 3 integration points (GI3) and the improved methods with 2 integration points (IMP_GI2, GI&SDI2) are recommended.
3) In general the GI-based integration methods are numerically more efficient and robust as compared to the respective NCI-based integration schemes. This is particularly true when the element size is comparable to the cohesive zone size, and when the fracture process is associated with a global instability.
4) The improved numerical accuracy and stability of all the improved integration schemes enable the use of cohesive element size as large as the cohesive zone size without significant compromise of the numerical solution accuracy. This is a significant improvement over the existing cohesive elements which typically require the mesh size be less than 1/3 ~ 1/5 of the cohesive zone size.

Furthermore, the addition of a thermal portion to the cohesive law allows the cohesive element to transfer heat across the cohesive surface. In both steady state and transient heat transfer, the TM-CZ element is able to transfer the heat between the cohesive surface and resolve the discontinuity in the temperature field. Temperature profiles reflected behavior given the assumption of constant coefficient of cohesive heat transfer.

Chapter 3 Single Crack Formulation for 1D ACTM-FE

3.1 Overview

This chapter details the derivation of the equations for a 1D TM-AFEM element by first analyzing a thermo-elastic bar separately under mechanical and heat transfer processes. It is an extension of the A-FEM procedure for the mechanical problem. The heat transfer process adds extra temperature DoFs into the overall FE equations, and it will be shown how the A-FEM condensation algorithm can be applied in the thermo-mechanical problem. Mechanical and heat transfer processes are coupled by the coefficient of thermal expansion that relates a temperature change to a strain change. For simplicity, the heat transfer process is assumed to be steady state. The main concepts and procedures in this chapter will be later extended to derive the formulation for a 2D TM-AFEM element where the transient problem will be considered.

3.2 Strength of Materials Approach to a Thermo-elastic Bar

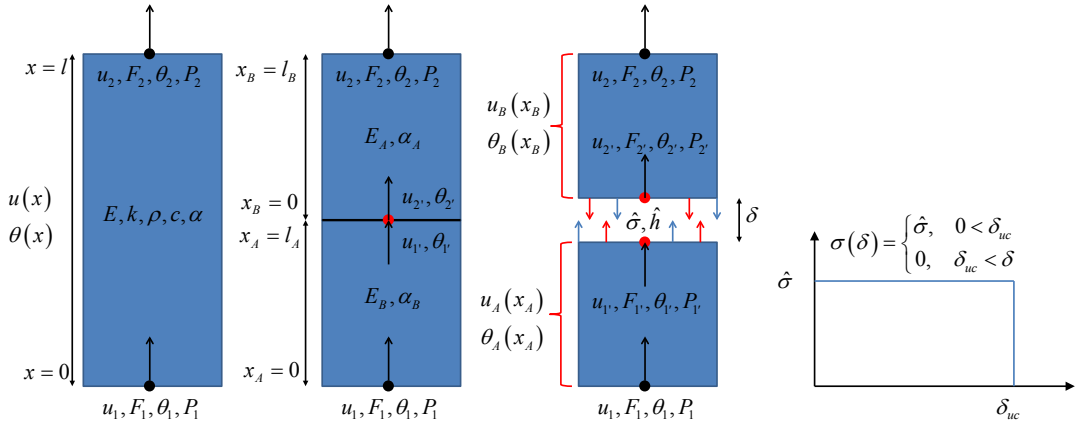

Figure 3.1: A bar in longitudinal tension due to some thermo-mechanical loading progresses from (a) a thermo-elastic stage (b) to a point of cohesive crack initiation (c) where afterwards a bridged cohesive crack is determined by (d) a rectangular mechanical cohesive law.

Consider a bar of length l and cross sectional area A with displacement and temperature fields $u(x)$ and $\theta(x)$ respectively as shown in Figure 3.1(a). If the displacement and temperature are assumed to be linearly distributed so that $u(0)=u_1$, $u(l)=u_2$, $\theta(0)=\theta_1$ and $\theta(l)=\theta_2$, the displacement and temperature fields are given by

$$u(x)=\frac{u_2-u_1}{l}x+u_1, \tag{3.1}$$

$$\theta(x)=\frac{\theta_2-\theta_1}{l}x+\theta_1. \tag{3.2}$$

The bar has reference stress free temperature θ_0, modulus E, linear coefficient of thermal expansion α, thermal conductivity k, density ρ, and specific heat c. It is thermo-elastic until fracture, upon which it follows the simple rectangular mechanical cohesive law shown in Figure 3.1(d). Let ε_t and ε_θ bet the total strain and thermal strain of the bar respectively. They are given by

$$\varepsilon_t=\frac{\mathrm{d}u(x)}{\mathrm{d}x}=\frac{u_2-u_1}{l}, \tag{3.3}$$

$$\varepsilon_\theta=\alpha\left(\theta(x)-\theta_0\right)=\alpha\left(\frac{\theta_2-\theta_1}{l}x+\theta_1-\theta_0\right). \tag{3.4}$$

Then the uniaxial stress is given by

$$\sigma=E\left(\varepsilon_t-\varepsilon_\theta\right)=E\left(\frac{u_2-u_1}{l}-\alpha\left(\frac{\theta_2-\theta_1}{l}x+\theta_1-\theta_0\right)\right). \tag{3.5}$$

Note that the stress is a linear function of x. Suppose through some thermo-mechanical loading, the bar builds up longitudinal tension until a critical stress $\hat{\sigma}$ is reached. Figure 3.1(a)-(c) illustrates the stages of the fracture for the bar under arbitrary displacement and

temperature. At the bar ends in the figures, the respective displacements, forces, temperatures and heat flows at those points follow the sign convention of being positive in the direction of the arrows. The same convention applies once the bar breaks into two parts of lengths l_A and l_B respectively, bridged by a cohesive crack with displacement and temperatures at the crack surfaces $u_{1'}, u_{2'}, \theta_{1'}, \theta_{2'}$ as well as cohesive loads and heat flows $F_{1'}, F_{2'}, P_{1'}, P_{2'}$. The crack surfaces and bar parts are separated by crack separation δ as seen in Figure 3.1(c).

Now assuming linear displacement and temperature fields in each bar part as well gives

$$u_A\left(x_A\right) = \frac{u_{1'} - u_1}{l_A} x_A + u_1, \quad \theta_A\left(x_A\right) = \frac{\theta_{1'} - \theta_1}{l_A} x_A + \theta_1, \tag{3.6}$$

$$u_B\left(x_B\right) = \frac{u_2 - u_{2'}}{l_B} x_B + u_{2'}, \quad \theta_B\left(x_B\right) = \frac{\theta_2 - \theta_{2'}}{l_B} x_B + \theta_{2'}. \tag{3.7}$$

Suppose that some thermo-mechanical loading is applied to the two separate parts so that the crack separation δ increases. The uniaxial stress in each bar part is simply

$$\sigma_A\left(x_A\right) = E_A\left(\frac{u_{1'} - u_1}{l_A} - \alpha_A\left(\frac{\theta_{1'} - \theta_1}{l_A} x_A + \theta_1 - \theta_0\right)\right), \tag{3.8}$$

$$\sigma_B\left(x_B\right) = E_B\left(\frac{u_2 - u_{2'}}{l_B} - \alpha_B\left(\frac{\theta_2 - \theta_{2'}}{l_B} x_B + \theta_{2'} - \theta_0\right)\right). \tag{3.9}$$

From the cohesive law and stress continuity, $\sigma\left(\delta\right) = \sigma_A\left(l_A\right) = \sigma_B\left(0\right)$ where $\sigma\left(\delta\right)$ is the cohesive stress as a function of crack separation δ. Solving for the internal displacements gives

$$u_{1'} = u_1 + l_A \frac{\sigma\left(\delta\right)}{E_A} + l_A \alpha_A \left(\theta_{1'} - \theta_0\right), \tag{3.10}$$

$$u_{2'} = u_2 - l_B \frac{\sigma(\delta)}{E_B} - l_B \alpha_B \left(\theta_{2'} - \theta_0\right). \tag{3.11}$$

From Figure 3.1, the crack separation can be defined as $\delta = u_{2'} - u_{1'}$ so that the crack separation is

$$\delta = u_2 - u_1 - \left(\frac{l_A}{E_A} + \frac{l_B}{E_B}\right)\sigma(\delta) - l_A \alpha_A \left(\theta_{1'} - \theta_0\right) - l_B \alpha_B \left(\theta_{2'} - \theta_0\right). \tag{3.12}$$

This relation expresses the idea that in the general case, arbitrary temperature and displacement changes affect the crack separation. The material properties of the two bar parts need not be the same in the general case and is reflected by subscripts A and B.

To simplify the problem, assume a homogenous material so that $E = E_A = E_B$ and $\alpha = \alpha_B = \alpha_B$, uniform temperature change throughout the bar, $\theta_1 = \theta_2 = \theta_{1'} = \theta_{2'} = \theta$, and fixed top and bottom ends, $u_1 = u_2 = 0$. Any induced stress and crack separation now is completely a temperature driven process. Then the crack separation as a function of temperature only is

$$\delta = -l \frac{\sigma(\delta)}{E} - l\alpha\left(\theta - \theta_0\right). \tag{3.13}$$

Note that the crack separation is a function of the cohesive stress which itself is a function of crack separation. This nonlinear problem requires special solution methods but it can be shown in this case, for the cohesive law shown in Figure 3.1(d), that the separations as functions of a uniform temperature change only is

$$\delta(\theta) = \begin{cases} -l\dfrac{\hat{\sigma}}{E} - l\alpha\left(\theta - \theta_0\right), & \theta_{uc} \le \theta < \theta_c \\ -l\alpha\left(\theta - \theta_0\right), & \theta < \theta_{uc} \end{cases}. \tag{3.14}$$

In this case, it is possible to calculate the characteristic uniform temperatures that correspond to crack initiation and complete failure as

$$\theta_c = \theta_0 - \frac{\hat{\sigma}}{E\alpha}, \tag{3.15}$$

$$\theta_{uc} = \theta_0 - \frac{1}{\alpha}\left(\frac{\delta_{cu}}{l} + \frac{\hat{\sigma}}{E}\right). \tag{3.16}$$

It follows from the cohesive law that the reaction forces as functions of uniform temperature only are

$$F_2 = -F_1 = \begin{cases} -AE\alpha\left(\theta - \theta_0\right), & \theta_c \le \theta \\ A\hat{\sigma}, & \theta_{uc} \le \theta < \theta_c \\ 0, & \theta < \theta_{uc} \end{cases}. \tag{3.17}$$

The deformation process comprises of four stages as detailed below:

1. When $\theta_c < \theta$, the bar is in the thermo-elastic stage and remains intact. The reaction forces at the fixed ends are $F_2 = -F_1 = -AE\alpha\left(\theta - \theta_0\right)$.
2. When $\theta = \theta_c$, a cohesive crack initiates and two separate domains with uniform temperature θ and lengths l_A, l_B form. The reaction forces at the fixed ends are $F_2 = -F_1 = A\hat{\sigma}$.
3. When $\theta_{uc} \le \theta < \theta_c$, the bar parts continue to contract as a crack separation $\delta = -l\frac{\hat{\sigma}}{E} - l\alpha\left(\theta - \theta_0\right)$ increases. Reaction forces remain constant because cohesive stress is constant when $\delta < \delta_{uc}$ and are given by $F_2 = -F_1 = A\hat{\sigma}$.
4. When $\theta < \theta_{uc}$, the stress in the separated parts drop to zero so $F_2 = -F_1 = 0$.

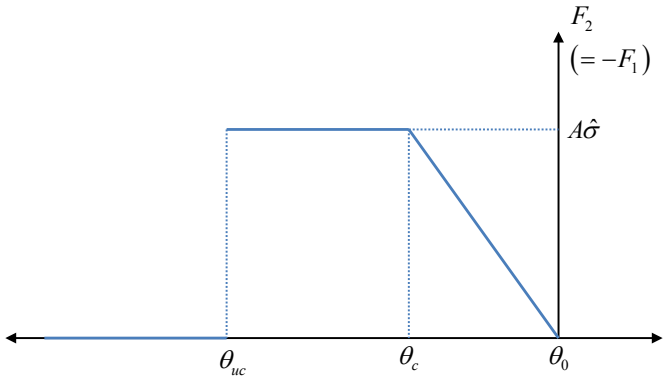

Figure 3.2: Load-temperature curve of a fixed thermo-elastic bar contracting.

Figure 3.2 gives the load-temperature curve through all four stages described. For a more complicated thermo-mechanical cohesive law such as in Figure 3.3(a), the crack separation as a function of uniform temperature in a fixed bar is

$$\delta(\theta)=\begin{cases} -l\dfrac{\hat{\sigma}}{E}-l\alpha(\theta-\theta_0), & \theta_{cu1}\le\theta<\theta_c \\ \dfrac{1}{(1+\beta l/E)}\left(\dfrac{\beta l}{E}\delta_{cu2}-l\alpha(\theta-\theta_0)\right), & \theta_{cu2}\le\theta<\theta_{cu1} \\ -l\alpha(\theta-\theta_0), & \theta<\theta_{cu2} \end{cases}, \tag{3.18}$$

where

$$\beta=-\hat{\sigma}/(\delta_{cu2}-\delta_{cu1}), \tag{3.19}$$

is the slope of the softening phase of the cohesive law. The characteristic temperatures and reaction forces as functions of uniform temperature only are found to be

$$\theta_c=\theta_0-\hat{\sigma}/E\alpha, \tag{3.20}$$

$$\theta_{cu1}=\theta_0-\frac{1}{\alpha}\left(\frac{\delta_{cu1}}{l}+\frac{\hat{\sigma}}{E}\right), \tag{3.21}$$

$$\theta_{cu2}=\theta_0-\delta_{cu2}/l\alpha, \tag{3.22}$$

$$F_2=-F_1=\begin{cases} -AE\alpha(\theta-\theta_0), & \theta_c\le\theta<\theta \\ A\hat{\sigma}, & \theta_{cu1}\le\theta<\theta_c \\ A\beta\left(\dfrac{1}{(1+\beta l/E)}\left(\dfrac{\beta l}{E}\delta_{cu2}-l\alpha(\theta-\theta_0)\right)-\delta_{cu2}\right), & \theta_{cu2}\le\theta<\theta_{cu1} \\ 0, & \theta<\theta_{cu2} \end{cases}. \tag{3.23}$$

Figure 3.3(b)-(c) are the curves generated from Equations (3.18) and(3.23). Because the cohesive law is piece-wise linear, so are the crack separation temperature and load-temperature curves.

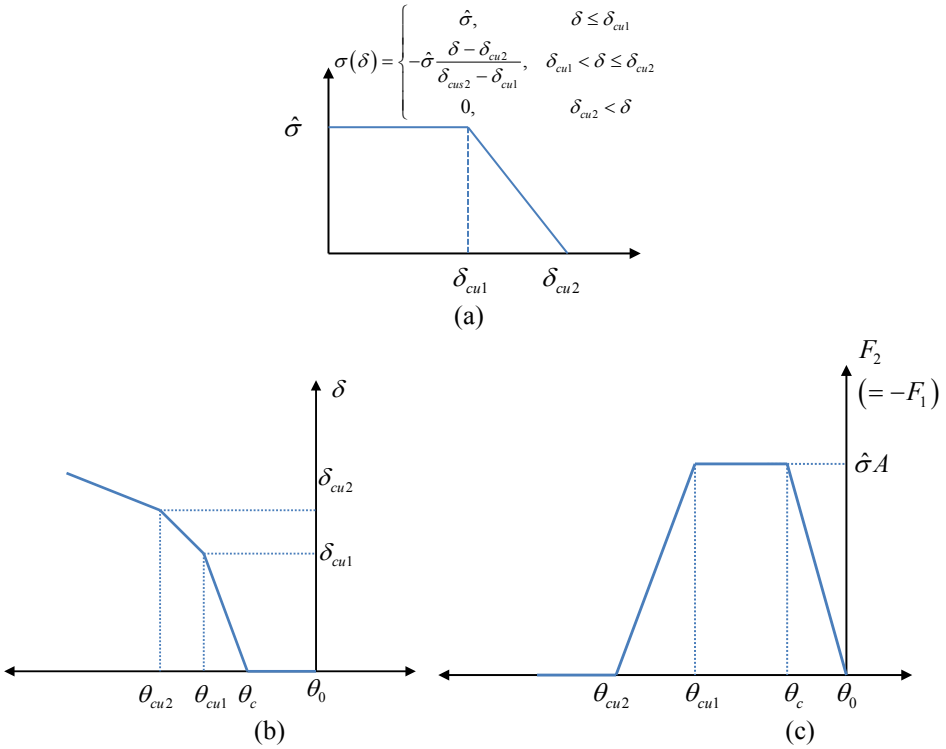

Figure 3.3: (a) Trapezoidal cohesive law. (b) Temperature-separation curve. (c) Load-temperature curve.

Suppose the bar were fixed only at one end ($u_1 = 0$) and displaced at the other ($u_2 = u$) so that $u_2 - u_1 = u$. Under the simplifying assumptions of homogeneity and uniform temperature, the crack separation becomes

$$\delta = u - \frac{l}{E}\sigma(\delta) - l\alpha(\theta - \theta_0). \tag{3.24}$$

Now that crack separation is a function of both temperature and displacement, it follows then for the piece-wise linear mechanical cohesive law in Figure 3.3(a) that the crack separation as a function of uniform temperature and displacement in for the bar is

$$\delta(u,\theta) = \begin{cases} u - \dfrac{l}{E}\hat{\sigma} - l\alpha(\theta-\theta_0), & \delta \le \delta_{cu1} \\ \dfrac{1}{(1+\beta l/E)}\left(u + \dfrac{\beta l}{E}\delta_{cu2} - l\alpha(\theta-\theta_0)\right), & \delta_{cu1} < \delta \le \delta_{cu2} \\ u - l\alpha(\theta-\theta_0), & \delta_{cu2} < \delta \end{cases}. \tag{3.25}$$

Likewise, reaction forces can be shown to be

$$F_2 = -F_1 = \begin{cases} AE\left(\dfrac{u}{l} - \alpha\left(\theta - \theta_0\right)\right), & E\left(\dfrac{u}{l} - \alpha\left(\theta - \theta_0\right)\right) \le \hat{\sigma} \\ A\hat{\sigma}, & 0 < \delta \le \delta_{cu1} \\ A\beta\left(\delta - \delta_{cu2}\right), & \delta_{cu1} < \delta \le \delta_{cu2} \\ 0, & \delta_{cu2} < \delta \end{cases} . \tag{3.26}$$

It is not possible to derive general relations for characteristic temperatures and displacements where critical separations occur due to the dependence of the crack separation on both displacement and temperature. Instead, Equations (3.25) and (3.26) are implied to be solved by a consistency check where the correct δ is the δ whose value falls within corresponding range of the expression used to calculate it given inputs (u, θ).

3.3 FEM Approach to a Thermo-elastic Bar

Approximate the bar as a two node, linear 1D element with displacement and temperature degrees of freedom $u_1, u_2, \theta_1, \theta_2$ as shown prior in Figure 3.1(a). In the standard FEM displacement approach, these nodal values are known. Beginning with the initial thermo-elastic stage, the displacement and temperature at any point $x \in [0, l]$ can be interpolated using shape functions

$$u(x) = \begin{Bmatrix} N_1(x) & N_2(x) \end{Bmatrix} \begin{Bmatrix} u_1 \\ u_2 \end{Bmatrix}, \tag{3.27}$$

$$\theta(x) = \begin{Bmatrix} N_1(x) & N_2(x) \end{Bmatrix} \begin{Bmatrix} \theta_1 \\ \theta_2 \end{Bmatrix}, \tag{3.28}$$

where the shape functions are simply

$$N_1(x) = \frac{l - x}{l} \quad N_2(x) = \frac{x}{l}. \tag{3.29}$$

3.3.1 Mechanical Process

The total strain in the element is found from the displacement-stain relation

$$\varepsilon_t(x) = \frac{\mathrm{d}u(x)}{\mathrm{d}x} = \frac{1}{l}\{-1 \quad 1\}\begin{Bmatrix} u_1 \\ u_2 \end{Bmatrix} = \frac{u_2 - u_1}{l}, \tag{3.30}$$

and the thermal strain, from Equation (3.4), is

$$\varepsilon_\theta(x) = \alpha\left[\theta(x) - \theta_0\right] = \alpha\left[N_1(x)\theta_1 + N_2(x)\theta_2 - \theta_0\right]. \tag{3.31}$$

Recall Equation (3.5), the element stress then is

$$\sigma(x) = E\frac{u_2 - u_1}{l} - E\alpha\left[\frac{l-x}{l}\theta_1 + \frac{x}{l}\theta_2 - \theta_0\right]. \tag{3.32}$$

From the expression for stress, it can be seen that the equilibrium equation is satisfied when the temperature is uniform.

$$\frac{\mathrm{d}\sigma(x)}{\mathrm{d}x} = -\frac{E\alpha}{l}(\theta_2 - \theta_1) = 0 \rightarrow \theta_2 = \theta_1.$$

Consider the force equilibrium at the nodes where the reaction forces are F_1 and F_2. From Equation (3.32), the these reaction forces are

$$F_1 = -\sigma(0)A = -EA\frac{u_2 - u_1}{l} + EA\alpha(\theta_1 - \theta_0), \tag{3.33}$$

$$F_2 = \sigma(l)A = EA\frac{u_2 - u_1}{l} - EA\alpha(\theta_2 - \theta_0). \tag{3.34}$$

Note that the negative sign for stress in the expression for F_2 accounts for the assumed positive direction of F_2 creating compression at node 2. Equations (3.33) and (3.34) can be combined into a single matrix as

$$\begin{Bmatrix} F_1 \\ F_2 \end{Bmatrix} = \frac{EA}{l}\begin{bmatrix} 1 & -1 \\ -1 & 1 \end{bmatrix}\begin{Bmatrix} u_1 \\ u_2 \end{Bmatrix} + \begin{Bmatrix} EA\alpha(\theta_1 - \theta_0) \\ -EA\alpha(\theta_2 - \theta_0) \end{Bmatrix}. \tag{3.35}$$

Suppose a cohesive crack initiates and the bar separates into two. Internal nodes 1' and 2' are introduced to accommodate extra displacement and temperature DoFs at the crack surfaces. A-FEM's approach is to condense these additional DoFs within the element so that the discontinuous displacement can be expressed by the DoFs of the regular nodes. The application of this procedure with extra DoFs follows.

Since each of the separated domains are thermo-elastic, the finite element equations can be written for each as

$$\begin{Bmatrix} F_1 \\ F_{1'} \end{Bmatrix} + \begin{Bmatrix} -EA\alpha\left(\theta_1 - \theta_0\right) \\ EA\alpha\left(\theta_{1'} - \theta_0\right) \end{Bmatrix} = \begin{bmatrix} k_{11} & k_{11'} \\ k_{1'1} & k_{1'1'} \end{bmatrix} \begin{Bmatrix} u_1 \\ u_{1'} \end{Bmatrix}, \tag{3.36}$$

$$\begin{Bmatrix} F_{2'} \\ F_2 \end{Bmatrix} + \begin{Bmatrix} -EA\alpha\left(\theta_{2'} - \theta_0\right) \\ EA\alpha\left(\theta_2 - \theta_0\right) \end{Bmatrix} = \begin{bmatrix} k_{2'2'} & k_{2'2} \\ k_{22'} & k_{22} \end{bmatrix} \begin{Bmatrix} u_{2'} \\ u_2 \end{Bmatrix}, \tag{3.37}$$

where $k_{11} = k_{1'1'} = EA/l_1$; $k_{11'} = k_{1'1} = -EA/l_1$; $k_{22} = k_{2'2'} = EA/l_2$; $k_{22'} = k_{2'2} = -EA/l_2$. Crack separation, i.e. the displacement jump between the two crack surfaces, is $\delta = u_{2'} - u_{1'}$. Resultant forces at nodes 1' and 2' follow from the cohesive law in Figure 3.3(a) as

$$F_{1'} = -F_{2'} = A\sigma\left(\delta\right) = \begin{cases} A\hat{\sigma}, & \delta \le \delta_{cu1} \\ A\beta\left(\delta - \delta_{cu2}\right), & \delta_{cu1} < \delta \le \delta_{cu2} \end{cases}. \tag{3.38}$$

Consider the first stage of the mechanical cohesive law, $\delta \le \delta_{cu1}$. Equations (3.36) and (3.37) become

$$\begin{Bmatrix} F_1 \\ A\hat{\sigma} \end{Bmatrix} + \begin{Bmatrix} -EA\alpha\left(\theta_1 - \theta_0\right) \\ EA\alpha\left(\theta_{1'} - \theta_0\right) \end{Bmatrix} = \begin{bmatrix} k_{11} & k_{11'} \\ k_{1'1} & k_{1'1'} \end{bmatrix} \begin{Bmatrix} u_1 \\ u_{1'} \end{Bmatrix}, \tag{3.39}$$

$$\begin{Bmatrix} -A\hat{\sigma} \\ F_2 \end{Bmatrix} + \begin{Bmatrix} -EA\alpha\left(\theta_{2'} - \theta_0\right) \\ EA\alpha\left(\theta_2 - \theta_0\right) \end{Bmatrix} = \begin{bmatrix} k_{2'2'} & k_{2'2} \\ k_{22'} & k_{22} \end{bmatrix} \begin{Bmatrix} u_{2'} \\ u_2 \end{Bmatrix}. \tag{3.40}$$

This can be recast as four equations

$$\left[k_{11}\right]\left\{u_1\right\}+\left[k_{11'}\right]\left\{u_{1'}\right\}=\left\{F_1\right\}-\left\{EA\alpha\left(\theta_1-\theta_0\right)\right\}, \tag{3.41}$$

$$\left[k_{1'1}\right]\left\{u_1\right\}+\left[k_{1'1'}\right]\left\{u_{1'}\right\}=\left\{A\hat{\sigma}\right\}+\left\{EA\alpha\left(\theta_{1'}-\theta_0\right)\right\}, \tag{3.42}$$

$$\left[k_{2'2'}\right]\left\{u_{2'}\right\}+\left[k_{2'2}\right]\left\{u_2\right\}=\left\{-A\hat{\sigma}\right\}-\left\{EA\alpha\left(\theta_{2'}-\theta_0\right)\right\}, \tag{3.43}$$

$$\left[k_{22'}\right]\left\{u_{2'}\right\}+\left[k_{22}\right]\left\{u_2\right\}=\left\{F_2\right\}+\left\{EA\alpha\left(\theta_2-\theta_0\right)\right\}. \tag{3.44}$$

Solve Equations (3.42) and (3.43) for $\left\{u_{1'}\right\}$ and $\left\{u_{2'}\right\}$ to get

$$\left\{u_{1'}\right\}=\left[k_{1'1'}\right]^{-1}\left(\left\{A\hat{\sigma}\right\}+\left\{EA\alpha\left(\theta_{1'}-\theta_0\right)\right\}-\left[k_{1'1}\right]\left\{u_1\right\}\right), \tag{3.45}$$

$$\left\{u_{2'}\right\}=\left[k_{2'2'}\right]^{-1}\left(\left\{-A\hat{\sigma}\right\}-\left\{EA\alpha\left(\theta_{2'}-\theta_0\right)\right\}-\left[k_{2'2}\right]\left\{u_2\right\}\right). \tag{3.46}$$

From these relations, the internal displacements can be eliminated and the regular nodal forces expressed as

$$\left\{F_1\right\}=\begin{pmatrix}+\left[k_{11'}\right]\left[k_{1'1'}\right]^{-1}\left\{A\hat{\sigma}\right\}\\+\left(\left[k_{11}\right]-\left[k_{11'}\right]\left[k_{1'1'}\right]^{-1}\left[k_{1'1}\right]\right)\left\{u_1\right\}\\+\left\{EA\alpha\left(\theta_1-\theta_0\right)\right\}\\+\left[k_{11'}\right]\left[k_{1'1'}\right]^{-1}\left\{EA\alpha\left(\theta_{1'}-\theta_0\right)\right\}\end{pmatrix}, \tag{3.47}$$

$$\left\{F_2\right\}=\begin{pmatrix}-\left[k_{22'}\right]\left[k_{2'2'}\right]^{-1}\left\{A\hat{\sigma}\right\}\\+\left(\left[k_{22}\right]-\left[k_{22'}\right]\left[k_{2'2'}\right]^{-1}\left[k_{2'2}\right]\right)\left\{u_2\right\}\\-\left\{EA\alpha\left(\theta_2-\theta_0\right)\right\}\\-\left[k_{22'}\right]\left[k_{2'2'}\right]^{-1}\left\{EA\alpha\left(\theta_{2'}-\theta_0\right)\right\}\end{pmatrix}. \tag{3.48}$$

Furthermore, the crack separation can be expressed as

$$\delta = \begin{pmatrix} -\left(\left[k_{1'1'}\right]^{-1} + \left[k_{2'2'}\right]^{-1}\right)\{A\hat{\sigma}\} \\ +\left[k_{1'1'}\right]^{-1}\left[k_{1'1}\right]\{u_1\} \\ -\left[k_{2'2'}\right]^{-1}\left[k_{2'2}\right]\{u_2\} \\ -\left[k_{1'1'}\right]^{-1}\left\{EA\alpha\left(\theta_{1'} - \theta_0\right)\right\} \\ -\left[k_{2'2'}\right]^{-1}\left\{EA\alpha\left(\theta_{2'} - \theta_0\right)\right\} \end{pmatrix}. \tag{3.49}$$

Assuming that nodal temperatures at regular and internal nodes are known, nodal reaction forces F_1, F_2 and internal displacements $u_{1'}, u_{2'}$ are functions of regular nodal displacements u_1, u_2 for $\delta \le \delta_{cu1}$.

The same procedure can be applied in the softening phase, $\delta_{cu1} < \delta \le \delta_{cu2}$ where internal nodal forces are now

$$F_{1'} = -F_{2'} = A\beta\left(\delta - \delta_{cu2}\right) = A\beta\left(u_{2'} - u_{1'}\right) - A\beta\delta_{cu2}. \tag{3.50}$$

This results in

$$\{F_1\} = \begin{pmatrix} -\beta A\left[k_{11'}\right]\left[k_{1'1'}\right]^{-1}\left[\bar{\beta}\right]^{-1}\{\delta_{cu2}\} \\ +\left(\left[k_{11}\right] - \left[k_{11'}\right]\left[k_{1'1'}\right]^{-1}\left(\left[\mathbf{I}\right] - \beta A\left[\bar{\beta}\right]^{-1}\left[k_{1'1'}\right]^{-1}\right)\left[k_{1'1}\right]\right)\{u_1\} \\ -\beta A\left[k_{11'}\right]\left[k_{1'1'}\right]^{-1}\left[\bar{\beta}\right]^{-1}\left[k_{2'2'}\right]^{-1}\left[k_{2'2}\right]\{u_2\} \\ +\alpha EA\{\theta_1\} \\ +\alpha EA\left[k_{11'}\right]\left(\left[\mathbf{B}_{11}\right]\left[k_{1'1'}\right]^{-1}\{\theta_{1'}\} - \beta A\left[k_{1'1'}\right]^{-1}\left[\bar{\beta}\right]^{-1}\left[k_{2'2'}\right]^{-1}\{\theta_{2'}\}\right) \\ -\alpha EA\left(\left[\mathbf{I}\right] + \left[k_{11'}\right]\left[\mathbf{B}_{11}\right]\left[k_{1'1'}\right]^{-1} - \beta A\left[k_{11'}\right]\left[k_{1'1'}\right]^{-1}\left[\bar{\beta}\right]^{-1}\left[k_{2'2'}\right]^{-1}\right)\{\theta_0\} \end{pmatrix}, \tag{3.51}$$

$$\{F_2\} = \begin{pmatrix} +\beta A[k_{22'}][k_{2'2'}]^{-1}\left[\bar{\beta}\right]^{-1}\{\delta_{cu2}\} \\ -\beta A[k_{22'}][k_{2'2'}]^{-1}\left[\bar{\beta}\right]^{-1}[k_{1'1'}]^{-1}[k_{1'1}]\{u_1\} \\ +\left([k_{22}]-[k_{22'}][k_{2'2'}]^{-1}\left([\mathbf{I}]-\beta A\left[\bar{\beta}\right]^{-1}[k_{2'2'}]^{-1}\right)[k_{2'2}]\right)\{u_2\} \\ -\alpha EA\{\theta_2\} \\ +\alpha EA[k_{22'}]\left(\beta A[k_{2'2'}]^{-1}\left[\bar{\beta}\right]^{-1}[k_{1'1'}]^{-1}\{\theta_{1'}\}-[\mathbf{B}_{22}][k_{2'2'}]^{-1}\{\theta_{2'}\}\right) \\ +\alpha EA\left([\mathbf{I}]+[k_{22'}][\mathbf{B}_{22}][k_{2'2'}]^{-1}-\beta A[k_{22'}][k_{2'2'}]^{-1}\left[\bar{\beta}\right]^{-1}[k_{1'1'}]^{-1}\right)\{\theta_0\} \end{pmatrix}, \quad (3.52)$$

$$\delta = \begin{pmatrix} +\left([\mathbf{I}]-\left[\bar{\beta}\right]^{-1}\right)\{\delta_{cu2}\} \\ +\left[\bar{\beta}\right]^{-1}\left([k_{1'1'}]^{-1}[k_{1'1}]\{u_1\}-[k_{2'2'}]^{-1}[k_{2'2}]\{u_2\}\right) \\ -\alpha EA\left[\bar{\beta}\right]^{-1}\left([k_{1'1'}]^{-1}\{\theta_{1'}\}+[k_{2'2'}]^{-1}\{\theta_{2'}\}\right) \\ +\alpha EA\left[\bar{\beta}\right]^{-1}\left([k_{1'1'}]^{-1}+[k_{2'2'}]^{-1}\right)\{\theta_0\} \end{pmatrix}, \quad (3.53)$$

where

$$\left[\bar{\beta}\right] = [\mathbf{I}] + \beta A\left([k_{1'1'}]^{-1}+[k_{2'2'}]^{-1}\right), \quad (3.54)$$

$$[\mathbf{B}_{11}] = [\mathbf{I}] - \beta A[k_{1'1'}]^{-1}\left[\bar{\beta}\right]^{-1}, \quad (3.55)$$

$$[\mathbf{B}_{22}] = [\mathbf{I}] - \beta A[k_{2'2'}]^{-1}\left[\bar{\beta}\right]^{-1}. \quad (3.56)$$

When there is no temperature change, i.e. $\theta_1 = \theta_2 = \theta_{1'} = \theta_{2'} = \theta_0$, all of the derived equations reduce to the forms obtained in the purely mechanical case. The condensation procedure applied to the mechanical process of the 1D bar gives FE equations in terms of original DoFs $u_1, u_2, \theta_1, \theta_2$. However, terms associated with the internal temperature DoFs are also present. These can be expressed in terms of the original DoFs by applying the A-FEM condensation procedure for the heat transfer equations as well.

3.3.2 Heat Transfer Process

It was assumed that the temperature field is linear and given by Equation (3.28). Assuming Fourier's law of conduction applies, the heat flux in the x direction by conduction in the bar is given by

$$q(x) = k\frac{\partial \theta}{\partial x} = \frac{k}{l}\{-1 \quad 1\}\begin{Bmatrix}\theta_1\\ \theta_2\end{Bmatrix}. \tag{3.57}$$

Note that $q(x)$ is not a function of x but constant throughout the bar. From Figure 3.1(a) , the heat flows at nodes 1 and 2 are denoted as P_1 and P_2 respectively. Since the bar is a closed system, the net heat flow into it must be zero, i.e. $P_2 = -P_1$. Then

$$P_1 = -q(0)\,A = \frac{kA}{l}\{1 \quad -1\}\begin{Bmatrix}\theta_1\\ \theta_2\end{Bmatrix}, \tag{3.58}$$

$$P_2 = q(l)\,A = \frac{kA}{l}\{-1 \quad 1\}\begin{Bmatrix}\theta_1\\ \theta_2\end{Bmatrix}. \tag{3.59}$$

Combing Equations (3.58) and (3.59) into a single matrix results in the FE equation of heat transfer by conduction only.

$$\begin{Bmatrix}P_1\\ P_2\end{Bmatrix} = \frac{kA}{l}\begin{bmatrix}1 & -1\\ -1 & 1\end{bmatrix}\begin{Bmatrix}\theta_1\\ \theta_2\end{Bmatrix}. \tag{3.60}$$

When the bar reaches the critical stress $\hat{\sigma}$ and a cohesive crack divides the bar into two parts, the heat transfer between the cohesive surfaces can be considered an interface problem where heat flux across the surfaces is defined as

$$q(\delta) = h(\delta)\left(\theta_{2'} - \theta_{1'}\right), \tag{3.61}$$

where $h(\delta)$ is the cohesive heat transfer coefficient which is a function of crack separation δ as shown in the heat transfer cohesive laws in Figure 3.4.

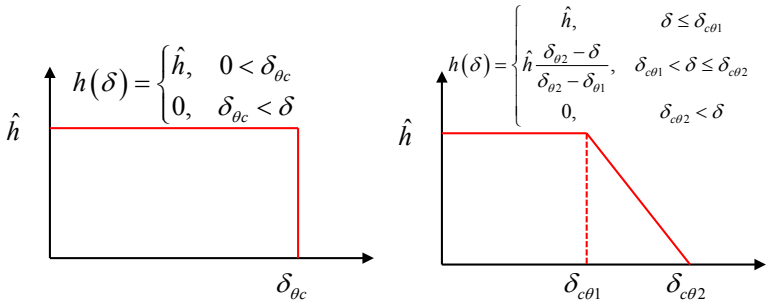

Figure 3.4: Heat transfer cohesive laws (a) rectangular (b) trapezoidal.

Following the same procedure as in the mechanical process, the heat transfer FE equations for the two bar parts are

$$\begin{bmatrix} a_{11} & a_{11'} \\ a_{1'1} & a_{1'1'} \end{bmatrix} \begin{Bmatrix} \theta_1 \\ \theta_{1'} \end{Bmatrix} = \begin{Bmatrix} P_1 \\ P_{1'} \end{Bmatrix}, \tag{3.62}$$

$$\begin{bmatrix} a_{2'2'} & a_{2'2} \\ a_{22'} & a_{22} \end{bmatrix} \begin{Bmatrix} \theta_{2'} \\ \theta_2 \end{Bmatrix} = \begin{Bmatrix} P_{2'} \\ P_2 \end{Bmatrix}, \tag{3.63}$$

where $a_{11} = a_{1'1'} = kA/l_A$; $a_{22} = a_{2'2'} = kA/l_B$; $a_{1'1} = a_{11'} = -a_{11}$; $a_{2'2} = a_{22'} = -a_{22}$. The heat flows at nodes 1' and 2' are calculated from the heat transfer cohesive law and the temperature jump across the crack.

For the trapezoidal cohesive heat transfer law in Figure 3.4, the heat flows at the internal nodes are

$$P_{1'} = -P_{2'} = q(\delta)A = \begin{cases} \hat{h}(\theta_{2'} - \theta_{1'})A, & \delta \le \delta_{c\theta 1} \\ \kappa(\delta - \delta_{\theta 2})(\theta_{2'} - \theta_{1'})A, & \delta_{c\theta 1} < \delta \le \delta_{c\theta 2} \\ 0, & \delta_{c\theta 2} < \delta \end{cases}, \tag{3.64}$$

where $\kappa = -\hat{h}/(\delta_{\theta 2} - \delta_{\theta 1})$. In the first stage of the cohesive heat transfer law, $\delta \le \delta_{c\theta 1}$, the cohesive heat transfer coefficient is constant and does not depend on crack separation δ and thus

$$\begin{bmatrix} a_{11} & a_{11'} \\ a_{1'1} & a_{1'1'} \end{bmatrix} \begin{Bmatrix} \theta_1 \\ \theta_{1'} \end{Bmatrix} = \begin{Bmatrix} P_1 \\ \hat{h}\left(\theta_{2'} - \theta_{1'}\right) A \end{Bmatrix} \tag{3.65}$$

$$\begin{bmatrix} a_{2'2'} & a_{2'2} \\ a_{22'} & a_{22} \end{bmatrix} \begin{Bmatrix} \theta_{2'} \\ \theta_2 \end{Bmatrix} = \begin{Bmatrix} -\hat{h}\left(\theta_{2'} - \theta_{1'}\right) A \\ P_2 \end{Bmatrix}. \tag{3.66}$$

Following the condensation procedure gives the temperature jump as

$$\{\theta_{2'}\} - \{\theta_{1'}\} = [\bar{\kappa}]^{-1} [a_{1'1'}]^{-1} [a_{1'1}] \{\theta_1\} - [\bar{\kappa}]^{-1} [a_{2'2'}]^{-1} [a_{2'2}] \{\theta_2\}, \tag{3.67}$$

where

$$[\bar{\kappa}] = [\mathbf{I}] + \hat{h}A\left([a_{1'1'}]^{-1} + [a_{2'2'}]^{-1}\right). \tag{3.68}$$

The internal nodal temperatures are given by

$$\{\theta_{1'}\} = -[\mathbf{E}_{11}][a_{1'1'}]^{-1} [a_{1'1}] \{\theta_1\} - \hat{h}A[a_{1'1'}]^{-1} [\bar{\kappa}]^{-1} [a_{2'2'}]^{-1} [a_{2'2}] \{\theta_2\}, \tag{3.69}$$

$$\{\theta_{2'}\} = -\hat{h}A[a_{2'2'}]^{-1} [\bar{\kappa}]^{-1} [a_{1'1'}]^{-1} [a_{1'1}] \{\theta_1\} - [\mathbf{E}_{22}][a_{2'2'}]^{-1} [a_{2'2}] \{\theta_2\}, \tag{3.70}$$

where

$$[\mathbf{E}_{11}] = [\mathbf{I}] - \hat{h}A[a_{1'1'}]^{-1} [\bar{\kappa}]^{-1}, \tag{3.71}$$

$$[\mathbf{E}_{22}] = [\mathbf{I}] - \hat{h}A[a_{2'2'}]^{-1} [\bar{\kappa}]^{-1}. \tag{3.72}$$

Then the nodal heat flows are

$$\{P_1\} = \begin{pmatrix} +\left([a_{11}] - [a_{11'}][a_{1'1'}]^{-1} [a_{1'1}] + \hat{h}A[a_{11'}][a_{1'1'}]^{-1} [\bar{\kappa}]^{-1} [a_{1'1'}]^{-1} [a_{1'1}]\right) \{\theta_1\} \\ -\hat{h}A[a_{11'}][a_{1'1'}]^{-1} [\bar{\kappa}]^{-1} [a_{2'2'}]^{-1} [a_{2'2}] \{\theta_2\} \end{pmatrix}, \tag{3.73}$$

$$\{P_2\} = \begin{pmatrix} +\left([a_{22}] - [a_{22'}][a_{2'2'}]^{-1} [a_{2'2}] + \hat{h}A[a_{22'}][a_{2'2'}]^{-1} [\bar{\kappa}]^{-1} [a_{2'2'}]^{-1} [a_{2'2}]\right) \{\theta_2\} \\ -\hat{h}A[a_{22'}][a_{2'2'}]^{-1} [\bar{\kappa}]^{-1} [a_{1'1'}]^{-1} [a_{1'1}] \{\theta_1\} \end{pmatrix}. \tag{3.74}$$

This set of equations for this stage is fully determined from the original temperature DoFs and relevant material parameters.

In the second stage of the cohesive heat transfer law, $\delta_{c\theta 1} < \delta \le \delta_{c\theta 2}$, the cohesive heat transfer coefficient decreases linearly as a function of crack separation. Now

$$\begin{bmatrix} a_{11} & a_{11'} \\ a_{1'1} & a_{1'1'} \end{bmatrix} \begin{Bmatrix} \theta_1 \\ \theta_{1'} \end{Bmatrix} = \begin{Bmatrix} P_1 \\ \kappa(\delta - \delta_{\theta 2})(\theta_{2'} - \theta_{1'}) A \end{Bmatrix}, \tag{3.75}$$

$$\begin{bmatrix} a_{2'2'} & a_{2'2} \\ a_{22'} & a_{22} \end{bmatrix} \begin{Bmatrix} \theta_{2'} \\ \theta_2 \end{Bmatrix} = \begin{Bmatrix} -\kappa(\delta - \delta_{\theta 2})(\theta_{2'} - \theta_{1'}) A \\ P_2 \end{Bmatrix}, \tag{3.76}$$

and so following the condensation procedure Equation (3.67)-(3.74) become

$$\{\theta_{2'}\} - \{\theta_{1'}\} = [\bar{\kappa}']^{-1}[a_{1'1'}]^{-1}[a_{1'1}]\{\theta_1\} - [\bar{\kappa}']^{-1}[a_{2'2'}]^{-1}[a_{2'2}]\{\theta_2\}, \tag{3.77}$$

$$[\bar{\kappa}'] = [\mathbf{I}] + \kappa(\delta - \delta_{\theta 2}) A\left([a_{1'1'}]^{-1} + [a_{2'2'}]^{-1}\right), \tag{3.78}$$

$$\{\theta_{1'}\} = -[\mathbf{E}_{11}'][a_{1'1'}]^{-1}[a_{1'1}]\{\theta_1\} - \kappa(\delta - \delta_{\theta 2}) A[a_{1'1'}]^{-1}[\bar{\kappa}']^{-1}[a_{2'2'}]^{-1}[a_{2'2}]\{\theta_2\}, \tag{3.79}$$

$$\{\theta_{2'}\} = -\kappa(\delta - \delta_{\theta 2}) A[a_{2'2'}]^{-1}[\bar{\kappa}']^{-1}[a_{1'1'}]^{-1}[a_{1'1}]\{\theta_1\} - [\mathbf{E}_{22}'][a_{2'2'}]^{-1}[a_{2'2}]\{\theta_2\}, \tag{3.80}$$

$$\begin{aligned} \{P_1\} = &\begin{pmatrix} [a_{11}] - [a_{11'}][a_{1'1'}]^{-1}[a_{1'1}] \\ +\kappa(\delta - \delta_{\theta 2}) A[a_{11'}][a_{1'1'}]^{-1}[\bar{\kappa}']^{-1}[a_{1'1'}]^{-1}[a_{1'1}] \end{pmatrix}\{\theta_1\} \\ &-\kappa(\delta - \delta_{\theta 2}) A[a_{11'}][a_{1'1'}]^{-1}[\bar{\kappa}']^{-1}[a_{2'2'}]^{-1}[a_{2'2}]\{\theta_2\} \end{aligned}, \tag{3.81}$$

$$\begin{aligned} \{P_2\} = &\begin{pmatrix} [a_{22}] - [a_{22'}][a_{2'2'}]^{-1}[a_{2'2}] \\ +\kappa(\delta - \delta_{\theta 2}) A[a_{22'}][a_{2'2'}]^{-1}[\bar{\kappa}']^{-1}[a_{2'2'}]^{-1}[a_{2'2}] \end{pmatrix}\{\theta_2\} \\ &-\kappa(\delta - \delta_{\theta 2}) A[a_{22'}][a_{2'2'}]^{-1}[\bar{\kappa}']^{-1}[a_{1'1'}]^{-1}[a_{1'1}]\{\theta_1\} \end{aligned}, \tag{3.82}$$

where

$$[\mathbf{E}_{11}'] = [\mathbf{I}] - \kappa(\delta - \delta_{\theta 2}) A[a_{1'1'}]^{-1}[\bar{\kappa}']^{-1} \tag{3.83}$$

$$[\mathbf{E}_{22}'] = [\mathbf{I}] - \kappa(\delta - \delta_{\theta 2}) A[a_{2'2'}]^{-1}[\bar{\kappa}']^{-1} \tag{3.84}$$

In this stage of the cohesive heat transfer law, the internal nodal temperatures given by Equations (3.79) and (3.80) are in terms of the external nodes and crack separation δ, which from Equations (3.49) and (3.53) is a function of internal nodal temperatures.

3.4 Thermo-Mechanical FE Equations

The combined set of thermo-mechanical equations derived from the mechanical and heat transfer equations of prior sections is nonlinear and cannot be expressed explicitly in terms of the original displacement and temperatures at the nodes because of the dependence of the crack separation on internal temperature DoFs. However, if the cohesive heat transfer coefficient is constant, temperature is independent of displacement. Then temperature at the internal DoFs is fully determined by the original external DoFs and crack separation can be expressed completely in terms of external displacement and temperature DoFs. In this case, it is possible to follow the condensation procedure to the end and express the complete set of thermo-mechanical equations in terms of the original external displacement and temperature DoFs.

Such a set of thermo-mechanical equations has the general form

$$\begin{bmatrix} \mathbf{K}_{uu} & \mathbf{K}_{u\theta} \\ \mathbf{0} & \mathbf{K}_{\theta\theta} \end{bmatrix} \begin{Bmatrix} \mathbf{u} \\ \boldsymbol{\theta} \end{Bmatrix} = \begin{Bmatrix} \mathbf{f} \\ \mathbf{p} \end{Bmatrix} + \begin{Bmatrix} \mathbf{f} \\ \mathbf{0} \end{Bmatrix}_{cohesive} + \begin{Bmatrix} \mathbf{f} \\ \mathbf{0} \end{Bmatrix}_{\theta_0}, \tag{3.85}$$

where $\mathbf{u} = \{u_1, u_2\}^T$ and $\boldsymbol{\theta} = \{\theta_1, \theta_2\}^T$ are the displacement and temperature DoFs to which $\mathbf{f} = \{F_1, F_2\}^T$ and $\mathbf{p} = \{P_1, P_2\}^T$ are the corresponding loads and heat flows. The submatrix $\mathbf{K}_{u\theta}$ represents the coupling of the displacement DoFs to the temperature DoFs due to the coefficient of thermal expansion and $\mathbf{K}_{uu}$ and $\mathbf{K}_{\theta\theta}$ represent respectively the coupling of displacement and temperature DoFs with themselves. In addition, there exists two extra load terms $\mathbf{f}_{cohesive}$ and $\mathbf{f}_{\theta_0}$ associated with the cohesive law and reference temperature θ_0.

In the first stage of the mechanical cohesive law, $\delta \le \delta_{cu1}$, crack separation is

$$\begin{aligned}\delta = &-\left(\left[k_{1'1'}\right]^{-1}+\left[k_{2'2'}\right]^{-1}\right)\{A\hat{\sigma}\}\\ &+\left[k_{1'1'}\right]^{-1}\left[k_{1'1}\right]\{u_1\}\\ &-\left[k_{2'2'}\right]^{-1}\left[k_{2'2}\right]\{u_2\}\\ &+\left(\hat{h}\alpha EA^2\left[k_{2'2'}\right]^{-1}\left[a_{2'2'}\right]^{-1}\left[\bar{\kappa}\right]^{-1}\left[a_{1'1'}\right]^{-1}\left[a_{1'1}\right]+EA\alpha\left[k_{1'1'}\right]^{-1}\left[\mathbf{E}_{11}\right]\left[a_{1'1'}\right]^{-1}\left[a_{1'1}\right]\right)\{\theta_1\}\\ &+\left(\hat{h}\alpha EA^2\left[k_{1'1'}\right]^{-1}\left[a_{1'1'}\right]^{-1}\left[\bar{\kappa}\right]^{-1}\left[a_{2'2'}\right]^{-1}\left[a_{2'2}\right]+EA\alpha\left[k_{2'2'}\right]^{-1}\left[\mathbf{E}_{22}\right]\left[a_{2'2'}\right]^{-1}\left[a_{2'2}\right]\right)\{\theta_2\}\\ &+EA\alpha\left(\left[k_{1'1'}\right]^{-1}+\left[k_{2'2'}\right]^{-1}\right)\{\theta_0\}\end{aligned},$$

(3.86)

where $\mathbf{E}_{11}$ and $\mathbf{E}_{22}$ are given by Equations (3.71) and (3.72) respectively. The relevant matrices and vectors in Equation (3.85) are given by

$$\left[\mathbf{K}_{uu}\right]=\begin{bmatrix}\left[k_{11}\right]-\left[k_{11'}\right]\left[k_{1'1'}\right]^{-1}\left[k_{1'1}\right] & 0\\ 0 & \left[k_{22}\right]-\left[k_{22'}\right]\left[k_{2'2'}\right]^{-1}\left[k_{2'2}\right]\end{bmatrix}, \tag{3.87}$$

$$\left[\mathbf{K}_{u\theta}\right]=\begin{bmatrix}EA\alpha\left(\left[\mathbf{I}\right]-\left[k_{11'}\right]\left[k_{1'1'}\right]^{-1}\left[\mathbf{E}_{11}\right]\left[a_{1'1'}\right]^{-1}\left[a_{1'1}\right]\right) & -h_c\alpha EA^2\left[k_{11'}\right]\left[k_{1'1'}\right]^{-1}\left[a_{1'1'}\right]^{-1}\left[\bar{\kappa}\right]^{-1}\left[a_{2'2'}\right]^{-1}\left[a_{2'2}\right]\\ h_c\alpha EA^2\left[k_{22'}\right]\left[k_{2'2'}\right]^{-1}\left[a_{2'2'}\right]^{-1}\left[\bar{\kappa}\right]^{-1}\left[a_{1'1'}\right]^{-1}\left[a_{1'1}\right] & -EA\alpha\left(\left[\mathbf{I}\right]-\left[k_{22'}\right]\left[k_{2'2'}\right]^{-1}\left[\mathbf{E}_{22}\right]\left[a_{2'2'}\right]^{-1}\left[a_{2'2}\right]\right)\end{bmatrix},$$

(3.88)

$$\left[\mathbf{K}_{\theta\theta}\right]=\begin{bmatrix}\begin{pmatrix}\left[a_{11}\right]-\left[a_{11'}\right]\left[a_{1'1'}\right]^{-1}\left[a_{1'1}\right]\\ +h_cA\left[a_{11'}\right]\left[a_{1'1'}\right]^{-1}\left[\bar{\kappa}\right]^{-1}\left[a_{1'1'}\right]^{-1}\left[a_{1'1}\right]\end{pmatrix} & -h_cA\left[a_{11'}\right]\left[a_{1'1'}\right]^{-1}\left[\bar{\kappa}\right]^{-1}\left[a_{2'2'}\right]^{-1}\left[a_{2'2}\right]\\ -h_cA\left[a_{22'}\right]\left[a_{2'2'}\right]^{-1}\left[\bar{\kappa}\right]^{-1}\left[a_{1'1'}\right]^{-1}\left[a_{1'1}\right] & \begin{pmatrix}\left[a_{22}\right]-\left[a_{22'}\right]\left[a_{2'2'}\right]^{-1}\left[a_{2'2}\right]\\ +h_cA\left[a_{22'}\right]\left[a_{2'2'}\right]^{-1}\left[\bar{\kappa}\right]^{-1}\left[a_{2'2'}\right]^{-1}\left[a_{2'2}\right]\end{pmatrix}\end{bmatrix}, \tag{3.89}$$

$$\mathbf{f}_{cohesive}=A\hat{\sigma}\begin{Bmatrix}-\left[k_{11'}\right]\left[k_{1'1'}\right]^{-1}\\ \left[k_{22'}\right]\left[k_{2'2'}\right]^{-1}\end{Bmatrix}, \tag{3.90}$$

$$\mathbf{f}_{\theta_0}=\theta_0\begin{Bmatrix}EA\alpha\left(\left[\mathbf{I}\right]+\left[k_{11'}\right]\left[k_{1'1'}\right]^{-1}\right)\\ -EA\alpha\left(\left[\mathbf{I}\right]+\left[k_{22'}\right]\left[k_{2'2'}\right]^{-1}\right)\end{Bmatrix}. \tag{3.91}$$

In the softening phase of the mechanical cohesive law, $\delta_{cu1} < \delta \le \delta_{cu2}$, crack separation is given by

$$\begin{aligned}\delta = &\left(\left[\mathbf{I}\right]-\left[\bar{\beta}\right]^{-1}\right)\{\delta_{cu2}\}+\alpha EA\left[\bar{\beta}\right]^{-1}\left(\left[k_{1'1'}\right]^{-1}+\left[k_{2'2'}\right]^{-1}\right)\{\theta_0\}\\ &+\left[\bar{\beta}\right]^{-1}\left[k_{1'1'}\right]^{-1}\left[k_{1'1}\right]\{u_1\}\\ &-\left[\bar{\beta}\right]^{-1}\left[k_{2'2'}\right]^{-1}\left[k_{2'2}\right]\{u_2\}\\ &+\alpha EA\begin{pmatrix}\left[\bar{\beta}\right]^{-1}\left[k_{1'1'}\right]^{-1}\left[\mathbf{E}_{11}\right]\left[a_{1'1'}\right]^{-1}\left[a_{1'1}\right]\\ +\hat{h}A\left[\bar{\beta}\right]^{-1}\left[k_{2'2'}\right]^{-1}\left[a_{2'2'}\right]^{-1}\left[\bar{\kappa}\right]^{-1}\left[a_{1'1'}\right]^{-1}\left[a_{1'1}\right]\end{pmatrix}\{\theta_1\}\\ &+\alpha EA\begin{pmatrix}\left[\bar{\beta}\right]^{-1}\left[k_{2'2'}\right]^{-1}\left[\mathbf{E}_{22}\right]\left[a_{2'2'}\right]^{-1}\left[a_{2'2}\right]\\ +\hat{h}A\left[\bar{\beta}\right]^{-1}\left[k_{1'1'}\right]^{-1}\left[a_{1'1'}\right]^{-1}\left[\bar{\kappa}\right]^{-1}\left[a_{2'2'}\right]^{-1}\left[a_{2'2}\right]\end{pmatrix}\{\theta_2\}\end{aligned}. \tag{3.92}$$

The relevant matrices and vectors are then

$$\left[\mathbf{K}_{uu}\right]=\begin{bmatrix}\left[k_{11}\right]-\left[k_{11'}\right]\left[k_{1'1'}\right]^{-1}\left(\left[\mathbf{I}\right]-\beta A\left[\bar{\beta}\right]^{-1}\left[k_{1'1'}\right]^{-1}\right)\left[k_{1'1}\right] & -\beta A\left[k_{11'}\right]\left[k_{1'1'}\right]^{-1}\left[\bar{\beta}\right]^{-1}\left[k_{2'2'}\right]^{-1}\left[k_{2'2}\right]\\ -\beta A\left[k_{22'}\right]\left[k_{2'2'}\right]^{-1}\left[\bar{\beta}\right]^{-1}\left[k_{1'1'}\right]^{-1}\left[k_{1'1}\right] & \left[k_{22}\right]-\left[k_{22'}\right]\left[k_{2'2'}\right]^{-1}\left(\left[\mathbf{I}\right]-\beta A\left[\bar{\beta}\right]^{-1}\left[k_{2'2'}\right]^{-1}\right)\left[k_{2'2}\right]\end{bmatrix}, \tag{3.93}$$

$$\left[\mathbf{K}_{u\theta}\right]=\begin{bmatrix}\alpha EA\begin{pmatrix}\left[\mathbf{I}\right]-\left[k_{11'}\right]\left[\mathbf{B}_{11}\right]\left[k_{1'1'}\right]^{-1}\left[\mathbf{E}_{11}\right]\left[a_{1'1'}\right]^{-1}\left[a_{1'1}\right]\\ +\beta A\hat{h}A\left[k_{11'}\right]\left[k_{1'1'}\right]^{-1}\left[\bar{\beta}\right]^{-1}\left[k_{2'2'}\right]^{-1}\left[a_{2'2'}\right]^{-1}\left[\bar{\kappa}\right]^{-1}\left[a_{1'1'}\right]^{-1}\left[a_{1'1}\right]\end{pmatrix} & -\alpha EA\begin{pmatrix}\hat{h}A\left[k_{11'}\right]\left[\mathbf{B}_{11}\right]\left[k_{1'1'}\right]^{-1}\left[a_{1'1'}\right]^{-1}\left[\bar{\kappa}\right]^{-1}\left[a_{2'2'}\right]^{-1}\left[a_{2'2}\right]\\ -\beta A\left[k_{11'}\right]\left[k_{1'1'}\right]^{-1}\left[\bar{\beta}\right]^{-1}\left[k_{2'2'}\right]^{-1}\left[\mathbf{E}_{22}\right]\left[a_{2'2'}\right]^{-1}\left[a_{2'2}\right]\end{pmatrix}\\ \alpha EA\begin{pmatrix}\hat{h}A\left[k_{22'}\right]\left[\mathbf{B}_{22}\right]\left[k_{2'2'}\right]^{-1}\left[a_{2'2'}\right]^{-1}\left[\bar{\kappa}\right]^{-1}\left[a_{1'1'}\right]^{-1}\left[a_{1'1}\right]\\ -\beta A\left[k_{22'}\right]\left[k_{2'2'}\right]^{-1}\left[\bar{\beta}\right]^{-1}\left[k_{1'1'}\right]^{-1}\left[\mathbf{E}_{11}\right]\left[a_{1'1'}\right]^{-1}\left[a_{1'1}\right]\end{pmatrix} & -\alpha EA\begin{pmatrix}\left[\mathbf{I}\right]-\left[k_{22'}\right]\left[\mathbf{B}_{22}\right]\left[k_{2'2'}\right]^{-1}\left[\mathbf{E}_{22}\right]\left[a_{2'2'}\right]^{-1}\left[a_{2'2}\right]\\ +\beta A\hat{h}A\left[k_{22'}\right]\left[k_{2'2'}\right]^{-1}\left[\bar{\beta}\right]^{-1}\left[k_{1'1'}\right]^{-1}\left[a_{1'1'}\right]^{-1}\left[\bar{\kappa}\right]^{-1}\left[a_{2'2'}\right]^{-1}\left[a_{2'2}\right]\end{pmatrix}\end{bmatrix}, \tag{3.94}$$

$$\left[\mathbf{K}_{\theta\theta}\right]=\begin{bmatrix}\begin{pmatrix}\left[a_{11}\right]-\left[a_{11'}\right]\left[a_{1'1'}\right]^{-1}\left[a_{1'1}\right]\\ +\hat{h}A\left[a_{11'}\right]\left[a_{1'1'}\right]^{-1}\left[\bar{\kappa}\right]^{-1}\left[a_{1'1'}\right]^{-1}\left[a_{1'1}\right]\end{pmatrix} & -\hat{h}A\left[a_{11'}\right]\left[a_{1'1'}\right]^{-1}\left[\bar{\kappa}\right]^{-1}\left[a_{2'2'}\right]^{-1}\left[a_{2'2}\right]\\ -\hat{h}A\left[a_{22'}\right]\left[a_{2'2'}\right]^{-1}\left[\bar{\kappa}\right]^{-1}\left[a_{1'1'}\right]^{-1}\left[a_{1'1}\right] & \begin{pmatrix}\left[a_{22}\right]-\left[a_{22'}\right]\left[a_{2'2'}\right]^{-1}\left[a_{2'2}\right]\\ +\hat{h}A\left[a_{22'}\right]\left[a_{2'2'}\right]^{-1}\left[\bar{\kappa}\right]^{-1}\left[a_{2'2'}\right]^{-1}\left[a_{2'2}\right]\end{pmatrix}\end{bmatrix}, \tag{3.95}$$

$$\mathbf{f}_{cohesive}=\delta_{cu2}\begin{Bmatrix}\beta A\left[k_{11'}\right]\left[k_{1'1'}\right]^{-1}\left[\bar{\beta}\right]^{-1}\\ -\beta A\left[k_{22'}\right]\left[k_{2'2'}\right]^{-1}\left[\bar{\beta}\right]^{-1}\end{Bmatrix}, \tag{3.96}$$

$$\mathbf{f}_{\theta_0}=\theta_0\begin{Bmatrix}\alpha EA\left(\left[\mathbf{I}\right]+\left[k_{11'}\right]\left[\mathbf{B}_{11}\right]\left[k_{1'1'}\right]^{-1}-\beta A\left[k_{11'}\right]\left[k_{1'1'}\right]^{-1}\left[\bar{\beta}\right]^{-1}\left[k_{2'2'}\right]^{-1}\right)\\ -\alpha EA\left(\left[\mathbf{I}\right]+\left[k_{22'}\right]\left[\mathbf{B}_{22}\right]\left[k_{2'2'}\right]^{-1}-\beta A\left[k_{22'}\right]\left[k_{2'2'}\right]^{-1}\left[\bar{\beta}\right]^{-1}\left[k_{1'1'}\right]^{-1}\right)\end{Bmatrix}. \tag{3.97}$$

It can be seen that even in the 1D case, the thermo-mechanical FE equations are not trivial to solve even with the simplified assumption of a constant coefficient of cohesive heat transfer which allowed for the formulation to be in terms of the original displacement and temperature DoFs. A nonlinearity in the set of thermo-mechanical equations still exists because crack separation δ depends on the assumed segment of the mechanical cohesive law used to derive the FE equations. However, this problem is easily solved by a simple consistency check to ensure the crack separation calculated is within the assumed segment.

3.5 Summary

This chapter derived the set of thermo-mechanical FE equations in 1D through the novel A-FEM's condensation algorithm. It has been demonstrated that the coefficient of thermal expansion couples the mechanical process with the thermal one so that crack separation is function of both displacement and temperature DoFs. The interplay of the displacement and temperature fields either work together or against each other to evolve fracture.

When the thermal part of the cohesive law is a function of both crack separation and temperature jump, this thermo-mechanical coupling makes it so the set of combined thermo-mechanical FE equations cannot be explicitly expressed in terms of the original displacement and temperature DoFs. Special solution methods such as an iterative technique are required to solve this nonlinear problem. However, when the thermal part of the cohesive law assumes that the cohesive coefficient of heat transfer is constant, the novel A-FEM condensation procedure can be applied and the set of combined thermo-mechanical FE equations expressed in terms of original displacement temperature DoFs.

Chapter 4 Single Crack Formulation for 2-D TM-AFEM

4.1 Overview

This chapter extends the derivation for a 1D bar into two dimensions beginning from a general formulation of the quasi-static, transient thermo-elastic problem with and without an internal discontinuity. Mechanical and heat transfer FE equations are then derived using the condensation procedure of the novel A-FEM with reference to the thermo-mechanical cohesive law detailed in Section 2.4. The chapter concludes with validation of the 2D TM-AFEM through comparison with known analytical results and examples of the novel capabilities of the TM-AFEM.

4.2 Problem Statement

4.2.1 Thermo-elastic Domain With No Discontinuity

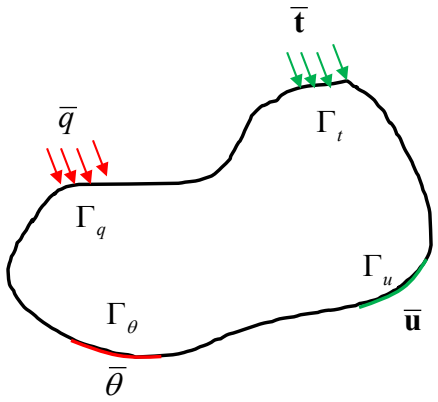

Figure 4.1:Thermo-elastic body under thermo-mechanical loading.

For the coupled thermo-mechanical problem of a domain Ω bounded by Γ in Figure 4.1, the domain is subjected to displacement $\bar{\mathbf{u}}$ and traction $\bar{\mathbf{t}}$ boundary conditions on the boundaries Γ_u and Γ_t respectively. Likewise, the temperature $\bar{\theta}$ and heat flux $\bar{q}$ are

specified on boundaries Γ_θ and Γ_q. The mechanical and thermal equilibrium equations are given by

$$\nabla \bullet \boldsymbol{\sigma} + \mathbf{b} = \mathbf{0}, \tag{4.1}$$

$$\rho c \frac{\partial \theta}{\partial t} + \nabla \bullet \mathbf{q} + Q = 0, \tag{4.2}$$

where $\boldsymbol{\sigma}$ is the Cauchy stress tensor, $\mathbf{b}$ is the body force vector, ρ is the density, c is the specific heat, $\mathbf{q}$ is the heat flux vector and Q is the internal heat source. Surface tractions and heat fluxes are defined as

$$\overline{\mathbf{t}} = \boldsymbol{\sigma} \bullet \mathbf{n}, \tag{4.3}$$

$$\overline{q} = \mathbf{q} \bullet \mathbf{n}. \tag{4.4}$$

The generalized stress-strain equation for an elastic material is given by

$$\boldsymbol{\sigma} = \mathbf{C} : \left(\boldsymbol{\varepsilon} - \boldsymbol{\varepsilon}_\theta \right), \tag{4.5}$$

where $\mathbf{C}$ is the fourth order stiffness tensor, $\boldsymbol{\varepsilon} = 1/2\left[\nabla \mathbf{u} + \left(\nabla \mathbf{u} \right)^T \right]$ is the infinitesimal strain tensor due to deformation and $\boldsymbol{\varepsilon}_\theta = \boldsymbol{\alpha} \Delta\theta$ is the thermally induced strain. The domain is thermo-elastic and thus given a net change in temperature $\Delta\theta = \theta - \theta_0$ from a stress free reference temperature θ_0, there is a corresponding thermal induced strain defined by the product of the change in temperature and the thermal expansion coefficient vector $\boldsymbol{\alpha} = \left\{ \alpha_{xx}, \alpha_{yy} \right\}^T$. Through the variational method, the weak forms of the thermo-elastic equations can be derived to be

$$\int_\Omega \boldsymbol{\sigma} : \nabla \delta \mathbf{u} \, \mathrm{d}\Omega = \int_\Omega \mathbf{b} \bullet \delta \mathbf{u} \, \mathrm{d}\Omega + \int_\Omega \overline{\mathbf{t}} \bullet \delta \mathbf{u} \, \mathrm{d}\Gamma, \tag{4.6}$$

$$\int_\Omega \rho c \frac{\partial \theta}{\partial t} \delta\theta \, \mathrm{d}\Omega + \int_\Omega \mathbf{q} \bullet \nabla \delta\theta \, \mathrm{d}\Omega = \int_\Omega Q \delta\theta \, \mathrm{d}\Omega + \int_{\Gamma_q} \delta\theta \left(\mathbf{q} \bullet \mathbf{n} \right) \mathrm{d}\Gamma. \tag{4.7}$$

Note that this set of thermo-mechanical equations is mechanically quasi-static and thermally transient and reduces to steady state heat transfer when the time derivative term becomes zero.

4.2.2 Thermo-elastic Domain With a Discontinuity

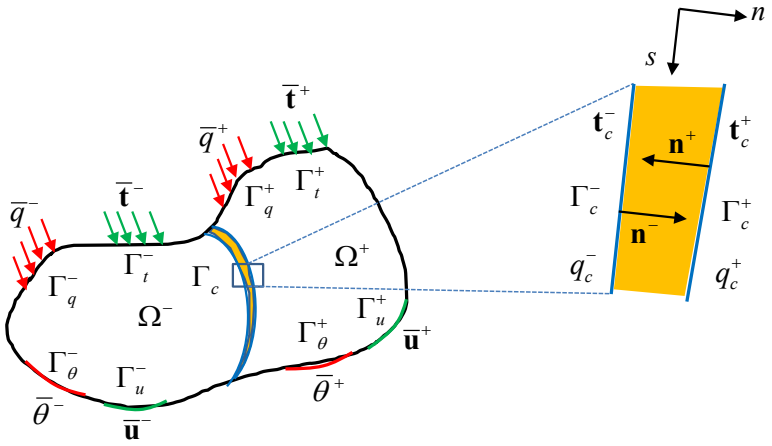

Figure 4.2: Thermo-elastic body with an internal discontinuity.

Suppose the domain is now separated by a discontinuity defined by the boundary Γ_c that divides the domain into subdomains Ω^+ and Ω^- which are assumed to be thermo-elastic. Superscripts + and – denote the respective subdomain. At the discontinuity, define the traction and heat flux as

$$\mathbf{t}_c = \mathbf{t}_c\left(\Delta\mathbf{u}_c, \Delta\theta_c\right) = \mathbf{t}_c^+ = -\mathbf{t}_c^-, \tag{4.8}$$

$$\mathbf{q}_c = \mathbf{q}_c\left(\Delta\mathbf{u}_c, \Delta\theta_c\right) = \mathbf{q}_c^+ = -\mathbf{q}_c^-, \tag{4.9}$$

where the displacement and temperature jumps across the discontinuity are $\Delta\mathbf{u}_c = \mathbf{u}_c^+ - \mathbf{u}_c^-$ and $\Delta\theta_c = \theta_c^+ - \theta_c^-$. Equations (4.6) and (4.7) apply to both subdomains and similarly the weak form of the mechanical and thermal equilibrium equations are

$$\int_\Omega \boldsymbol{\sigma}^+ : \nabla \delta \mathbf{u}^+ \, d\Omega = \int_\Omega \mathbf{b}^+ \bullet \delta \mathbf{u}^+ \, d\Omega + \int_{\Gamma_t} \bar{\mathbf{t}}^+ \bullet \delta \mathbf{u}^+ \, d\Gamma + \int_{\Gamma_c} \mathbf{t}^+ \bullet \delta \mathbf{u} \, d\Gamma, \quad (4.10)$$

$$\int_\Omega \boldsymbol{\sigma}^- : \nabla \delta \mathbf{u}^- \, d\Omega = \int_\Omega \mathbf{b}^- \bullet \delta \mathbf{u}^- \, d\Omega + \int_{\Gamma_t} \bar{\mathbf{t}}^- \bullet \delta \mathbf{u}^- \, d\Gamma + \int_{\Gamma_c} \mathbf{t}^- \bullet \delta \mathbf{u} \, d\Omega, \quad (4.11)$$

$$\begin{aligned} &\int_\Omega \rho^+ c^+ \frac{\partial \theta^+}{\partial t} \delta\theta^+ \, d\Omega + \int_\Omega \mathbf{q}^+ \bullet \nabla \delta\theta^+ \, d\Omega \\ &\quad = \int_\Omega Q^+ \delta\theta^+ \, d\Omega + \int_{\Gamma_q} \delta\theta^+ \left(\mathbf{q}^+ \bullet \mathbf{n}^+ \right) d\Gamma + \int_{\Gamma_c} \delta\theta_c \left(\mathbf{q}_c^+ \bullet \mathbf{n}_c \right) d\Gamma \end{aligned}, \quad (4.12)$$

$$\begin{aligned} &\int_\Omega \rho^- c^- \frac{\partial \theta^-}{\partial t} \delta\theta^- \, d\Omega + \int_\Omega \mathbf{q}^- \bullet \nabla \delta\theta^- \, d\Omega \\ &\quad = \int_\Omega Q^- \delta\theta^- \, d\Omega + \int_{\Gamma_q} \delta\theta^- \left(\mathbf{q}^- \bullet \mathbf{n}^- \right) d\Gamma + \int_{\Gamma_c} \delta\theta_c \left(\mathbf{q}_c^- \bullet \mathbf{n}_c \right) d\Gamma \end{aligned}. \quad (4.13)$$

Note that the presence of an embedded discontinuity generates extra terms that account for the cohesive stress and heat flux at the interface which are generalized to be functions of both the displacement and temperature jumps across the discontinuity.

4.3 Formulation of TM-AFEM with a Single Crack

Consider a bilinear isoparametric quadrilateral element defined by 4 nodes with DoFs u, v, θ at each node. What follows is the derivation of the discrete finite element equations for such an element through the evolution from no discontinuity to weak discontinuity and finally to a strong discontinuity. The problem posed is uncoupled and quasi-static thermo-elastic, meaning that the mechanical coupling terms in the energy and heat conduction equations are neglected. This allows for the thermal conduction and thermo-elastic deformation problem to be solved separately. In physical terms, this is analogous to problems where mechanical deformations are influenced by heat transfer but not vice versa.

4.3.1 TM-AFEM With no Discontinuity

The element is thermo-elastic in this stage and the discrete finite element equations are derived from the weak forms of the mechanical and thermal equilibrium equations. Displacements and temperature are approximated over a single element using nodal values u_i, v_i, θ_i and shape functions N_i as

$$u = \sum_{i=1}^{n_e} u_i N_i \,, \tag{4.14}$$

$$v = \sum_{i=1}^{n} v_i N_i \,, \tag{4.15}$$

$$\theta = \sum_{i=1}^{n_e} \theta_i N_i \,. \tag{4.16}$$

Substituting these approximations into Equations (4.6) and (4.7) and following standard FEM procedure results in the discrete form of the thermo-mechanical FE equations

$$\mathbf{K}_u \mathbf{u} = \mathbf{f} + \mathbf{a} \,, \tag{4.17}$$

$$\mathbf{C}\dot{\boldsymbol{\theta}} + \mathbf{K}_\theta \boldsymbol{\theta} = \mathbf{p} \,, \tag{4.18}$$

where $\mathbf{u} = \{u_1, v_1, ..., u_4, v_4\}^T$ and $\boldsymbol{\theta} = \{\theta_1, ..., \theta_4\}^T$ are nodal displacement and temperature vectors respectively. The stiffness, capacitance and heat transfer matrices are

$$\mathbf{K}_u = \int_\Omega [\mathbf{B}_u]^T [\mathbf{D}_u][\mathbf{B}_u] \, \mathrm{d}\Omega \,, \tag{4.19}$$

$$\mathbf{K}_\theta = \int_\Omega [\mathbf{B}_\theta]^T [\mathbf{D}_\theta][\mathbf{B}_\theta] \, \mathrm{d}\Omega \,, \tag{4.20}$$

$$\mathbf{C} = \int_\Omega [\mathbf{N}_\theta]^T \rho c [\mathbf{N}_\theta] \, \mathrm{d}\Omega \,, \tag{4.21}$$

where **B** is the shape function derivative matrix, **D** is the material matrix and **N** is the shape function matrix. Subscripts u and θ denote association with either the

displacement or temperature DoFs. The mechanical load ($\mathbf{f} = \left\{F_{1x}, F_{1y}, ..., F_{4x}, F_{4y}\right\}^T$) and heat flow ($\mathbf{p} = \left\{P_1, ..., P_4\right\}^T$) vectors are defined as

$$\mathbf{f} = \int_\Omega \left[\mathbf{N}_u\right]^T \left\{\mathbf{b}\right\} \mathrm{d}\Omega + \int_{\Gamma_t} \left[\mathbf{N}_u\right]^T \left\{\overline{\mathbf{t}}\right\} \mathrm{d}\Gamma\,, \tag{4.22}$$

$$\mathbf{p} = \int_\Omega Q\left[\mathbf{N}_\theta\right] \mathrm{d}\Omega + \int_{\Gamma_q} \overline{q}\left[\mathbf{N}_\theta\right] \mathrm{d}\Gamma\,. \tag{4.23}$$

The thermal expansion load vector $\mathbf{a} = \left\{A_{1x}, A_{1y}, ..., A_{4x}, A_{4y}\right\}^T$ comes from solving the integral

$$\mathbf{a} = \int_\Omega \left[\mathbf{B}_u\right]^T \left[\mathbf{D}_u\right]\left\{\boldsymbol{\alpha}\right\}\left[\mathbf{N}_\theta\right]\left\{\Delta\boldsymbol{\theta}\right\} \mathrm{d}\Omega\,, \tag{4.24}$$

where $\Delta\boldsymbol{\theta} = \left\{\theta_1 - \theta_0, ..., \theta_4 - \theta_0\right\}^T$ is the nodal temperature change vector. Explicit forms of the matrices and vectors in Equations (4.19)-(4.24) are given in Appendix B.1.

A backward finite difference scheme is used to evaluate the time integration for the transient heat transfer process to ensure compatibility with the ABAQUS solver. The time increment at time index n is $\Delta t_n = t_n - t_{n-1}$. Thus the time rate change of temperature vector is calculated as

$$\dot{\boldsymbol{\theta}} = \frac{1}{\Delta t_n}\left(\boldsymbol{\theta}_n - \boldsymbol{\theta}_{n-1}\right), \tag{4.25}$$

where nodal temperatures at time indices are $\boldsymbol{\theta}_n = \left\{\theta_1, ..., \theta_4\right\}_n^T$ and $\boldsymbol{\theta}_{n-1} = \left\{\theta_1, ..., \theta_4\right\}_{n-1}^T$.

4.3.2 Single Embedded Discontinuity for 4 Node Rectangular Elements

Prior to being cut, the element is thermo-elastic and standard FE equations (4.17) and (4.18) apply. Due to some thermo-mechanical loading condition, the element eventually reaches a state meeting the crack initiation criterion. Now the 4 node bilinear rectangular element defined by nodes 1, 2, 3 and 4 is "cut" by a cohesive crack, i.e. augmented with

internal nodes 5, 6, 5' and 6', into one of two subdomain configurations: (1) rectangular-rectangular as in Figure 4.3 or (2) triangular-pentagonal as in Figure 4.4 where the subdomains are denoted by Ω^+ and Ω^-. The novel A-FEM assumes that (1) the crack tip resides at an element boundary during growth and (2) crack tip singularities are resolved by a cohesive zone. Each crack then has length l_e and is oriented at an angle ϕ to the global Cartesian coordinate system. A local coordinate system can be defined tangential (s) and normal (n) to the crack path. Normal (δ_n) and tangential (δ_s) crack separations can be calculated from the global x (Δu) and y (Δv) crack separations as

$$\{\delta_s, \delta_n\}^T = [\mathbf{R}]\{\Delta u, \Delta v\}^T, \tag{4.26}$$

via a rotation matrix $\mathbf{R}$ defined earlier in Equation (2.38).

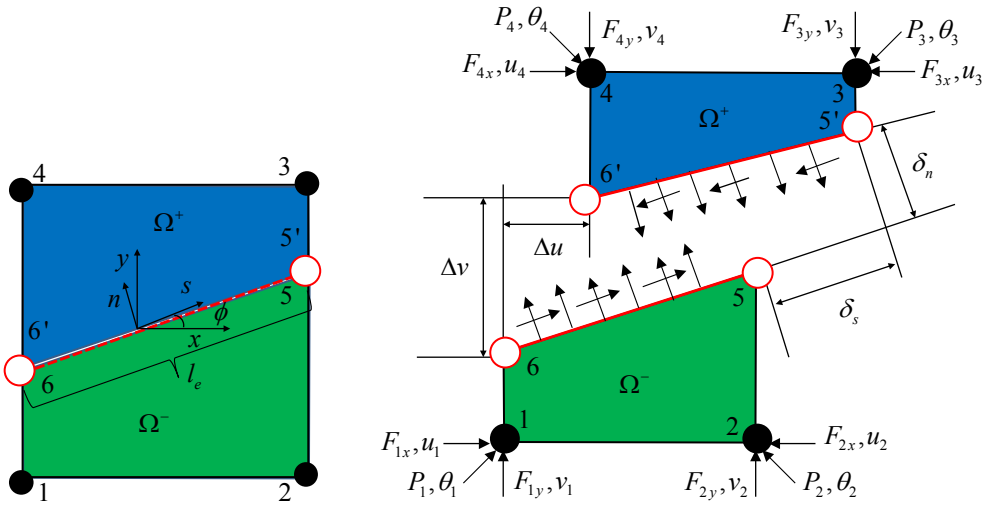

Figure 4.3: Rectangular-rectangular subdomains cut configuration for a 4 node rectangular element associated DoFs, loads and heat flows.

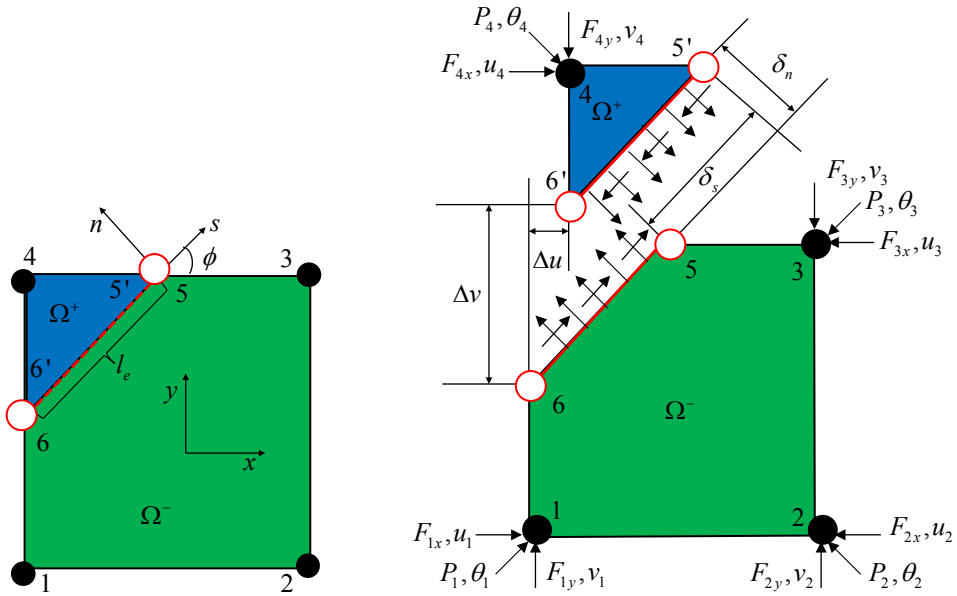

Figure 4.4: Triangular-pentagonal subdomains cut configuration for a 4 node rectangular element with associated DoFs, loads and heat flows.

For a 2D TM-AFEM element, internal nodes will always be 6',5' for the Ω^+ domain and 6,5 for the Ω^- domain so that the associated augmented DoFs, loads and heat flows can be grouped for convenience as

$$\mathbf{u}_{\text{int}}^{-} = \mathbf{u}_{65} = \{u_6, v_6, u_5, v_5\}^T, \quad \mathbf{u}_{\text{int}}^{+} = \mathbf{u}_{6'5'} = \{u_{6'}, v_{6'}, u_{5'}, v_{5'}\}^T, \tag{4.27}$$

$$\boldsymbol{\theta}_{\text{int}}^{-} = \boldsymbol{\theta}_{65} = \{\theta_6, \theta_5\}^T, \quad \boldsymbol{\theta}_{\text{int}}^{+} = \boldsymbol{\theta}_{6'5'} = \{\theta_{6'}, \theta_{5'}\}^T. \tag{4.28}$$

Similarly, associated loads and heat flows are

$$\begin{aligned} \mathbf{f}_{\text{int}}^{-} &= \mathbf{f}_{65} = \{F_{6x}, F_{6y}, F_{5x}, F_{5y}\}^T, \quad \mathbf{f}_{\text{int}}^{+} = \mathbf{f}_{6'5'} = \{F_{6'x}, F_{6'y}, F_{5'x}, F_{5'y}\}^T, \\ \mathbf{a}_{\text{int}}^{-} &= \mathbf{a}_{65} = \{A_{6x}, A_{6y}, A_{5x}, A_{5y}\}^T, \quad \mathbf{a}_{\text{int}}^{+} = \mathbf{a}_{6'5'} = \{A_{6'x}, A_{6'y}, A_{5'x}, A_{5'y}\}^T, \end{aligned} \tag{4.29}$$

$$\mathbf{p}_{\text{int}}^{-} = \mathbf{p}_{65} = \{P_6, P_5\}^T, \quad \mathbf{p}_{\text{int}}^{+} = \mathbf{p}_{6'5'} = \{P_{6'}, P_{5'}\}^T. \tag{4.30}$$

Depending on whether the subdomains are rectangular-rectangular or triangular-pentagonal, external nodes, loads and heat flows are grouped differently. In a rectangular-rectangular division as seen in Figure 4.3, nodes are equally divided between subdomains so that

$$\begin{aligned}
\mathbf{u}_{ext}^{-} &= \mathbf{u}_{12} = \{u_1, v_1, u_2, v_2\}^T, \qquad \mathbf{u}_{ext}^{+} = \mathbf{u}_{34} = \{u_3, v_3, u_4, v_4\}^T \\
\mathbf{f}_{ext}^{-} &= \mathbf{f}_{12} = \{F_{1x}, F_{1y}, F_{2x}, F_{2y}\}^T, \quad \mathbf{f}_{ext}^{+} = \mathbf{f}_{34} = \{F_{3x}, F_{3y}, F_{4x}, F_{4y}\}^T \\
\mathbf{a}_{ext}^{-} &= \mathbf{a}_{12} = \{A_{1x}, A_{1y}, A_{2x}, A_{2y}\}^T, \quad \mathbf{a}_{ext}^{+} = \mathbf{a}_{34} = \{A_{3x}, A_{3y}, A_{4x}, A_{4y}\}^T,
\end{aligned} \tag{4.31}$$

$$\begin{aligned}
\boldsymbol{\theta}_{ext}^{-} &= \boldsymbol{\theta}_{12} = \{\theta_1, \theta_2\}^T, \quad \boldsymbol{\theta}_{ext}^{+} = \boldsymbol{\theta}_{34} = \{\theta_3, \theta_4\}^T \\
\mathbf{p}_{ext}^{-} &= \mathbf{p}_{12} = \{P_1, P_2\}^T, \quad \mathbf{p}_{ext}^{-} = \mathbf{p}_{34} = \{P_3, P_4\}^T.
\end{aligned} \tag{4.32}$$

If the configuration is triangular-pentagonal as in Figure 4.4, then

$$\begin{aligned}
\mathbf{u}_{ext}^{-} &= \mathbf{u}_{123} = \{u_1, v_1, u_2, v_2, u_3, v_3\}^T, \qquad \mathbf{u}_{ext}^{+} = \mathbf{u}_4 = \{u_4, v_4\}^T \\
\mathbf{f}_{ext}^{-} &= \mathbf{f}_{123} = \{F_{1x}, F_{1y}, F_{2x}, F_{2y}, F_{3x}, F_{3y}\}^T, \quad \mathbf{f}_{ext}^{+} = \mathbf{f}_4 = \{F_{4x}, F_{4y}\}^T \\
\mathbf{a}_{ext}^{-} &= \mathbf{a}_{123} = \{A_{1x}, A_{1y}, A_{2x}, A_{2y}, A_{3x}, A_{3y}\}^T, \quad \mathbf{a}_{ext}^{+} = \mathbf{a}_4 = \{A_{4x}, A_{4y}\}^T,
\end{aligned} \tag{4.33}$$

$$\begin{aligned}
\boldsymbol{\theta}_{ext}^{-} &= \boldsymbol{\theta}_{123} = \{\theta_1, \theta_2, \theta_3\}^T, \quad \boldsymbol{\theta}_{ext}^{+} = \boldsymbol{\theta}_4 = \{\theta_4\}^T \\
\mathbf{p}_{ext}^{-} &= \mathbf{p}_{123} = \{P_1, P_2, P_3\}^T, \quad \mathbf{p}_{ext}^{-} = \mathbf{p}_4 = \{P_4\}^T.
\end{aligned} \tag{4.34}$$

What form the condensed FE equations take for the thermo-mechanical process when cut into subdomains is detailed in the following sections.

The behavior of the original element now being cut can be considered analogous to the net behavior of two solid elements interacting with each other through a cohesive element. Adaptive mesh methods in the literature are based on this concept. One of the problems with this approach is that the introduction of the internal discontinuity adds four nodes 5, 6, 5' and 6' that greatly increases the computational expense. The novel A-FEM solves this problem by condensing these additional DoFs and their corresponding loads and heat flows from the FE equations so that the final form is in terms of only the original DoFs, loads and heat flows. This same procedure is extended here for the thermo-mechanical problem to formulate the TM-AFEM. The derivation procedure relies on the assumption of stress and heat flux continuity across the internal crack surfaces and a piece-wise linear thermo-mechanical cohesive law.

From Equations (4.8) and (4.9) it follows that $\mathbf{f}_{65} = -\mathbf{f}_{6'5'}$ and $\mathbf{p}_{65} = -\mathbf{p}_{6'5'}$. In a weak discontinuity, both the displacement and temperature are continuous across the crack boundary, i.e., $\mathbf{u}_{65} = \mathbf{u}_{6'5'}$ and $\boldsymbol{\theta}_{65} = \boldsymbol{\theta}_{6'5'}$. While in a strong discontinuity, displacement and temperature undergo a "jump", i.e., $\Delta\mathbf{u}_c = \mathbf{u}_{6'5'} - \mathbf{u}_{65} \neq 0$ and $\Delta\boldsymbol{\theta}_c = \boldsymbol{\theta}_{6'5'} - \boldsymbol{\theta}_{65} \neq 0$. Internal loads and heat flows are determined from cohesive laws which are functions of these displacement and temperature jumps.

4.3.3 Heat Transfer FE Equations for 4 Node TM-AFEM With Two Subdomains

Equation (4.18) represents a first order differential system with respect to time where the time rate change in temperature is defined by Equation (4.25). Thus Equation (4.18) can be expressed as

$$\left[\bar{\mathbf{K}}_\theta\right]\{\boldsymbol{\theta}\}_n = \{\mathbf{p}\}_n + \frac{1}{\Delta t_n}[\mathbf{C}]\{\boldsymbol{\theta}\}_{n-1} \tag{4.35}$$

where

$$\left[\bar{\mathbf{K}}_\theta\right] = \frac{1}{\Delta t_n}[\mathbf{C}] + [\mathbf{K}_\theta]. \tag{4.36}$$

The heat transfer and capacitance matrices can be expressed in terms of their respective submatrices as

$$\bar{\mathbf{K}}_\theta = \begin{bmatrix} \bar{\mathbf{R}}_{11} & \bar{\mathbf{R}}_{12} \\ \bar{\mathbf{R}}_{21} & \bar{\mathbf{R}}_{22} \end{bmatrix} \tag{4.37}$$

$$\mathbf{C} = \begin{bmatrix} \mathbf{C}_{11} & \mathbf{C}_{12} \\ \mathbf{C}_{21} & \mathbf{C}_{22} \end{bmatrix}. \tag{4.38}$$

For two subdomains Ω^+ and Ω^-, the heat transfer FE equations are then

$$\begin{bmatrix} \bar{\mathbf{R}}^+_{11} & \bar{\mathbf{R}}^+_{12} \\ \bar{\mathbf{R}}^+_{21} & \bar{\mathbf{R}}^+_{22} \end{bmatrix} \begin{Bmatrix} \boldsymbol{\theta}^+_{ext} \\ \boldsymbol{\theta}_{6'5'} \end{Bmatrix}_n = \begin{Bmatrix} \mathbf{p}^+_{ext} \\ \mathbf{p}_{6'5'} \end{Bmatrix}_n + \frac{1}{\Delta t_n} \begin{bmatrix} \mathbf{C}^+_{11} & \mathbf{C}^+_{12} \\ \mathbf{C}^+_{21} & \mathbf{C}^+_{22} \end{bmatrix} \begin{Bmatrix} \boldsymbol{\theta}^+_{ext} \\ \boldsymbol{\theta}_{6'5'} \end{Bmatrix}_{n-1} \tag{4.39}$$

$$\begin{bmatrix} \bar{\mathbf{R}}_{11}^{-} & \bar{\mathbf{R}}_{12}^{-} \\ \bar{\mathbf{R}}_{21}^{-} & \bar{\mathbf{R}}_{22}^{-} \end{bmatrix} \begin{Bmatrix} \boldsymbol{\theta}_{ext}^{-} \\ \boldsymbol{\theta}_{65} \end{Bmatrix}_{n} = \begin{Bmatrix} \mathbf{p}_{ext}^{-} \\ \mathbf{p}_{65} \end{Bmatrix}_{n} + \frac{1}{\Delta t_n} \begin{bmatrix} \mathbf{C}_{11}^{-} & \mathbf{C}_{12}^{-} \\ \mathbf{C}_{21}^{-} & \mathbf{C}_{22}^{-} \end{bmatrix} \begin{Bmatrix} \boldsymbol{\theta}_{ext}^{-} \\ \boldsymbol{\theta}_{65} \end{Bmatrix}_{n-1}. \tag{4.40}$$

4.3.3.1 Weak Discontinuity

In this case, temperature and heat flux are continuous at the bonded interface, i.e. $\boldsymbol{\theta}_{65} = \boldsymbol{\theta}_{6'5'}$ and $\mathbf{p}_{6'5'} = -\mathbf{p}_{65}$. Internal nodal temperatures at time interval n can be shown to be

$$\left\{\boldsymbol{\theta}_{65}\right\}_n = \left\{\boldsymbol{\theta}_{6'5'}\right\}_n = \begin{pmatrix} -\left[\bar{\boldsymbol{\Psi}}\right]^{-1}\left[\bar{\mathbf{R}}_{21}^{-}\right]\left\{\boldsymbol{\theta}_{ext}^{-}\right\}_n - \left[\bar{\boldsymbol{\Psi}}\right]^{-1}\left[\bar{\mathbf{R}}_{21}^{+}\right]\left\{\boldsymbol{\theta}_{ext}^{+}\right\}_n \\ +\frac{1}{\Delta t_n}\left[\bar{\boldsymbol{\Psi}}\right]^{-1}\left[\mathbf{C}_{21}^{-}\right]\left\{\boldsymbol{\theta}_{ext}^{-}\right\}_{n-1} + \frac{1}{\Delta t_n}\left[\bar{\boldsymbol{\Psi}}\right]^{-1}\left[\mathbf{C}_{21}^{+}\right]\left\{\boldsymbol{\theta}_{ext}^{+}\right\}_{n-1} \\ +\frac{1}{\Delta t_n}\left[\bar{\boldsymbol{\Psi}}\right]^{-1}\left[\mathbf{X}\right]\left\{\boldsymbol{\theta}_{65}\right\}_{n-1} \end{pmatrix} \tag{4.41}$$

where

$$\begin{aligned} \left[\bar{\boldsymbol{\Psi}}\right] &= \left[\bar{\mathbf{R}}_{22}^{+}\right] + \left[\bar{\mathbf{R}}_{22}^{-}\right] \\ \left[\mathbf{X}\right] &= \left[\mathbf{C}_{22}^{+}\right] + \left[\mathbf{C}_{22}^{-}\right] \end{aligned}. \tag{4.42}$$

The condensed finite element equations for transient heat transfer following the A-FEM condensation algorithm are then

$$\begin{aligned} \begin{Bmatrix} \mathbf{p}_{ext}^{-} \\ \mathbf{p}_{ext}^{+} \end{Bmatrix}_n = & \begin{bmatrix} \left[\bar{\mathbf{R}}_{11}^{-}\right] - \left[\bar{\mathbf{R}}_{12}^{-}\right]\left[\bar{\boldsymbol{\Psi}}\right]^{-1}\left[\bar{\mathbf{R}}_{21}^{-}\right] & -\left[\bar{\mathbf{R}}_{12}^{-}\right]\left[\bar{\boldsymbol{\Psi}}\right]^{-1}\left[\bar{\mathbf{R}}_{21}^{+}\right] \\ -\left[\bar{\mathbf{R}}_{12}^{+}\right]\left[\bar{\boldsymbol{\Psi}}\right]^{-1}\left[\bar{\mathbf{R}}_{21}^{-}\right] & \left[\bar{\mathbf{R}}_{11}^{+}\right] - \left[\bar{\mathbf{R}}_{12}^{+}\right]\left[\bar{\boldsymbol{\Psi}}\right]^{-1}\left[\bar{\mathbf{R}}_{21}^{+}\right] \end{bmatrix} \begin{Bmatrix} \boldsymbol{\theta}_{ext}^{-} \\ \boldsymbol{\theta}_{ext}^{+} \end{Bmatrix}_n \\ & -\frac{1}{\Delta t_n}\begin{bmatrix} \left[\mathbf{C}_{11}^{-}\right] - \left[\bar{\mathbf{R}}_{12}^{-}\right]\left[\bar{\boldsymbol{\Psi}}\right]^{-1}\left[\mathbf{C}_{21}^{-}\right] & -\left[\bar{\mathbf{R}}_{12}^{-}\right]\left[\bar{\boldsymbol{\Psi}}\right]^{-1}\left[\mathbf{C}_{21}^{+}\right] \\ -\left[\bar{\mathbf{R}}_{12}^{+}\right]\left[\bar{\boldsymbol{\Psi}}\right]^{-1}\left[\mathbf{C}_{21}^{-}\right] & \left[\mathbf{C}_{11}^{+}\right] - \left[\bar{\mathbf{R}}_{12}^{+}\right]\left[\bar{\boldsymbol{\Psi}}\right]^{-1}\left[\mathbf{C}_{21}^{+}\right] \end{bmatrix} \begin{Bmatrix} \boldsymbol{\theta}_{ext}^{-} \\ \boldsymbol{\theta}_{ext}^{+} \end{Bmatrix}_{n-1} \\ & -\frac{1}{\Delta t_n}\begin{bmatrix} \left[\mathbf{C}_{12}^{-}\right] - \left[\bar{\mathbf{R}}_{12}^{-}\right]\left[\bar{\boldsymbol{\Psi}}\right]^{-1}\left[\mathbf{X}\right] & \mathbf{0} \\ \mathbf{0} & \left[\mathbf{C}_{12}^{+}\right] - \left[\bar{\mathbf{R}}_{12}^{+}\right]\left[\bar{\boldsymbol{\Psi}}\right]^{-1}\left[\mathbf{X}\right] \end{bmatrix} \begin{Bmatrix} \boldsymbol{\theta}_{65} \\ \boldsymbol{\theta}_{6'5'} \end{Bmatrix}_{n-1} \end{aligned}. \tag{4.43}$$

Note the transient terms include contributions from the internal DoFs of last time interval $n-1$.

4.3.3.2 Strong Discontinuity

In this case, temperature is no longer continuous but heat flux remains so. Recall the piece-wise linear cohesive heat transfer law described in Section 2.4.2, provided this law is assumed, the heat flow at the internal nodes are given by

$$\mathbf{p}_{65} = -\mathbf{p}_{6'5'} = \left[\mathbf{H}_0\right]\left\{\boldsymbol{\theta}_{6'5'} - \boldsymbol{\theta}_{65}\right\}_n \tag{4.44}$$

where

$$\mathbf{H}_0 = \left[\mathbf{T}_\theta\right]\mathrm{Diag}\left[\left\{\mathbf{h}_0\right\} + \left[\boldsymbol{\beta}_0\right]\left[\mathbf{N}_{\theta u}\right]\mathrm{Diag}\left[\mathbf{R};\mathbf{R}\right]\left\{\mathbf{u}_{6'5'} - \mathbf{u}_{65}\right\}\right]\left[\mathbf{N}_\theta\right]. \tag{4.45}$$

The integration $\mathbf{T}_\theta$ and interpolation $\mathbf{N}_\theta$ matrices are of the form given by Equations (2.51) and (2.49). In the implementation of the TM-AFEM element, integration points for GI2 given in Table 2.1 are used. Since cohesive heat transfer only depends on normal crack separation, the temperature-displacement interpolation matrix for integration points chosen from Table 2.1 is given by

$$\mathbf{N}_{\theta u} = \begin{bmatrix} 0 & 1-\xi_I & 0 & \xi_I \\ 0 & 1-\xi_{II} & 0 & \xi_{II} \end{bmatrix}. \tag{4.46}$$

The characteristic cohesive heat transfer coefficient vector $\mathbf{h}_0$ and slope matrix $\boldsymbol{\beta}_0$ are given by

$$\mathbf{h}_0^{(p,q)} = \left\{\hat{h}^{(p-1)} - \beta_n^{(p)}\delta_{\theta n}^{(p-1)}, \hat{h}^{(q-1)} - \beta_n^{(q)}\delta_{\theta n}^{(q-1)}\right\}^T \tag{4.47}$$

$$\boldsymbol{\beta}_0 = \mathrm{Diag}\left[\beta_n^{(p)}; \beta_n^{(q)}\right]. \tag{4.48}$$

Here, indices p, q designate the segment of the cohesive heat transfer law to which the characteristic coefficients and slopes belong. The temperature at the internal nodes through the novel A-FEM procedure are derived to be

$$\left\{\boldsymbol{\theta}_{6'5'}\right\}_n = \begin{pmatrix} -\left[\boldsymbol{\kappa}_A\right]^{-1}\left[\mathbf{H}_0\right]\left[\boldsymbol{\kappa}_{22}^-\right]^{-1}\left[\bar{\mathbf{R}}_{21}^-\right]\left\{\boldsymbol{\theta}_{ext}^-\right\}_n - \left[\boldsymbol{\kappa}_A\right]^{-1}\left[\bar{\mathbf{R}}_{21}^+\right]\left\{\boldsymbol{\theta}_{ext}^+\right\}_n \\ +\frac{1}{\Delta t_n}\left[\boldsymbol{\kappa}_A\right]^{-1}\left[\mathbf{H}_0\right]\left[\boldsymbol{\kappa}_{22}^-\right]^{-1}\left[\mathbf{C}_{21}^-\right]\left\{\boldsymbol{\theta}_{ext}^-\right\}_{n-1} + \frac{1}{\Delta t_n}\left[\boldsymbol{\kappa}_A\right]^{-1}\left[\mathbf{C}_{21}^+\right]\left\{\boldsymbol{\theta}_{ext}^+\right\}_{n-1} \\ +\frac{1}{\Delta t_n}\left[\boldsymbol{\kappa}_A\right]^{-1}\left[\mathbf{H}_0\right]\left[\boldsymbol{\kappa}_{22}^-\right]^{-1}\left[\mathbf{C}_{22}^-\right]\left\{\boldsymbol{\theta}_{65}\right\}_{n-1} + \frac{1}{\Delta t_n}\left[\boldsymbol{\kappa}_A\right]^{-1}\left[\mathbf{C}_{22}^+\right]\left\{\boldsymbol{\theta}_{6'5'}\right\}_{n-1} \end{pmatrix}, \quad (4.49)$$

$$\left\{\boldsymbol{\theta}_{65}\right\}_n = \begin{pmatrix} -\left[\boldsymbol{\kappa}_B\right]^{-1}\left[\bar{\mathbf{R}}_{21}^-\right]\left\{\boldsymbol{\theta}_{ext}^-\right\}_n - \left[\boldsymbol{\kappa}_B\right]^{-1}\left[\mathbf{H}_0\right]\left[\boldsymbol{\kappa}_{22}^+\right]^{-1}\left[\bar{\mathbf{R}}_{21}^+\right]\left\{\boldsymbol{\theta}_{ext}^+\right\}_n \\ +\frac{1}{\Delta t_n}\left[\boldsymbol{\kappa}_B\right]^{-1}\left[\mathbf{C}_{21}^-\right]\left\{\boldsymbol{\theta}_{ext}^-\right\}_{n-1} + \frac{1}{\Delta t_n}\left[\boldsymbol{\kappa}_B\right]^{-1}\left[\mathbf{H}_0\right]\left[\boldsymbol{\kappa}_{22}^+\right]^{-1}\left[\mathbf{C}_{21}^+\right]\left\{\boldsymbol{\theta}_{ext}^+\right\}_{n-1} \\ +\frac{1}{\Delta t_n}\left[\boldsymbol{\kappa}_B\right]^{-1}\left[\mathbf{C}_{22}^-\right]\left\{\boldsymbol{\theta}_{65}\right\}_{n-1} + \frac{1}{\Delta t_n}\left[\boldsymbol{\kappa}_B\right]^{-1}\left[\mathbf{H}_0\right]\left[\boldsymbol{\kappa}_{22}^+\right]^{-1}\left[\mathbf{C}_{22}^+\right]\left\{\boldsymbol{\theta}_{6'5'}\right\}_{n-1} \end{pmatrix}, \quad (4.50)$$

where

$$\begin{aligned} \left[\boldsymbol{\kappa}_{22}^+\right] &= \left[\bar{\mathbf{R}}_{22}^+\right] + \left[\mathbf{H}_0\right] \\ \left[\boldsymbol{\kappa}_{22}^-\right] &= \left[\bar{\mathbf{R}}_{22}^-\right] + \left[\mathbf{H}_0\right] \\ \left[\boldsymbol{\kappa}_A\right] &= \left[\boldsymbol{\kappa}_{22}^+\right] - \left[\mathbf{H}_0\right]\left[\boldsymbol{\kappa}_{22}^-\right]^{-1}\left[\mathbf{H}_0\right] \\ \left[\boldsymbol{\kappa}_B\right] &= \left[\boldsymbol{\kappa}_{22}^-\right] - \left[\mathbf{H}_0\right]\left[\boldsymbol{\kappa}_{22}^+\right]^{-1}\left[\mathbf{H}_0\right] \end{aligned}. \quad (4.51)$$

In a more compact, the usual FE form is

$$\left[\mathbf{K}_{\theta\theta}\right]\begin{Bmatrix}\boldsymbol{\theta}_{ext}^- \\ \boldsymbol{\theta}_{ext}^+\end{Bmatrix}_n = \begin{Bmatrix}\mathbf{p}_{ext}^- \\ \mathbf{p}_{ext}^+\end{Bmatrix} + \frac{1}{\Delta t_n}\left[\mathbf{K}_{\theta\theta}\right]_{ext}\begin{Bmatrix}\boldsymbol{\theta}_{ext}^- \\ \boldsymbol{\theta}_{ext}^+\end{Bmatrix}_{n-1} + \frac{1}{\Delta t_n}\left[\mathbf{K}_{\theta\theta}\right]_{int}\begin{Bmatrix}\boldsymbol{\theta}_{65} \\ \boldsymbol{\theta}_{6'5'}\end{Bmatrix}_{n-1}, \quad (4.52)$$

where

$$\left[\mathbf{K}_{\theta\theta}\right] = \begin{bmatrix} \left[\bar{\mathbf{R}}_{11}^-\right] - \left[\bar{\mathbf{R}}_{12}^-\right]\left[\boldsymbol{\kappa}_B\right]^{-1}\left[\bar{\mathbf{R}}_{21}^-\right] & -\left[\bar{\mathbf{R}}_{12}^-\right]\left[\boldsymbol{\kappa}_B\right]^{-1}\left[\mathbf{H}_0\right]\left[\boldsymbol{\kappa}_{22}^+\right]^{-1}\left[\bar{\mathbf{R}}_{21}^+\right] \\ -\left[\bar{\mathbf{R}}_{12}^+\right]\left[\boldsymbol{\kappa}_A\right]^{-1}\left[\mathbf{H}_0\right]\left[\boldsymbol{\kappa}_{22}^-\right]^{-1}\left[\bar{\mathbf{R}}_{21}^-\right] & \left[\bar{\mathbf{R}}_{11}^+\right] - \left[\bar{\mathbf{R}}_{12}^+\right]\left[\boldsymbol{\kappa}_A\right]^{-1}\left[\bar{\mathbf{R}}_{21}^+\right] \end{bmatrix}, \quad (4.53)$$

$$\left[\mathbf{K}_{\theta\theta}\right]_{ext} = \begin{bmatrix} \left[\mathbf{C}_{11}^-\right] - \left[\bar{\mathbf{R}}_{12}^-\right]\left[\boldsymbol{\kappa}_B\right]^{-1}\left[\mathbf{C}_{21}^-\right] & -\left[\bar{\mathbf{R}}_{12}^-\right]\left[\boldsymbol{\kappa}_B\right]^{-1}\left[\mathbf{H}_0\right]\left[\boldsymbol{\kappa}_{22}^+\right]^{-1}\left[\mathbf{C}_{21}^+\right] \\ -\left[\bar{\mathbf{R}}_{12}^+\right]\left[\boldsymbol{\kappa}_A\right]^{-1}\left[\mathbf{H}_0\right]\left[\boldsymbol{\kappa}_{22}^-\right]^{-1}\left[\mathbf{C}_{21}^-\right] & \left[\mathbf{C}_{11}^+\right] - \left[\bar{\mathbf{R}}_{12}^+\right]\left[\boldsymbol{\kappa}_A\right]^{-1}\left[\mathbf{C}_{21}^+\right] \end{bmatrix}, \quad (4.54)$$

$$\left[\mathbf{K}_{\theta\theta}\right]_{int} = \begin{bmatrix} \left[\mathbf{C}_{12}^-\right] - \left[\bar{\mathbf{R}}_{12}^-\right]\left[\boldsymbol{\kappa}_B\right]^{-1}\left[\mathbf{C}_{22}^-\right] & -\left[\bar{\mathbf{R}}_{12}^-\right]\left[\boldsymbol{\kappa}_B\right]^{-1}\left[\mathbf{H}_0\right]\left[\boldsymbol{\kappa}_{22}^+\right]^{-1}\left[\mathbf{C}_{22}^+\right] \\ -\left[\bar{\mathbf{R}}_{12}^+\right]\left[\boldsymbol{\kappa}_A\right]^{-1}\left[\mathbf{H}_0\right]\left[\boldsymbol{\kappa}_{22}^-\right]^{-1}\left[\mathbf{C}_{22}^-\right] & \left[\mathbf{C}_{12}^+\right] - \left[\bar{\mathbf{R}}_{12}^+\right]\left[\boldsymbol{\kappa}_A\right]^{-1}\left[\mathbf{C}_{22}^+\right] \end{bmatrix}. \quad (4.55)$$

For the cohesive law assumed, the cohesive coefficient of heat transfer is a function of normal crack separation δ_n only, i.e. $\left[\mathbf{H}_0\right]=\left[\mathbf{H}_0\left(\delta_n\right)\right]$. It is known from the analysis of the 1D bar in Chapter 3, that crack separation is a function of both nodal displacements and temperature, both of which also depend on the crack separation through cohesive thermo-mechanical cohesive law. This results in a highly nonlinear problem that is difficult to solve in the final coupled thermo-mechanical equations because the mechanical and heat transfer equations cannot be expressed explicitly in terms of external DoFs only.

A simplification is to assume that the cohesive coefficient of heat transfer is constant, i.e. independent of crack separation, and that the crack only becomes adiabatic at some critical separation. In this case, Equations (4.47)and (4.45) become

$$\mathbf{h}^{(p,q)}=\left\{\hat{h}^{(p-1)},\hat{h}^{(q-1)}\right\}^T \tag{4.56}$$

$$\mathbf{H}_0{}'=\left[\mathbf{T}_\theta\right]\mathrm{Diag}\left[\left\{\mathbf{h}\right\}\right]\left[\mathbf{N}_\theta\right], \tag{4.57}$$

Thus the coefficient of cohesive heat transfer is independent of crack separation. This changes the thermo-mechanical problem into a form where mechanical and heat transfer parts can be solved separately and sequentially. Equations (4.49)-(4.55) hold with the substitution of $\mathbf{H}_0{}'$ for $\mathbf{H}_0$.

4.3.4 Mechanical FE Equations for 4 Node TM-AFEM With Two Subdomains

The general FE equations for the mechanical process are highly nonlinear and complex because the thermal expansion term introduces a temperature dependence for the crack separation when the temperature depends on the crack separation. Thus temperature DoFs can be considered known inputs so that thermal expansion load vectors

$\mathbf{a}^+_{ext}, \mathbf{a}_{6'5'}, \mathbf{a}^-_{ext}, \mathbf{a}_{65}$ can be considered known in the mechanical FE equations. Thus the general form of the mechanical FE equations for a 2D, 4 node bilinear element with a single internal discontinuity is

$$\begin{bmatrix} \mathbf{L}^+_{11} & \mathbf{L}^+_{12} \\ \mathbf{L}^+_{21} & \mathbf{L}^+_{22} \end{bmatrix} \begin{Bmatrix} \mathbf{u}^+_{ext} \\ \mathbf{u}_{6'5'} \end{Bmatrix} = \begin{Bmatrix} \mathbf{f}^+_{ext} \\ \mathbf{f}_{6'5'} \end{Bmatrix} + \begin{Bmatrix} \mathbf{a}^+_{ext} \\ \mathbf{a}_{6'5'} \end{Bmatrix} \text{ for } \Omega^+_e \tag{4.58}$$

$$\begin{bmatrix} \mathbf{L}^-_{11} & \mathbf{L}^-_{12} \\ \mathbf{L}^-_{21} & \mathbf{L}^-_{22} \end{bmatrix} \begin{Bmatrix} \mathbf{u}^-_{ext} \\ \mathbf{u}_{65} \end{Bmatrix} = \begin{Bmatrix} \mathbf{f}^-_{ext} \\ \mathbf{f}_{65} \end{Bmatrix} + \begin{Bmatrix} \mathbf{a}^-_{ext} \\ \mathbf{a}_{65} \end{Bmatrix} \text{ for } \Omega^-_e . \tag{4.59}$$

4.3.4.1 Weak discontinuity

The two domains are bonded by a rigid interface so the displacement and stress is continuous, i.e. $\mathbf{u}_{65} = \mathbf{u}_{6'5'}$ and $\mathbf{f}_{6'5'} = -\mathbf{f}_{65}$. With these conditions, it can be shown that the external nodal forces are

$$\begin{aligned} \begin{Bmatrix} \mathbf{f}^-_{ext} \\ \mathbf{f}^+_{ext} \end{Bmatrix} = & \begin{bmatrix} \left[\mathbf{L}^-_{11}\right] - \left[\mathbf{L}^-_{12}\right]\left[\Lambda\right]^{-1}\left[\mathbf{L}^-_{21}\right] & -\left[\mathbf{L}^-_{12}\right]\left[\Lambda\right]^{-1}\left[\mathbf{L}^+_{21}\right] \\ -\left[\mathbf{L}^+_{12}\right]\left[\Lambda\right]^{-1}\left[\mathbf{L}^-_{21}\right] & \left[\mathbf{L}^+_{11}\right] - \left[\mathbf{L}^+_{12}\right]\left[\Lambda\right]^{-1}\left[\mathbf{L}^+_{21}\right] \end{bmatrix} \begin{Bmatrix} \mathbf{u}^-_{ext} \\ \mathbf{u}^+_{ext} \end{Bmatrix} \\ & - \begin{Bmatrix} \mathbf{a}^-_{ext} \\ \mathbf{a}^+_{ext} \end{Bmatrix} + \begin{bmatrix} \left[\mathbf{L}^-_{12}\right]\left[\Lambda\right]^{-1} & \left[\mathbf{L}^-_{12}\right]\left[\Lambda\right]^{-1} \\ \left[\mathbf{L}^+_{12}\right]\left[\Lambda\right]^{-1} & \left[\mathbf{L}^+_{12}\right]\left[\Lambda\right]^{-1} \end{bmatrix} \begin{Bmatrix} \mathbf{a}_{65} \\ \mathbf{a}_{6'5'} \end{Bmatrix} \end{aligned} \tag{4.60}$$

where $\left[\Lambda\right] = \left[\mathbf{L}^+_{22}\right] + \left[\mathbf{L}^-_{22}\right]$. Furthermore, the internal forces are found to be

$$\begin{aligned} \mathbf{f}_{65} &= -\mathbf{f}_{6'5'} \\ &= \begin{bmatrix} \left(\left[\mathbf{I}\right] - \left[\mathbf{L}^-_{22}\right]\left[\Lambda\right]^{-1}\right)\left[\mathbf{L}^-_{21}\right] & -\left[\mathbf{L}^-_{22}\right]\left[\Lambda\right]^{-1}\left[\mathbf{L}^+_{21}\right] \end{bmatrix} \begin{Bmatrix} \mathbf{u}^-_{ext} \\ \mathbf{u}^+_{ext} \end{Bmatrix} \\ &\quad + \begin{bmatrix} -\left(\left[\mathbf{I}\right] - \left[\Lambda\right]^{-1}\right) & \left[\mathbf{L}^-_{22}\right]\left[\Lambda\right]^{-1} \end{bmatrix} \begin{Bmatrix} \mathbf{a}_{65} \\ \mathbf{a}_{6'5'} \end{Bmatrix} \end{aligned} \tag{4.61}$$

With internal forces known, tractions acting along the interface can be calculated. For example, average normal and shear stresses along the interface in local coordinates is

$$\begin{Bmatrix} \overline{\tau}_{\text{int}} \\ \overline{\sigma}_{\text{int}} \end{Bmatrix} = [\mathbf{R}] \begin{Bmatrix} \left(F_{x5} + F_{x6}\right)/l_e \\ \left(F_{y5} + F_{y6}\right)/l_e \end{Bmatrix} \tag{4.62}$$

where l_e is the interface length. These stresses are used to determine the initiation of interface debonding through the commonly used initiation criterion

$$\left(\frac{\left\langle \overline{\sigma}_{int} \right\rangle}{\hat{\sigma}_1}\right)^2 + \left(\frac{\overline{\tau}_{int}}{\hat{\tau}_1}\right)^2 = 1 . \tag{4.63}$$

The bracket $\langle \bullet \rangle$ operation is defined as $\langle \bullet \rangle = \left(\bullet + |\bullet|\right)/2$ and is used to be consistent with the physical observation that compressive normal stress does not contribute to crack initiation.

4.3.4.2 Strong discontinuity

In this case the condition $\mathbf{f}_{65} = -\mathbf{f}_{6'5'}$ holds while $\Delta\mathbf{u}_c \neq 0$. There is now a crack separation defined as the displacement jump between internal node pairs

$$\Delta\mathbf{u}_c = \mathbf{u}_{6'5'} - \mathbf{u}_{65} = \left\{\Delta u_{6'6}, \Delta v_{6'6}, \Delta u_{5'5}, \Delta v_{5'5}\right\}^T . \tag{4.64}$$

Following the thermo-mechanical cohesive law described in Section 2.4, the cohesive stresses between the internal node pairs 5'-5 and 6'-6 can be expressed in the local coordinate system normal and tangent to the crack surface as

$$\left\{\tau_{6'6}^{(i)}, \sigma_{6'6}^{(j)}, \tau_{5'5}^{(k)}, \sigma_{5'5}^{(l)}\right\}^T = \boldsymbol{\sigma}_0^{(i,j,k,l)} + \boldsymbol{\alpha}_0^{(i,j,k,l)} \left\{\delta_{s6'6}, \delta_{n6'6}, \delta_{s5'5}, \delta_{n5'5}\right\}^T . \tag{4.65}$$

The indices $i, j, k, l \in [1, 2, 3, 4]$ indicate the current segment of the cohesive stress in the thermo-mechanical cohesive zone law. $\boldsymbol{\sigma}_0^{(i,j,k,l)}$ and $\boldsymbol{\alpha}_0^{(i,j,k,l)}$ are the characteristic cohesive stress and cohesive stiffness matrices respectively. In terms of the critical stresses, crack separations and cohesive slopes defined in Section 2.4.1, they are given by

$$\boldsymbol{\sigma}_0^{(i,j,k,l)} = \left\{\hat{\tau}^{(i-1)} - \alpha_s^{(i)}\delta_s^{(i-1)}, \hat{\sigma}^{(j-1)} - \alpha_n^{(j-1)}\delta_n^{(j-1)}, \hat{\tau}^{(k-1)} - \alpha_s^{(k)}\delta_s^{(k-1)}, \hat{\sigma}^{(l-1)} - \alpha_n^{(l)}\delta_n^{(l-1)}\right\}^T \quad (4.66)$$

$$\boldsymbol{\alpha}_0^{(i,j,k,l)} = \mathrm{Diag}\left[\alpha_s^{(i)}; \alpha_n^{(j)}; \alpha_s^{(k)}; \alpha_n^{(l)}\right]. \quad (4.67)$$

From Equation (4.26), crack separations at the node pairs in global coordinates are related to crack separations in local coordinates by the relation

$$\left\{\delta_{s6'6}, \delta_{n6'6}, \delta_{s5'5}, \delta_{n5'5}\right\}^T = \mathrm{Diag}\left[\mathbf{R}; \mathbf{R}\right]\left\{\Delta u_{6'6}, \Delta v_{6'6}, \Delta u_{5'5}, \Delta v_{5'5}\right\}^T. \quad (4.68)$$

Internal cohesive loads $\mathbf{f}_{65}$ and $\mathbf{f}_{6'5'}$ are found by integrating the cohesive stresses over the crack plane in local crack plane coordinates and rotating the final result to global coordinates

$$\left\{\mathbf{f}_{65}\right\} = -\left\{\mathbf{f}_{6'5'}\right\} = \left\{\mathbf{S}_0\right\} + \left[\mathbf{A}_0\right]\left\{\mathbf{u}_{6'5'} - \mathbf{u}_{65}\right\} \quad (4.69)$$

where the characteristic cohesive stress and stiffness matrices in global coordinates are given by

$$\mathbf{S}_0 = \mathrm{Diag}\left[\mathbf{R}^T; \mathbf{R}^T\right]\left[\mathbf{T}_u\right]\left\{\boldsymbol{\sigma}_0\right\} \quad (4.70)$$

$$\mathbf{A}_0 = \mathrm{Diag}\left[\mathbf{R}^T; \mathbf{R}^T\right]\left[\mathbf{T}_u\right]\left[\boldsymbol{\alpha}_0\right]\left[\mathbf{N}_u\right]\mathrm{Diag}\left[\mathbf{R}; \mathbf{R}\right]. \quad (4.71)$$

Let $\mathbf{T}_u$ and $\mathbf{N}_u$ be the integration and interpolation matrices for cohesive stress integration and displacement interpolation along the crack plane. They are obtained from Table 2.1 in Section 2.5.3. Unless otherwise stated, for the implementation as an ABAQUS user subroutine, the chosen integration scheme is IMP_GI2.

Substituting Equation (4.69) into Equations (4.58) and (4.59) gives the set of equations

$$\begin{aligned} \left(\left[\mathbf{L}_{22}^+\right] + \left[\mathbf{A}_0\right]\right)\left\{\mathbf{u}_{6'5'}\right\} - \left[\mathbf{A}_0\right]\left\{\mathbf{u}_{65}\right\} &= -\left\{\mathbf{S}_0\right\} - \left[\mathbf{L}_{21}^+\right]\left\{\mathbf{u}_{ext}^+\right\} + \left\{\mathbf{a}_{6'5'}\right\} \\ -\left[\mathbf{A}_0\right]\left\{\mathbf{u}_{6'5'}\right\} + \left(\left[\mathbf{L}_{22}^-\right] + \left[\mathbf{A}_0\right]\right)\left\{\mathbf{u}_{65}\right\} &= \left\{\mathbf{S}_0\right\} - \left[\mathbf{L}_{21}^-\right]\left\{\mathbf{u}_{ext}^-\right\} + \left\{\mathbf{a}_{65}\right\} \end{aligned}. \quad (4.72)$$

Now solving for the internal node pair crack separations gives

$$\begin{Bmatrix}\mathbf{u}_{6'5'}\\ \mathbf{u}_{65}\end{Bmatrix}=\begin{bmatrix}-[\mathbf{A}]^{-1}\left([\mathbf{I}]-[\mathbf{A}_0][\boldsymbol{\Psi}_{22}^{-}]^{-1}\right) & \mathbf{0}\\ \mathbf{0} & [\mathbf{B}]^{-1}\left([\mathbf{I}]-[\mathbf{A}_0][\boldsymbol{\Psi}_{22}^{+}]^{-1}\right)\end{bmatrix}\begin{Bmatrix}\mathbf{S}_0\\ \mathbf{S}_0\end{Bmatrix}$$
$$+\begin{bmatrix}-[\mathbf{A}]^{-1}[\mathbf{A}_0][\boldsymbol{\Psi}_{22}^{-}]^{-1}[\mathbf{L}_{21}^{-}] & -[\mathbf{A}]^{-1}[\mathbf{L}_{21}^{+}]\\ -[\mathbf{B}]^{-1}[\mathbf{L}_{21}^{-}] & -[\mathbf{B}]^{-1}[\mathbf{A}_0][\boldsymbol{\Psi}_{22}^{+}]^{-1}[\mathbf{L}_{21}^{+}]\end{bmatrix}\begin{Bmatrix}\mathbf{u}_{ext}^{-}\\ \mathbf{u}_{ext}^{+}\end{Bmatrix} \quad (4.73)$$
$$+\begin{bmatrix}[\mathbf{A}]^{-1}[\mathbf{A}_0][\boldsymbol{\Psi}_{22}^{-}]^{-1} & [\mathbf{A}]^{-1}\\ [\mathbf{B}]^{-1} & [\mathbf{B}]^{-1}[\mathbf{A}_0][\boldsymbol{\Psi}_{22}^{+}]^{-1}\end{bmatrix}\begin{Bmatrix}\mathbf{a}_{65}\\ \mathbf{a}_{6'5'}\end{Bmatrix}$$

where

$$[\boldsymbol{\Psi}_{22}^{+}]=[\mathbf{L}_{22}^{+}]+[\mathbf{A}_0] \quad (4.74)$$

$$[\boldsymbol{\Psi}_{22}^{-}]=[\mathbf{L}_{22}^{-}]+[\mathbf{A}_0] \quad (4.75)$$

$$[\mathbf{A}]=[\boldsymbol{\Psi}_{22}^{+}]-[\mathbf{A}_0][\boldsymbol{\Psi}_{22}^{-}]^{-1}[\mathbf{A}_0] \quad (4.76)$$

$$[\mathbf{B}]=[\boldsymbol{\Psi}_{22}^{-}]-[\mathbf{A}_0][\boldsymbol{\Psi}_{22}^{+}]^{-1}[\mathbf{A}_0]. \quad (4.77)$$

Crack separation is found from Equation (4.64). Using the derived equations, the fully condensed equilibrium equation in terms of only the original external DoFs and forces are

$$\begin{Bmatrix}\mathbf{f}_{ext}^{-}\\ \mathbf{f}_{ext}^{+}\end{Bmatrix}=\begin{bmatrix}[\mathbf{L}_{12}^{-}][\mathbf{B}]^{-1}\left([\mathbf{I}]-[\mathbf{A}_0][\boldsymbol{\Psi}_{22}^{+}]^{-1}\right) & \mathbf{0}\\ \mathbf{0} & -[\mathbf{L}_{12}^{+}][\mathbf{A}]^{-1}\left([\mathbf{I}]-[\mathbf{A}_0][\boldsymbol{\Psi}_{22}^{-}]^{-1}\right)\end{bmatrix}\begin{Bmatrix}\mathbf{S}_0\\ \mathbf{S}_0\end{Bmatrix}$$
$$+\begin{bmatrix}[\mathbf{L}_{11}^{-}]-[\mathbf{L}_{12}^{-}][\mathbf{B}]^{-1}[\mathbf{L}_{21}^{-}] & -[\mathbf{L}_{12}^{-}][\mathbf{B}]^{-1}[\mathbf{A}_0][\boldsymbol{\Psi}_{22}^{+}]^{-1}[\mathbf{L}_{21}^{+}]\\ -[\mathbf{L}_{12}^{+}][\mathbf{A}]^{-1}[\mathbf{A}_0][\boldsymbol{\Psi}_{22}^{-}]^{-1}[\mathbf{L}_{21}^{-}] & [\mathbf{L}_{11}^{+}]-[\mathbf{L}_{12}^{+}][\mathbf{A}]^{-1}[\mathbf{L}_{21}^{+}]\end{bmatrix}\begin{Bmatrix}\mathbf{u}_{ext}^{-}\\ \mathbf{u}_{ext}^{+}\end{Bmatrix} \quad .$$
$$-\begin{Bmatrix}\mathbf{a}_{ext}^{-}\\ \mathbf{a}_{ext}^{+}\end{Bmatrix}+\begin{bmatrix}[\mathbf{L}_{12}^{-}][\mathbf{B}]^{-1} & [\mathbf{L}_{12}^{-}][\mathbf{B}]^{-1}[\mathbf{A}_0][\boldsymbol{\Psi}_{22}^{+}]^{-1}\\ [\mathbf{L}_{12}^{+}][\mathbf{A}]^{-1}[\mathbf{A}_0][\boldsymbol{\Psi}_{22}^{-}]^{-1} & [\mathbf{L}_{12}^{+}][\mathbf{A}]^{-1}\{\mathbf{a}_{6'5'}\}\end{bmatrix}\begin{Bmatrix}\mathbf{a}_{65}\\ \mathbf{a}_{6'5'}\end{Bmatrix}$$

(4.78)

The result is nonlinear because matrices $\mathbf{S}_0$, $\mathbf{A}_0$, $\mathbf{A}$, $\mathbf{B}$, $\mathbf{\Psi}_{22}^{+}$ and $\mathbf{\Psi}_{22}^{-}$ are all nonlinear functions of crack separation $\Delta\mathbf{u}_c$ through $\boldsymbol{\alpha}_0$ and $\boldsymbol{\sigma}_0$, see Equations (4.70)-(4.77). Because the cohesive law is piece-wise linear and assumed segments were used to derive the aforementioned matrices, a solution algorithm unique the novel A-FEM can be applied. A detailed discussion of the algorithm can found in [89].

4.3.5 Subdomain Configurations for TM-AFEM with a Single Crack

4.3.5.1 4 Node 2D TM-AFEM With Rectangular and Rectangular Subdomains

The original stiffness and heat transfer matrices in Equations (4.17) and (4.18) are applied to each subdomain and partitioned into submatrices to give

$$\begin{bmatrix} \left[\mathbf{L}_{11}^{+}\right]_{4\times4} & \left[\mathbf{L}_{12}^{+}\right]_{4\times4} \\ \left[\mathbf{L}_{21}^{+}\right]_{4\times4} & \left[\mathbf{L}_{22}^{+}\right]_{4\times4} \end{bmatrix} \begin{Bmatrix} \mathbf{u}_{34} \\ \mathbf{u}_{6'5'} \end{Bmatrix} = \begin{Bmatrix} \mathbf{f}_{34} \\ \mathbf{f}_{6'5'} \end{Bmatrix} + \begin{Bmatrix} \mathbf{a}_{34} \\ \mathbf{a}_{65} \end{Bmatrix}$$

$$\begin{bmatrix} \left[\mathbf{R}_{11}^{+}\right]_{2\times2} & \left[\mathbf{R}_{12}^{+}\right]_{2\times2} \\ \left[\mathbf{R}_{21}^{+}\right]_{2\times2} & \left[\mathbf{R}_{22}^{+}\right]_{2\times2} \end{bmatrix} \begin{Bmatrix} \boldsymbol{\theta}_{34} \\ \boldsymbol{\theta}_{6'5'} \end{Bmatrix} = \begin{Bmatrix} \mathbf{p}_{34} \\ \mathbf{p}_{6'5'} \end{Bmatrix} + \frac{1}{\Delta t_n} \begin{bmatrix} \left[\mathbf{C}_{11}^{+}\right]_{2\times2} & \left[\mathbf{C}_{12}^{+}\right]_{2\times2} \\ \left[\mathbf{C}_{21}^{+}\right]_{2\times2} & \left[\mathbf{C}_{22}^{+}\right]_{2\times2} \end{bmatrix} \begin{Bmatrix} \boldsymbol{\theta}_{ext}^{+} \\ \boldsymbol{\theta}_{6'5'} \end{Bmatrix}_{n-1} \quad \text{for } \Omega^{+}$$

(4.79)

$$\begin{bmatrix} \left[\mathbf{L}_{11}^{-}\right]_{4\times4} & \left[\mathbf{L}_{12}^{-}\right]_{4\times4} \\ \left[\mathbf{L}_{21}^{-}\right]_{4\times4} & \left[\mathbf{L}_{22}^{-}\right]_{4\times4} \end{bmatrix} \begin{Bmatrix} \mathbf{u}_{12} \\ \mathbf{u}_{65} \end{Bmatrix} = \begin{Bmatrix} \mathbf{f}_{12} \\ \mathbf{f}_{65} \end{Bmatrix} + \begin{Bmatrix} \mathbf{a}_{12} \\ \mathbf{a}_{65} \end{Bmatrix}$$

$$\begin{bmatrix} \left[\mathbf{R}_{11}^{-}\right]_{2\times2} & \left[\mathbf{R}_{12}^{-}\right]_{2\times2} \\ \left[\mathbf{R}_{21}^{-}\right]_{2\times2} & \left[\mathbf{R}_{22}^{-}\right]_{2\times2} \end{bmatrix} \begin{Bmatrix} \boldsymbol{\theta}_{12} \\ \boldsymbol{\theta}_{65} \end{Bmatrix} = \begin{Bmatrix} \mathbf{p}_{12} \\ \mathbf{p}_{65} \end{Bmatrix} + \frac{1}{\Delta t_n} \begin{bmatrix} \left[\mathbf{C}_{11}^{-}\right]_{2\times2} & \left[\mathbf{C}_{12}^{-}\right]_{2\times2} \\ \left[\mathbf{C}_{21}^{-}\right]_{2\times2} & \left[\mathbf{C}_{22}^{-}\right]_{2\times2} \end{bmatrix} \begin{Bmatrix} \boldsymbol{\theta}_{ext}^{-} \\ \boldsymbol{\theta}_{65} \end{Bmatrix}_{n-1} \quad \text{for } \Omega^{-} \quad .$$

(4.80)

All $\left[\mathbf{L}_{ij}^{+}\right]$ and $\left[\mathbf{L}_{ij}^{-}\right]$ $(i,j=1,2)$ stiffness submatrices are 4×4 while all heat transfer and capacitance submatrices $\left[\mathbf{R}_{ij}^{+}\right]$, $\left[\mathbf{R}_{ij}^{-}\right]$, $\left[\mathbf{C}_{ij}^{+}\right]$ and $\left[\mathbf{C}_{ij}^{-}\right]$ $(i,j=1,2)$ are 2×2 because both subdomains are rectangular.

4.3.5.2 4 Node 2D TM-AFEM With Triangular and Pentagonal Subdomains

From Figure 4.4, the finite element equations for the triangular and pentagonal subdomains are

$$\begin{bmatrix} \left[\mathbf{L}_{11}^{+}\right]_{2\times2} & \left[\mathbf{L}_{12}^{+}\right]_{2\times4} \\ \left[\mathbf{L}_{21}^{+}\right]_{4\times2} & \left[\mathbf{L}_{22}^{+}\right]_{4\times4} \end{bmatrix} \begin{Bmatrix} \mathbf{u}_4 \\ \mathbf{u}_{6'5'} \end{Bmatrix} = \begin{Bmatrix} \mathbf{f}_4 \\ \mathbf{f}_{6'5'} \end{Bmatrix} + \begin{Bmatrix} \mathbf{a}_4 \\ \mathbf{a}_{6'5'} \end{Bmatrix}$$
$$\begin{bmatrix} \left[\mathbf{R}_{11}^{+}\right]_{1\times1} & \left[\mathbf{R}_{12}^{+}\right]_{1\times2} \\ \left[\mathbf{R}_{21}^{+}\right]_{2\times1} & \left[\mathbf{R}_{22}^{+}\right]_{2\times2} \end{bmatrix} \begin{Bmatrix} \boldsymbol{\theta}_4 \\ \boldsymbol{\theta}_{6'5'} \end{Bmatrix} = \begin{Bmatrix} \mathbf{p}_4 \\ \mathbf{p}_{6'5'} \end{Bmatrix} + \frac{1}{\Delta t_n} \begin{bmatrix} \left[\mathbf{C}_{11}^{+}\right]_{1\times1} & \left[\mathbf{C}_{12}^{+}\right]_{1\times2} \\ \left[\mathbf{C}_{21}^{+}\right]_{2\times1} & \left[\mathbf{C}_{22}^{+}\right]_{2\times2} \end{bmatrix} \begin{Bmatrix} \boldsymbol{\theta}_{ext}^{+} \\ \boldsymbol{\theta}_{6'5'} \end{Bmatrix}_{n-1} \quad \text{for } \Omega^{+}$$

(4.81)

$$\begin{bmatrix} \left[\mathbf{L}_{11}^{-}\right]_{6\times6} & \left[\mathbf{L}_{12}^{-}\right]_{6\times4} \\ \left[\mathbf{L}_{21}^{-}\right]_{4\times6} & \left[\mathbf{L}_{22}^{-}\right]_{4\times4} \end{bmatrix} \begin{Bmatrix} \mathbf{u}_{123} \\ \mathbf{u}_{65} \end{Bmatrix} = \begin{Bmatrix} \mathbf{f}_{123} \\ \mathbf{f}_{65} \end{Bmatrix} + \begin{Bmatrix} \mathbf{a}_{123} \\ \mathbf{a}_{65} \end{Bmatrix}$$
$$\begin{bmatrix} \left[\mathbf{R}_{11}^{-}\right]_{3\times3} & \left[\mathbf{R}_{12}^{-}\right]_{3\times2} \\ \left[\mathbf{R}_{21}^{-}\right]_{2\times3} & \left[\mathbf{R}_{22}^{-}\right]_{2\times2} \end{bmatrix} \begin{Bmatrix} \boldsymbol{\theta}_{123} \\ \boldsymbol{\theta}_{65} \end{Bmatrix} = \begin{Bmatrix} \mathbf{p}_{123} \\ \mathbf{p}_{65} \end{Bmatrix} + \frac{1}{\Delta t_n} \begin{bmatrix} \left[\mathbf{C}_{11}^{-}\right]_{3\times3} & \left[\mathbf{C}_{12}^{-}\right]_{3\times2} \\ \left[\mathbf{C}_{21}^{-}\right]_{2\times3} & \left[\mathbf{C}_{22}^{-}\right]_{2\times2} \end{bmatrix} \begin{Bmatrix} \boldsymbol{\theta}_{123}^{-} \\ \boldsymbol{\theta}_{65} \end{Bmatrix}_{n-1} \quad \text{for } \Omega^{-} \quad .$$

(4.82)

Note that the submatrices are no longer 4×4 and 2×2 because the geometry of the subdomains are triangular and pentagonal. The changes in the matrix dimensions are indicated by the subscripts. Again, Equations (4.81) and (4.82) are valid for both weak and strong discontinuities. The triangular and pentagonal subdomains configuration presents two unique issues that require discussion.

First, submatrix $\mathbf{L}_{22}^{+}$ is not invertible ($\mathbf{L}_{22}^{-}$ is, however) because in the triangular subdomain the four internal DoFs, $\mathbf{u}_{6'5'}$, cannot be fully determined from two external DoFs, $\mathbf{u}_4$. The formulation of the TM-AFEM alleviates this problem through Equation (4.74). As long as there is non-zero stiffness in the mechanical part of the cohesive law, the matrix condition is regularized and $\boldsymbol{\Psi}_{22}^{+}$ is invertible.

Second, there is no standard method in FEM to calculate the stiffness, heat transfer and capacitance matrices for the pentagonal subdomain. The novel A-FEM and by extension the implementation of the TM-AFEM uses the generalized Gaussian quadrature rules [103] and conforming polygonal FEs [104] for the evaluation of pentagon elements. A summary of the element shape functions and quadrature rule is found in Appendix C.

4.4 Numerical Implementation

The TM-AFEM described by the preceding formulation can easily be integrated into existing displacement based FEM software with slight modifications. ABAQUS is the chosen software of choice due to its capabilities in solving a variety of nonlinear FE problems and the option of using a user subroutine coded in FORTRAN as a means of implementing the TM-AFEM [105]. Typical of displacement based FEM software, ABAQUS requires two inputs for element definition: (1) the Jacobian matrix, i.e. the instantaneous element stiffness matrix, and (2) the external force array. These have been defined for both parts of the thermo-mechanical problem in prior sections. ABAQUS then automatically converts the inputs into an incremental scheme appropriate for numerical analysis of specified loadings.

The TM-AFEM is built upon the same framework as the novel A-FEM and the code is an extension of the existing one for purely mechanical problems. A more in depth discussion of the implementation can be found in [89] but one of the main advantages of the novel A-FEM is that it allows for a simple local crack tracking algorithm capable of dealing with multiple, interacting cracks as opposed to global crack track algorithms such as the level-set method used in X-FEM. Additions to the code include the option for a quasi-static mechanical process coupled with either a steady state or transient heat

transfer problem. For transient problems, the FE equations have been formulated with a backward finite difference time scheme to be compatible with the ABAQUS solver.

4.5 Single Element Validation

In this section, the single TM-AFEM element is validated by comparison to the analytical solution derived from the analysis of a 1D thermo-elastic bar. In addition, the cohesive heat transfer response of a TM-AFEM element is compared with a TM-CZM element that bridges two bulk ABAQUS CPS4T elements.

4.5.1 Comparison of TM-AFEM and Analytical Solutions to 1D Thermo-elastic Bar

The 1D thermo-elastic bar problem is modeled by a single 2D 4 node quadrilateral TM-AFEM element of size 2 mm x 2 mm with displacement and temperature DoFs $\mathbf{u} = \{u_1, v_1, u_2, v_2, u_3, v_3, u_4, v_4\}^T$ and $\boldsymbol{\theta} = \{\theta_1, \theta_2, \theta_3, \theta_4\}^T$. The material is homogeneous with Young's modulus $E = 1 \times 10^5$ N/mm^2, Poisson's ration $\nu = 0.25$ and linear thermal coefficient of thermal expansion $\alpha = 1 \times 10^{-4}$ K^{-1}. The element follows the thermo-mechanical cohesive law summarized in Figure 4.5. The mechanical portion of the thermo-mechanical cohesive law is taken to be linear for the mechanical part with critical cohesive stress $\hat{\sigma} = 10$ N/mm^2 and critical crack separation $\delta_c = 0.01$ mm in both mode I and II. For the heat transfer portion, the simplifying assumption is that upon crack initiation the cohesive heat transfer coefficient is constant, i.e. $\hat{h} = 1.0 \text{ W} \cdot \text{mm}^{-2} \cdot \text{K}^{-1}$. In reference to the heat transfer cohesive law in Figure 4.5(c), this is achieved by taking the critical crack separation δ_θ to be at infinity (numerically a very large number relative to the scale of the critical mechanical crack separation).

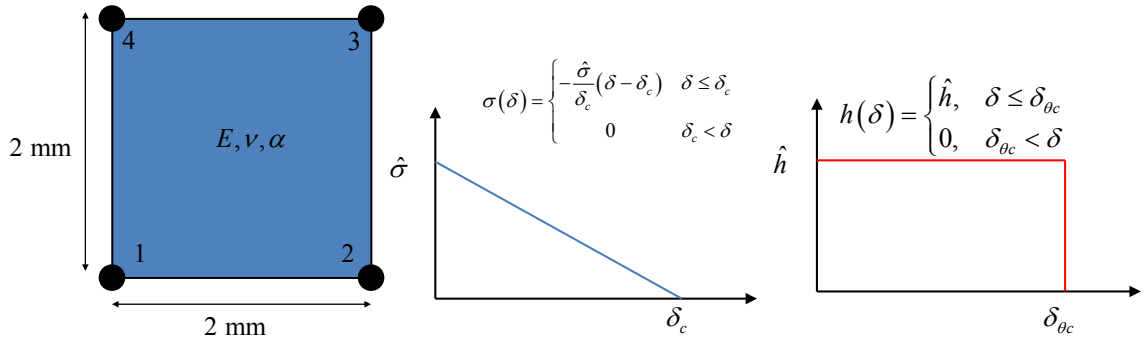

(a) (b) (c)

Figure 4.5: (a) Thermo-elastic element (b) Traction-separation law (c) Heat Transfer Law.

4.5.1.1 Analytical Solution to 1D Bar

The temperature θ is assumed uniform and known from solving the heat transfer problem first. It follows from the thermo-mechanical cohesive law in Figure 4.5(b)-(c) that the displacement at crack initiation and complete failure for a given θ are

$$u_i = \frac{l}{E}\hat{\sigma} + l\alpha\left(\theta - \theta_0\right), \tag{4.83}$$

$$u_c = \delta_c + \frac{l}{E}\hat{\sigma} + l\alpha\left(\theta - \theta_0\right). \tag{4.84}$$

Recall that from Chapter 3, the displacement u is actually the difference in displacements from the top and bottom of the bar. Likewise if displacement is fixed at $u < \delta_c$, then the temperatures at crack initiation and complete failure are

$$\theta_i = \theta_0 + \frac{u}{l\alpha} - \frac{\hat{\sigma}}{E\alpha}, \tag{4.85}$$

$$\theta_c = \theta_0 + \frac{1}{l\alpha}\left(u - \delta_c\right). \tag{4.86}$$

It was shown in Chapter 3 that crack separation as a function of displacement and uniform temperature is given by

$$\delta(u,\theta) = u - \frac{l}{E}\sigma(\delta) - l\alpha(\theta - \theta_0).$$

Thus crack separation as a function of displacement for a given θ in a fixed bar is

$$\delta(u) = \begin{cases} \dfrac{1}{1-\hat{\sigma}/\delta_c}\left(u - \dfrac{l}{E}\hat{\sigma} - l\alpha(\theta - \theta_0)\right), & u_i < u \le u_c \\ u - l\alpha(\theta - \theta_0), & u_c < u \end{cases} \tag{4.87}$$

Similarly, crack separation as a function of temperature for fixed $u < \delta_c$ is

$$\delta(\theta) = \begin{cases} \dfrac{1}{1-\hat{\sigma}/\delta_c}\left(u - \dfrac{l}{E}\hat{\sigma} - l\alpha(\theta - \theta_0)\right), & \theta_c \le \theta < \theta_i \\ u - l\alpha(\theta - \theta_0), & \theta < \theta_c \end{cases}. \tag{4.88}$$

Note that Equations (4.87) and (4.88) are identical but depending on what is fixed and what is variable, the ranges are dictated by either the displacements or temperatures at crack initiation and complete failure. Thus reaction forces are functions of displacement or temperature are

$$F_2 = -F_1 = \begin{cases} AE\left(\dfrac{u}{l} - \alpha(\theta - \theta_0)\right), & u \le u_i; \quad \theta_i \le \theta \\ -\dfrac{A\hat{\sigma}}{\delta_c}\left(\dfrac{1}{1-\hat{\sigma}/\delta_c}\left(u - \dfrac{l}{E}\hat{\sigma} - l\alpha(\theta - \theta_0)\right) - \delta_c\right), & u_i < u \le u_c; \quad \theta_c \le \theta < \theta_i \\ 0, & u > u_c; \quad \theta < \theta_c \end{cases}. \tag{4.89}$$

For convenience, the stress free reference temperature is taken to be $\theta_0 = 0\ \mathrm{K}$ from which a uniform temperature linearly changes $\pm 100\ \mathrm{K}$. From Equation (4.89) and the material and cohesive properties assumed, load-displacement and load-temperature curves can be tabulated and plotted as shown in Figure 4.6. The solid blue and red curves represent load-displacement and load-temperature curves generated by displacement or

temperature change only. With displacement change only, $u_i = 2 \times 10^{-4}$ mm and $u_c = 1.02 \times 10^{-2}$ mm. The crack initiates almost instantaneously and immediately enters the softening phase of the traction-separation curve until complete failure at a displacement of u_c. Crack separation only occurs when the temperature change is negative when it is solely dependent on temperature because only the contraction of the bar generates tensile stress when displacement is fixed at u. In this case, the characteristic temperatures are $\theta_i = -1$ K for crack initiation and $\theta_c = -50$ K at complete failure.

In the combined case of both displacement and temperature change, two curves indicated by dashed lines are given from a negative and positive temperature change along with the same displacement change. When the temperature change is positive, the displacement and temperature change where complete failure occurs and the reaction force drops to zero are $u_c = 0.03$ mm and $\theta_c = 100$ K. This reflects the fact that increasing the temperature causes the bar to expand in the direction of displacement loading, cancelling out the displacement contribution to the crack separation. When the temperature change is negative, the displacement and temperature change at complete failure are $u_c = 0.006$ mm and $\theta_c = -20$ K. Both displacement and temperature are such that they both contribute to increasing the crack separation and failure occurs at a smaller displacement and net temperature change.

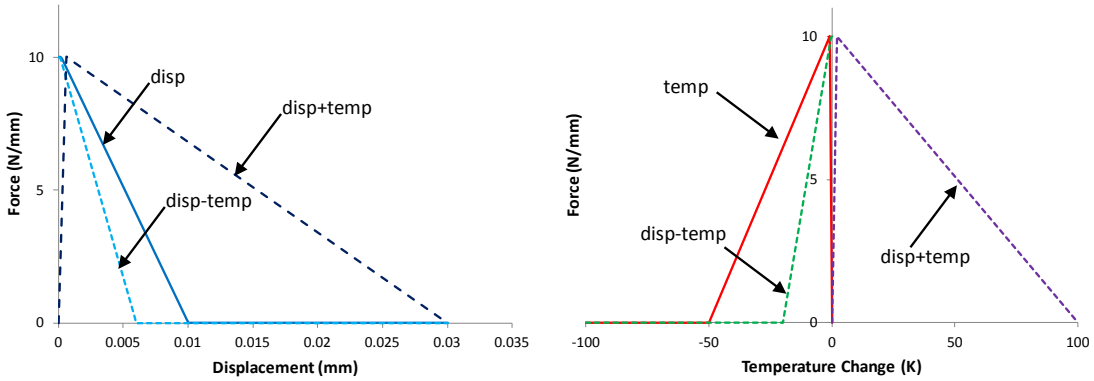

(a) (b)

Figure 4.6: (a) Load-displacement and (b) Load-temperature curves for thermo-mechanical cohesive law.

4.5.1.2 TM-AFEM Solution to 1D Bar

To approximate the 1D problem with the 2D element, boundary conditions where crack separation only occurs in mode I as illustrated in Figure 4.7 are enforced. In order to directly compare with the analytical solutions derived for the 1D thermo-elastic bar, three sets of boundary conditions are considered: (1) crack separation due to displacement only; (2) crack separation due to temperature change only; and (3) crack separation due to both displacement and temperature. Displacement and temperature boundary conditions are applied linearly as a ramp function over 100 increments. Reference stress free temperature is taken to be $\theta_0 = 0$ K and the heat transfer is steady state. Results are plotted as load-displacement and load-temperature curves in Figure 4.8 for easy comparison with the analytical solution. It can be seen that the TM-AFEM generated curves are identical with their analytical counterpart. Characteristic displacements and temperatures at complete failure as well as peak reaction force are the same in both cases.

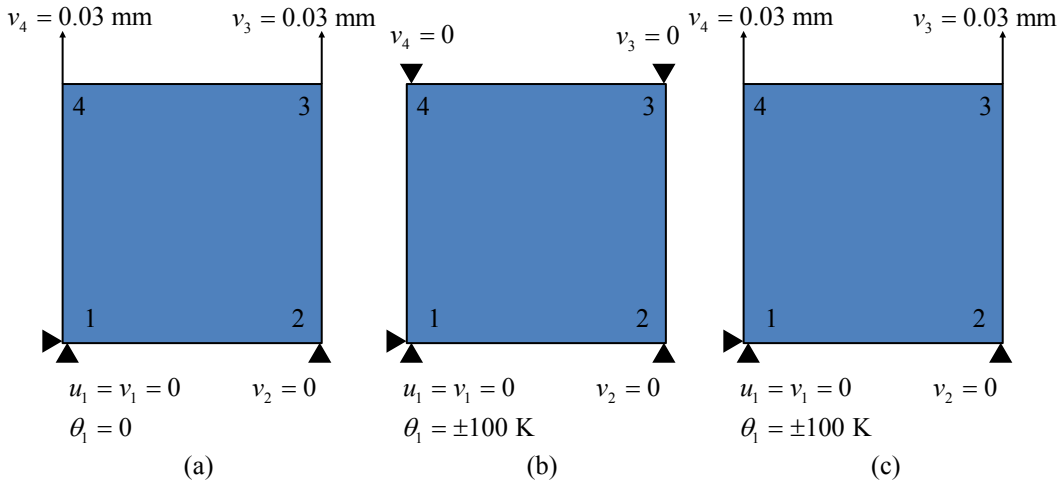

Figure 4.7: (a) Displacement only (b) temperature only (c) displacement and temperature boundary conditions for 1D comparison.

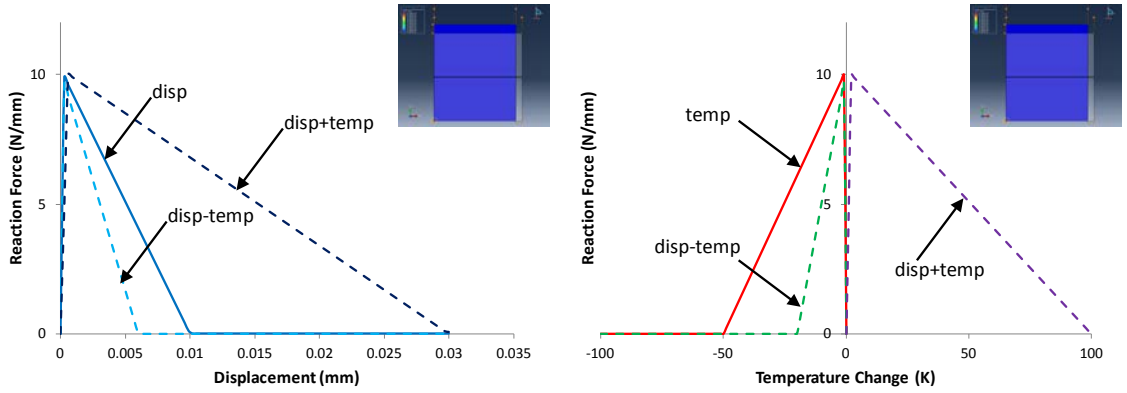

Figure 4.8: (a) Load-displacement and (b) load-temperature curves from TM-AFEM element.

4.5.2 Cohesive Heat Transfer Response

Here the both steady state and transient heat transfer of a single element are evaluated. The heat transfer response of a single TM-AFEM element with an internal discontinuity is compared to its FEM equivalent, two bulk ABAQUS CPS4T elements bridged by a TM-CZM element derived in Chapter 2. Model setup is shown in Figure 4.9. CPS4T elements are defined by nodes 1,2,3,4 and 5,6,7,8. The cohesive element is defined by nodes 4,3,6,5 which correspond to the internal nodes 6,5,6',5' of the TM-AFEM element

with external nodes 1,2,7,8. The cohesive law used is the same as in the prior section and given in Figure 4.5(b)&(c) where the cohesive strengths $\hat{\sigma} = 10$ N/mm^2 and critical crack separation $\delta_c = 0.02$ mm are the same in both mode I and II. For the heat transfer portion, the cohesive heat transfer coefficient is constant, $\hat{h} = 1.0\ \mathrm{W \cdot mm^{-2} \cdot K^{-1}}$, until it becomes zero after the separation $\delta_{\theta c} = 0.01$ mm is met and exceeded. Similarly, the material properties are the same as in the prior section except the coefficient of thermal expansion is set zero and the density and specific heat are taken to be $\rho = 1\ \mathrm{kg \cdot m^{-3}}$ and $c = 1\ \mathrm{J \cdot kg^{-1} \cdot K^{-1}}$.

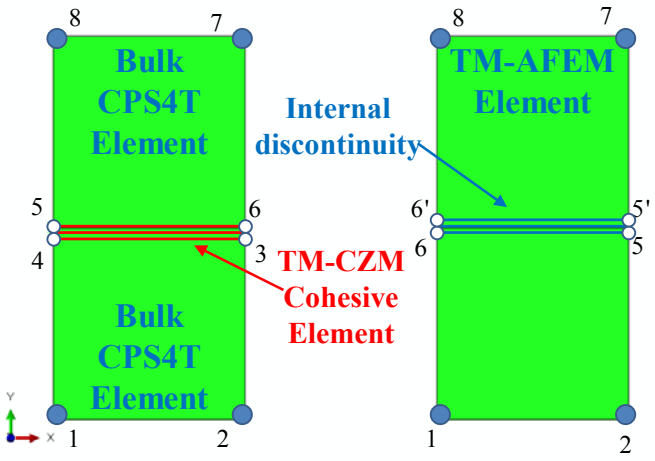

Figure 4.9 : Node numbering for comparison between two bulk CPS4T elements bridged by a TM-CZM element and a single TM-AFEM element.

A temperature gradient of 100 K across the top and bottom surfaces of the models is applied as initial boundary conditions, 0 K at nodes 1,2 and 100 K at nodes 7,8. Two mechanical loading conditions are considered for both steady state and transient heat transfer for a duration of 5 seconds. The first loading is a mode I opening where nodes 1 and 2 are fixed ($u_1 = u_2 = v_2 = 0$) and nodes 7 and 8 are displaced

($u_8 = 0,\ v_8 = v_7 = 0.02$ mm). The second type of loading is a wedge opening enforced by fixing nodes 1 and 8 ($u_1 = v_1 = u_8 = v_8 = 0$) and displacing nodes 2 and 7 ($-v_2 = v_7 = 0.02$ mm). The temperature-displacement curves for both types of loading conditions are shown in Figure 4.10 and Figure 4.11, respectively. Overall, the temperature-displacement curves are the same for both the single TM-AFEM and the two CPS4T elements bridged by a TM-CZM element, indicating their equivalency.

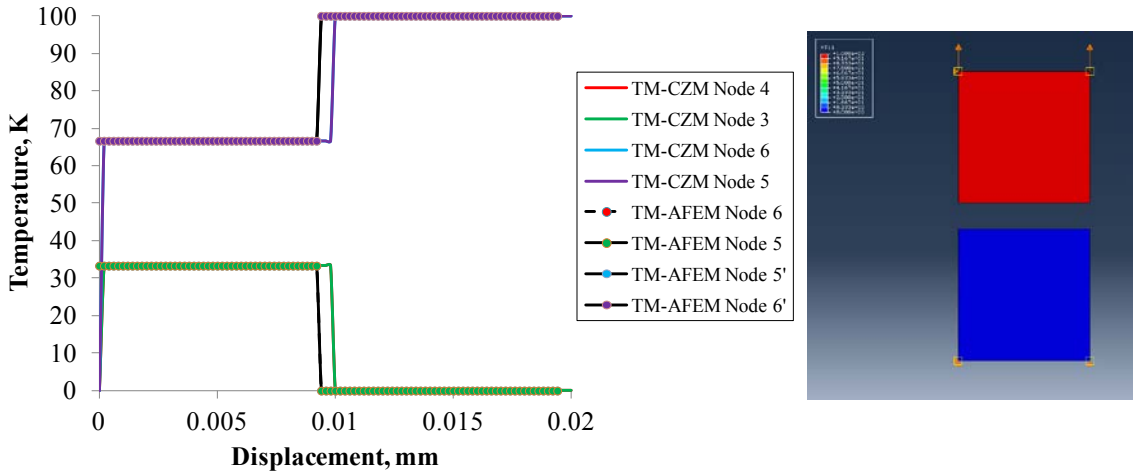

(a)

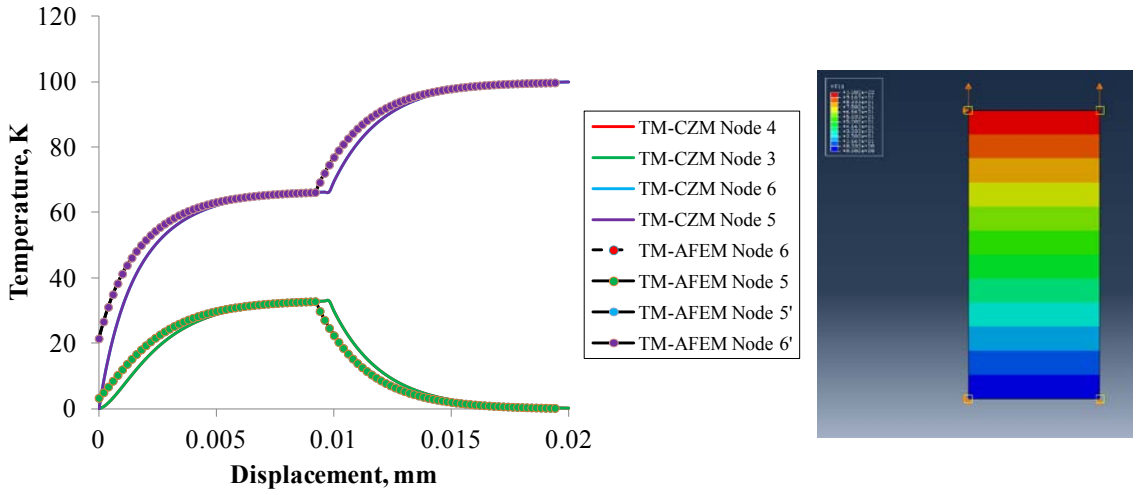

(b)

Figure 4.10 : Temperature at nodes for (a) steady state heat and (b) transient transfer for 5 s across a cohesive crack using TM-CZM and bulk CPS4T elements for Mode I opening.

In the opening stages of displacement loading for the steady state curves in Figure 4.10(a) there is a temperature jump of about 66 K (because of constant $\hat{h}$) between equivalent node pairs until a displacement of 0.01 mm is reached. Because of the material and cohesive properties chosen, the applied displacement is roughly equivalent to the separation between the cohesive surfaces. Thus the critical point after which the cohesive surfaces become adiabatic is also at 0.01 mm. This is why after this displacement, temperature at nodes associated with the top cohesive surface (TM-CZM nodes 5,6 and TM-AFEM nodes 5',6') instantly jump to 100 K and temperature at nodes associated with the bottom cohesive surface (TM-CZM nodes 3,4 and TM-AFEM nodes 5,6) drop to 0 K. The transient temperature-displacement curves in Figure 4.10(b) approach first a thermal equilibrium where the temperature jump between the top and bottom surfaces is 66 K. After critical displacement of 0.01 mm, the temperature jump becomes 100 K because the adiabatic cohesive surfaces equalize to their steady state values. Note that what appears to be a temperature jump initially for the TM-AFEM transient curves is actually a result of fluctuations in temperature as the numerical solution of the transient problem stabilizes. Similarly, the slight differences in the TM-CZM and TM-AFEM curves are attributed to numerical differences in the integration schemes used between the TM-AFEM and the ABAQUS CPS4T elements.

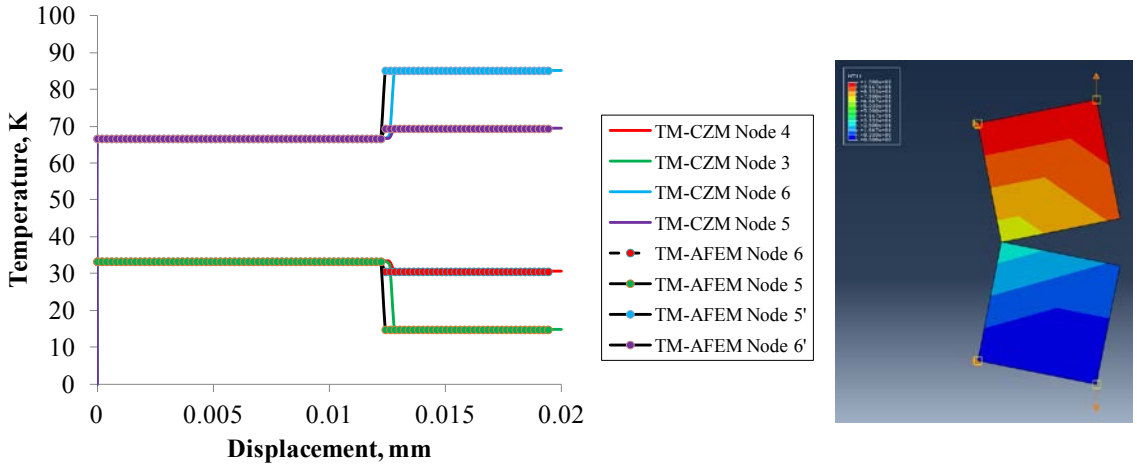

(a)

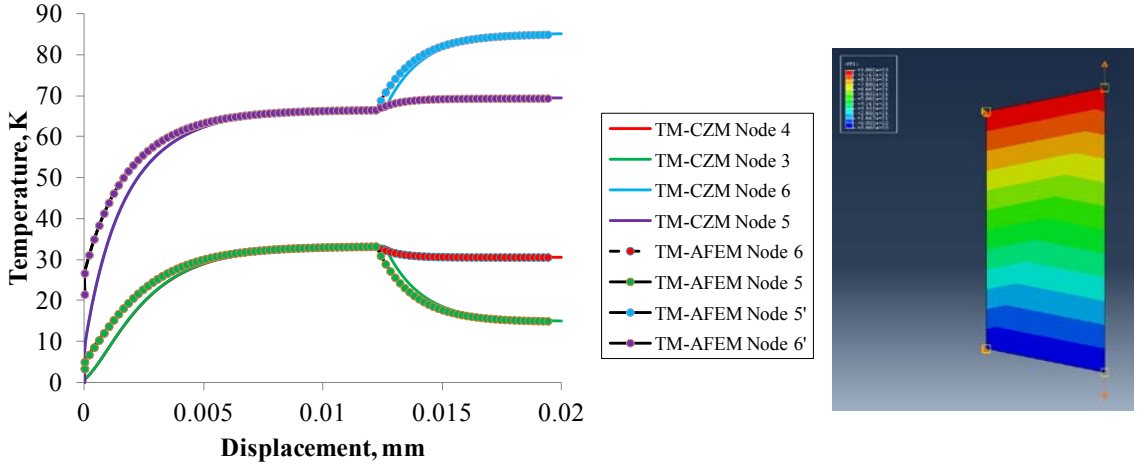

(b)

Figure 4.11 : Temperature at nodes for (a) steady state heat and (b) transient transfer for 5 s across a cohesive crack using TM-CZM and bulk CPS4T elements for wedge opening.

In the wedge opening, the left node pairs (TM-CZM nodes 4,5 and TM-AFEM 6,6') remain bonded while the right node pairs (TM-CZM nodes 3,6 and TM-AFEM 5,5') undergo gradual separation and eventually debond when the critical separation for adiabatic cohesive surfaces is reached. Both steady state and transient curves have a shift after about 0.012 mm, slightly higher than 0.01 mm because of the wedge opening. After 0.012 mm the associated temperatures of the right node pair equalize to give a temperature jump of about 70 K (15 K on the bottom and 85 K on the top) and the temperatures of the left node pair settle to a jump of 40 K (30 K on the bottom and 70 K

on the top). The temperature jump at the left node pair after 0.012 mm is higher than the temperature jump of 33 K at constant $\hat{h}$ (before the displacement reaches 0.012 mm) because heat flux must increase through this node pair to preserve thermal equilibrium if the other node pair is adiabatic. Inversely, the temperature jump at the right node pair is less than the mode I temperature jump of 100 K at adiabatic cohesive surfaces because of the heat flowing from the bonded node pair. Finally, it can be seen that transient temperature-displacement curves correctly approach to their steady state values over time (the time scale of 5 seconds corresponds with the displacement loading of 0.02 mm).

4.6 Summary

This chapter has demonstrated that the application of the A-FEM procedure can be extended to include temperature DoFs. A temperature-displacement formulation has been derived explicitly in terms of the original DoFs if the assumption of a constant coefficient of cohesive heat transfer is made. Evaluation of a single TM-AFEM element reveals that a crack can form as a result of either the interaction of thermal and mechanical processes or the respective individual process themselves. When heated, solids tend to expand and when cooled, solids tend to contract. Depending on the loading conditions, the expansion or contraction due to temperature works with or against fracture of the solid. This principle is explicitly reflected in the load-displacement curves for different temperatures. Through single element evaluation, the mechanical and thermal response of the TM-AFEM is demonstrated to agree with the analytical solution as well as the numerical results obtained using explicit TM-CZM elements developed in Chapter 2.

Chapter 5 Application of TM-AFEM Elements and Future Study

5.1 Overview

In this chapter the formulated TM-AFEM element of prior chapters is applied to simulate several thermo-mechanical engineering problems of practical interest: (1) mode I fracture of a single edge notch test (SENT); (2) mode I fracture of a double cantilever beam (DCB); (3) a two-layer composite beam; (4) crack density of transverse ply cracking in cross-ply laminates; and (5) crack patterns in a thermal barrier coating (TBC) due to thermal stress. Through these numerical examples, the capabilities of the 2D TM-AFEM element to simulate fracture under thermo-mechanical conditions from crack initiation to crack propagation to complete failure are demonstrated. The chapter concludes with a discussion on TM-AFEM elements and avenues for future study and development.

Unless stated otherwise, the thermo-mechanical cohesive law is taken to be the one defined in Figure 4.5(b)&(c) where the relevant parameters are the cohesive strength $\hat{\sigma}$, the constant cohesive heat transfer coefficient $\hat{h}$, and the critical crack separation δ_c. Crack initiation occurs when the strength criterion in Equation (4.63) is met. Furthermore, normal and shear cohesive parameters are assumed equal.

5.2 Crack Propagation in Single Edge Notch Test Configuration

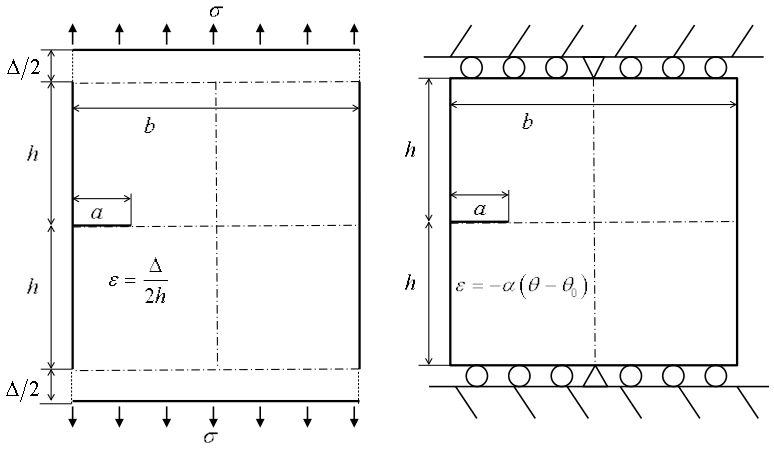

(a) (b)

Figure 5.1 : Configuration for single edge notch test for (b) mechanical loading and (b) an equivalent thermal loading.

For a SENT configuration as seen in Figure 5.1, the stress intensity factor is given by [1]

$$K_I = \sigma\sqrt{\pi a}\; F\left(a/b\right), \tag{5.1}$$

where

$$F\left(a/b\right) = \sqrt{\frac{2b}{\pi a}\tan\left(\frac{\pi a}{2b}\right)}\,\frac{0.752 + 2.02\left(\frac{a}{b}\right) + 0.37\left(1-\sin\frac{\pi a}{2b}\right)^3}{\cos\frac{\pi a}{2b}}, \tag{5.2}$$

is better than 0.5% accuracy for any a/b. The energy release rate then is

$$G = K_I^2/E', \tag{5.3}$$

where

$$E' = \begin{cases} E, & \text{plane stress} \\ E/\left(1-\nu^2\right), & \text{plane strain} \end{cases}. \tag{5.4}$$

From Figure 5.1(a), the far field displacement Δ is given by

$$\Delta = \Delta_{nocrack} + \Delta_{crack}, \tag{5.5}$$

where $\Delta_{nocrack}$ is the displacement due to a crack free uniform stress condition and Δ_{crack} is the displacement at remote points due to the existence of the crack. These are given by

$$\Delta_{nocrack} = \frac{\sigma}{E} 2h, \tag{5.6}$$

$$\Delta_{crack} = \frac{\sigma}{E'} 4aV_2\left(a/b\right), \tag{5.7}$$

$$V_2\left(a/b\right) = \frac{a/b}{\left(1-a/b\right)^2}\left[0.99 - a/b\left(1-a/b\right)\left(1.3 - 1.2\,a/b + 0.7\left(a/b\right)^2\right)\right], \tag{5.8}$$

with better than 1% accuracy for any a/b provided the size condition, $h/b > 1$, applies. Thus the far field strain is then simply

$$\varepsilon = \frac{\Delta}{2h} = \frac{\sigma}{E'}\left(1 + 2\frac{a}{h}V_2\left(a/b\right)\right). \tag{5.9}$$

In an equivalent thermal problem absent of mechanical loading, this strain manifests as a consequence of a uniform temperature change from a stress free reference temperature θ_0 given by $\varepsilon = -\alpha\left(\theta - \theta_0\right)$. The uniform temperature change equivalent to the total far field displacement is simply

$$\theta - \theta_0 = -\frac{\sigma}{\alpha E'}\left(1 + 2\frac{a}{h}V_2\left(a/b\right)\right). \tag{5.10}$$

If the toughness of the specimen, G_C, is known, Equations (5.1)-(5.9) completely describe the fracture problem. LEFM holds that if $G \geq G_C$, the crack grows. Solving Equation (5.1) for the stress using Equation (5.3) and equating G_C for G gives

$$\sigma_c = \frac{E'}{F(a/b)}\sqrt{\frac{G_C}{2bE'}\left(\frac{\pi a}{2b}\right)^{-1}}. \tag{5.11}$$

This is the critical stress that must be met in order for the crack to grow. Note that in Equation (5.11), σ_c is proportional to $1/\sqrt{a}$ so that in the limit $a \to 0$, $\sigma_c \to \infty$. But a real material fails before reaching infinite stress. Thus, Equation (5.11) is only valid until the ultimate strength of a material $\hat{\sigma}$ is reached, i.e. $\sigma_c = \hat{\sigma}$. A physical explanation is that when the crack length is sufficiently small, its strength is determined by maximum stress instead of crack size. This limiting crack length is

$$a_{min} = \frac{1}{\pi F^2(a/b)} \frac{E' G_C}{\hat{\sigma}^2}. \tag{5.12}$$

This result implies that LEFM is valid when $a > a_{min}$ and indicates that a length exists which is completely determined by material properties, i.e.

$$\frac{a_{min}}{\hat{l}} = \frac{1}{\pi F^2(a/b)}, \tag{5.13}$$

where

$$\hat{l} = E' G_C / \hat{\sigma}^2 . \tag{5.14}$$

In the limit as $a/b \to 0$, or when crack size is small, $F(a/b) \to 1.122$ and $a_{min}/\hat{l} \to 0.2838$. From the viewpoint of nonlinear cohesive failure mechanics (NCFM), the length $\hat{l}$ characterizes the fracture process zone. In terms of this inherent length scale, the normalized critical stress and displacement (nominal strain) can be expressed as

$$\frac{\sigma_c}{\hat{\sigma}} = \frac{1}{\sqrt{\pi} F(a/b)} \left(\frac{a}{\hat{l}} \right)^{-1/2}, \tag{5.15}$$

$$\frac{\Delta}{2h} = \frac{\hat{\sigma}/E'}{\sqrt{\pi} F(a/b)} \left(1 + 2\frac{a}{h} V_2(a/b) \right) \left(\frac{a}{\hat{l}} \right)^{-1/2}. \tag{5.16}$$

In these equations, $b/\hat{l}$ is included implicitly through the relation $a/b = \left(a/\hat{l}\right)\left(\hat{l}/b\right)$. These equations are plotted for various specimens of sizes $b/\hat{l} = \{5.69, 11.38, 22.75\}$ under the size condition that $h/b = 3$ in Figure 5.2 using the material properties listed in Table 5.1. Figure 5.2(a) indicates that the limit on the validity of LEFM is not the ultimate stress but on the minimum crack size $a_{min}/\hat{l}$, which lowers the predicted required peak stress for crack propagation to about 90% of the ultimate strength. The strain-crack length curves in Figure 5.2(b) show a gradual decrease from a strain of about 0.2% (that corresponds $a_{min}/\hat{l}$) to a sharp rise in strain as the crack approaches the width. This behavior hints at a second rise in stress and snap-back due to the crack approaching the free edge.

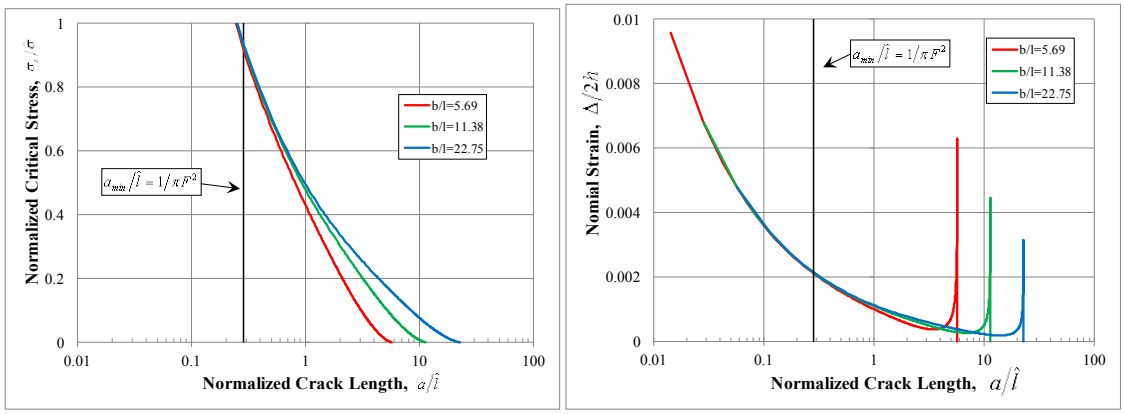

(a) (b

Figure 5.2: (a) Normalized crack length versus normalized critical stress and (b)) nominal strain length versus nominal strain for a SENT fracture configuration.

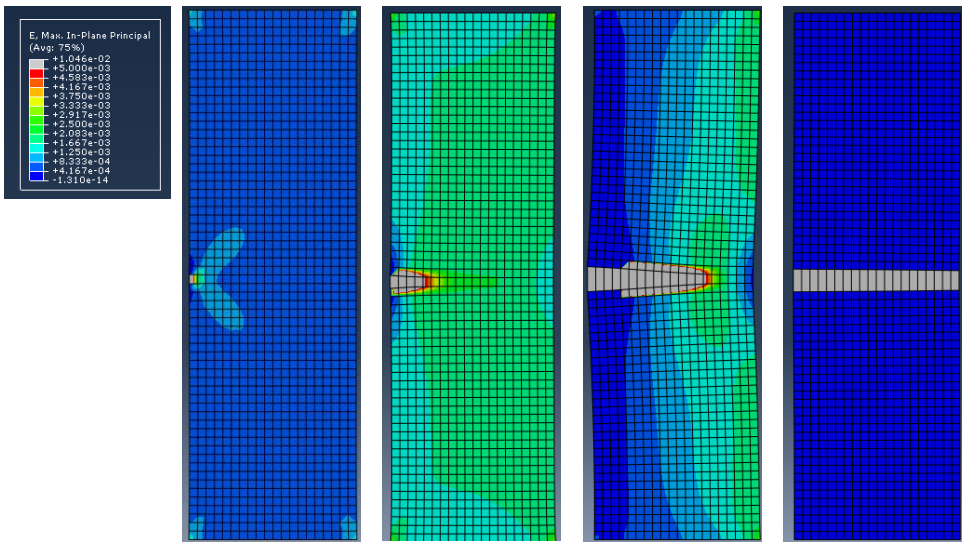

Figure 5.3: Maximum in-plane strain contours for SENT configuration for mesh size of 1240 elements in different stages of edge crack propagation.

A SENT model is built with a mesh size of 1240 TM-AFEM elements. Material and geometry parameters for this model is summarized in Table 5.1. Elements are 0.5 mm in length and smaller than the fracture process zone length of 0.879 mm to ensure adequate resolution. Maximum in-plane strain contours for the stages of crack propagation are shown in Figure 5.3 where areas of high strain (white contour denotes strain greater 0.5 %) indicate the presence of a crack.. Upon loading, the stress concentrates around the initial crack of 0.5 mm in the center of the left side. The crack grows steadily as the specimen deforms under decreasing (snap-back) loading. Upon complete failure, the strain in the separated parts become uniform.

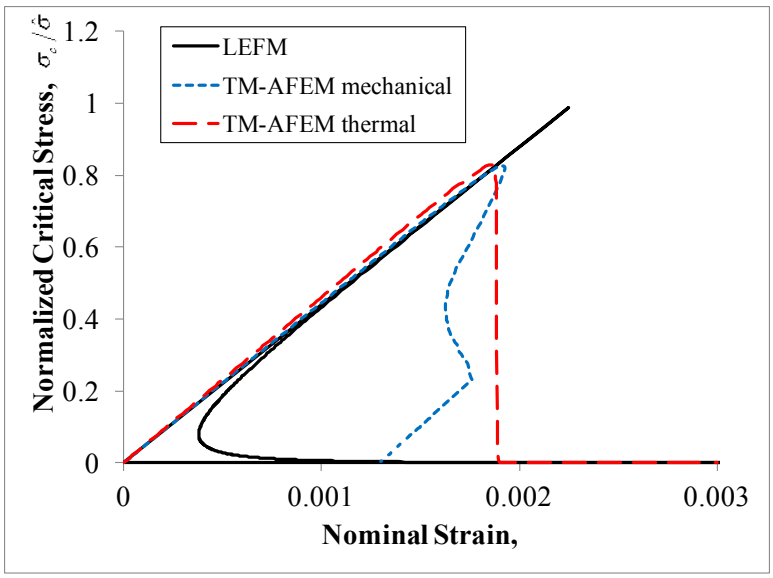

Figure 5.4: Nominal strain versus normalized critical stress curves for LEFM solution and equivalent mechanical and thermal loadings.

Respective stress-strain curves for mechanical and equivalent thermal loadings are plotted in Figure 5.4. The analytical LEFM curve predicts a sharp snap-back behavior upon crack extension during constant load or displacement, indicative of fast crack growth. In anticipation of this snap-back behavior, the static mechanical analysis is run using the arc length method (RIKS option in ABAQUS). Respective stress-strain curves for the equivalent mechanical and thermal loadings are blue and red as indicated by the legend. The cohesive law used by the TM-AFEM elements results in a stress strain curve that has comparable slope (i.e. similar modulus) and shape to the LEFM solution. Peak stress for the TM-AFEM model is less than that predicted by LEFM because the initial crack value of 0.5 mm reduces the stress necessary for crack propagation. Both mechanical and thermal curves reach the same normalized peak stress of but only the mechanical curve exhibits a snap-back. The thermal loading curve fails to capture the snap-back because the option for the arc length method is not supported for the a temperature-displacement analysis in ABAQUS. Furthermore, the equivalent thermal

problem is essentially a load control condition which has difficulty converging to a solution when snap-back behavior is present. Numerical damping is used to mimic the sudden drop in stress in the thermal loading stress-strain curve.

Table 5.1: Geometric and material properties for SENT specimen models.

Geometry			**Material Properties**		
Fracture process zone length, $\hat{l}$	0.879	mm	Poisson's ratio, ν	0.3	
Width, b	10	mm	Young's modulus, E	$2\text{x}10^5$	N/mm^2
Half-height, h	15.5	mm	Fracture toughness, G_C	1	N/mm
			Cohesive strength, $\hat{\sigma}$	500	N/mm^2
			Critical crack separation, δ_c	$4\text{x}10^{-2}$	mm
			Coefficient of thermal expansion, α	$1\text{x}10^{-4}$	K^{-1}

5.3 Double Cantilever Beam

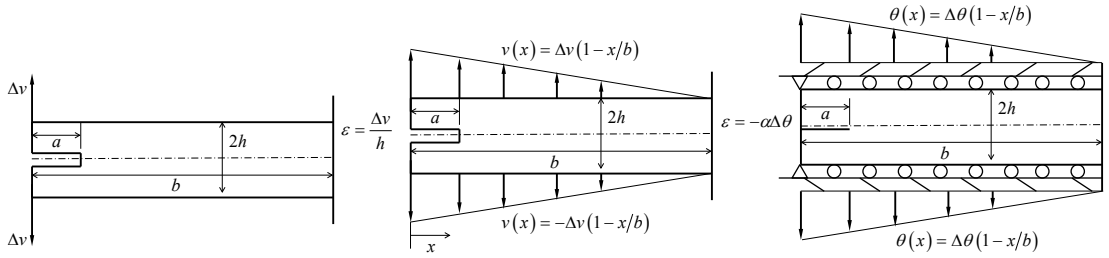

(a) (b) (c)

Figure 5.5 : Configuration for a DCB under (a) displacement control loading (b) displacement control wedge opening and (c) equivalent thermal condition for wedge opening.

In the preceding example, the fast crack growth resulted in a snap-back behavior in the stress-strain curve that could not be captured by a thermo-mechanical analysis owing to the instability of the equivalent temperature loading and unsupported arc length method for coupled temperature-displacement analysis in ABAQUS. This section presents the problem of a double cantilever beam (DCB) of initial crack length a, width

b, and height $2h$ that is opened from the left side by a vertical displacement Δv. As before, equivalent mechanical and thermal loading cases are considered and compared for the geometry and material properties listed in Table 5.2. Note that the chosen coefficient of thermal expansion is artificially high ($\alpha = 1 \times 10^{-2}$ K^{-1}) so that temperature effects on the mechanical response is more easily discernible in cases a thermo-context when comparing the load-displacement response under different uniform temperature changes. The DCB is meshed using TM-AFEM elements in a structured meshed that is 100 x 5 where each element is 1 mm x 1 mm. In Figure 5.5(a)-(c), the initial crack a is taken to be zero.

Table 5.2: Geometry and material properties for DCB model.

Geometry			**Material Properties**		
thickness, t	1	mm	Poisson's ratio, ν	0.3	
width, b	100	mm	Young's modulus, E	1x10^5	N/mm^2
half-height, h	2.5	mm	Fracture toughness, Γ_{IC}	1	N/mm
			Cohesive strength, $\hat{\sigma}$	50	N/mm^2
			Critical crack separation, δ_c	4x10^{-2}	mm
			Coefficient of thermal expansion, α	1x10^{-2}	K^{-1}

First consider the typical DCB problem that has been done prior in Section 2.6.3 using the TM-CZM element. Part of the validation here is to demonstrate the equivalence of the TM-AFEM element in modeling the same example. Recall that the analytical solution based on beam bending analysis [2] for the problem shown in Figure 5.5 (a) is given by

$$\frac{F}{b} = \left(\frac{\Gamma_{\mathrm{IC}}{}^3 E h^3}{108 \Delta v^2} \right)^{\frac{1}{4}}. \tag{5.17}$$

This analytical load-displacement curve is plotted in Figure 5.6 along with numerical results using TM-AFEM elements for a DCB model. A purely mechanical process of imposing an opening displacement Δv gives a curve that closely matches the analytical one. This is to be expected because the behavior of the TM-AFEM element upon fracture is the same as the TM-CZM element since the cohesive model is embedded internally by virtue of the A-FEM formulation. Temperature effects on the baseline load-displacement curve are considered by applying uniform temperature of $\pm 20\,\mathrm{K}$ over a pseudo time step of 1 concurrent with the applied displacement of 0.5 mm. The effects on the load-displacement curve follow the trends seen in the single element validation case in Section 4.5.1. A concurrent increase in temperature during the opening of the beam shifts the load-displacement curve up (green dashed curve) because since the material is expanding in the direction of loading, more bending deformation (i.e. more force) is needed to achieve the same effect as a purely mechanical loading. Conversely, a decreases in temperature lowers the load-displacement curve (blue dashed curve) because the material contracts and resists the direction of loading so that less force is needed to achieve the same effect.

A direct comparison with a temperature equivalent loading for the typical DBC loading case is difficult but in the case of a wedge opening as seen in Figure 5.5(b) where the applied displacement is a linear function across the length of the DCB, an equivalent temperature loading shown in Figure 5.5(c) can easily be derived. The maximum strain at the left end in the mechanical loading is set equal to the thermal strain and solving for the maximum temperature change at the left end gives the equivalent maximum temperature change $\Delta\theta = -\Delta v/\alpha h$. Load-displacement curves for the same node for both of these

loading cases are shown in Figure 5.7 where the temperature equivalent displacement is computed as $\Delta v = -\alpha h \Delta\theta$ given the known applied temperature. The curves are virtually identical, initially increasing in load until a peak value of 50 N/mm (corresponding to the prescribed cohesive strength) and decreasing to zero at a displacement of 0.02 mm (half of the prescribed critical crack separation because the bottom surface displacement accounts for the other half). After the critical displacement, the reaction forces are zero indicating complete failure and loss of load carrying capability.

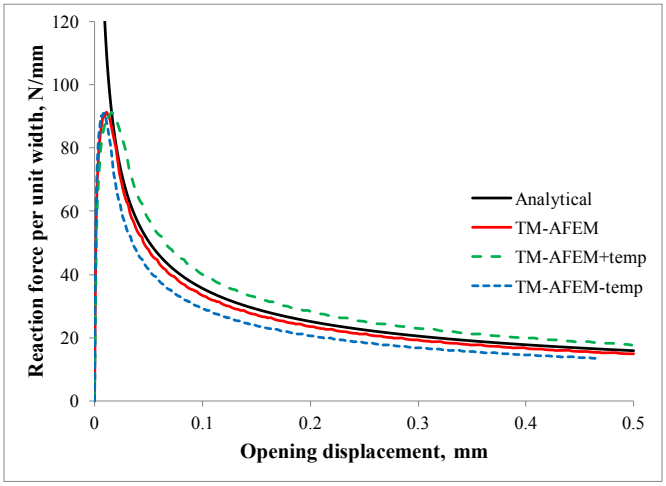

Figure 5.6 : Load-displacement plot for DCB comparing analytical and numerical results with the influence of temperature.

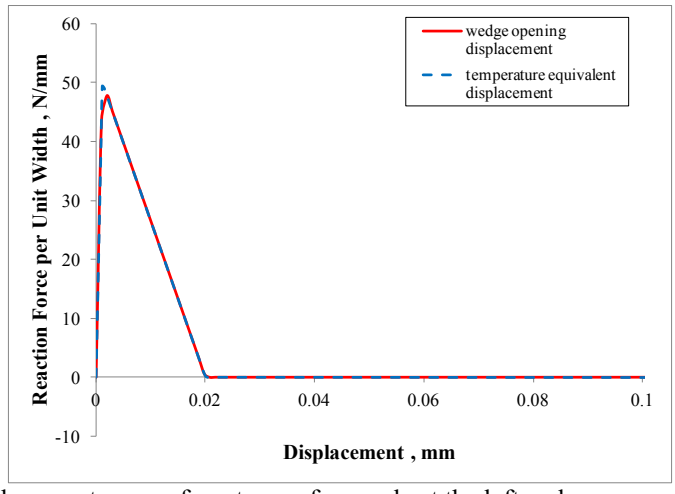

Figure 5.7 : Load-displacement curves for a top surface node at the left end.

5.4 Two-Layered Composite Beam

A general two-layered composite beam of length l is shown in Figure 5.8 consisting of two layers with Young's modulus E_i and coefficient of thermal expansion α_i bonded together by a thin interface and subjected to temperature changes $T_i(y)$ where $i = 1, 2$ denotes the respective layer. Respective i-th widths and heights are b_i and h_i. Consider the special case that both layer cross sections are the same and temperature changes in the layers are constant but different, i.e.

$$h_1 = h_2 = h \quad b_1 = b_2 = b \tag{5.18}$$

$$T_1(y) = T_1 \quad T_2(y) = T_2 . \tag{5.19}$$

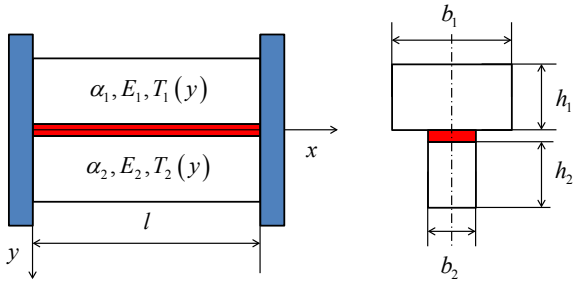

Figure 5.8: A beam consisting of two layers bonded together.

It can be shown that for such a case, the thermal stresses along the length of the beam are given by [3]

$$\sigma_{xi}(y) = -\alpha_i E_i T_i + \frac{E_i}{D}\begin{bmatrix} \alpha_1 E_1 T_1 (E_1 + 7E_2) + \alpha_2 E_2 T_2 (7E_1 + E_2) \\ -12\frac{y}{h} E_1 E_2 (\alpha_1 T_1 - \alpha_2 T_2) \end{bmatrix}, \tag{5.20}$$

where

$$D = (E_1 + E_2)^2 + 12E_1 E_2 . \tag{5.21}$$

Likewise, in the case where the temperature distribution is linear and the widths are equal, i.e.

$$b_1 = b_2 = b \tag{5.22}$$

$$T_1(y) = A_1 + B_1 y \quad T_2(y) = A_2 + B_2 y \tag{5.23}$$

thermal stresses along the beam length are [3]

$$\begin{aligned}\sigma_{xi}(y) = &-\alpha_i E_i (A_i + B_i y) \\ &+\frac{E_i}{D}\begin{Bmatrix} 2\left[\alpha_1 E_1 h_1 (2A_1 - B_1 h_1) + \alpha_2 E_2 h_2 (2A_2 + B_2 h_2)\right]\left(E_2 h_2^3 + E_1 h_1^3\right) \\ -\left[\alpha_1 E_1 h_1^2 (-3A_1 + 2B_1 h_1) + \alpha_2 E_2 h_2^2 (3A_2 + 2B_2 h_2)\right]\left(E_2 h_2^2 - E_1 h_1^2\right) \end{Bmatrix} \\ &+\frac{E_i y}{D}\begin{Bmatrix} 2\left[\alpha_1 E_1 h_1^2 (-3A_1 + 2B_1 h_1) + \alpha_2 E_2 h_2^2 (3A_2 + 2B_2 h_2)\right]\left(E_2 h_2 + E_1 h_1\right) \\ -3\left[\alpha_1 E_1 h_1 (2A_1 - 2B_1 h_1) + \alpha_2 E_2 h_2 (2A_2 + B_2 h_2)\right]\left(E_2 h_2^2 - E_1 h_1^2\right) \end{Bmatrix}\end{aligned}, \tag{5.24}$$

where

$$D = \left(E_2 h_2^2 - E_1 h_1^2\right)^2 + 4E_1 E_2 h_1 h_2 (h_1 + h_2)^2 . \tag{5.25}$$

Plots of Equations (5.20) and (5.24) are shown for their respective constant and linear temperature distributions using the geometry and material properties given in Table 5.3.

A thermo-mechanical cohesive law is assumed where the crack is adiabatic when formed, i.e. $\hat{h} = 0$ W/(mm^2·K) , and the mechanical cohesive law is linear. The assumption of linearity allows for the mechanical traction-separation law to be defined completely by the cohesive strength $\hat{\sigma}$ and critical separation δ_c such that the fracture toughness is given by

$$G_c = \hat{\sigma}\delta_c / 2 . \tag{5.26}$$

Modes I and II are assumed to have the same cohesive stress and critical separation. With reference to the stress distributions, the cohesive strengths for layer 1, layer 2 and the interface are assumed to be 100, 500 and 50 MPa respectively so that the crack will more likely initiate and propagate along the interface and branch into the upper layer. Since each element is roughly 1 mm in length, Equation (5.14) is used to estimate the

characteristic cohesive length such that $\hat{l}/l_e \approx 5$ to ensure adequate resolution for modeling the cohesive zone. Fracture toughness is varied for each cohesive strength to achieve this criterion and the corresponding critical separations are calculated through Equation (5.26). Resulting cohesive properties are summarized in Table 5.4.

Plotted alongside the temperature distribution and thermal stresses from the analytical solution are the numerical result from using TM-AFEM elements in a 200 x 21 element mesh to model the composite beam. The model is divided into three material regions corresponding to layer 1, layer 2 and the thin interface connecting the layers composed of a single layer of elements of thickness $h_{int} = 0.01h_2$. Material property values of the interface are taken to be the average of the material properties of its two connecting layer so that $E_{interface} = 128.5$ GPa, $\alpha_{interface} = 9.45 \times 10^{-6}$ 1/K and $k_{interface} = 4.8 \times 10^{-3}$ W/(mm·K). Equations (5.20) and (5.24) are derived from beam theory where the tensile thermal stress is a result of the bending of the composite beam. To allow for the composite beam to bend, boundary conditions for the numerical model are to fix displacement in the *x* direction at a node coincident with the interface and to fix the displacement in *y* direction for the left and right corners to prevent rotation. A reference stress free temperature of $\theta_0 = 0$ K is assumed and 400 K and 300 K are prescribed on the top and bottom surfaces of the numerical model respectively. To achieve a uniform temperature distribution on the top and bottom layers, the interface thermal conductivity is taken to be $k_{int} = 0 \times 10^{-3}$ W/(mm·K). Temperature and stress distributions are read along a path along the left edge of the numerical mesh to correspond with the analytical solution which is a function of beam height. As can be seen in Figure 5.9, the TM-AFEM

elements model result agrees fairly well with the analytical solution. Stresses between the analytical and TM-AFEM solution are close far away from the neutral axis but deviate near it.

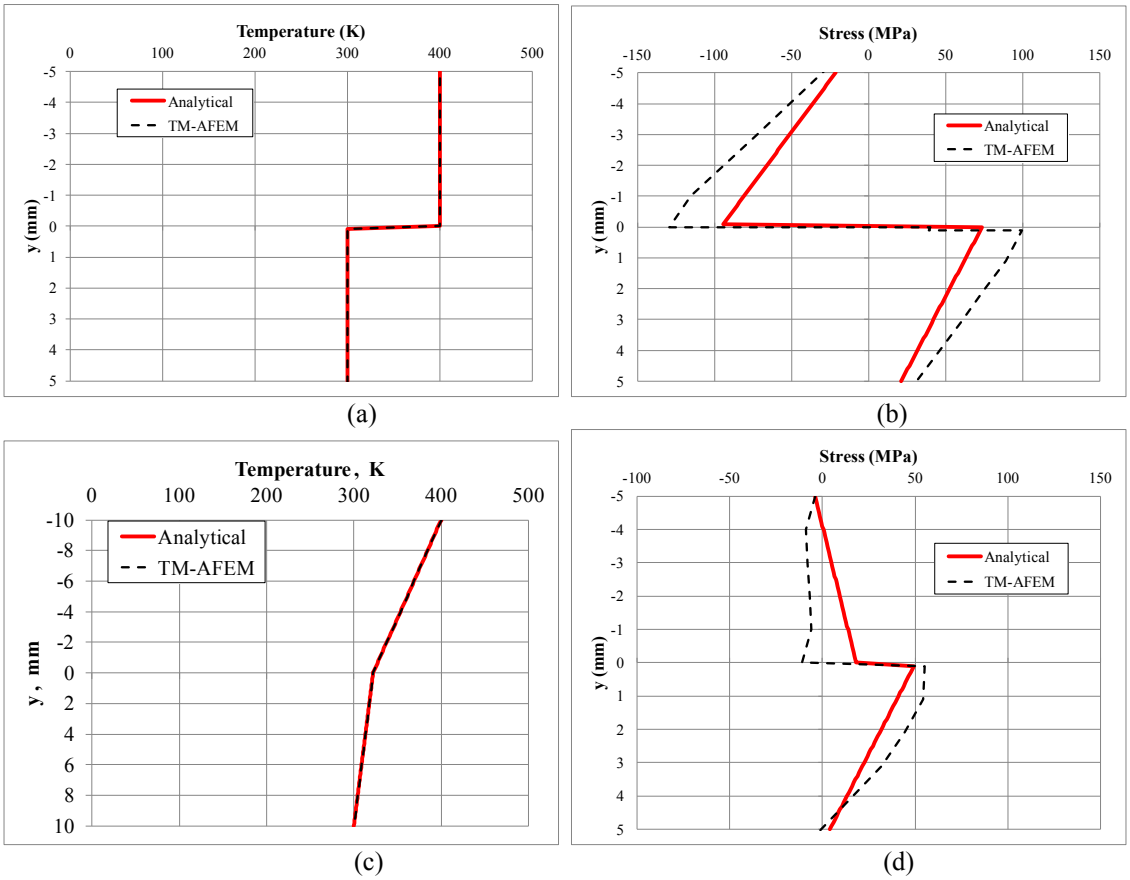

Figure 5.9 : Temperatures and thermal stresses in a two-layered beam for (a) uniform temperature distribution; (b) thermal stress due to uniform temperature; (c) linear temperature distribution; and (d) thermal stress due to linear temperature.

There is a mild mismatch in the stress distribution at the interface evident in Figure 5.9(b)&(d) where the layers are bonded due to the differences in material properties and temperature. Under certain conditions, fracture can occur and interface cracks can initiate and propagate. The two-layer composite beam actually is a basis for modeling a material

structure of great interest in high temperature applications, a thermal barrier coating (TBC). TBCs will be explored in a subsequent section.

Table 5.3: Geometric and material properties for two layer bi-material composite beam.

Geometry			**Material Properties**		
Layer 1 width, b_1	1	mm	Layer 1 modulus, E_1	$151\text{x}10^{3}$	N/mm^2
Layer 1 height, h_1	10	mm	Layer 1 thermal expansion, α_1	$10\text{x}10^{-6}$	1/K
Layer 2 width, b_2	1	mm	Layer 1 conductivity, k_1	$2.09\text{x}10^{-3}$	W/(mm·K)
Layer 2 height, h_2	10	mm	Layer 2 modulus, E_2	$106\text{x}10^{3}$	N/mm
Length, l	200	mm	Layer 2 thermal expansion, α_2	$8.9\text{x}10^{-6}$	1/K
			Layer 2 conductivity, k_2	$7.5\text{x}10^{-3}$	W/(mm·K)

Table 5.4: Cohesive properties for TM-AFEM model of two layer composite beam.

Cohesive Properties		
Layer 1 fracture toughness, G_{1c}	0.3	N/mm
Layer 1 cohesive strength, $\hat{\sigma}_1$	100	N/mm^2
Layer 1 critical separation, $\delta_c^{(1)}$	$6\text{x}10^{-3}$	mm
Layer 2 fracture toughness, G_{2c}	10	N/mm
Layer cohesive strength, $\hat{\sigma}_2$	500	N/mm^2
Layer 2 critical separation, $\delta_c^{(2)}$	$4\text{x}10^{-2}$	mm
Interface fracture toughness, $G_{\text{int}\,c}$	0.1	N/mm
Interface cohesive strength, $\hat{\sigma}_{\text{int}}$	50	N/mm^2
Interface critical separation, $\delta_c^{(\text{int})}$	$4\text{x}10^{-3}$	mm

5.5 Transverse Ply Cracking in Cross-ply Laminates

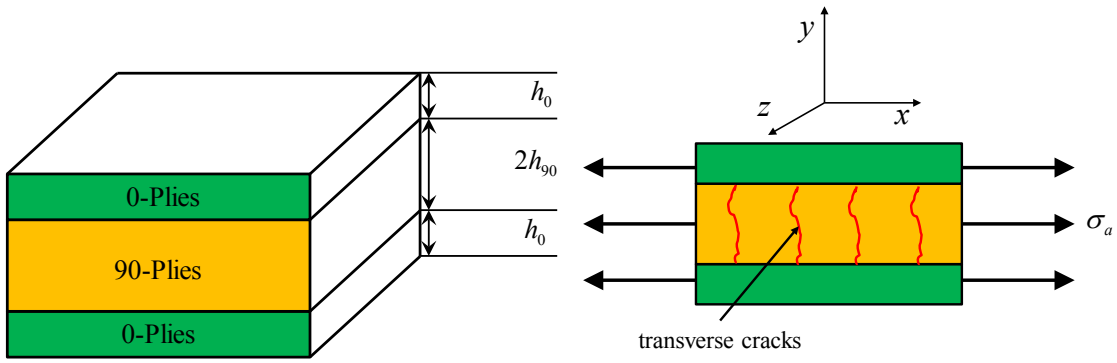

Figure 5.10: A cross-ply laminate, $[0/90_n/0]_T$, under uniaxial stress exhibiting transverse cracking in the 90-plies.

Consider the $[0/90_n/0]_T$ T300/934 laminate shown in Figure 5.10 where the material properties of each ply is given in Table 5.5. This laminate is modeled using TM-AFEM elements under the assumption of plane strain with dimensions and material properties shown in Figure 5.11. Note that the thermal expansion coefficient for 0 and 90-plies is taken to be α_2, the coefficient for the transverse direction (i.e. 90-ply), because $\alpha_2 >> \alpha_1$ and its effect dominates assuming perfectly bonded plies. The heat transfer process is steady state so choices for thermal conductivities and the cohesive heat transfer coefficient are trivial provided they are larger than zero, but they chosen to have the values $k = 1.0$ W·mm^{-1}·^{0}C^{-1} and $\hat{h} = 1.0$ W·mm^{-2}·^{0}C^{-1}.

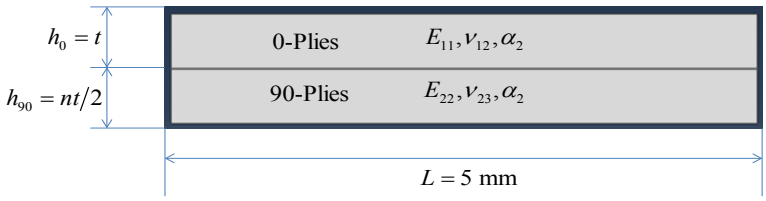

Figure 5.11 : Geometry and material properties for TM-AFEM models of T300/934 $[0/90_n/0]_T$ laminates.

Under uniaxial loading, transverse cracks form in the 90-plies region. The applied stress, σ_a, is a combination of mechanical and thermal loading. Suppose that the $[0/90_n/0]_T$ T300/934 laminate at a stress free reference temperature of θ_0 is constrained at both the left and right sides in the longitudinal direction. Given a uniform negative temperature drop, $\Delta\theta = \theta - \theta_0 < 0$, the resulting applied stress can be shown to be

$$\sigma_a = \frac{E_{11}h_0 + E_{22}h_{90}}{h_0 + h_{90}}\alpha_2 \Delta\theta \,. \tag{5.27}$$

The stress $\hat{\sigma}_n$ required to initiate a crack in n 90-plies is approximately [4]

$$\hat{\sigma}_n = \sqrt{\frac{4G_{Ic}}{\pi h\left(1/E_{22} - \nu_{12}^2/E_{11}\right)}}\,, \tag{5.28}$$

where $h = nt$ is the ply thickness of the 90-plies. The cohesive strengths and corresponding critical separations estimated using Equations (5.27) and (5.26) for different number of 90-plies are listed in Table 5.6.

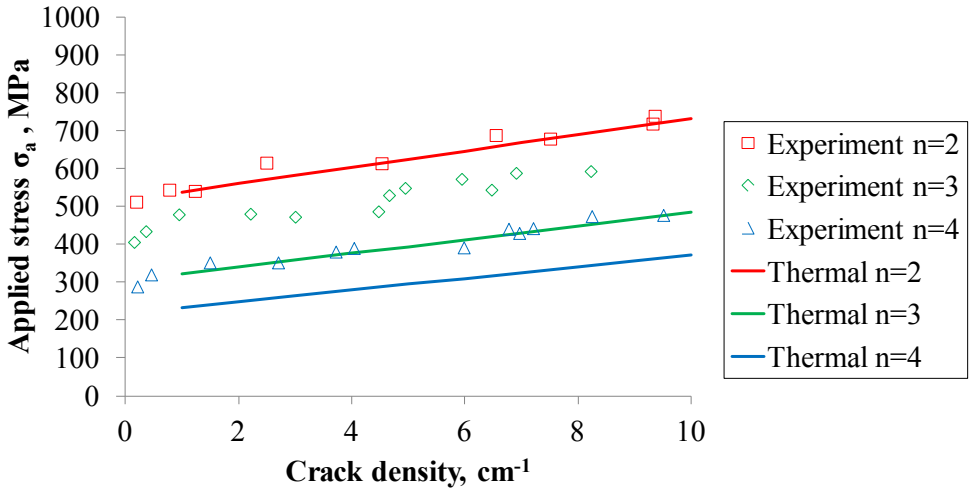

Figure 5.12: Applied stress σ_a vs. crack density in T300/934 $[0/90_n/0]_T$ laminates using Equation (5.28) to estimate cohesive strengths.

The results of the predicted thermal stress, σ_a, which produces a given crack density using TM-AFEM is compared with experimental data [5] for uniaxially loaded $[0/90_n/0]_T$ T300/934 laminates in Figure 5.12. Here, the TM-AFEM results use Equation (5.28) to estimate cohesive strengths. It can be seen that for $n = 2$ 90-plies, the TM-AFEM result is in excellent agreement with experimental data. It correctly captures the linear relationship between applied stress and crack density. But for $n = 3$ and $n = 4$, the TM-AFEM results under predict the required applied stress because of a corresponding drop in cohesive strength. However, the linear relationship between applied stress and crack density is preserved. As the number of plies increases, the strength estimated by Equation (5.28) scales inversely with the square root of ply thickness, i.e. $\hat{\sigma}_n \propto 1/\sqrt{h}$. For even a modest increase in the number of plies, the reduction of cohesive strength is significant and leads to the under predicted applied stress seen in Figure 5.12. Given that the cohesive zone size (estimated from Equation (5.14)) is about 1 mm (about 8 ply thickness), the inverse square root dependence on h is perhaps overestimated.

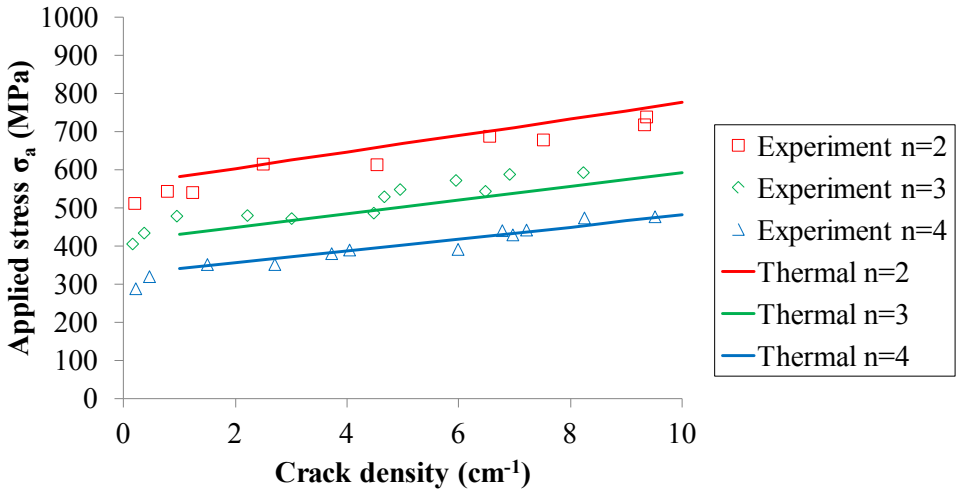

Figure 5.13: Applied stress σ_a vs. crack density in $[0/90_n/0]_T$ laminates using cohesive strengths that best fit experimental data.

Figure 5.13 compares the experimental data with the TM-AFEM result using a best fit approach where the cohesive strengths for the different number of plies as chosen to best fit the experimental data. The cohesive parameters for this best fit approach are given in Table 5.6. Cohesive stresses for the best fit approach vary within a smaller range, a 10 MPa difference in strength between $n = 2$ and $n = 4$, and do not drop significantly with increasing number of plies in comparison to estimates using Equation (5.28).

Table 5.5: Mechanical properties of T300/934.

Longitudinal modulus, E_{11}	138 GPa
Transverse modulus, E_{22}	11.7 GPa
In-plane Poisson's ratio, ν_{12}	0.29
Out-plane Poisson's ratio, ν_{23}	0.4
Thermal expansion coefficient, α_1	0.09 $\mu m \cdot m^{-1} \cdot °C^{-1}$
Thermal expansion coefficient, α_2	28.8 $\mu m \cdot m^{-1} \cdot °C^{-1}$
Critical energy release rate, G_{Ic} **(90/90 interface)**	228 $J \cdot m^{-2}$
Lamina thickness, t	0.132 mm

Table 5.6: Cohesive parameters for different number of 90 plies.

	Using Equation (5.28)		Best fit to data	
Number of 90-plies, n	**Mode I cohesive strength,** $\hat{\sigma}$ **(MPa)**	**Critical separation,** δ_c **(µm)**	**Cohesive strength,** $\hat{\sigma}$ **(MPa)**	**Critical separation,** δ_c **(µm)**
2	114*	4.01	120	3.80
3	92.9*	4.91	115	3.96
4	80.5*	5.67	110	4.15

*The values are calculated using the transverse ply strength of 44.7 MPa as reported in [6].

5.6 Crack Patterns in Thermal Barrier Coating (TBCs) Systems

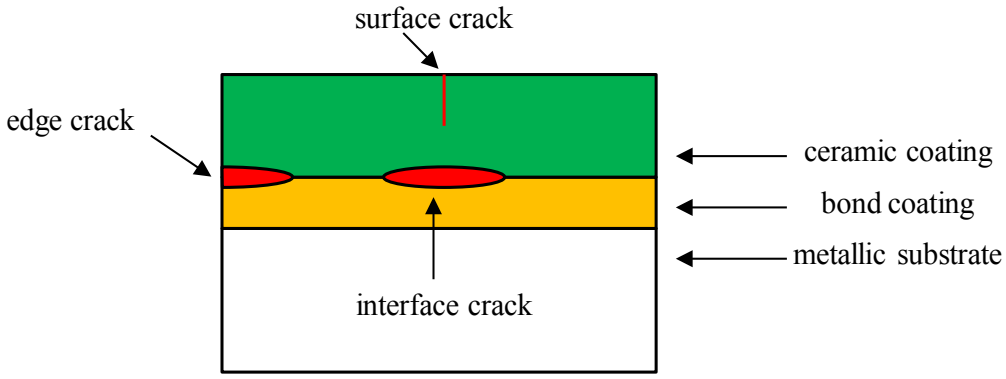

Figure 5.14: Example of a TBC with surface, interface and edge cracks..

Frequently used metallic materials are unsuited for the high temperature environment of systems such as jet engines, gas turbines or diesel engines where temperature gradients can reach and exceed 1000 K. A solution to this problem is to coat the metallic materials with a TBC, typically ceramic, that protects the metallic materials against the adverse conditions of a high temperature environment. A generic TBC system as shown in Figure 5.14 illustrates the three parts of a TBC: a ceramic coating or film, a bond coating acting as the interface and the (often metallic) substrate. Large differences in material properties of metals and ceramics subject to a high heat flux (and therefore large thermal gradient) environment result in the initiation of cracks that can lead to spalling of the protective coating and the eventual failure of the material system. Thermal fracture in TBCs is an example of cracking in pre-tensioned films which has been studied by Hutchinson and Suo under the more general analysis of fracture in layered materials [7]. Crack patterns that result have been found to depend on film thickness, elastic moduli of the layers, residual stress from thermal loading as well as fracture properties [8]. Three significant mechanisms of thermal fracture initiation and propagation in TBCs are surface cracking, free-edge

cracking and interface cracking [9]. Surface cracks refer to vertical cracks that appear on the ceramic coating surface. For zirconia coatings under high heat flux loading [10]–[13], compressive stresses relax with time at high temperatures because the coating exhibits thermally activated viscoplastic behavior. Thus when cooled, the TBC does not return to its initial state and instead tensile stresses develop in the ceramic coating and initiate vertical surface cracks. Edge cracks form mainly due to the mismatch in the rate of expansion between the ceramic coating and the substrate. Stresses that develop at the edge are singular in nature and in general experience mixed-mode fracture. Finally the interface cracks, so called because they form along the interface that connects the ceramic coating to the substrate, are driven by bending moments due to the tensile stresses that develop upon cooling. These three typical types of cracks are illustrated in Figure 5.14. In the subsequent sections, the TBC is modeled with TM-AFEM elements, and it will be demonstrated how the arbitrary initiation and propagation of all three types of cracks can be simulated.

5.6.1 Geometry and Thermo-elastic Properties of TBC Numerical Model

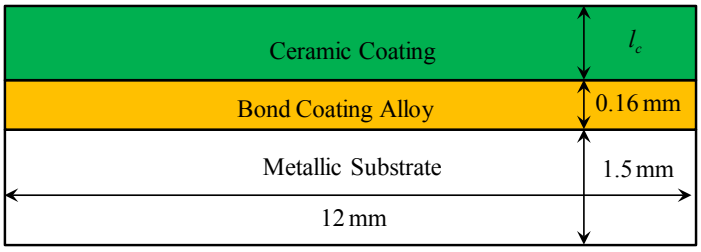

Figure 5.15 : Idealized cross section of TBC test specimen used for numerical model with TM-AFEM elements.

Three bonded material regions consisting of the ceramic coating, bond coating alloy and metallic substrate make up the numerical model with the dimensions as shown in

Figure 5.15. The dimensions approximate the section of the larger TBC test specimen subjected to approximately uniform high heat flux laser heating in [14]. Three numerical models are made for ceramic coating thicknesses of $l_c = 0.25$, 0.75 and 1.5 mm with an element size of approximately 0.1 mm for meshes of 2400, 3000 and 3840 TM-AFEM elements, respectively. Surface and interface cracks form in experiment after a heating and cooling thermal cycle because the stress relaxes at high temperature with time so that when cooled, a net tensile stress develops and drives the formation of cracks. Thus in reality, material behavior is both time and temperature dependent but the current formulation and implementation of the TM-AFEM element is thermo-elastic and does not support temperature dependent material properties. Therefore, the material properties are assumed temperature independent, and the values are taken to be the average of the temperature dependent properties reported in [15] for a the simulation of thermal shock tests of a TBC over different temperature ranges. This approximation retains some accuracy as the majority of the material properties in [15] do not exhibit significant temperature dependence. The values of the mechanical and thermal properties used in the numerical simulations are summarized in Table 5.7.

Table 5.7: Temperature independent thermo-elastic properties of material regions in the TBC.

Material Region	**Specific Heat (J/kg·K)**	**Density (kg/m^3)**	**Elastic Modulus (GPa)**	**Poisson's Ratio**	**Thermal Expansion Coefficient ($x10^{-5}$ K^{-1})**	**Thermal Conductivity (W/m·K)**
Ceramic Coating (YSZ)	586	5257	10.67	0.25	0.87	0.89
Bond Coating Alloy	565	6291	53.50	0.30	1.07	25.0

Material Region	Specific Heat (J/kg·K)	Density (kg/m^3)	Elastic Modulus (GPa)	Poisson's Ratio	Thermal Expansion Coefficient (x10^{-5} K^{-1})	Thermal Conductivity (W/m·K)
Metallic Substrate (Steel)	434	7850	200	0.30	1.50	51.9

5.6.2 Determination of Cohesive Properties and Crack Initiation Criterion

The toughness of YSZ is known to range from 45-150 J·m^{-2} [16] while most steel alloys have a fracture toughness of close to 50 MPa·m$^{1/2}$ [17]. As an estimate, from LEFM, the mode I fracture toughness K_{Ic} is related to the fracture energy G_{Ic} in the case of plane stress through Equation (5.3). The TM-AFEM element uses a linear traction-separation law where the area under the curve is the fracture energy while the relation between the critical crack separation δ_c, cohesive strength $\hat{\sigma}$ and fracture energy G_{Ic} is given in Equation (5.26). The fracture toughness of YSZ then is assumed to be $K_{Ic} = 0.7$ MPa·m$^{1/2}$ from which the fracture energy, $G_{Ic} = 48.8$ J·m^{-2}, can be obtained from Equation (5.3). Thermal stresses on the ceramic coating surface in the cooling phase with the effects of stress relaxation have been shown to be about 15 MPa [18]. Therefore, the normal and shear cohesive strengths are taken to be 15 MPa so that cracks can initiate and grow within the temperature differences applied. The critical separations in the normal and shear directions are solved for from Equation (5.26) using the assumed fracture toughness of 0.7 MPa·m$^{1/2}$ for both modes I and II. The cohesive strength of the metallic substrate is to be the typical yield strength of steel, 350 MPa. The bond coating is assumed to have the same fracture toughness and cohesive strength as the ceramic coating to enable the expected interface cracks near or within the material region.

Resulting estimated cohesive properties used in the simulations for the different material regions are summarized in Table 5.8. Cracks initiate when the stress criterion described in Section 4.3.4.1 is satisfied. The resulting heat flow is essentially one dimensional in the direction of thickness so that the cooler temperatures are closer to the top surface.

Table 5.8 : Cohesive properties for the material regions of TBC for surface-interface cracks.

Material Region	**Fracture Toughness ($MPa \cdot m^{1/2}$)**	**Normal Cohesive Strength (MPa)**	**Normal Critical Separation (mm)**	**Shear Cohesive Strength (MPa)**	**Shear Critical Separation (mm)**
Ceramic Coating (YSZ)	0.7	15	6.11×10^{-3}	15	6.11×10^{-3}
Bond Coating Alloy	0.7	15	1.22×10^{-3}	15	1.22×10^{-3}
Metallic Substrate (Steel)	50	350	0.0714	350	0.0714

5.6.3 Boundary Conditions for Simulation of a TBC System

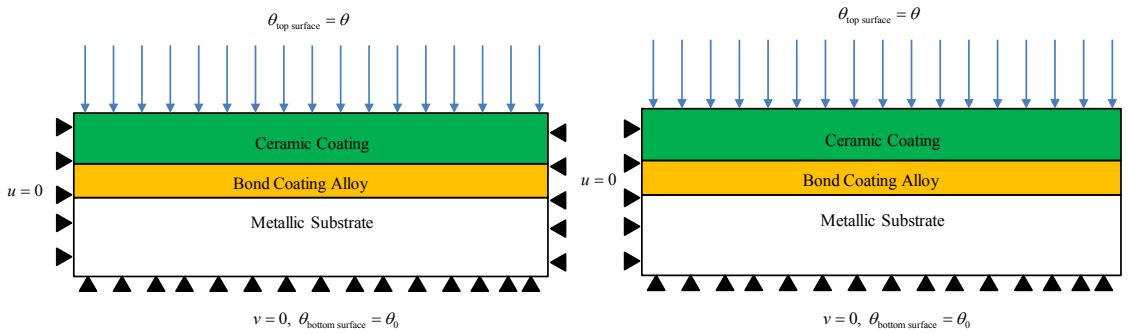

Figure 5.16: Boundary conditions for uniform temperature change across the ceramic coating surface favorable for (a) surface and interface cracks and (b) edge cracks.

A stress free reference temperature of $\theta_0 = 0$ K is assumed. A temperature gradient is applied in the transverse direction of the TBC system such that $\theta_{\text{top surface}} = \theta$ and $\theta_{\text{bottom surface}} = \theta_0$. The temperature change is negative to induce tensile thermal stress and

approximate the cooling process of a heated TBC that develops cracks. Two boundary conditions are considered here as shown in Figure 5.16 for a steady state heat transfer process. In the first setup, Figure 5.16(a), the left and right edges of the model are constrained in the *x* direction while the bottom surface is constrained in the *y* direction, allowing tensile stresses to result, predominantly in the *x* direction, and initiate cracks. The second setup, Figure 5.16(b), removes the constraint in the *x* direction on the right side to create a free edge where edge interface cracks can form.

5.6.4 Effect of Applied Temperature Gradient and Coating Thickness on Surface Cracks

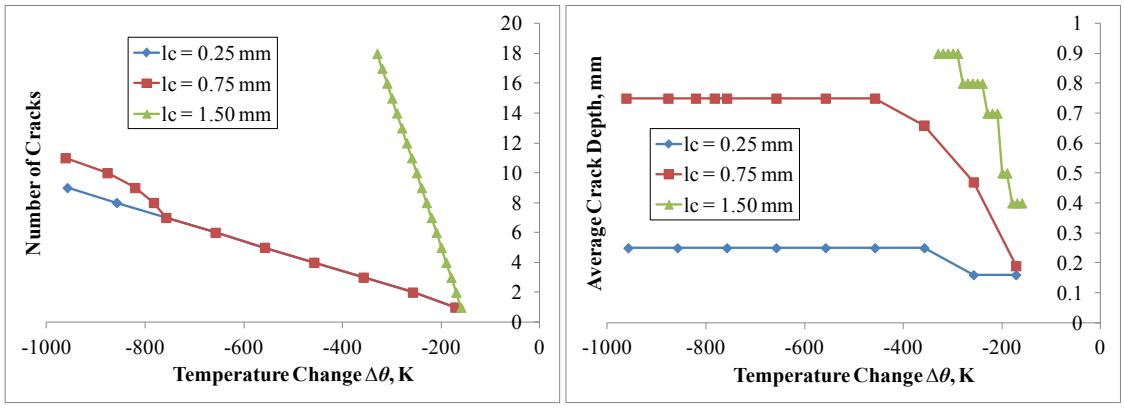

(a) (b)

Figure 5.17 : The (a) number of surface cracks initiated and (b) average crack depth as functions of θ_0 for the boundary conditions in Figure 5.16(a).

Only surface cracks are considered by inhibiting cracks to form within the bond coating material region. The results of the simulations for steady state heat transfer of an applied thermal gradient, $\Delta\theta = \theta - \theta_0$, for the first boundary condition setup are shown in Figure 5.17. For all three meshes, increasing the temperature change in general increases the number of cracks initiated and the average depth of the surface cracks. Because the simulation diverges at higher temperature difference for the largest coating thickness

$l_c = 1.5$ mm, the trends associated with this coating thickness is unclear. However, Figure 5.17(a) shows a linear relationship between the applied temperature gradient and the number of surface cracks that initiate. There is an increase in the rate at which cracks initiate with the applied temperature gradient between the smaller coating thicknesses of $l_c = 0.25,\ 0.75$ mm and the larger one of $l_c = 1.50$ mm. This suggests an intriguing but unclear relationship between coating thickness and the number of surface cracks. As seen in Figure 5.17(b), for smaller ceramic coating thicknesses, average crack depth approaches the respective ceramic coating thickness with an increasing negative temperature gradient (a temperature change of about $\Delta\theta = -350$ K for $l_c = 0.25$ mm and $\Delta\theta = -450$ K for $l_c = 0.75$ mm). This is because the propagating cracks are arrested at the bonding interface from propagating due to the higher cohesive strength in the bond coating and substrate material regions. Before divergence, average crack depth steadily increases with a larger temperature gradient for $l_c = 1.50$ mm. In general, the cracking behavior of the TM-AFEM models is congruent with the experimental observations of Choules et. al. [14] that higher maximum surface temperatures prior to the cooling of heated TBCs (i.e. higher temperature changes) cause longer surface cracks regardless of ceramic coating thickness.

5.6.5 Crack patterns in TBC Systems

In the prior section, only surface cracks were considered. Here both interface and edge cracks are demonstrated to naturally emerge when not inhibited. A condition is imposed so that only horizontal cracks can initiate within the bond coating region because it is known from experiments [10]–[14], [19]–[21] that horizontal cracks are the

preferred mode of fracture near the interface region of the bond coating. The results of the simulations with this condition are illustrated in Figure 5.18 and Figure 5.19 for the two loading cases in Figure 5.16 with ceramic coating thicknesses of 0.25 mm and 0.75 mm under an applied temperature gradient of $\Delta\theta = -1000$ K . The inserts in both figures are strain contours of the TM-AFEM models where cracks are represented by solid black lines and the element region associated with the bond coating are outlined by red horizontal lines.

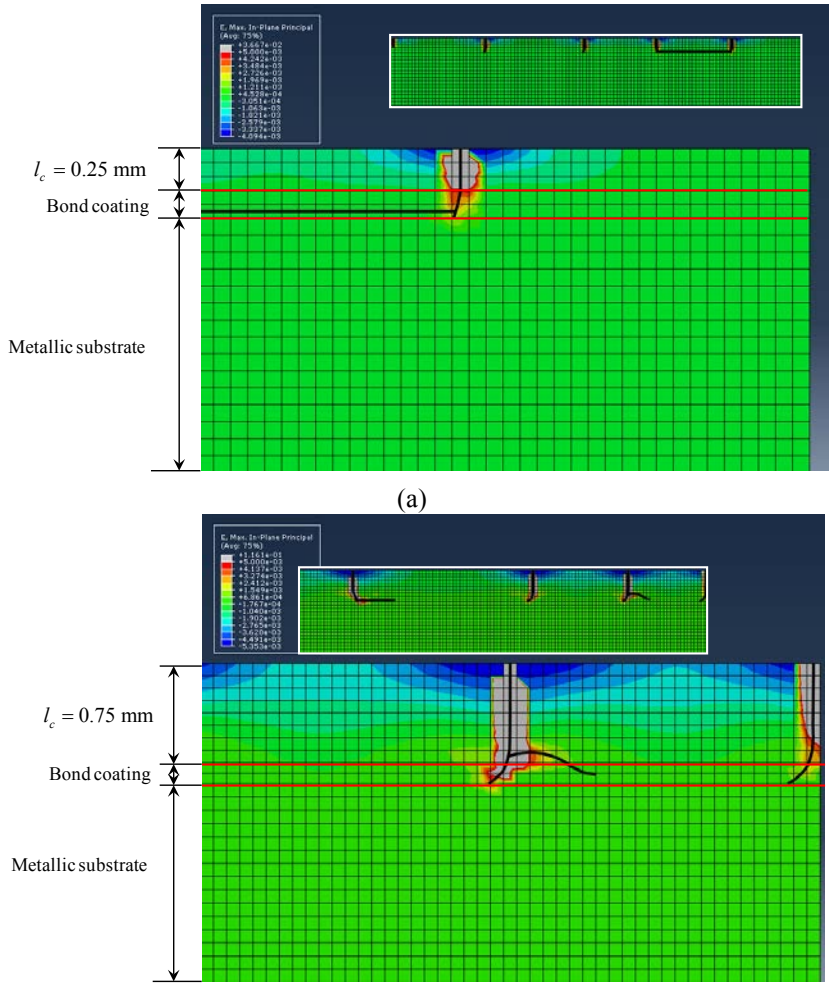

Figure 5.18: Cracking patterns as a result of applied temperature gradient of $\Delta\theta$ = -1000 K for the boundary condition in Figure 5.16(a) for (a) l_c = 0.25 mm and (b) l_c = 0.75 mm.

In the experiment by Choules et. al. [14], horizontal interface cracks form at higher temperature changes when the number of surface cracks are lower and specifically underneath surface cracks. This is because during cooling, the horizontal tensile stress σ_x that opens surface cracks creates a bending moment that induces vertical tensile stress σ_y which creates an interface crack [12]. This mechanism of thermal fracture is realized with the TM-AFEM element model. Crack patterns for both ceramic coating thicknesses in Figure 5.18 show a clear transition from a propagating vertical surface crack to a horizontal interface crack for both coating thicknesses. In Figure 5.18(b), the surface cracks curve towards the horizontal direction as they approach the interface and then successfully transition into an interface crack. The temperature at this transition for 0.75 mm thickness is about $\Delta\theta = -558$ K. The model for 0.25 mm in particular presents a long interface crack indicative of a delamination of the ceramic coating that occurs at a temperature gradient of $\Delta\theta = -658$ K. Like in experiment, interface cracks only form in proximity to surface cracks because the former is induced by the latter. A rather interesting result is a bifurcating crack in Figure 5.18(b) which forms at about an applied temperature gradient of $\Delta\theta = -558$ K. This cracking pattern has been well observed in experiment [10], [13] to occur as a result of larger temperature changes.

Crack patterns in Figure 5.19 are simulated under the boundary condition in Figure 5.16(b), a favorable situation for edge cracks to form and propagate. Thus Figure 5.19(a)&(b) both exhibit an edge crack on the unconstrained right edge of the TBC model due to the stress mismatch at the interface. Again, interface cracks form under surface cracks for as seen for 0.25 mm in Figure 5.19(a). There is also evidence of surface cracks attempting to curve to a more horizontal direction at the larger ceramic coating thickness

of 0.75 mm. It is also observed that interior interface cracks underneath the surface cracks are inhibited by the interface crack at the right edge. This is the likely result of the relieving of the bending moment that drives the formation of interface cracks at a particular surface crack because of the proximity of the formed interface edge crack.

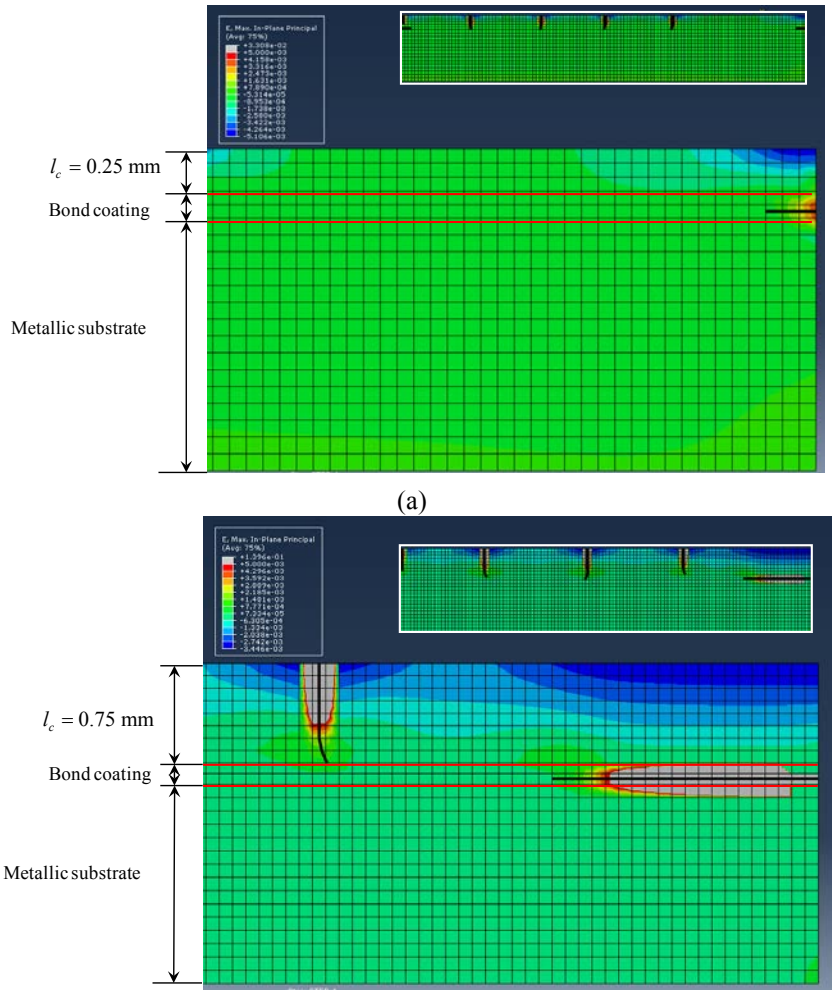

Figure 5.19: Cracking patterns as a result of applied temperature gradient of $\Delta\theta$ = -1000 K for the free edge boundary condition in Figure 5.16(b) for (a) l_c = 0.25 mm and (b) l_c = 0.75 mm.

It is worth noting that the number of surface cracks allowed to initiate were found to have a strong influence on whether interface cracks occur, and thus surface cracks were limited to be no more than five in number for the examples in Figure 5.18 and Figure

5.19 in order to see presence of interface cracks. More surface cracks relieve the tensile stress in the ceramic coating and dampen the effect of the bending moment in creating interface cracks so that a characteristic number of surface cracks exists that is sufficient to inhibit the initiation of interface cracks. These results corroborate the experimental observations found in [14] where the response of interface cracks to thermal load is dependent on the morphology of surface cracks in the ceramic coating.

5.7 Discussion on the Utility of TM-AFEM Elements for Thermal Fracture

Through the various numerical examples used to evaluate the performance of the TM-AFEM element developed in this work, it has been demonstrated that the effects of temperature on fracture can be realistically captured. Fracture is demonstrated to be capable of being completely temperature driven as a temperature change produces an equivalent force loading at constrained boundaries. Since a temperature change boundary condition is effectively an equivalent mechanical load condition, numerically it is less stable than applying a displacement boundary condition. Use of the TM-AFEM element may need to be accompanied with some form of numerical damping in certain problems to ensure convergence.

The numerical example of transverse ply cracking in laminates demonstrates how effective the TM-AFEM can be in simulating experimental results. From knowing only basic material parameters and estimates for the cohesive strength, experimental results can accurately be reproduced. This result gives confidence in the capabilities of the TM-AFEM as a research and design tool.

Through the numerical example of a TBC, TM-AFEM elements have been demonstrated to be capable of simulating the arbitrary initiation and growth of the three

prominent crack patterns that arise in TBC systems due to thermal loading. The numerical example shows that crack patterns are sensitive to changes in applied temperature gradient and ceramic coating thickness. Simulation results are in reasonably good agreement with experimental observations in spite of the idealizations in the numerical model. This provides assurance in the capabilities of TM-AFEM elements in correctly accounting for the basic underlying mechanisms of thermal fracture. Further, all three crack types are successfully simulated without the need to predefine their location. Crack patterns of each type arbitrarily initiate when the stress criterion is met and propagate under prescribed boundary conditions.

The TM-AFEM elements however still have some limitations in their use in simulating thermal fracture. For example, at higher temperature changes in the prior numerical TBC examples, simulations have difficulty in converging to a solution. This is attributed to the instability of the fracture process because of the fracture properties and the thermal loading condition which is essentially a load-controlled scheme which is known for unstable fracture. There is also the question of how to calibrate appropriate thermo-mechanical properties for the cohesive zone model. This is a relatively unexplored research area. Finally, the current thermo-elasticity based TM-AFEM needs to be expanded to include temperature-dependent, nonlinear material properties in order to simulate general thermo-mechanical problems.

5.8 Future Study

The current iteration of the TM-AFEM element shows great promise as a tool for engineering research and design. Many avenues for future development in thermal fracture are possible. They include

1. Inclusion of temperature dependence for material properties.
2. Extension of the current TM-AFEM element to 3D.
3. Refinement and validation of the thermo-mechanical cohesive zone law.
4. Finite element formulation for elastic-plastic stress analysis.
5. Capability for thermal creep at high temperature

This list is by no means exhaustive but represents important topics to be explored for high fidelity simulation of thermal fracture.

References

[1] J. Hutchinson and Z. Suo, "Mixed mode cracking in layered materials," *Adv. Appl. Mech.*, 1992.

[2] J. W. Hutchinson and A. G. Evans, "On the delamination of thermal barrier coatings in a thermal gradient," *Surf. Coatings Technol.*, vol. 149, no. 2–3, pp. 179–184, Jan. 2002.

[3] B. N. Cox, J. B. Davis, D. B. Marshall, and Q. D. Yang, "Integral textile ceramic composites for turbine engine combustors," in *Volume 4: Turbo Expo 2002, Parts A and B*, 2002, pp. 1–7.

[4] K. F. Wesling, D. F. Socie, and B. Beardsley, "Fatigue of thick thermal barrier coatings," *J. Am. Ceram. Soc.*, vol. 77, no. 7, pp. 1863–1868, Jul. 1994.

[5] R. C. Brink, "Material property evaluation of thick thermal barrier coating systems," *J. Eng. Gas Turbines Power*, vol. 111, no. 3, p. 570, Jul. 1989.

[6] K. Kokini and B. D. Choules, "Surface thermal fracture of functionally graded ceramic coatings: Effect of architecture and materials," *Compos. Eng.*, vol. 5, no. 7, pp. 865–877, Jan. 1995.

[7] K. Kokini, B. D. Choules, and Y. R. Takeuchi, "Thermal fracture mechanisms in ceramic thermal barrier coatings," *J. Therm. Spray Technol.*, vol. 6, no. 1, pp. 43–49, Mar. 1997.

[8] B. . Choules, K. Kokini, and T. . Taylor, "Thermal fracture of thermal barrier coatings in a high heat flux environment," *Surf. Coatings Technol.*, vol. 106, no. 1, pp. 23–29, Jul. 1998.

[9] B. D. Choules, K. Kokini, and T. A. Taylor, "Thermal fracture of ceramic thermal barrier coatings under high heat flux with time-dependent behavior.," *Mater. Sci. Eng. A*, vol. 299, no. 1–2, pp. 296–304, Feb. 2001.

[10] K. Kokini, A. Banerjee, and T. A. Taylor, "Thermal fracture of interfaces in precracked thermal barrier coatings," *Mater. Sci. Eng. A*, vol. 323, no. 1–2, pp. 70–82, Jan. 2002.

[11] S. Rangaraj and K. Kokini, "Interface thermal fracture in functionally graded zirconia–mullite–bond coat alloy thermal barrier coatings," *Acta Mater.*, vol. 51, no. 1, pp. 251–267, Jan. 2003.

[12] B. Zhou and K. Kokini, "Effect of pre-existing surface crack morphology on the interfacial thermal fracture of thermal barrier coatings: a numerical study," *Mater. Sci. Eng. A*, vol. 348, no. 1–2, pp. 271–279, May 2003.

[13] S. Rangaraj and K. Kokini, “Fracture in single-layer zirconia (YSZ)–bond coat alloy (NiCoCrAlY) composite coatings under thermal shock,” *Acta Mater.*, vol. 52, no. 2, pp. 455–465, Jan. 2004.

[14] B. Zhou and K. Kokini, “Effect of preexisting surface cracks on the interfacial thermal fracture of thermal barrier coatings: an experimental study,” *Surf. Coatings Technol.*, vol. 187, no. 1, pp. 17–25, Oct. 2004.

[15] A. Gilbert, K. Kokini, and S. Sankarasubramanian, “Thermal fracture of zirconia–mullite composite thermal barrier coatings under thermal shock: An experimental study,” *Surf. Coatings Technol.*, vol. 202, no. 10, pp. 2152–2161, Feb. 2008.

[16] A. Gilbert, K. Kokini, and S. Sankarasubramanian, “Thermal fracture of zirconia–mullite composite thermal barrier coatings under thermal shock: A numerical study,” *Surf. Coatings Technol.*, vol. 203, no. 1–2, pp. 91–98, Oct. 2008.

[17] A. Florence and J. Goodier, “Thermal stress at spherical cavities and circular holes in uniform heat flow,” *J. appl. Mech*, 1959.

[18] A. Florence and J. Goodier, “The linear thermoelastic problem of uniform heat flow disturbed by a penny-shaped insulated crack,” *Int. J. Eng. Sci.*, 1963.

[19] G. C. Sih, “On the singular character of thermal stresses near a crack tip,” *J. Appl. Mech.*, vol. 29, no. 3, p. 587, Sep. 1962.

[20] J. R. Barber, “Steady-state thermal stresses caused by an imperfectly conducting penny-shaped crack in an elastic solid,” *J. Therm. Stress.*, vol. 3, no. 1, pp. 77–83, Jan. 1980.

[21] W.-H. Chen and C.-C. Huang, “Three-dimensional thermal analysis of an infinite solid containing an elliptical surface crack,” *Int. J. Fract.*, vol. 54, no. 3, pp. 225–234, Apr. 1992.

[22] Y. Lee and F. Erdogan, “Interface cracking of FGM coatings under steady-state heat flow,” *Eng. Fract. Mech.*, vol. 59, no. 3, pp. 361–380, Feb. 1998.

[23] G. Qian, T. Nakamura, and C. C. Berndt, “Effects of thermal gradient and residual stresses on thermal barrier coating fracture,” *Mech. Mater.*, vol. 27, no. 2, pp. 91–110, Feb. 1998.

[24] T. C. Miller and R. Chona, “Finite element analysis of a thermally loaded interface crack in a ceramic coating,” *Eng. Fract. Mech.*, vol. 59, no. 2, pp. 203–214, Jan. 1998.

[25] B. Cox and Q. Yang, “In quest of virtual tests for structural composites.,” *Science*, vol. 314, no. 5802, pp. 1102–7, Nov. 2006.

[26] J. Barson and S. Rolfe, “Fracture and fatigue control in structures. Applications of fracture mechanics,” *Am. Soc. Test. Mater. West …*, 1999.

[27] J. Ignaczak and M. Ostoja-Starzewski, *Thermoelasticity with finite wave speeds*. Oxford, New York: Oxford University Press, 2010, p. 411.

[28] A. C. Fischer-Cripps, “Introduction to contact mechanics,” in *Introduction to Contact Mechanics*, 2nd ed., 2007, p. 221.

[29] C. E. Inglis, “Stresses in a plate due to the presence of cracks and sharp corners,” *SPIE MILESTONE Ser. MS*, 1997.

[30] A. A. Griffith, “VI. The phenomena of rupture and flow in solids.,” *Phil. Trans. Roy. Soc.(Lon.) A*, 1920.

[31] G. R. Irwin, “Analysis of stresses and strains near the end of a crack traversing a plate,” *J. Appl. Mech.*, 1957.

[32] G. R. Irwin, J. A. Kies, and H. L. Smith, *Fracture strengths relative to onset and arrest of crack propagation*, vol. 58. pp. 640–657.

[33] T.-R. Hsu, *The finite element method in thermomechanics*. Winchester, Massachussetts: Allen & Unwin, Inc., 1986.

[34] D. Dugdale, “Yielding of steel sheets containing slits,” *J. Mech. Phys. Solids*, vol. D, pp. 100–104, 1960.

[35] G. Barenblatt, “The formation of equilibrium cracks during brittle fracture. General ideas and hypotheses. Axially-symmetric cracks,” *J. Appl. Math. Mech.*, 1959.

[36] G. Barenblatt, “The mathematical theory of equilibrium cracks in brittle fracture,” *Adv. Appl. Mech.*, 1962.

[37] A. Hillerborg, M. Modéer, and P. Petersson, “Analysis of crack formation and crack growth in concrete by means of fracture mechanics and finite elements,” *Cem. Concr. Res.*, vol. 6, 1976.

[38] R. M. L. Foote, Y.-W. Mai, and B. Cotterell, “Crack growth resistance curves in strain-softening materials,” *J. Mech. Phys. Solids*, vol. 34, no. 6, pp. 593–607, Jan. 1986.

[39] J. G. Williams, “Fracture mechanics of polymers,” *Polym. Eng. Sci.*, vol. 17, no. 3, pp. 144–149, Mar. 1977.

[40] V. Tvergaard and J. W. Hutchinson, “The relation between crack growth resistance and fracture process parameters in elastic-plastic solids,” *J. Mech. Phys. Solids*, vol. 40, no. 6, pp. 1377–1397, Aug. 1992.

[41] A. Needleman, “An analysis of tensile decohesion along an interface,” *J. Mech. Phys. Solids*, vol. 38, no. 3, pp. 289–324, Jan. 1990.

[42] J. Planas, M. Elices, G. . Guinea, F. . Gómez, D. . Cendón, and I. Arbilla, “Generalizations and specializations of cohesive crack models,” *Eng. Fract. Mech.*, vol. 70, no. 14, pp. 1759–1776, Sep. 2003.

[43] A. Hillerborg, “The theoretical basis of a method to determine the fracture energyG F of concrete,” *Mater. Struct.*, vol. 18, no. 4, pp. 291–296, Jul. 1985.

[44] P. Rahulkumar, A. Jagota, S. J. Bennison, and S. Saigal, “Cohesive element modeling of viscoelastic fracture: application to peel testing of polymers,” *Int. J. Solids Struct.*, vol. 37, no. 13, pp. 1873–1897, Mar. 2000.

[45] I. Mohammed and K. M. Liechti, “Cohesive zone modeling of crack nucleation at bimaterial corners,” *J. Mech. Phys. Solids*, vol. 48, no. 4, pp. 735–764, Apr. 2000.

[46] J. . Hutchinson and A. . Evans, “Mechanics of materials: top-down approaches to fracture,” *Acta Mater.*, vol. 48, no. 1, pp. 125–135, Jan. 2000.

[47] S. R. Hallett, “Numerical investigation of progressive damage and the effect of layup in notched tensile tests,” *J. Compos. Mater.*, vol. 40, no. 14, pp. 1229–1245, Sep. 2005.

[48] F. P. van der Meer, C. Oliver, and L. J. Sluys, “Computational analysis of progressive failure in a notched laminate including shear nonlinearity and fiber failure,” *Compos. Sci. Technol.*, vol. 70, no. 4, pp. 692–700, Apr. 2010.

[49] Q. D. Yang, B. N. Cox, R. K. Nalla, and R. O. Ritchie, “Fracture length scales in human cortical bone: the necessity of nonlinear fracture models.,” *Biomaterials*, vol. 27, no. 9, pp. 2095–113, Mar. 2006.

[50] Q. D. Yang, B. N. Cox, R. K. Nalla, and R. O. Ritchie, “Re-evaluating the toughness of human cortical bone.,” *Bone*, vol. 38, no. 6, pp. 878–87, Jun. 2006.

[51] C. G. Dávila, P. P. Camanho, and A. Turon, “Effective simulation of delamination in aeronautical structures using shells and cohesive elements,” *J. Aircr.*, vol. 45, no. 2, pp. 663–672, May 2008.

[52] C. G. Davila, “Failure criteria for FRP laminates,” *J. Compos. Mater.*, vol. 39, no. 4, pp. 323–345, Feb. 2005.

[53] F. Costanzo, “Steady growth of a crack with a rate and temperature sensitive cohesive zone,” *J. Mech. Phys. Solids*, vol. 50, no. 8, pp. 1649–1679, Aug. 2002.

[54] T. W. Bjerke and J. Lambros, “Theoretical development and experimental validation of a thermally dissipative cohesive zone model for dynamic fracture of amorphous polymers,” *J. Mech. Phys. Solids*, vol. 51, no. 6, pp. 1147–1170, Jun. 2003.

[55] A. Hattiangadi and T. Siegmund, “Bridging effects in cracked laminates under thermal gradients,” *Mech. Res. Commun.*, vol. 29, no. 6, pp. 457–464, Nov. 2002.

[56] A. Hattiangadi and T. Siegmund, “A thermomechanical cohesive zone model for bridged delamination cracks,” *J. Mech. Phys. Solids*, vol. 52, no. 3, pp. 533–566, Mar. 2004.

[57] A. Hattiangadi and T. Siegmund, “A numerical study on interface crack growth under heat flux loading,” *Int. J. Solids Struct.*, vol. 42, no. 24–25, pp. 6335–6355, Dec. 2005.

[58] I. Özdemir, W. A. M. Brekelmans, and M. G. D. Geers, “A thermo-mechanical cohesive zone model,” *Comput. Mech.*, vol. 46, no. 5, pp. 735–745, Jun. 2010.

[59] L. Benabou, Z. Sun, and P. R. Dahoo, “A thermo-mechanical cohesive zone model for solder joint lifetime prediction,” *Int. J. Fatigue*, vol. 49, pp. 18–30, Apr. 2013.

[60] N. Moës and T. Belytschko, “Extended finite element method for cohesive crack growth,” *Eng. Fract. Mech.*, vol. 69, no. 7, pp. 813–833, May 2002.

[61] N. Moës, J. Dolbow, and T. Belytschko, “A finite element method for crack growth without remeshing,” *Int. J. Numer. Methods Eng.*, vol. 46, no. 1, pp. 131–150, 1999.

[62] T. Strouboulis, K. Copps, and I. Babuška, “The generalized finite element method,” *Comput. Methods Appl. Mech. Eng.*, vol. 190, no. 32–33, pp. 4081–4193, May 2001.

[63] C. Daux, N. Moes, J. Dolbow, N. Sukumar, and T. Belytschko, “Arbitrary branched and intersecting cracks with the extended finite element method,” *Int. J. Numer. Methods Eng.*, vol. 48, no. 12, pp. 1741–1760, Aug. 2000.

[64] T. Hettich, A. Hund, and E. Ramm, “Modeling of failure in composites by X-FEM and level sets within a multiscale framework,” *Comput. Methods Appl. Mech. Eng.*, vol. 197, no. 5, pp. 414–424, Jan. 2008.

[65] D. B. P. Huynh and T. Belytschko, “The extended finite element method for fracture in composite materials,” *Int. J. Numer. Methods Eng.*, vol. 77, no. 2, pp. 214–239, Jan. 2009.

[66] J.-H. Song, P. M. A. Areias, and T. Belytschko, “A method for dynamic crack and shear band propagation with phantom nodes,” *Int. J. Numer. Methods Eng.*, vol. 67, no. 6, pp. 868–893, Aug. 2006.

[67] F. P. Meer and L. J. Sluys, “A phantom node formulation with mixed mode cohesive law for splitting in laminates,” *Int. J. Fract.*, vol. 158, no. 2, pp. 107–124, May 2009.

[68] J. J. C. Remmers, R. de Borst, and A. Needleman, “A cohesive segments method for the simulation of crack growth,” *Comput. Mech.*, vol. 31, no. 1–2, pp. 69–77, May 2003.

[69] J. J. C. Remmers, “Discontinuities in materials and structures: a unifying computational approach,” Oct. 2006.

[70] A. Hansbo and P. Hansbo, “A finite element method for the simulation of strong and weak discontinuities in solid mechanics,” *Comput. Methods Appl. Mech. Eng.*, vol. 193, no. 33–35, pp. 3523–3540, Aug. 2004.

[71] X. J. Fang, Z. Q. Zhou, B. N. Cox, and Q. D. Yang, “High-fidelity simulations of multiple fracture processes in a laminated composite in tension,” *J. Mech. Phys. Solids*, vol. 59, no. 7, pp. 1355–1373, Jul. 2011.

[72] D. Ling, Q. Yang, and B. Cox, “An augmented finite element method for modeling arbitrary discontinuities in composite materials,” *Int. J. Fract.*, vol. 156, no. 1, pp. 53–73, May 2009.

[73] M. Holl, S. Loehnert, and P. Wriggers, “An adaptive multiscale method for crack propagation and crack coalescence,” *Int. J. Numer. Methods Eng.*, vol. 93, no. 1, pp. 23–51, Jan. 2013.

[74] M. J. Borden, C. V. Verhoosel, M. A. Scott, T. J. R. Hughes, and C. M. Landis, “A phase-field description of dynamic brittle fracture,” *Comput. Methods Appl. Mech. Eng.*, vol. 217–220, pp. 77–95, Apr. 2012.

[75] C. Miehe, M. Hofacker, and F. Welschinger, “A phase field model for rate-independent crack propagation: Robust algorithmic implementation based on operator splits,” *Comput. Methods Appl. Mech. Eng.*, vol. 199, no. 45–48, pp. 2765–2778, Nov. 2010.

[76] B. Bourdin, G. A. Francfort, and J.-J. Marigo, “The variational approach to fracture,” *J. Elast.*, vol. 91, no. 1–3, pp. 5–148, Mar. 2008.

[77] J. Alfaiate, G. N. Wells, and L. J. Sluys, “On the use of embedded discontinuity elements with crack path continuity for mode-I and mixed-mode fracture,” *Eng. Fract. Mech.*, vol. 69, no. 6, pp. 661–686, Apr. 2002.

[78] A. Ibrahimbegovic and S. Melnyk, “Embedded discontinuity finite element method for modeling of localized failure in heterogeneous materials with structured mesh: an alternative to extended finite element method,” *Comput. Mech.*, vol. 40, no. 1, pp. 149–155, Jan. 2007.

[79] L. J. Sluys and A. H. Berends, “Discontinuous failure analysis for mode-I and mode-II localization problems,” *Int. J. Solids Struct.*, vol. 35, no. 31–32, pp. 4257–4274, Nov. 1998.

[80] C. Linder and F. Armero, “Finite elements with embedded branching,” *Finite Elem. Anal. Des.*, vol. 45, no. 4, pp. 280–293, Mar. 2009.

[81] C. Linder and F. Armero, “Finite elements with embedded strong discontinuities for the modeling of failure in solids,” *Int. J. Numer. Methods Eng.*, vol. 72, no. 12, pp. 1391–1433, Dec. 2007.

[82] D. Dias-da-Costa, J. Alfaiate, L. J. Sluys, and E. Júlio, “Towards a generalization of a discrete strong discontinuity approach,” *Comput. Methods Appl. Mech. Eng.*, vol. 198, no. 47–48, pp. 3670–3681, Oct. 2009.

[83] T. Belytschko, J. Fish, and B. E. Engelmann, “A finite element with embedded localization zones,” *Comput. Methods Appl. Mech. Eng.*, vol. 70, no. 1, pp. 59–89, Sep. 1988.

[84] E. N. Dvorkin, A. M. Cuitiño, and G. Gioia, “Finite elements with displacement interpolated embedded localization lines insensitive to mesh size and distortions,” *Int. J. Numer. Methods Eng.*, vol. 30, no. 3, pp. 541–564, Aug. 1990.

[85] M. Ortiz, Y. Leroy, and A. Needleman, “A finite element method for localized failure analysis,” *Comput. Methods Appl. Mech. Eng.*, vol. 61, no. 2, pp. 189–214, Mar. 1987.

[86] D. Dias-da-Costa, J. Alfaiate, L. J. Sluys, P. Areias, and E. Júlio, “An embedded formulation with conforming finite elements to capture strong discontinuities,” *Int. J. Numer. Methods Eng.*, vol. 93, no. 2, pp. 224–244, Jan. 2013.

[87] Q. Yang and W. Liu, “An efficient A-FEM for arbitrary cracking in solids,” in *ICF13*, 2013.

[88] W. Liu, Q. D. Yang, S. Mohammadizadeh, X. Y. Su, and D. S. Ling, “An accurate and efficient augmented finite element method for arbitrary crack interactions,” *J. Appl. Mech.*, vol. 80, no. 4, p. 041033, May 2013.

[89] S. Mohammadizadeh, “A novel augmented finite element method for modeling arbitrary cracking in solids,” 2013.

[90] B. C. Do, W. Liu, Q. D. Yang, and X. Y. Su, “Improved cohesive stress integration schemes for cohesive zone elements,” *Eng. Fract. Mech.*, vol. 107, pp. 14–28, Jul. 2013.

[91] J.-S. Wang and Z. Suo, “Experimental determination of interfacial toughness curves using Brazil-nut-sandwiches,” *Acta Metall. Mater.*, vol. 38, no. 7, pp. 1279–1290, Jul. 1990.

[92] Q. Yang and B. Cox, “Cohesive models for damage evolution in laminated composites,” *Int. J. Fract.*, vol. 133, no. 2, pp. 107–137, May 2005.

[93] Q. D. Yang, “Numerical simulations of adhesively-bonded beams failing with extensive plastic deformation,” *J. Mech. Phys. Solids*, vol. 47, no. 6, pp. 1337–1353, Apr. 1999.

[94] Q. D. Yang and M. D. Thouless, “Mixed-mode fracture analyses of plastically-deforming adhesive joints,” *Int. J. Fract.*, vol. 110, no. 2, pp. 175–187, Jul. 2001.

[95] J. C. J. Schellekens and R. De Borst, “On the numerical modelling of edge delamination in composites,” *Key Eng. Mater.*, vol. 120–121, pp. 131–160, May 1996.

[96] P. . Camanho and C. . Dávila, “Mixed-mode decohesion finite elements for the simulation of delamination in composite materials,” *NASA-Technical Pap.*, no. June, 2002.

[97] H. Qiao, W. Q. Chen, Q. D. Yang, and J. Lua, “Augmented cohesive elements for efficient delamination analyses of composite laminates,” *J. Eng. Mater. Technol.*, vol. 133, no. 4, p. 041010, Oct. 2011.

[98] A. Turon, P. P. Camanho, J. Costa, and C. G. Dávila, “A damage model for the simulation of delamination in advanced composites under variable-mode loading,” *Mech. Mater.*, vol. 38, no. 11, pp. 1072–1089, Nov. 2006.

[99] P. P. Camanho, C. G. Davila, and M. F. De Moura, “Numerical simulation of mixed-mode progressive delamination in composite materials,” *J. Compos. Mater.*, vol. 37, no. 16, pp. 1415–1438, Jan. 2003.

[100] C. G. Dávila, C. A. Rose, and P. P. Camanho, “A procedure for superposing linear cohesive laws to represent multiple damage mechanisms in the fracture of composites,” *Int. J. Fract.*, vol. 158, no. 2, pp. 211–223, Jun. 2009.

[101] Q. D. Yang, X. J. Fang, J. X. Shi, and J. Lua, “An improved cohesive element for shell delamination analyses,” *Int. J. Numer. Methods Eng.*, vol. 83, no. 5, p. n/a–n/a, 2010.

[102] J. Williams, “Analytical solutions for cohesive zone models,” *J. Mech. Phys. Solids*, vol. 50, no. 4, pp. 809–825, Apr. 2002.

[103] S. Mousavi, H. Xiao, and N. Sukumar, “Generalized Gaussian quadrature rules on arbitrary polygons,” *Int. J. ...*, no. October 2009, pp. 99–113, 2010.

[104] N. Sukumar and a. Tabarraei, “Conforming polygonal finite elements,” *Int. J. Numer. Methods Eng.*, vol. 61, no. 12, pp. 2045–2066, Nov. 2004.

[105] K. Hibbitte, “ABAQUS user subroutines reference manual,” *HKS INC*, 2005.

[106] H. Tada, P. C. Paris, and G. R. Irwin, *The analysis of cracks handbook*. New York: ASME Press, 2000.

[107] N. Noda, R. B. Hetnarski, and Y. Tanigawa, *Thermal stresses*, 2nd ed. New York: Taylor & Francis, 2003, pp. 39–79.

[108] P. P. Camanho, C. G. Dávila, S. T. Pinho, L. Iannucci, and P. Robinson, “Prediction of in situ strengths and matrix cracking in composites under transverse tension and in-plane shear,” *Compos. Part A Appl. Sci. Manuf.*, vol. 37, no. 2, pp. 165–176, Feb. 2006.

[109] A. S. Wang, “Fracture analysis of matrix cracking in laminated composites.,” Jan. 1985.

[110] Y. M. Han, H. T. Hahn, and R. B. Croman, “A simplified analysis of transverse ply cracking in cross-ply laminates,” *Compos. Sci. Technol.*, vol. 31, no. 3, pp. 165–177, Jan. 1988.

[111] T. Ye, Z. Suo, and A. G. Evans, “Thin film cracking and the roles of substrate and interface,” *Int. J. Solids Struct.*, vol. 29, no. 21, pp. 2639–2648, Jan. 1992.

[112] R. P. Ingel, D. Lewis, B. A. Bender, and R. W. Rice, “Temperature dependence of strength and fracture toughness of ZrO2 single crystals,” *J. Am. Ceram. Soc.*, vol. 65, no. 9, pp. c150–c152, Sep. 1982.

[113] C. J. Gilbert, R. O. Ritchie, and W. L. Johnson, “Fracture toughness and fatigue-crack propagation in a Zr–Ti–Ni–Cu–Be bulk metallic glass,” *Appl. Phys. Lett.*, vol. 71, no. 4, p. 476, Jul. 1997.

[114] K. Kokini and Y. R. Takeuchi, “Multiple surface thermal fracture of graded ceramic coatings,” *J. Therm. Stress.*, vol. 21, no. 7, pp. 715–725, Oct. 1998.

[115] B. Zhou, “Effect of surface pre-crack morphology on the fracture of thermal barrier coatings under thermal shock,” *Acta Mater.*, vol. 52, no. 14, pp. 4189–4197, Aug. 2004.

Appendix A Vectors and Matrices for TMCZ Element

A.1 Linear operators and interpolation matrices

The linear operator and interpolation matrices for node pair displacement and temperature jumps at natural coordinate ξ are given by

$$\mathbf{L}_{\Delta u} = \begin{bmatrix} -1 & 0 & 0 & 0 & 0 & 0 & 1 & 0 \\ 0 & -1 & 0 & 0 & 0 & 0 & 0 & 1 \\ 0 & 0 & -1 & 0 & 1 & 0 & 0 & 0 \\ 0 & 0 & 0 & -1 & 0 & 1 & 0 & 0 \end{bmatrix}, \tag{A.1}$$

$$\mathbf{L}_{\Delta\theta} = \begin{bmatrix} -1 & 0 & 1 & 0 \\ 0 & -1 & 0 & 1 \end{bmatrix}, \tag{A.2}$$

$$\mathbf{N}_{\Delta u} = \begin{bmatrix} 1-\xi & 0 & \xi & 0 \\ 0 & 1-\xi & 0 & \xi \end{bmatrix}, \tag{A.3}$$

$$\mathbf{N}_{\Delta\theta} = \begin{bmatrix} 1-\xi & \xi \end{bmatrix} \tag{A.4}$$

A.2 Stresses at the integration points

For the piece-wise linear cohesive laws described in Section 2.4.1, the cohesive stress can be expressed as

$$\begin{aligned} \tau(\delta_s) &= \operatorname{sgn}(\delta_s)[\hat{\tau}^{(i-1)} - \alpha_s{}^{(i-1)}\delta_s{}^{(i-1)} + \alpha_s{}^{(i-1)}|\delta_s|], && \text{for } \delta_s{}^{(i-1)} < |\delta_s| \le \delta_s{}^{(i)} \\ \sigma(\delta_n) &= \hat{\sigma}^{(j-1)} - \alpha_n{}^{(j)}\delta_n{}^{(j-1)} + \alpha_n{}^{(j)}\delta_n, && \text{for } \delta_n{}^{(j-1)} < \delta_n \le \delta_n{}^{(j)} \end{aligned} \tag{A.5}$$

where free indices i, j ranging from 1 to 4 reference the appropriate cohesive segment. The cohesive stresses at N integration points can then be expressed as

$$\begin{Bmatrix} \tau_A \\ \sigma_A \\ \cdots \\ \tau_N \\ \sigma_N \end{Bmatrix} = \begin{Bmatrix} \hat{\tau}^{(I_1)} + \alpha_s{}^{(I_1)}(\delta_{sA} - \delta_{s0}{}^{(I_1)}) \\ \hat{\sigma}^{(I_2)} + \alpha_n{}^{(I_2)}(\delta_{nA} - \delta_{n0}{}^{(I_2)}) \\ \cdots \\ \hat{\tau}^{(I_{2N-1})} + \alpha_s{}^{(I_{2N-1})}(\delta_{sB} - \delta_{s0}{}^{(I_{2N-1})}) \\ \hat{\sigma}^{(I_{2N})} + \alpha_n{}^{(I_{2N})}(\delta_{nB} - \delta_{n0}{}^{(I_{2N})}) \end{Bmatrix} = \{\boldsymbol{\sigma}_0\} + [\boldsymbol{\alpha}_0] \begin{Bmatrix} \delta_{sA} \\ \delta_{nA} \\ \cdots \\ \delta_{sN} \\ \delta_{nN} \end{Bmatrix} \tag{A.6}$$

where $I_1, I_2, \ldots I_{2N-1}, I_{2N}$ are free indices each ranging from 1 to 4, indexing which linear segment the cohesive stresses should be computed from the crack displacements. The characteristic stress vector $\boldsymbol{\sigma}_0$ and characteristic stiffness matrix $\boldsymbol{\alpha}_0$ at the integration points are given by

$$\boldsymbol{\sigma}_0 = \begin{Bmatrix} \hat{\tau}^{(I_1)} - \alpha_s^{(I_1)} \delta_{s0}^{(I_1)} \\ \hat{\sigma}^{(I_2)} - \alpha_n^{(I_2)} \delta_{n0}^{(I_2)} \\ \cdots \\ \hat{\tau}^{(I_{2N-1})} - \alpha_s^{(I_{2N-1})} \delta_{s0}^{(I_{2N-1})} \\ \hat{\sigma}^{(I_{2N})} - \alpha_n^{(I_{2N})} \delta_{n0}^{(I_{2N})} \end{Bmatrix}, \tag{A.7}$$

$$\boldsymbol{\alpha}_0 = \begin{bmatrix} \alpha_s^{(I_1)} & 0 & 0 & 0 \\ 0 & \alpha_n^{(I_2)} & 0 & 0 \\ \cdots & \cdots & \cdots & \cdots \\ 0 & 0 & \alpha_s^{(I_{2N-1})} & 0 \\ 0 & 0 & 0 & \alpha_n^{(I_{2N})} \end{bmatrix}. \tag{A.8}$$

Recall that crack separation as a function of ξ along the reference line is given by

$$\left\{\delta_s(\xi), \delta_n(\xi)\right\}^T = \left[\mathbf{N}_{\Delta u}(\xi)\right] \mathrm{Diag}\left[\mathbf{R}; \mathbf{R}\right] \left[\mathbf{L}_{\Delta u}\right] \{\mathbf{u}\}. \tag{A.9}$$

Therefore, crack separations at N integration points is simply

$$\begin{Bmatrix} \delta_{sA} \\ \delta_{nA} \\ \cdots \\ \delta_{sN} \\ \delta_{nN} \end{Bmatrix} = \left[\mathbf{N}_{\mathbf{std}\Delta u}(\xi)\right] \mathrm{Diag}\left[\mathbf{R}; \mathbf{R}\right] \left[\mathbf{L}_{\Delta u}\right] \{\mathbf{u}\}, \tag{A.10}$$

where $\mathbf{N}_{\mathbf{std}\Delta u}$ is the general interpolation matrix for N integration points. Thus Equation (A.6) can alternatively be expressed as

$$\begin{Bmatrix} \tau_A \\ \sigma_A \\ \cdots \\ \tau_N \\ \sigma_N \end{Bmatrix} = \{\boldsymbol{\sigma}_0\} + [\boldsymbol{\alpha}_0]\left[\mathbf{N}_{\mathbf{std}\Delta u}(\xi)\right]\mathrm{Diag}\left[\mathbf{R};\mathbf{R}\right]\left[\mathbf{L}_{\Delta u}\right]\{\mathbf{u}\} \tag{A.11}$$

A.3 Heat fluxes at the integration points

For the piece-wise linear cohesive law described in Section 2.4.2, the cohesive heat flux can be expressed as

$$q_c(\delta_n, \Delta\theta_c) = \left[\hat{h}^{(k-1)} - \beta_n^{(k)}\delta_{\theta n}^{(k-1)} + \beta_n^{(k)}\delta_n\right]\Delta\theta_c \quad \delta_n \in \Delta\delta_{\theta n}^{(k)}. \tag{A.12}$$

Thus the cohesive heat fluxes at N integration points can then be expressed as

$$\begin{Bmatrix} q_A \\ \vdots \\ q_N \end{Bmatrix} = \mathrm{Diag}\left[\begin{Bmatrix} \delta_{nA} \\ \vdots \\ \delta_{nN} \end{Bmatrix} + \left[\boldsymbol{\beta}_0\right]\right]\begin{Bmatrix} \Delta\theta_A \\ \vdots \\ \Delta\theta_N \end{Bmatrix} \tag{A.13}$$

where $\mathbf{h}_0$ is the characteristic heat transfer coefficient vector and $\boldsymbol{\beta}_0$ is the matrix

$$\{\mathbf{h}_0\} = \begin{Bmatrix} h_A^{(i-1)} - \beta_n^{(i)}\delta_n^{(i-1)} \\ \vdots \\ h_N^{(j-1)} - \beta_n^{(j)}\delta_n^{(j-1)} \end{Bmatrix} \tag{A.14}$$

$$\left[\boldsymbol{\beta}_0\right] = \mathrm{Diag}\left[\beta_n^{(i)};\cdots;\beta_n^{(j)}\right] = \begin{bmatrix} \beta_n^{(i)} & \cdots & 0 \\ \vdots & \ddots & \vdots \\ 0 & \cdots & \beta_n^{(j)} \end{bmatrix} \tag{A.15}$$

Normal crack separation and temperature jump are interpolated through the relations

$$\delta_n(\xi) = \left[\mathbf{N}_{\theta u}(\xi)\right]\mathrm{Diag}\left[\mathbf{R};\mathbf{R}\right]\left[\mathbf{L}_{\Delta u}\right]\{\mathbf{u}\}, \tag{A.16}$$

$$\Delta\theta_c(\xi) = \left[\mathbf{N}_{\Delta\theta}(\xi)\right]\left[\mathbf{L}_{\Delta\theta}\right]\{\boldsymbol{\theta}\}, \tag{A.17}$$

where $\mathbf{N}_{\theta u}$ is the temperature-displacement interpolation matrix that interpolates only the normal crack separation and is defined as

$$\mathbf{N}_{\theta u} = \begin{bmatrix} 0 & 1-\xi & 0 & \xi \end{bmatrix}. \tag{A.18}$$

Therefore, the normal crack separations and temperature jumps at N integration points are given by

$$\left\{\delta_{nA},...,\delta_{nN}\right\}^T = \left[\mathbf{N}_{\mathbf{std}\theta u}\left(\xi\right)\right]\mathrm{Diag}\left[\mathbf{R};\mathbf{R}\right]\left[\mathbf{L}_{\Delta u}\right]\left\{\mathbf{u}\right\}, \tag{A.19}$$

$$\left\{\Delta\theta_A,...,\Delta\theta_N\right\}^T = \left[\mathbf{N}_{\mathbf{std}\Delta\theta}\left(\xi\right)\right]\left[\mathbf{L}_{\Delta\theta}\right]\left\{\boldsymbol{\theta}\right\}, \tag{A.20}$$

where $\mathbf{N}_{\mathbf{std}\theta u}$ and $\mathbf{N}_{\mathbf{std}\Delta\theta}$ are the modified temperature-displacement and temperature jump interpolation matrices. Thus alternatively, Equation (A.13) may be expressed as

$$\begin{Bmatrix} q_A \\ \vdots \\ q_N \end{Bmatrix} = \mathrm{Diag}\left[\left\{\mathbf{h}_0\right\} + \left[\boldsymbol{\beta}_0\right]\left[\mathbf{N}_{\mathbf{std}\theta u}\right]\mathrm{Diag}\left[\mathbf{R};\mathbf{R}\right]\left[\mathbf{L}_{\Delta u}\right]\left\{\mathbf{u}\right\}\right]\left[\mathbf{N}_{\mathbf{std}\Delta\theta}\right]\left[\mathbf{L}_{\Delta\theta}\right]\left\{\boldsymbol{\theta}\right\}. \tag{A.21}$$

Appendix B Vectors and Matrices for TM-AFEM Element

B.1 Matrices for TM-AFEM With No Discontinuity

For a 4 node quadrilateral element, relevant matrices are

$$\mathbf{N}_u = \begin{bmatrix} N_1(x,y) & 0 & \cdots & N_4(x,y) & 0 \\ 0 & N_1(x,y) & \cdots & 0 & N_4(x,y) \end{bmatrix}, \tag{B.1}$$

$$\mathbf{N}_\theta = \begin{bmatrix} N_1(x,y) & \cdots & N_4(x,y) \end{bmatrix}, \tag{B.2}$$

$$\mathbf{B}_u = \begin{bmatrix} \dfrac{\partial}{\partial x} & 0 \\ 0 & \dfrac{\partial}{\partial y} \\ \dfrac{\partial}{\partial y} & \dfrac{\partial}{\partial x} \end{bmatrix} \begin{bmatrix} \mathbf{N}_u \end{bmatrix}, \tag{B.3}$$

$$\mathbf{B}_\theta = \begin{bmatrix} \dfrac{\partial}{\partial x} \\ \dfrac{\partial}{\partial y} \end{bmatrix} \begin{bmatrix} \mathbf{N}_\theta \end{bmatrix}, \tag{B.4}$$

$$\mathbf{D}_u = \frac{E}{1-\nu^2} \begin{bmatrix} 1 & \nu & 0 \\ \nu & 1 & 0 \\ 0 & 0 & \dfrac{1-\nu}{2} \end{bmatrix}, \qquad \sigma_{zz} = \sigma_{zx} = \sigma_{zy} = 0,$$

$$\mathbf{D}_u = \frac{E}{(1+\nu)(1-2\nu)} \begin{bmatrix} 1-\nu & \nu & 0 \\ \nu & 1-\nu & 0 \\ 0 & 0 & \dfrac{1-2\nu}{2} \end{bmatrix}, \qquad \varepsilon_{zz} = \varepsilon_{zx} = \varepsilon_{zy} = 0, \tag{B.5}$$

$$\mathbf{D}_\theta = \begin{bmatrix} k & 0 \\ 0 & k \end{bmatrix}. \tag{B.6}$$

The material matrices $\mathbf{D}_u$ and $\mathbf{D}_\theta$ assume a linear elastic, isotropic material with constant thermal conductivity but these matrices can take alternate forms depending on the material of interest.

Appendix C Shape Functions and Quadrature Rules for Pentagonal Subdomains

Computation of mass and stiffness matrices in FEM require integrating shape functions and their derivatives over the given element. From [102], sufficient numerical accuracy is achieved integrating with six Gaussian points for a five node pentagon, and the numerical algorithm described within for quadrature rules in 2D yields the appropriate integration points in natural coordinates (ξ,η) and corresponding weights given in Table C.1.

Table C.1: Gaussian Integration Points and Weights for Reference Pentagon.

Integration Point	**Weight**	ξ	η
1	0.3888911512256	-0.6384668826471	0.2755538465407
2	0.3888911512256	0.3811354947551	-0.5857544067996
3	0.4229907892206	-0.4373628915568	-0.5193915726330
4	0.6764031747827	0.1239925137274	0.1363336383644
5	0.2510295128990	0.0600583693602	0.7940563773360
6	0.2436405209859	0.7791353010792	0.1936754226687

It is shown in [103] that shape functions for a polygonal element can either be Wachpress, mean-value or Laplace functions and that for a regular *n*-polygon, Laplace and Wachpress shape functions are identical. Consider reference convex *n*-polygon defined in natural coordinates $\varsigma \equiv (\xi,\eta) \in \Omega_0$ as

$$\xi = \cos\left(\frac{2\pi m}{n}\right), \qquad \eta = \sin\left(\frac{2\pi m}{n}\right), \qquad \text{for } m = 1,...,n\,. \tag{C.1}$$

A reference regular pentagon element is created when $n = 5$. The Laplace interpolant on the physical element is constructed via an isoparametric mapping from the corresponding reference element (the regular polygon with the same number of nodes as the physical

element) to the physical element defined by global coordinates $\mathbf{x} \equiv (x, y) \in \Omega$ as shown in Figure C.1.

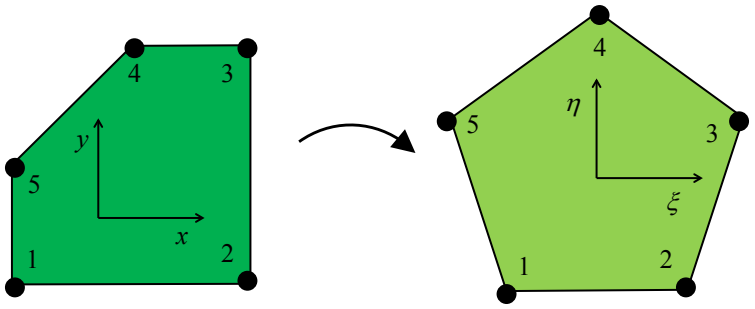

Figure C.1: One to one isoparametric mapping of (a) arbitrary physical pentagon element to (b) reference pentagon element.

A point $\mathbf{p}$ with natural coordinates $\varsigma = (\xi, \eta)$ in the interior of an n-gon element has Wachpress basis functions given by

$$N_i^w(\xi) = \frac{w_i(\xi)}{\sum_{j=1}^{n} w_j(\xi)} \quad , N_i^w(\eta) = \frac{w_i(\eta)}{\sum_{j=1}^{n} w_j(\eta)} \quad , \tag{C.2}$$

where

$$w_i(\varsigma) = \frac{A(\mathbf{p}_{i-1}, \mathbf{p}_i, \mathbf{p}_{i+1})}{A(\mathbf{p}_{i-1}, \mathbf{p}_i, \mathbf{p}) A(\mathbf{p}_i, \mathbf{p}_{i+1}, \mathbf{p})} = \frac{\cot \gamma_i + \cot \delta_i}{\|\varsigma - \varsigma_i\|^2} . \tag{C.3}$$

Let $A(a, b, c)$ denote the signed area of triangle $[a, b, c]$ and have γ_i and δ_i refer to the angles shown in Figure C.2 for the regular reference pentagon. In the natural coordinate system of the reference pentagon, the coordinates of the vertices $[\mathbf{p}_{i-1}, \mathbf{p}_i, \mathbf{p}_{i+1}, \mathbf{p}]$ are (a_1, a_2), (b_1, b_2), (c_1, c_2) and (ξ, η) respectively. Then relevant vectors are defined as

$$\begin{aligned}\mathbf{p}-\mathbf{p}_i &= (\xi-b_1)\mathbf{e}_1+(\eta-b_2)\mathbf{e}_2,\\ \mathbf{p}_{i-1}-\mathbf{p}_i &= (a_1-b_1)\mathbf{e}_1+(a_2-b_2)\mathbf{e}_2,\\ \mathbf{p}_{i+1}-\mathbf{p}_i &= (c_1-b_1)\mathbf{e}_1+(c_2-b_2)\mathbf{e}_2.\end{aligned} \tag{C.4}$$

where $\mathbf{e}_1, \mathbf{e}_2$ are unit vectors in the natural coordinate system. Vector cross product and dot product formulas are used to find the cotangents and distance as

$$\cot\gamma_i = \frac{(\mathbf{p}-\mathbf{p}_i)\bullet(\mathbf{p}_{i-1}-\mathbf{p}_i)}{\left|(\mathbf{p}-\mathbf{p}_i)\times(\mathbf{p}_{i-1}-\mathbf{p}_i)\right|} = \frac{(\xi-b_1)(a_1-b_1)+(\xi-b_2)(a_2-b_2)}{(\xi-b_1)(a_2-b_2)-(a_1-b_1)(\eta-b_2)} = \frac{\cos\gamma_i}{\sin\gamma_i}, \tag{C.5}$$

$$\cot\delta_i = \frac{(\mathbf{p}_{i+1}-\mathbf{p}_i)\bullet(\mathbf{p}-\mathbf{p}_i)}{\left|(\mathbf{p}_{i+1}-\mathbf{p}_i)\times(\mathbf{p}-\mathbf{p}_i)\right|} = \frac{(c_1-b_1)(\xi-b_1)+(c_2-b_2)(\eta-b_2)}{(c_1-b_1)(\eta-b_2)-(\xi-b_1)(c_2-b_2)} = \frac{\cos\delta_i}{\sin\delta_i}, \tag{C.6}$$

$$\left\|\boldsymbol{\varsigma}-\boldsymbol{\varsigma}_i\right\|^2 = \left\|\mathbf{p}-\mathbf{p}_i\right\|^2 = (\xi-b_1)^2+(\eta-b_2)^2. \tag{C.7}$$

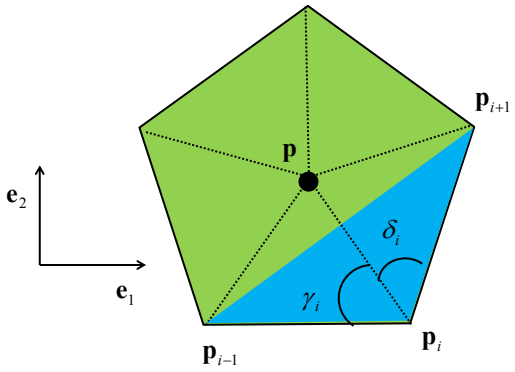

Figure C.2: Barycentric coordinates for Wachpress functions.

The partial derivatives necessary are

$$\frac{\partial N_i^w(\boldsymbol{\varsigma})}{\partial\xi} = \frac{\dfrac{\partial w_i(\boldsymbol{\varsigma})}{\partial\xi}}{\displaystyle\sum_{j=1}^{n}\frac{\partial w_j(\boldsymbol{\varsigma})}{\partial\xi}}, \qquad \frac{\partial N_i^w(\boldsymbol{\varsigma})}{\partial\eta} = \frac{\dfrac{\partial w_i(\boldsymbol{\varsigma})}{\partial\eta}}{\displaystyle\sum_{j=1}^{n}\frac{\partial w_j(\boldsymbol{\varsigma})}{\partial\eta}}, \tag{C.8}$$

$$\frac{\partial w_i(\varsigma)}{\partial \xi} = \frac{\left((\xi - a_1)^2 + (\eta - a_2)^2\right)\left(\frac{\partial(\cot\gamma_i)}{\partial \xi} + \frac{\partial(\cot\delta_i)}{\partial \xi}\right) - (\cot\gamma_i + \cot\delta_i)\left(2(\xi - b_1)\right)}{\left((\xi - b_1)^2 + (\eta - b_2)^2\right)^2},$$

$$\frac{\partial w_i(\varsigma)}{\partial \eta} = \frac{\left((\xi - b_1)^2 + (\eta - b_2)^2\right)\left(\frac{\partial(\cot\gamma_i)}{\partial \eta} + \frac{\partial(\cot\delta_i)}{\partial \eta}\right) - (\cot\gamma_i + \cot\delta_i)\left(2(\eta - b_2)\right)}{\left((\xi - b_1)^2 + (\eta - b_2)^2\right)^2},$$

(C.9)

$$\frac{\partial(\cot\gamma_i)}{\partial \xi} = \frac{(a_1 - b_1) - \cot\gamma_i (a_2 - b_2)}{\sin\gamma_i}, \qquad \frac{\partial(\cot\gamma_i)}{\partial \eta} = \frac{(a_2 - b_2) - \cot\gamma_i (b_1 - a_1)}{\sin\gamma_i},$$

$$\frac{\partial(\cot\delta_i)}{\partial \xi} = \frac{(c_1 - b_1) - \cot\delta_i (b_2 - c_2)}{\sin\delta_i}, \qquad \frac{\partial(\cot\delta_i)}{\partial \eta} = \frac{(c_2 - b_2) - \cot\delta_i (c_1 - b_1)}{\sin\delta_i}.$$

(C.10)

Therefore, following standard FEM, any point in the domain of the physical pentagon element is interpolated by the Wachpress shape functions as

$$x = \sum_{i=1}^{5} x_i N_i^w(\varsigma), \quad y = \sum_{i=1}^{5} y_i N_i^w(\varsigma), \tag{C.11}$$

the Jacobian and its determinant are then

$$[\mathbf{J}] = \begin{bmatrix} \frac{\partial x}{\partial \xi} & \frac{\partial y}{\partial \xi} \\ \frac{\partial x}{\partial \eta} & \frac{\partial y}{\partial \eta} \end{bmatrix} = \begin{bmatrix} \sum_{i=1}^{5} x_i \frac{\partial N_i^w(\varsigma)}{\partial \xi} & \sum_{i=1}^{5} y_i \frac{\partial N_i^w(\varsigma)}{\partial \xi} \\ \sum_{i=1}^{5} x_i \frac{\partial N_i^w(\varsigma)}{\partial \eta} & \sum_{i=1}^{5} y_i \frac{\partial N_i^w(\varsigma)}{\partial \eta} \end{bmatrix}, \tag{C.12}$$

$$\det[\mathbf{J}] = |\mathbf{J}| = \frac{\partial x}{\partial \xi}\frac{\partial y}{\partial \eta} - \frac{\partial x}{\partial \eta}\frac{\partial y}{\partial \xi}. \tag{C.13}$$

The integrals associated with the pentagon subdomain can be calculated in the standard FEM approach using the Wachpress shape functions and the integration points and weights given in Table C.1.